DESIGN AND DEVELOPMENT OF VISIBILITY RESTORATION TECHNIQUES FOR WEATHER DEGRADED IMAGES

A thesis submitted
in partial fulfillment of the requirements for the award of degree of
Doctor of Philosophy

Submitted By
DILBAG SINGH
(901503028)

Under the supervision of
DR. VIJAY KUMAR
(Assistant Professor)

THAPAR INSTITUTE
OF ENGINEERING & TECHNOLOGY
(Deemed to be University)

COMPUTER SCIENCE AND ENGINEERING DEPARTMENT

THAPAR INSTITUTE OF ENGINEERING AND TECHNOLOGY

PATIALA-147004, PUNJAB INDIA.

APRIL, 2019

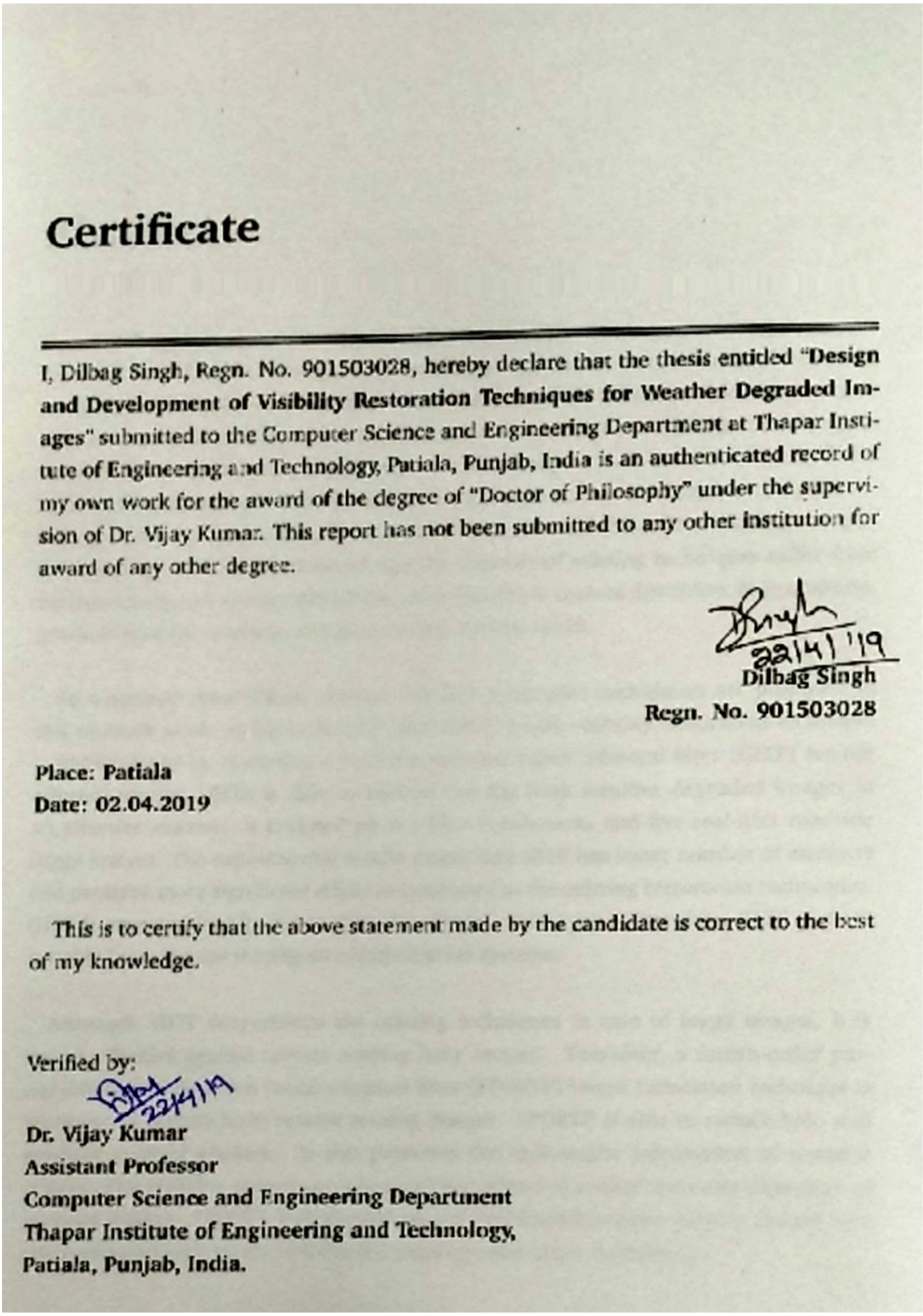

Certificate

I, Dilbag Singh, Regn. No. 901503028, hereby declare that the thesis entitled "**Design and Development of Visibility Restoration Techniques for Weather Degraded Images**" submitted to the Computer Science and Engineering Department at Thapar Institute of Engineering and Technology, Patiala, Punjab, India is an authenticated record of my own work for the award of the degree of "Doctor of Philosophy" under the supervision of Dr. Vijay Kumar. This report has not been submitted to any other institution for award of any other degree.

22/4/'19
Dilbag Singh
Regn. No. 901503028

Place: Patiala
Date: 02.04.2019

This is to certify that the above statement made by the candidate is correct to the best of my knowledge.

Verified by:
22/4/19
Dr. Vijay Kumar
Assistant Professor
Computer Science and Engineering Department
Thapar Institute of Engineering and Technology,
Patiala, Punjab, India.

Abstract

The visibility of outdoor images is greatly degraded due to the presence of fog, haze, smog, *etc.* The poor visibility may cause the failure of computer vision applications such as intelligent transportation systems, surveillance systems, and object tracking. To resolve this problem, many image restoration techniques have been developed. These techniques play an important role in improving the performance of various computer vision applications. Due to this, the researchers are attracted toward the visibility restoration techniques. It has been found that the majority of existing techniques suffer from various issues such as edge distortion, color distortion, texture distortion, halo artefacts, gradient reversal artefacts, and poor computational speed.

To overcome these issues, various visibility restoration techniques are proposed in this research work. A Dark channel prior (DCP) based visibility restoration technique is implemented by designing a Gain intervention based trilateral filter (GITF) for fog affected images. GITF is able to remove the fog from weather degraded images in an effective manner. It is tested on ten (five benchmarks and five real-life) roadside foggy images. The experimental results reveal that GITF has lesser number of artefacts and preserve more significant edges as compared to the existing restoration techniques. GITF is computationally faster than the existing techniques. Therefore, GITF is more suitable for real-time intelligent transportation systems.

Although, GITF outperforms the existing techniques in case of foggy images, it is not so effective against remote sensing hazy images. Therefore, a fourth-order partial differential equation based trilateral filter (FPDETF) based restoration technique is proposed to restore hazy remote sensing images. FPDETF is able to reduce halo and gradient reversal artefacts. It also preserves the radiometric information of restored images. The visibility restoration phase is also refined to reduce the color distortion of restored images. FPDETF is evaluated on ten well-known remote sensing images and also compared with seven well-known existing restoration techniques.

Although, FPDETF performs significantly better than the existing visibility restoration techniques. However, it suffers from sky-regions and color distortion, especially in the case of images effected from large weather gradients. Therefore, an Integrated visibility restoration model (IVRM) is proposed to solve the above-mentioned problems. It utilizes DCP, bright channel prior (BCP), and gain intervention filter. BCP is used to solve the sky-region problem associated with DCP based restoration. The gain intervention filter is also used to improve computational speed and edge preservation. IVRM is tested on ten well-known remote sensing images. The simulation results show that IVRM is able to remove halo and gradient reversal artefacts.

The designed restoration techniques (*i.e.,* GITF, FPDETF, and IVRM), suffer from noise when transmission map approaches toward zero. Thus, the evaluated atmospheric veil is more than the actual value, (*i.e.,* transmission evaluated by utilizing DCP is lesser as compared to an actual one). As a consequence, the restored color could deviate from the actual object and the restored restored image looks like an artificial image. To overcome this issue, a Modified restoration model (MRM) based DCP is designed and implemented. To further improve the atmospheric veil, a modified joint trilateral filter is also implemented to redefine the transmission map to reduce the color distortion problem. The results reveal that MRM performs effectively across a wide range of weather degradation levels without causing any visible artefacts.

The techniques designed so far such as GITF, FPDETF, IVRM, and MRM are not so-effective to preserve the texture details, especially in case of a complex background and large weather gradient image. Therefore, the exploration of new alternatives for designing an effective prior is desirable. Thus, in this research work, two novel channel priors are proposed to evaluate the depth map from weather degraded images. The main advantages of these channel priors over the existing prior are (a) eliminate sky region problem and (b) preserves better texture information of the restored image. These channels are Gradient profile prior (GPP) and Oblique gradient profile prior (OGPP).

GPP is designed to remove the haze from remote sensing images. The coarse estimated atmospheric veil is also refined by using guided L_0 minimization based filter. Moreover, the visibility restoration is also modified to overcome the over saturation and color distortion problems. Extensive experiments demonstrate that GPP can naturally restore the weather degraded image especially at the edges of sudden changes in the obtained depth map. It can achieve a good effect for single image visibility restoration.

GPP is able to evaluate horizontal and vertical edges in a local patch. However, it has been found that many oblique edges are present in an input image. Thus, the standard

gradient filter is unable to evaluate the oblique edges. Therefore, in this research work, an Oblique gradient profile prior (OGPP) is designed and developed to efficiently estimate the transmission map and atmospheric veil. The transmission map is also refined by developing a local activity-tuned anisotropic diffusion based filter. Thereafter, image restoration is performed using the estimated transmission function. OGPP has an ability to remove fog from still images in an effective manner. The performance of OGPP is compared with recently developed seven visibility restoration techniques over synthetic and real-life foggy images. The experimental results depict the supremacy of OGPP in removing the fog from still images when compared with the existing techniques. Experimental results reveal that the restored image has little or no artefacts.

Thorough extensive analyses, it has been observed that the proposed techniques can effectively suppress visual artefacts for weather degraded images and yield high-quality results as compared to the competitive visibility restoration techniques both quantitatively and qualitatively. Moreover, the relatively high computational speed of the proposed techniques will facilitate these in real-time applications.

Acknowledgments

Pursuing a Ph.D. project is both a painful and enjoyable experience. It's just like climbing a high peak, step by step, accompanied by bitterness, hardships, frustration, encouragement, and trust and with so many people's kinds help. When I found myself at the top enjoying the beautiful scenery. I realized that it was, in fact, teamwork that got me there. Though it will not be enough express my gratitude in words to all those people who helped me. I would still like to give my many, many thanks to all these people. First of all, I wish to acknowledge the benevolence of the Almighty, who gave me strength, courage, and patience to overcome all obstacles. With a profound sense of gratitude and heartiest regard,

I express my sincere feelings of indebtedness to my supervisor Dr. Vijay Kumar, Assistant Professor, Computer Science and Engineering Department, Thapar Institute of Engineering and Technology, Patiala, Punjab, India for his valuable guidance, motivation, encouragement, moral support, and invaluable cooperation. The generous and encouraging attitude with which he resolved all my problems will always have a shadow on my character. I deeply admire the delightful atmosphere for learning provided by him that made this thesis possible. It has been a great pleasure and experience to work under his guidance.

I am grateful to the Head of Department, Prof.(Dr.) Maninder Singh, who made my study a knowledgeable experience during my stay in the department. I am much obliged to the Director, Dean (RSP) and the Management of Thapar Institute of Engineering and Technology, who provided me all the necessary resources and encouraged to produce results. I am thankful to my doctoral committee members Dr. Sunil Kumar Singla, Dr. Singara Singh, and Dr. Shreelekha Pandey for their beneficial suggestions and ensuring the accurate pace of the progress of my thesis. I sincerely thank the faculty and support staff of Computer Science and Engineering department for their constant motivation. I would also like to thank Dr. Parshant Singh Rana and Dr. Husanbir Singh Pannu for sharing their deep knowledge with me in the initial phase of this journey.

I would like to shower hearty gratitude, feeling of indebtedness and endless love to my wife Manjit Kaur for her unconditional love, moral support and sacrifices which helped me achieve this target. I want to pay humble gratitude to Amandeep Singh Bhinder (Brother in law) for being my strength at every moment. I pay regard to one and everyone who knowingly or unknowingly supported me during this journey of knowledge.

Finally, I want to bestow all my love to my world, my son, Anveen Singh Gill, who came into my life during this journey and showed me in the path of positiveness with his heavenly and divine smile. Love you son.

Dilbag Singh

Contents

List of Figures

List of Tables

List of important abbreviations

Acronym	**Meaning**
ACO	Ant colony optimization
BA	Blocking artefacts
BCP	Bright channel prior
BHE	Bi-histogram equalization
CAP	Color attenuation prior
Cg	Contrast gain per pixel
CL	Color-lines
COD	Change of detail prior
DCP	Dark channel prior
DE	Depth estimation
ECBD	Effective contrast based restoration
EP	Edge preservation
ET	Execution time
FADE	Fog aware density evaluator
FHRT	Fast haze removal technique
FPDETF	Fourth-order partial differential equations based trilateral filter
FRIDA	Foggy road image database
FRIDA2	Foggy road image database 2
GA	Genetic algorithm
GF	Guided filter
GITF	Gain intervention based trilateral filter
GPP	Gradient profile prior
GRA	Gradient reversal artefacts
Gt	Ground truth images
HA	Halo artefacts
HSTS	Hybrid subjective testing set
I	Weather degraded image
I_r	Restored/clear image
ITS	Indoor training set

IVRM	Integrated visibility restoration model
KD	Known depth
L1	L_1 norm regularization based restoration technique
LHG	Large haze gradient
LTQ	Linear transform and quadtree
WHDR	Weighted the least square and high dynamic range
MDF	Multi-scale depth fusion
MI	Multiple images
MRM	Modified restoration model
MS	Multiple scattering
MSE	Mean squared error
OGPP	Oblique gradient profile prior
OTS	Outdoor training set
Pdf	Perceptual haze density
PF	Polarizing filter
PSNR	Peak signal to noise ratio
PSO	Particle swarm optimization
RESIDE	Realistic single image restoration
RSD	Remote sensing dehazing
RSWHE	Recursively separated weighted histogram equalization
RTTS	Real- world task-driven testing set
SI	Single image
SOTS	Synthetic objective testing set
S_p	Speed
SSIM	Structural similarity index metric
WGIF	Weighted guided image filter
WHDR	Weighted least square and high dynamic range

Chapter 1

Introduction

1.1 Weather degraded images

With the advancement in computer vision applications, the visibility restoration techniques have gained the attention of researchers [1]. The visibility of outdoor images is greatly degraded due to the presence of fog, haze, smog, *etc.* The poor visibility may cause the failure of computer vision applications such as intelligent transportation systems, surveillance systems, object tracking systems, *etc.* To resolve this problem, the visibility restoration techniques have been developed. These techniques play an important role in computer vision applications that are used in poor weather conditions. Due to this, the researchers are attracted toward the visibility restoration techniques. Visibility restoration techniques are extensively utilized in civil and military areas such as target detection [2], traffic surveillance [3], remote sensing [4], *etc.* Therefore, the development of visibility restoration models has become a task of great interest and significance.

In poor environmental conditions, illumination observed from a scene is sprinkled and immersed because of the considerable occurrence of molecules and aerosols are hanging in the environment [5]. With the worsening of environment eminence, fog phenomenon regularly happens. Because of the effect of intense fog, haze or smog, the intelligibility of environment and visibility are becoming weak considerably that results in significant disturbance of different vision applications. In poor environmental conditions, objects have poor visibility [6] and such images are often recognized as of low contrast and poor intensity.

Figure 1.1 (a) shows natural image captured in clear day. The fog affected image is shown in Figure 1.1 (b). The haze affected image is represented in Figure 1.1 (c). It clearly shows that it has poorer visibility than clear day and foggy images. The smoggy image is represented in Figure 1.1 (d). It is shown that the smoggy image is affected by more weather degradation as compared to the foggy and hazy image.

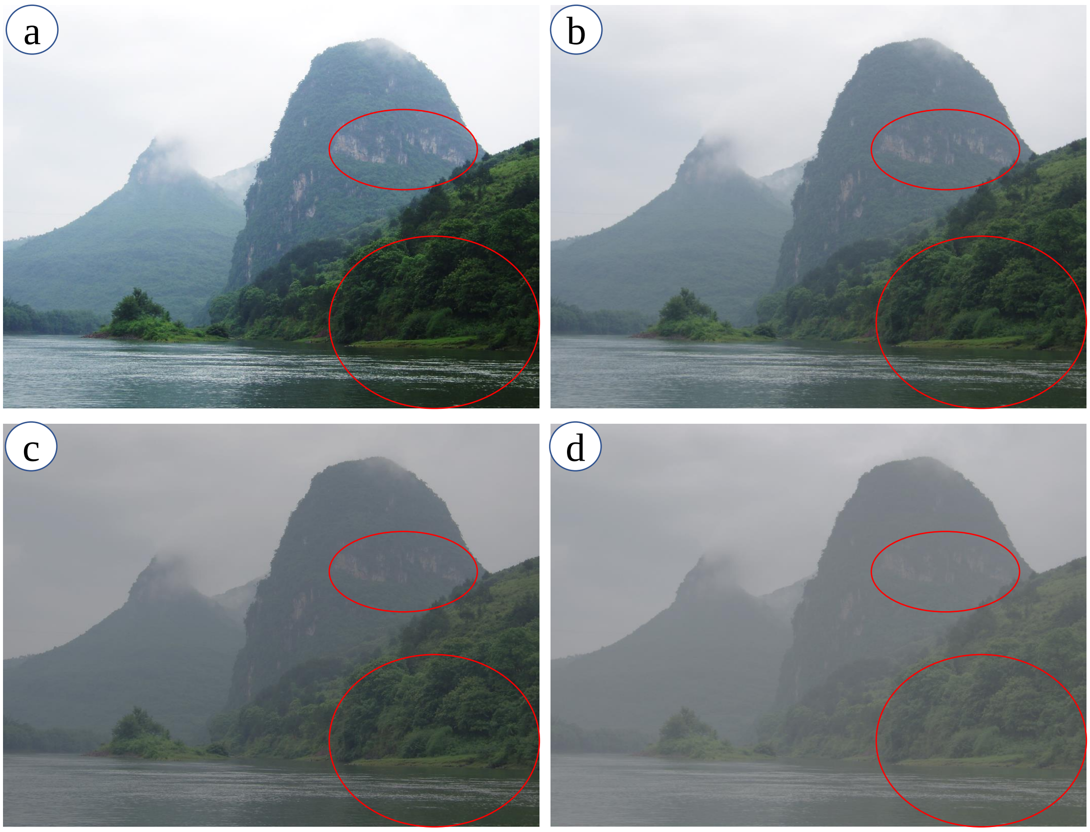

Figure 1.1: Weather degraded images (a) Natural, (b) Foggy, (c) Hazy, and (d) Smoggy image

Restoration of weather degraded image needs the information about physical features of the scene. One of these features is the depth of given scene [7]. It is evaluated from the visual camera to objects in the given scene. If the depth of the scene is known, then the visibility restoration becomes much easier [8]. However, the depth map is unknown in prior for real-life applications [9]. Therefore, the fundamental problem of visibility restoration techniques is the accurate estimation of depth map. The depth map estimation problem is not trivial and requires prior information about weather degraded image such as depth cues or atmospheric scattering [10]. The concept of depth map estimation is not new [11]. It has been extensively utilized by artists to express depth to a viewer in their paintings as early as the renaissance [12, 13].

Visibility restoration is a tough task because the transmission depends upon the unknown depth which fluctuates according to weather conditions [14]. Tan *et al.* [13] and Kawakami *et al.* [15] restored weather degraded images by utilizing the local contrast values. These techniques are successful in segments which have significant weather gradient. However, the color of the restored image is frequently over saturated [16].

The contrast maximization comes up with the over-saturation problem. The physics based restoration techniques have an ability to overcome the over-saturation problem [17, 18]. He *et al.* [16] proposed a simple and effective visibility restoration technique using DCP. However, it suffers from halo artefacts and color distortion problems [19].

Visibility restoration techniques have made considerable improvements in recent times due to the utilization of efficient suppositions and priors. Wang *et al.* [20] proposed a patch based DCP technique for solving this problem. But, it is worthless whenever the objects are intrinsically similar to airlight and no shadow is directed at them. The DCP has been found to be a well-defined restoration technique in the existing literature. However, its procedure may cause annoying halo and gradient reversal artefacts [21]. To handle these issues, several image filters have been developed to refine transmission map using a guided filter. However, these techniques have high computational time [22]. To handle this problem, a filter has been designed using gain intervention [5]. However, it suffers from the gradient reversal artefacts and color distortion problem.

Generally, weather conditions fluctuate in the category and number of particles available in the atmosphere. An enormous attempt has been made to quantify the size of these particles as shown in Table 1. Depending upon the category of visual belongings, poor weather circumstances are classified into two categories such as steady and dynamic [23]. In steady poor weather, ingredient droplets are minimized (1-10 μm) and steadily float in the atmosphere. The illumination effect at a given pixel is because of the collective consequence of high degree of droplets within the pixel's solid angle [5]. In dynamic poor weather circumstances, ingredient droplets are 1000 times more ($0.1 - 10$ mm) than steady weather [24].

Table 1.1: Weather conditions and associated particle types and sizes

Circumstances	Type	Radius(μm)
Fog	Water droplet	$1 - 10$
Cloud	Water droplet	$1 - 10$
Haze	Aerosol	$10^{-2} - 1$
Air	Molecule	10^{-4}
Rain	Water droplet	$10^{2} - 10^{4}$

Figure 1.2 demonstrates the optical imaging model. In the restored circumstances, the object imitates energy from illumination sources such as direct sunlight, diffuse skylight, and illumination reflected by the source. The energy of the input scene is reduced when it arrives in the vision system. Vision system integrates the received energy and centers it onto the image plane. Excluding the haze, images have brighter colors as shown in Figure 1.2 (a). In hazy circumstances, the situation turns out be more difficult (as seen in Figure 1.2) (b).

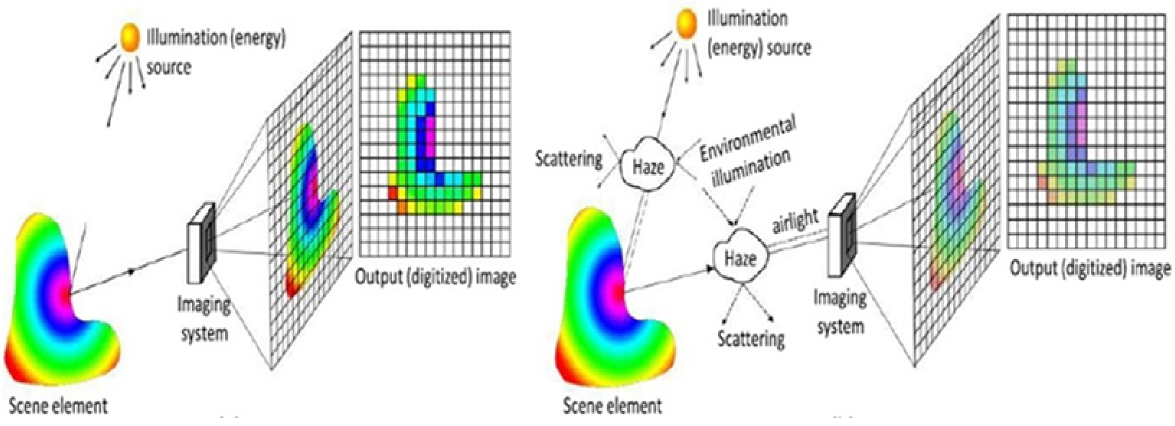

(a) (b)

Figure 1.2: Procedure of imaging under sunny weather (a) Clear day image acquisition and (b) Imaging in hazy weather

1.2 Imaging model

Koschmieder [25] and McCartney [26] defined a mathematical formulation of imaging model as:

$$I(j) = \underbrace{I_r(j)t(j)}_{\text{direct attenuation}} + \underbrace{\Upsilon(1-t(j))}_{\text{airlight}} \tag{1.1}$$

Here, I represents a weather degraded image. I_r shows actual object radiance. Υ and t show the atmospheric light and the transmission map, respectively. (j) shows the pixel coordinates of I. t demonstrates the illumination that is not sprinkled and received at camera [27, 28].

The transmission map (t) is evaluated as [16]:

$$t(j) = e^{-s_{cf}(j)D(j)} \tag{1.2}$$

Here, $D(j)$ shows the distance between an object and camera. $s_{cf}(j)$ shows the sprinkling factor that depends upon the wavelength (λ) and turbidity (t_d). In hazy environment, $s_{cf}(j)$ is assumed to be independent from λ. Also, $t \in [0,1]$ [29].

It can be observed from Eq. (1.1) that there exist two important aspects in the restoration process: (1) accurate estimation of transmission map and (2) accurate estimation of atmospheric light. Most of the techniques focus on the accurate estimation of the transmission map and they leverage empirical rule in estimating the atmospheric light. This is mainly due to the common belief that good estimation of transmission map will lead to better restoration.

Figure 1.3 shows a image formation model for remote sensing images. The transmission map (t) depicts the light which is not sprinkled and received at visual sensor [27]. It shows that in single image visibility restoration only I is known factor. Therefore, to restore I_r, it is required to estimate the t and Υ in an efficient manner. However, it has been proven that the filtering is also required to smooth t, to reduce the effect of noise from the estimated t.

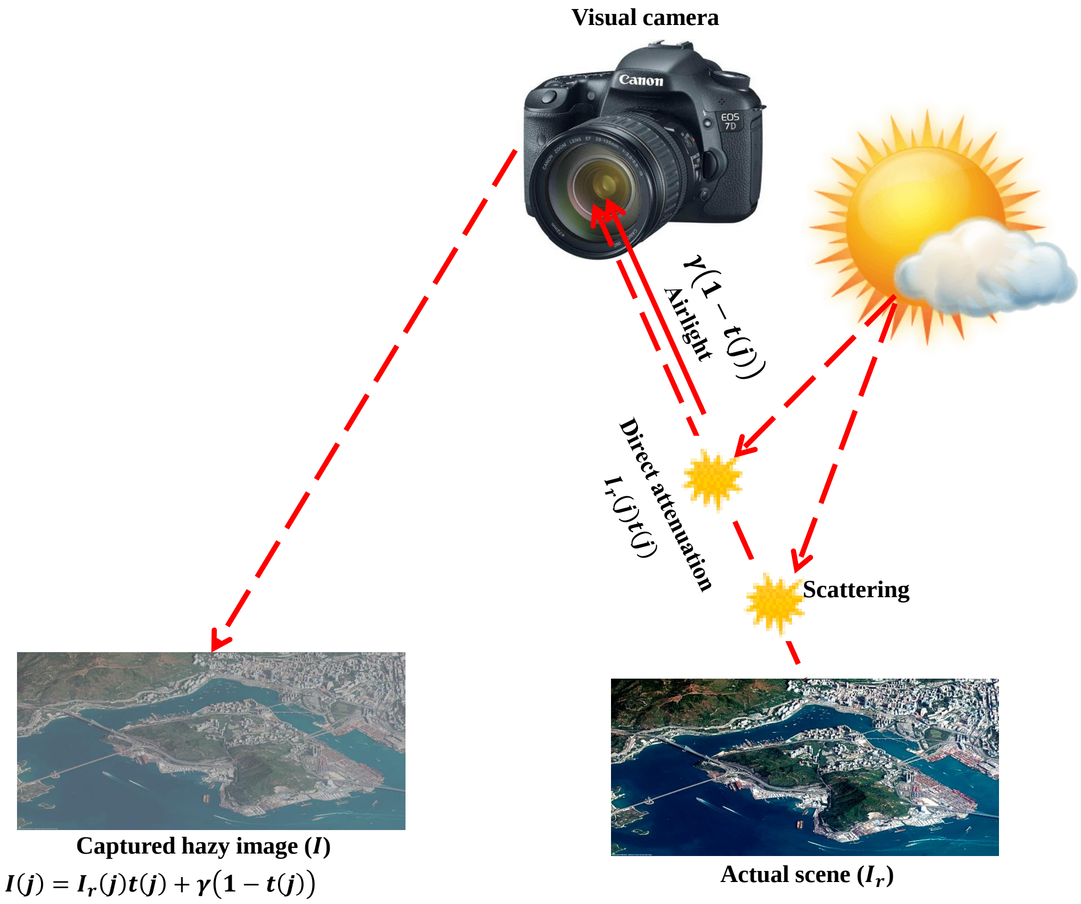

Figure 1.3: Imaging model

1.3 General framework of visibility restoration model

This section describes the mathematical formulation of DCP based visibility restoration model. DCP based restoration model consists of five main stages. These are DCP, atmospheric veil estimation, coarse atmospheric veil evaluation, transmission map refinement, and visibility restoration model [16]. Figure 1.4 shows the general framework of visibility restoration model.

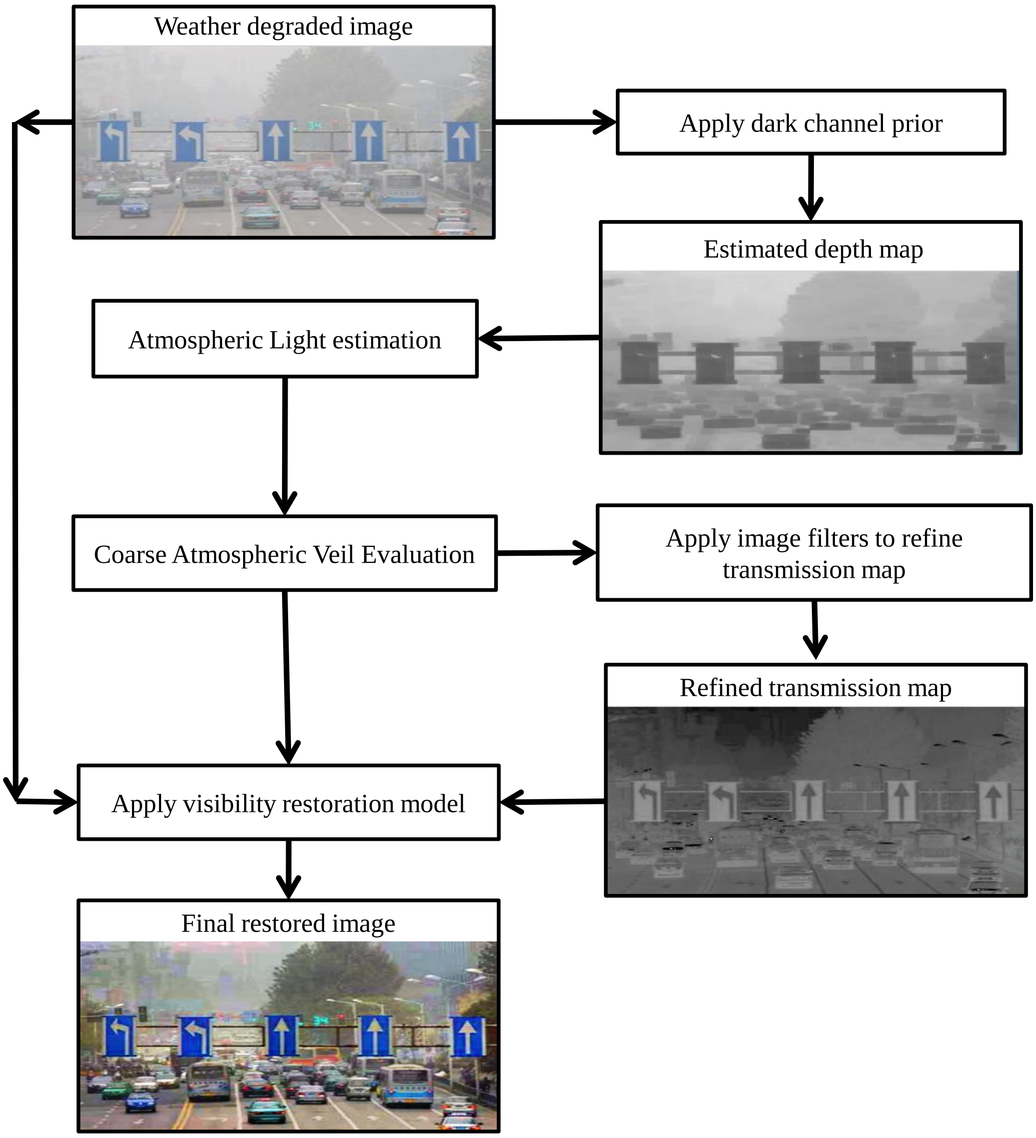

Figure 1.4: General framework of visibility restoration model

The brief description of these steps is given in the following sections.

1.3.1 Dark channel prior

Dark channel prior (DCP) states that one of color channels (R, G, or B) in weather degraded images has low illumination or even sometimes approaches towards zero [16]. For a scene (I), DCP can be mathematically evaluated as:

$$I^d(j) = \min_{y \in \mathscr{W}(j)} \left(\min_{c \in (R,G,B)} \left(I^c(j) \right) \right) \tag{1.3}$$

Here, $I^c(j)$ shows one of the RGB color channels at pixel j and $\mathscr{W}(j)$ denotes the local window centered at j. DCP states that for a weather degraded image (I), illumination of its DCP image (I^d) is minimum and even almost zero especially for darker areas.

Subsequent section, a detailed analysis of DCP of the restored outdoor images has been discussed. Figure 1.5 shows that the dark channel is applicable on hazy images. As Figure 1.5 (b) demonstrates that the dark channel of clear image approaches towards zero. Also, Figure 1.5 (d) shows the depth of a hazy image.

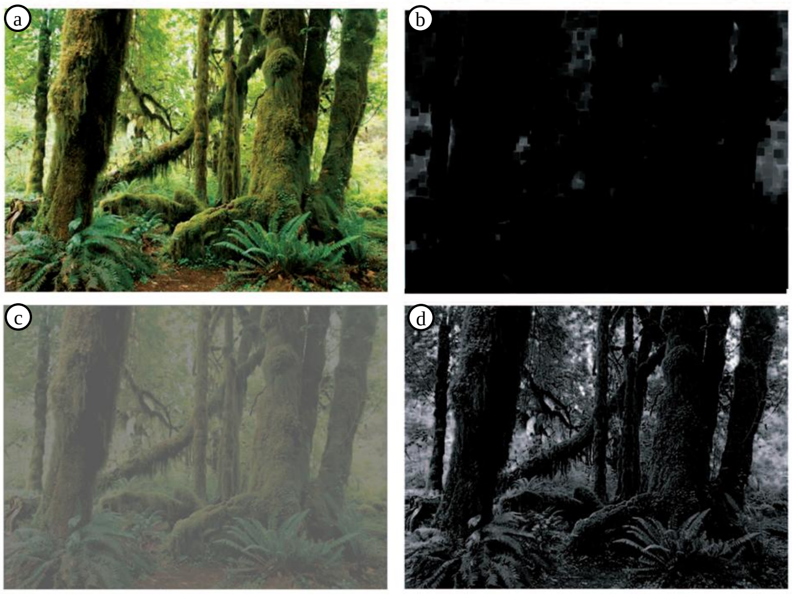

Figure 1.5: Analysis of DCP (a) Clear outdoor image, (b) Dark channel of clear image, (c) Hazy outdoor image, and (d) Dark channel of hazy image

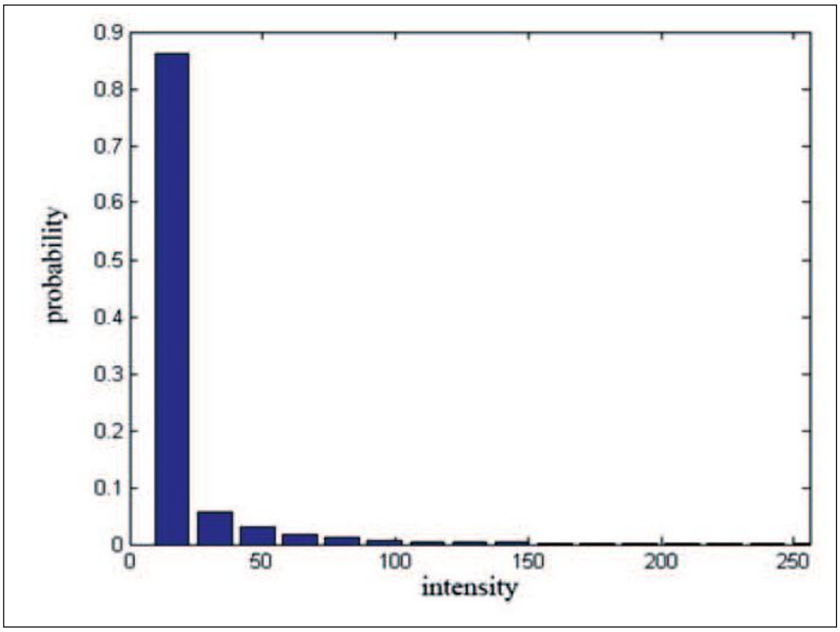

Figure 1.6: Histogram of the intensity of pixels in all 500 dark channels (each bin has 20 intensity levels).

To evaluate the effectiveness of DCP on outdoor images, 400 clear images are taken. These images are resized to 512×512 pixels. The patch size is set to 5×5 pixels. Figure 1.5 shows hazy free images along with their respective DCP. Figure 1.6 shows the intensity histogram over all 500 dark channels. It has been observed that the intensity of approximately 86 % of the pixels in the dark channels is under 12 and the intensity greater than 98 % of the pixels is under 40. These experimental analyses show that the DCP is applicable for outdoor images. However, for images captured in a hazy environment, the dark channel turns out to be invalid. Affected from the additive airlight, pixels in hazy affected segments have maximum intensity values in all color channels and the minimal intensity of local masks is maximum. Therefore, the dark channel of a hazy image will have maximum intensity in regions having higher hazy. Therefore, it proves that the intensity of the dark channel is a rough approximation of the thickness of hazy.

1.3.2 Global atmospheric light estimation

Global atmospheric light estimation plays a significant role in restoring the weather degraded image. In this work, an efficient technique based on a physical model is used to estimate the local atmospheric light. The brightest illumination value of each RGB pixel is utilized to estimate the initial atmospheric veil. Srinivasa *et al.* [30] defined Global atmospheric light estimation model (Υ).

He et al. utilized the detection of "most haze-opaque" region to estimate Υ [16]. In Tan's work [31], the brightest pixels in the weather degraded image are considered to be the most haze-opaque. However, it is true only when the weather is overcast and the sunlight can be ignored. In this case, the atmospheric light is the only illumination source of the scene. Therefore, the object radiance of each color channel is defined as [16]:

$$I_r(\mathbf{x}) = R(\mathbf{x})\Upsilon \tag{1.4}$$

where $R \leq 1$ is the reflectance of the scene points. The haze imaging Eq. (1.1) can be written as [16]:

$$I(\mathbf{x}) = R(\mathbf{x})\Upsilon(\mathbf{x}) + (1 - t(\mathbf{x}))\Upsilon \leq \Upsilon \tag{1.5}$$

When pixels at infinite distance ($t \approx 0$) exist in I, the brightest I is the "most haze-opaque" and it approximately equals Υ. But, in practice, the sunlight can be ignored. Considering the sunlight S, Eq. (1.5) can be rewritten as [16]:

$$I_r(\mathbf{x}) = R(\mathbf{x})(S + \Upsilon) \tag{1.6}$$

and Eq. (1.5) as:

$$I(\mathbf{x}) = R(\mathbf{x})St(\mathbf{x}) + R(\mathbf{x})\Upsilon(\mathbf{x}) + (1 - t(\mathbf{x}))\Upsilon \tag{1.7}$$

In this situation, the brightest pixel of the I can be brighter than Υ. They can be on a white car or a white building (Figures 1.7 (d) and 1.7 (e)).

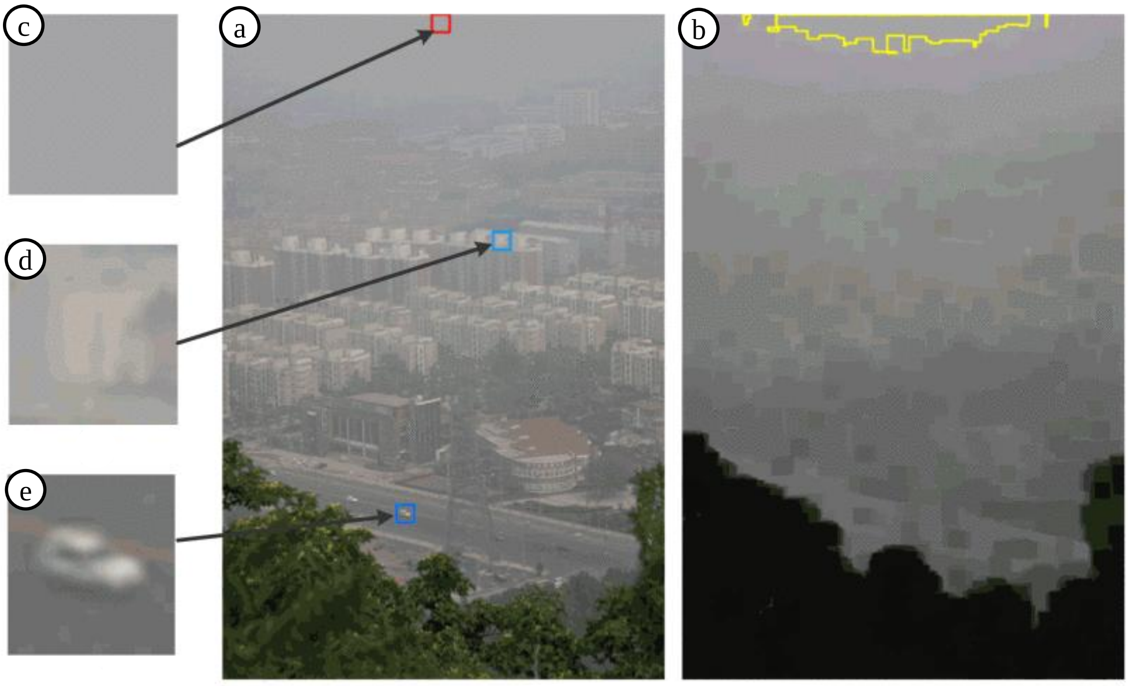

Figure 1.7: Estimating the atmospheric light: (a) Input image, (b) Dark channel and the most haze-opaque region, (c) The patch from where DCP automatically obtains Υ, (d), (e) Two patches that contain pixels brighter than Υ.

As, DCP of a weather degraded image approximates the haze denseness (see Figure 1.7 (b)). Therefore, DCP can be used to estimate the most haze-opaque region and improves the estimation of Υ. The top 0.1% brightest pixels in DCP are selected. These pixels are usually most haze-opaque (bounded by yellow lines in Figure 1.7 (b)). From these pixels, the pixels with highest intensity in I are selected as Υ. These pixels are in the red rectangle in Figure 1.7 (a). Note that these pixels may not be brightest ones in the whole I. This method works well even when pixels at infinite distance do not exist in an image [16].

In Figure 1.8 (b), DCP manages to detect the most haze-opaque regions. However, t is not close to zero here, therefore, the colors of these regions may be different from Υ. Fortunately, t is small in these most haze-opaque regions, therefore, the influence of sunlight is weak (Eq. (1.7)). Therefore, these regions can still provide a good approximation of Υ. The haze removal result of this image is shown in Figure 1.8 (c). Therefore, DCP based Υ estimation is more robust than the “brightest pixel” method. [16]

Figure 1.8: (a) Input image, (b) Dark channel (The red pixels are the most haze-opaque regions detected by DCP), (c) DCP based restored images, and (d) Image obtained using Fattal's approach.

The value of Υ is taken from an input image, from the similar area as the image obtained using DCP; a pixel with maximum luminance in I is called global atmospheric light [32]. A pixel with the highest dark channel is considered for monitoring of global atmospheric light estimation (Υ) as [33, 34]:

$$\Upsilon(j) = I\left(\max_j (I^c)\right). \tag{1.8}$$

Here, I^c shows scene radiance of each color channel. Also, $\max_j(I^c)$ represents top 10 % brightest pixels in I [35, 36].

1.3.3 Coarse atmospheric veil evaluation

Clearly, the transmission $t(j) = e^{-\gamma d(j)}$, this means $\gamma(j) \in [0,1]$. It identifies the effect of airlight on real object. The atmospheric veil generally develops when distance ($d(j)$) between the specific scene and camera increases. From Eq. (1.1), the imaging model can be redefined as:

$$I(j) = I_r(j)t(j) + \Upsilon \times \gamma(j) \tag{1.9}$$

The restoration model is normalized by splitting the global atmospheric light (Υ^c) in most color channel independently, which will be evaluated as:

$$\frac{I^c(j)}{\Upsilon^c} = \frac{I_r^c(j)t(j)}{\Upsilon^c} + \gamma(j) \tag{1.10}$$

The value of Υ is not optimum in real weather degraded image. It will originate the decomposition $\frac{I^c(j)}{\Upsilon^c} > 1$ for pixel values similar to those whose illumination is significantly more than atmospheric light (Υ). Thus, the normalized image is also confined into a range $[0,1]$ with linear stretch strategy as provided below:

$$\frac{I(j)}{\Upsilon} = \frac{I_r(j)t(j)}{\Upsilon} + \gamma(j) \tag{1.11}$$

The atmospheric veil ($\gamma(j)$) is based upon two conditions. These are
1) $\gamma(j) \in \mathbb{R}_{\geq 0}$
2) $\gamma(j) \leq \frac{\gamma(j)}{\Upsilon}$

Assume that transmission map and atmospheric veil in local window $\mathscr{W}(j)$ are constant. By addressing the transmission map as $\tilde{t}(j)$ and atmospheric veil as $\tilde{\gamma}(j)$, the minimal function is used on color channels and local window which can be defined as:

$$\min_{y\in\mathscr{W}(j)}\left(\min_{c\in(R,G,B)}\left(\frac{I^c(y)}{\Upsilon^c}\right)\right) = \tilde{t}(j)\min_{y\in\mathscr{W}(j)}\left(\min_{c\in(R,G,B)}\left(\frac{I_r^c(y)}{\Upsilon^c}\right)\right) + \tilde{\gamma}(j) \tag{1.12}$$

Based on the conditions of DCP, dark channel of $I_r(j)$ is near to zero, which can be provided under:

$$I^d(j) = \min_{y\in\mathscr{W}(j)}\left(\min_{c\in(R,G,B)}\left(I_r^c(y)\right)\right) = 0 \tag{1.13}$$

As $\Upsilon^c \in \mathbb{R}_{\geq 0}$, therefore Eq. (1.13) can be rewritten as:

$$\min_{c\in(R,G,B)}\left(\frac{I_r^c(y)}{\Upsilon^c}\right) = 0 \tag{1.14}$$

From Eqs. (1.12) and Eq. (1.14), atmospheric veil can be redefined as:

$$\tilde{\gamma}(j) = \min_{y\in\mathscr{W}(j)}\left(\min_{c\in(R,G,B)}\left(\frac{I^c(y)}{\Upsilon^c}\right)\right) \tag{1.15}$$

In this thesis, the minimal color channel is considered that supports visibility restoration to attain a significant information of objects. It is evaluated as:

$$\tilde{\gamma}(j) = \min_{c\in(R,G,B)}\left(\frac{I^c(j)}{\Upsilon^c}\right) \tag{1.16}$$

1.3.4 Transmission map refinement

Image filters are used to refine the coarse estimated atmospheric veil. The main objective of filtering is to refine the transmission map obtained from DCP. However, the selection of filter for transmission map refinement depends upon its edge preservation capability and computational speed.

Initially, the estimation of atmospheric veil ($\gamma(j)$) is done by considering the minimum operation of object $\frac{I(j)}{\Upsilon}$. It will result in $\gamma(j)$'s discontinuity, even if no unexpected depth discontinuities occur. In order to handle the halo artefacts of visibility restored image, a filtering technique is required for coarse atmospheric veil. The brief description of filters used in this thesis is mentioned in the preceding section.

A. Bilateral filter

The well-known edge-preserving Gaussian filter is a bilateral filter (S_{BL}). It replaces the intensity of each pixel with a weighted mean of intensity values from neighboring pixels [37]. This weight is computed with the help of Gaussian distribution. These weights do not depend only on the Euclidean distance of pixels, but also on the radiometric differences (e.g., range differences, color intensity, depth distance, *etc.*). Therefore, bilateral filter preserves sharp edges [38]. Mathematically, bilateral filter based filtered image $\left(s(j)\right)$ is computed by using the differences of I for the offsets of vectors (a):

$$s(j) = \frac{1}{\mathscr{N}(j)} \int_{\mathscr{D}} I(j+a).\mathscr{D}_1(a).\mathscr{D}_2[I(j+a) - I(j)]da \tag{1.17}$$

Here, $I(j)$ represents an input image. j denotes the coordinate of the pixel. $\mathscr{D}_1(a)$ shows the position of dependent weights for an offset vector a. $\mathscr{D}_2$ represents a magnitude weight scaling factor for filtering. n is the number of dimensions. $j \in \mathscr{D}$ represents the domain of underlying image and can be defined as $I(j) \in \Re^n$. The image domain is defined as $\phi \subseteq X_n \subset \mathscr{N}^n$. Here, J_n is the maximum index set related to the domain of an image in n dimensions.

The normalization function ($\mathscr{N}(j)$) is computed as:

$$\mathscr{N}(j) = \int_{\mathscr{D}} \mathscr{D}_1(a).\mathscr{D}_2[I(j+a) - I(j)]da \tag{1.18}$$

Both $\mathscr{D}_1$ and $\mathscr{D}_2$ weights are computed by Gaussian distributions with σ_1 and σ_2 standard deviations for color and spatial attributes, respectively. However, the bilateral filter is unable to remove high density of noise. It also suffers from a staircase effect (*i.e.,* intensity plateaus) that leads to image appearing like cartoon [39]. It also suffers from gradient reversal artefacts that introduce certain false edges in the filtered image [40]. To overcome these issues, a trilateral filter is designed.

B. Trilateral filter

Unlike bilateral filter that smooth towards piecewise constant solutions, trilateral filter (S_{TL}) provides efficient noise reduction and significant outlier rejection in high-gradient segments. This filter possesses the nature of gradient preserving. On the image signal's current plane, the bilateral filter is implemented. It needs the value of σ_1. Hence, bilateral filter is first employed on the gradients of I, which is given as below [41]:

$$s_g(j) = \frac{1}{k_\Delta(j)} \int_{\mathscr{D}} \Delta I(j+a).\mathscr{D}_1(a).\mathscr{D}_2(\|\Delta I(j+a) - \Delta I(j)\|)da \tag{1.19}$$

Here, $s_g(j)$ represents the output of bilateral filter when it is applied on gradient image. The forward differences are applied to calculate $\Delta I(j)$ and other popular techniques such as 5-point stencils. Sobel gradients are not used in the current research. In [42], for calculating the approximate plane ($p_I(j,a)$), the usage of smooth gradient ($s_g(j)$) is proposed for the following filter, instead of the gradient image ($\Delta I(j)$).

$$p_I(j,a) = I(j) + s_g(j).a \tag{1.20}$$

Here, gradient operator ($\Delta(j,a)$) can be defined as:

$$\Delta(j,a) = I(j+a) - p_I(j,a) \tag{1.21}$$

A neighborhood function ($p_I(j,a)$) is defined as:

$$p_I(j,a) = \begin{cases} 1, & \text{if } |s_g(j+a) - s_g(j)| < a_r \\ 0, & otherwise \end{cases} \tag{1.22}$$

Here, a_r is the adaptive region and $p_I(j,a)$ is used for second weighting phase.

Therefore, $s(j)$ can be computed as:

$$s(j) = I(j) + \frac{1}{k_\Delta(j)} \int_{\mathscr{D}} f_\Delta(j,a).\mathscr{D}_1(a).\mathscr{D}_2(f_\Delta(j,a)).N(j,a)da \tag{1.23}$$

and

$$k_\Delta(j) = \int_{\mathscr{D}} \mathscr{D}_1(a).s_2(f_\Delta(j,a)).N(j,a)da \tag{1.24}$$

C. Transmission map refinement

To improve the atmospheric veil, an image is utilized. From [43], the value of refined atmospheric veil is computed as:

$$\gamma(j) = \Upsilon(1 - t(j)) \tag{1.25}$$

Long *et al.* [44] utilized well-known Gaussian filter to refine the atmospheric veil. It has been achieved by using the following formulation:

$$t(j) = \frac{1}{W_g} \sum GF(||i - j||) \tag{1.26}$$

Here, W_g represents the weighted sum of local patch at i. Also, Gaussian filter (GF) is calculated as follows [45]:

$$GF(j) = e^{-i^2/2\sigma^2} \tag{1.27}$$

By deriving from Eq. (1.26), the refined transmission map can be obtained. The transmission refinement map can be redefined as:

$$t(j) = \sigma^2(j) - J^f_{\mathscr{W}} \left(|M_c - \sigma^2(j)| \right) \tag{1.28}$$

Here, $J^f_{\mathscr{W}}$ shows the given filter. $\sigma^2(j)$ represents the variance of pixel centered at position j, with its neighbors in local mask. Also, minimum color channel ($M_c(j)$) of $I(j)$ is computed as:

$$M_c(j) = \min_{c \in [R,G,B]} \left(I(j) \right) \tag{1.29}$$

Here, c represents color channel of $I(j)$. Hence, the atmospheric veil ($\gamma(j)$) can be rewritten as:

$$\gamma(j) = \max \left(\left(\min \left(t^f(j), M_c(j) \right) \right), 0 \right) \tag{1.30}$$

Here, $t^f(j)$ shows the refined transmission map by using an image filter. Transmission of every mask (t) can be redefined as:

$$\bar{t} = 1 - \frac{\gamma}{\Upsilon} \tag{1.31}$$

Υ is typically supposed to be a pixel illumination with maximum luminosity in an object. However, in real time, this hypothesis frequently delivers invalid outcomes because of the occurrence of self-luminous organisms. In the same way, the sky pixel values are also computed between all the local minimum that correspond to background illumination Υ, which is computed as:

$$\Upsilon = \max_{z \in I} \left(\min_{z \in \mathscr{W}(j)} \left(I^c(z) \right) \right) \tag{1.32}$$

Here, $I^c(z)$ is color components of $I(j)$ in every mask.

1.3.5 Visibility restoration model

After improving the coarse estimated atmospheric veil, there is a need to restore the weather degraded image by applying the visibility restoration model. The actual scene radiance can be restored from Eq. (1.1). The coarse estimated atmospheric veil ($\gamma(j)$) is examined by utilizing the minimal element of object $\frac{I(j)}{\Upsilon}$, dissimilarity between image ($\frac{I(j)}{\Upsilon}$) and coarse estimated atmospheric veil ($\gamma(j)$) is close to zero with maximum probability. Therefore, a consistent parameter c is employed to restrict the variation. It is observed From Eq. (4.4) that the minimal value of actual transmission may be small and also close to zero. However, the restored image may possibly involves some noise [44]. Hence, it is important to restrict the transmission map by a lower bound (x_0). The values of x_0 and c are set to 0.1 and 0.95, respectively, as reported in the literature [46]. The object illumination ($I_r(j)$) can be restored as:

$$I_r(j) = c \times \Upsilon + \frac{I(j) - c \times \Upsilon}{max(t(j), x_0)} \tag{1.33}$$

1.4 Applications of visibility restoration techniques or models

Visibility restoration techniques play an important role in computer vision applications. Figure 1.9 shows the most significant applications in which visibility restoration techniques are utilized as a pre-processing tool [47].

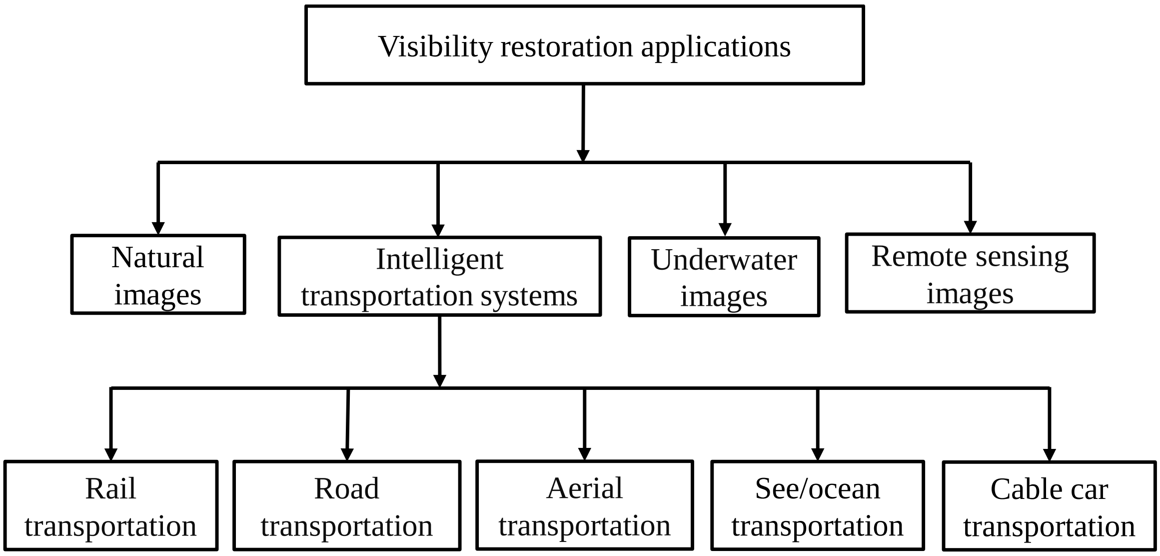

Figure 1.9: Applications of visibility restoration techniques

1.4.1 Remote sensing

Remote sensing images are widely used in different areas ranging from mineral exploration to agricultural applications [48]. However, the poor quality of hyperspectral images has an adverse effect on these applications [49]. Visibility restoration techniques are applied on remote sensing image to attain a high-quality image [50].

1.4.2 Underwater images

For researchers and divers, it is hard to attain maximum information from underwater images [51]. Underwater imaging often suffers from color sprinkle and color cast problems. Color cast is due to the fluctuating attenuation of light in dissimilar wavelengths, rendering underwater environments bluish. Therefore, the color cast distorts the color of underwater images [52]. Thus, visibility restoration techniques are required to remove the effect of color sprinkle and color cast from underwater images [53].

1.4.3 Intelligent transportation systems

Weather degradation decreases the effective range of visual surveillance. This degradation is a spatially varying phenomenon which makes this problem non-trivial [54]. Visibility restoration is an essential technique in applications such as intelligent transportation system, vehicle detection, lane detection, *etc.* [55]. The following subsections describe the most popular applications of visibility restoration techniques to design an intelligent transpiration system.

A. Road transportation

Due to poor visibility of roads, many accidents occurs on highways especially in hilly areas. Therefore, in order to prevent accidents on highways and hilly areas, a visibility restoration technique is required to provide restored image to a driver using some visual equipment. However, due to a high speed of vehicles, it needs a visibility restoration technique with constant time complexity [56].

B. Aerial transportation

Generally, takeoff and landing of airplanes become a challenging task in weather degraded environment. Many flights get delayed or sometimes are canceled due to poor weather environment. To handle this issue, one can use visibility restoration techniques to make the perceived scene as restored.

C. Rail transportation

Even while train remains trashed of equipment due to poor weather conditions every year. The railways have not developed fool-proof devices to mitigate this issue [57]. Many trains get a delay or sometimes even cancelled due to weather degraded environment. Therefore, in order to handle this issue, one can use visibility restoration techniques to stream the clear scene for drivers [58].

D. Sea/ocean transportation

Sea fog affects the navigation of ships. It can stop a ship from moving along the ship channel. It can also be adverted the inland traffic systems. The future forecasts of sea fog are significant for reporting potential information to traffic personnel [59].

E. Cable car transportation

A cable car is a transportation system that depends on cables to pull vehicles along or lower them at a steady rate [60]. Many cable cars get a delay or sometimes even cancelled due to heavy fog. To handle this issue, one can use visibility restoration techniques to stream visibility restored scene for cable car drivers.

1.5 Performance metrics

Performance metrics are used to analyze the quality of a visibility restoration technique.

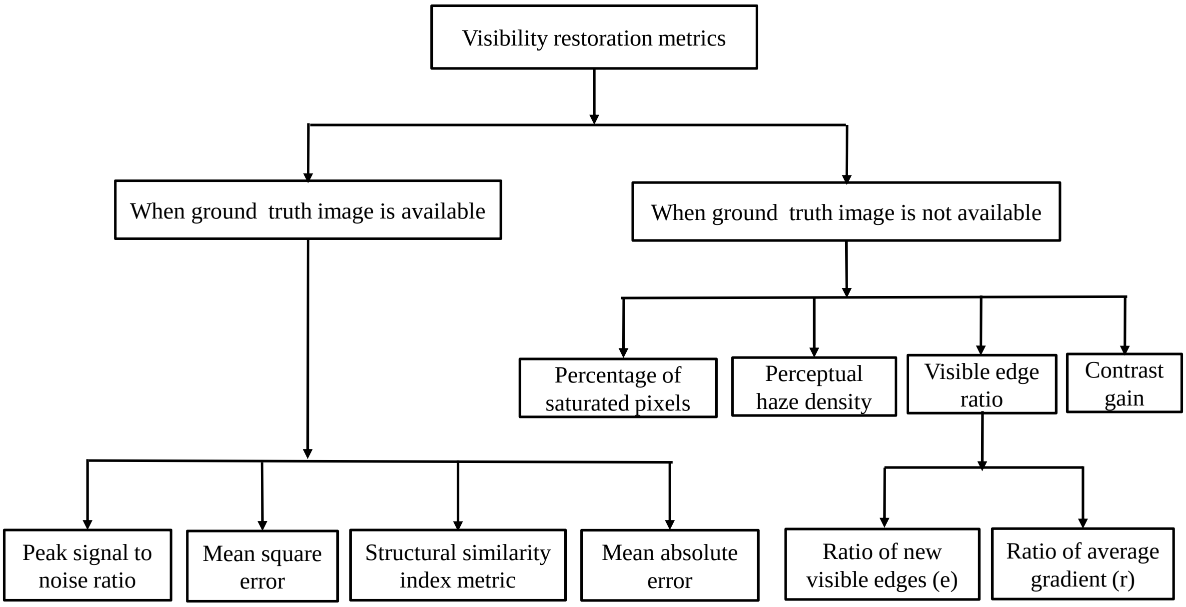

Figure 1.10: Performance metrics for visibility restoration techniques

Figure 1.10 shows various performance metrics which can be used to evaluate the effectiveness of the existing visibility restoration techniques [61]. In visibility restoration techniques, the quality metrics are divided into two parts, *i.e.,* when the ground truth image is available and when the ground truth image is not available [62].

1.5.1 When a ground truth image is available

In this case, a ground truth image (*i.e.,* reference image) is given in advance. It is an actual restored image of the same weather degraded image. However, actual restored images are only given when someone wants to validate its visibility restoration technique on standard weather degraded image datasets. When the reference image is given, several quality metrics such as Mean squared error (MSE), Peak signal to noise ratio (PSNR), and Structural similarity index metric (SSIM) are available for evaluating the performance of visibility restoration techniques.

A. Mean square error

Mean square error (MSE) is an error measure which is used to evaluate the difference between Ground Truth (G_t) image and Restored image (I_r) produced by the given technique. It is a positive integer which ranges from 0 to ∞. The mathematical representation of MSE can be defined as [63]:

$$MSE = \frac{1}{R \times C} \sum_{j=1}^{R} \sum_{i=1}^{C} [G_t(i,j) - I_r(i,j)]^2 \tag{1.34}$$

$G_t(i,j)$ represents pixel intensities of a ground truth image. Whereas $I_r(I,j)$ depicts the pixel value of a restored image. Also, i and j show the pixel's coordinate values. R and C represent rows and columns, respectively.

B. Peak signal to noise ratio

With respect to restored image, Peak signal to noise ratio (PSNR) evaluates the mean squared error after applying restoration technique. The maximum value of PSNR represents the effect of weather degradation is removed proficiently. PSNR can be computed as follows [63]:

$$PSNR = 10 \log_{10} \left(\frac{255^2}{MSE} \right) \tag{1.35}$$

C. Structural similarity index metric

Structural similarity index metric (SSIM) evaluates the relationship of edges that has been neglected during the computation of PSNR. The value of SSIM closes to 1 means that higher structural quality of restored image. It is computed as [63]:

$$SSIM(m,n) = \left(\frac{2\mu_m\mu_n + c_1}{\mu_m^2 + \mu_n^2 + c_1}\right)\left(\frac{2\mu_{mj} + c_2}{\sigma_m^2 + \sigma_n^2 + c_2}\right) \tag{1.36}$$

Here, μ_m and μ_n are sample means of m and n, respectively. σ_m^2 and σ_n^2 are the sample variances of m and n, and σ_{mj} is the sample cross-covariance between m and n. The values for c_1 and c_2 are set to 0.01 and 0.03, respectively.

1.5.2 When a ground truth image is not available

In real time applications, ground truth images are not given. Then it becomes difficult to measure the effectiveness of the given technique. In case of visibility restoration techniques, a restored image has more contrast as compared to the weather degraded image. Contrast gain (C_g) and Percentage of saturated pixels (ρ), Visible edges ratio, and Perceptual weather degradation density (D_f), are used for evaluating the visibility restoration technique.

A. Contrast gain

Contrast gain (C_g) is defined as an average contrast difference between input weather degraded image (I) and restored image (I_r). It is computed as [64]:

$$C_g = C_I - C_I^r \tag{1.37}$$

Here, C_I^r and C_I represent average contrast of restored image (I_r) and foggy image (I), respectively. Assume that an image ($I(i,j)$) with size ($R \times C$). The average contrast ($C_v(i,j)$) is computed as:

$$C_v(i,j) = \frac{1}{R \times C}\sum_{i=0}^{R-1}\sum_{j=0}^{C-1} C(i,j) \tag{1.38}$$

Here, $C(i,j)$ can be defined as:

$$C(i,j) = \frac{s(i,j)}{m(i,j)} \tag{1.39}$$

where

$$m(i,j) = \frac{1}{(2p+1)^2}\sum_{k=-p}^{p}\sum_{l=-p}^{p} I(i+k, y+l) \tag{1.40}$$

$$s(i,j) = \frac{1}{(2p+1)^2}\sum_{k=-p}^{p}\sum_{l=-p}^{p} |I(i+k, y+l) - m(i,j)| \tag{1.41}$$

Tripathi and Mukhopadhyay [65] shown that fog free image has more contrast than the weather degraded image. Hence, C_g should be a positive real number.

B. Percentage of saturated pixels

C_g should not be so high as the pixels of restored image become saturated. Therefore, Percentage of saturated pixels (ρ) are needed to be computed [64]. ρ can be defined as:

$$\rho = \frac{S_p}{R \times C} \tag{1.42}$$

Here, S_p represents the number of pixels that are saturated either completely black or white, after the visibility restoration technique, which were not present in the weather degraded image. The lower value of ρ indicates the given visibility restoration technique is better than the others.

C. Visible edges ratio

The ratio of new visible edges (e) and the ratio of average gradient ($\bar{r}$) are also utilized to monitor the performance of the proposed technique. The e represents the improved rate of visible edges of the restored images and is calculated as follows [66]:

$$e = \frac{n_k - n_l}{n_l} \tag{1.43}$$

Here, n_k and n_l represent the cardinal number of the visible edges in the weather degraded image (I_s) and the restored image (I_r), respectively.

The maximum e states that the edges of the restored image are stronger. $\bar{r}$ utilizes the gradients of visible edges in the restored image to depict the restoration degree of the image edge and texture information. $\bar{r}$ can be defined as:

$$\bar{r} = e^{\left[\frac{1}{n_k} \sum_{i \in \phi_k} log\, r_i\right]} \tag{1.44}$$

Here, r_i is set to $\frac{\Delta k}{\Delta l}$. The gradients of an image are represented using Δk and Δl, respectively. r_i denotes the set of visible edges of I_r. A maximum value of $\bar{r}$ states that the corresponding visibility restoration technique has improved the capacity of edge preservation than the others.

D. Perceptual weather degradation density

An effective technique for weather degradation density prediction is discussed in [67] in which the input image is divided into $N \times N$ sections and aggregate average values are computed. $N \times N$ sections are utilized to evaluate various weather degradation aware features such as variance, sharpness, contrast energy, image entropy, DCP, color saturation, colorfulness, *etc.* Mahalanobis measure [68] is applied on these features to evaluate the Multivariate Gaussian (MVG) fit of n dimensions and MVG can be mathematically computed as:

$$P(s) = \frac{1}{\sqrt{(2\pi)^n |D|}} exp\left(-0.5 * (s-\mu)^t C^{-1} (s-\mu)\right) \tag{1.45}$$

Here, s denotes the weather degradation aware statistical features, μ represents the mean and $n \times n$ demonstrates the covariance matrix of different weather degraded features. Also, D and C^{-1} depict determinant and covariance matrix inverse for MVG, respectively. D and C^{-1} can be derived using Maximum likelihood (ML) estimation [69]. Next, a Mahalanobis-like distance can be calculated as:

$$D = \sqrt{(m_1 - m_2)^t \left(\frac{C_1 + C_2}{2}\right)^{-1} (v_1 - v_2)} \tag{1.46}$$

Here, m_1 and m_2 are mean vectors and C_1 and C_2 are covariance matrices for MVG model of the restored corpus and MVG fit of the test image.

Another metric L_f which has restored a level of the test weather degraded image is calculated. L_f represents the distance norm of MVG versus weather degraded aware statistical features. This information is extracted from a weather degraded test image and normal MVG model from a group of 500 weather degraded images [67]. Afterward, weather degradation density (D_h) can be calculated as:

$$D_h = \frac{D}{1 + L_f} \tag{1.47}$$

Values of D_h are proportional to the corresponding weather degraded density.

1.6 Motivation

Images captured in poor weather conditions usually degraded due to the scattering of particles (such as haze, fog, smog, *etc.*) in the atmosphere. As a result, the obtained image suffers from poor contrast and color distortion issues. These images limit the performance of various computer vision systems which demand clear images. Therefore, visibility restoration techniques are required to restore the actual scene radiance. The existing visibility restoration techniques generally restore the weather degraded image by using multiple images of the same scene under different environmental circumstances. These techniques achieve remarkable performance. However, these are not applicable in single image visibility restoration because these techniques require multiple images to evaluate the depth map. Therefore, the development of novel single image visibility restoration techniques are required. These techniques are based upon certain assumptions and priors. Therefore, an accurate estimation of the depth information is still a challenging issue. Also, the estimated transmission map by using single image restoration techniques are not smooth. Thus, the design of new image filters are required to refine the evaluated transmission map.

Dark channel prior (DCP) is one of the popular single image visibility restoration techniques. It is based on the observation that some pixels in the local segments have very low intensity in at least one color channel. DCP has achieved remarkable results in the field of visibility restoration. However, DCP based techniques suffer from poor computational speed and suffer from sky region, color, and edge distortion issues. Therefore, novel filters are required to refine the transmission maps.

In case, if we completely restore the weather degraded image, then it may look like an artificial image. Therefore, the visibility restoration model will be modified to overcome this issue. Additionally, DCP fails to preserve the texture information especially in case of images affected by large weather gradients. Therefore, novel gradient based channel priors will be designed to preserve the texture, spatial, and spectral information. Therefore, the main motivation behind this work is to estimate an accurate transmission map that is not only smooth, but also makes the scene depth more clearly by preserving the texture information of weather degraded images.

1.7 Thesis organization

This thesis is devoted to design and development of visibility restoration techniques for weather degraded images. The extensive review of the existing visibility restoration techniques is discussed in Chapter 2. Design and implementation of the proposed visibility restoration techniques are discussed in Chapters 3 to 6. The concluding remarks and future directions are described in Chapter 7. The chapter-wise organization of thesis work is given below:

Chapter 2: Literature review

In Chapter 2, a comprehensive and illustrative literature review in the domain of visibility restoration techniques is provided. The details of various visibility restoration techniques along with their strengths and weaknesses are also presented. The existing techniques are compared with respect to different features.

Chapter 3: Transmission map refinement using modified filters

In Chapter 3, various filters are designed and implemented to restore the haze and fog from the weather degraded images. These filters are used to refine the transmission map obtained by applying DCP on weather degraded images. The main objective of these filters to refine the evaluated transmission map at good computational speed and to preserve the significant information (*i.e.,* edges, colors, texture, *etc.*) of restored images.

Chapter 4: Integrated visibility restoration model

In Chapter 4, a novel integrated visibility restoration model is designed by using DCP, Bright channel prior (BCP), and gain intervention filter. The main objective of this chapter is to solve the sky-region problem associated with DCP based visibility restoration technique.

Chapter 5: Modified restoration model

In this chapter, a Modified restoration model (MRM) based DCP is proposed to reduce color distortion and halo artefact issues. MRM modifies the restoration model to reduce the color distortion problem. The modified joint trilateral filter is also utilized to improve the coarse estimated atmospheric veil.

Chapter 6: Gradient based channel priors

In this chapter, various gradient based profile priors are proposed. The modified filters are also designed to remove the halo and gradient reversal artefact issues. Designed gradient based profile priors have an ability to minimize the color distortion rate and also preserve the texture information of weather degraded images in an efficient manner.

Chapter 7 Conclusions and future work

This chapter concludes the thesis by highlighting the contributions made towards the proposed research domain. Moreover, this chapter also provides the future directions in this research area.

Chapter 2

Literature review

Outline

This chapter carries out a comprehensive review of visibility restoration techniques. The visibility restoration techniques are broadly categorized into six categories. These are depth estimation, enhancement, filtering, fusion, meta-heuristic, and variational model. Finally, the comparisons have been done on the existing techniques based upon certain characteristics. The overall objective of this chapter is to evaluate the shortcomings present in the existing visibility restoration techniques.

2.1 Visibility restoration techniques

The visibility restoration techniques are categorized into six main categories. These are (1) Enhancement based visibility restoration, (2) Depth estimation based visibility restoration, (3) Filtering based visibility restoration, (4) Fusion based visibility restoration, (5) Meta-heuristic based visibility restoration, and (6) Variational restoration techniques. The subsequent section provides the detail description of these techniques along with their strengths and weaknesses.

2.1.1 Enhancement based visibility restoration

Image enhancement techniques such as histogram equalization [18], weighted histograms [70], bi-histogram modification [71], and histogram modification [61] have been extensively utilized to remove the haze from hazy images. However, these techniques suffer from over/under enhancement and saturation pixels issues [72]. Also, these approaches work inefficiently for images with large haze gradient or when images contain inhomogeneous haze [73].

In Table 2.1, Edge preservation, Speed, Color distortion, Halo artefacts, Large haze gradient, Gradient reversal, and Blocking artefacts are written as EP, S_P, HA, LHG, GRA, and BA, respectively.

Table 2.1: Comparative analysis of enhancement based restoration techniques

Ref.	Technique	Year	EP	S_P	CD	HA	LHG	GRA	BA
[74]	Multi-scale fusion	2013	✓	Average	✗	✓	✗	✓	✗
[75]	New optical model	2013	✗	Average	✓	✗	✗	✓	✓
[46]	Unsharp masking	2014	✗	Average	✓	✗	✗	✗	✗
[56]	Visibility enhancement	2014	✗	Average	✗	✗	✗	✗	✗
[71]	Histogram modification	2015	✗	Good	✗	✗	✓	✗	✗
[76]	Backward scaling	2015	✗	Good	✓	✗	✗	✓	✗
[77]	Blurriness	2015	✓	Average	✗	✓	✗	✓	✗
[78]	Multi-scale Gradient	2016	✗	Good	✓	✗	✗	✓	✗
[79]	Programmable gate array	2016	✓	Average	✗	✓	✗	✗	✗
[80]	Deep neural network	2016	✓	Average	✗	✓	✗	✗	✗
[47]	Global spatial entropy	2017	✓	Average	✗	✓	✗	✓	✗
[51]	Contrast enhancement	2017	✗	Average	✓	✗	✗	✓	✓

2.1.2 Depth estimation based visibility restoration

The multi-scale tone strategy is utilized to evaluate the atmospheric veil in an optimistic way. Therefore, it can manipulate the quality and illumination of an input image at multiple scales [81]. But, this technique experiences the same issue of the majority of visibility restoration techniques, *i.e.,* it does not attain consistent results especially for heavy degraded images [82]. It performs poorly whenever it fails to recognize local maxima and minima precisely.

Due to a maximum intensity of airlight, the existing techniques select pixels having greatest intensity to evaluate the airlight map. However, some pixels with maximum illumination are also produced by some other light conditions such as train headlights [78]. Gaussian distribution based visibility restoration technique selects the airlight contenders from the brightest segment of the degraded image. The color similarity assessment is also utilized to filter the airlight contenders. This means color from the filtered airlight contenders is utilized for airlight estimation [83]. In [84], fast visibility restoration technique is introduced. This model evaluated the atmospheric light by utilizing an infinite sky area and white area. However, it still suffers from the edge preservation issue because the potential edges may degrade during the restoration process.

Table 2.2 shows the comparative analysis of depth map visibility restoration techniques based upon certain features and artefacts.

Table 2.2: Comparative analysis of depth map based restoration techniques

Ref.	Technique	Year	EP	S_P	CD	HA	LHG	GRA	BA
[31]	Optical scattering	2008	✓	Average	✓	✓	✗	✗	✓
[43]	Inference technique	2009	✗	Good	✓	✗	✗	✗	✗
[85]	Multi-scale retinex	2010	✗	Good	✓	✗	✗	✗	✗
[16]	Dark channel prior	2011	✗	Average	✓	✗	✗	✗	✗
[86]	Bayesian probabilistic	2012	✗	Good	✓	✗	✗	✗	✗
[87]	Markov Random Field	2012	✗	Good	✓	✗	✗	✗	✗
[88]	Regularization technique	2013	✗	Average	✗	✓	✓	✓	✓
[89]	Joint bilateral filter	2013	✗	Average	✓	✗	✗	✗	✗
[90]	Dark channel prior	2013	✗	Good	✗	✓	✓	✓	✓
[91]	Markov random field	2014	✗	Average	✗	✗	✗	✗	✗
[44]	Gaussian filter	2014	✓	Average	✗	✓	✓	✗	✗
[83]	Hierarchical airlight	2015	✓	Average	✗	✗	✓	✓	✓
[92]	Dark channel prior	2015	✗	Good	✗	✓	✓	✗	✓
[93]	Multiscale retinex	2015	✓	Average	✗	✓	✓	✗	✗
[94]	Adaptive dark channel	2015	✓	Average	✗	✗	✓	✓	✓
[95]	Lock-up table	2015	✗	Good	✗	✓	✓	✓	✓
[96]	color attenuation prior	2015	✓	Average	✗	✗	✓	✓	✓
[97]	Supper pixel technique	2016	✗	Average	✗	✓	✓	✗	✓
[98]	Dark channel prior	2017	✓	Average	✗	✓	✓	✗	✗
[73]	Linear transformation	2017	✗	Good	✗	✓	✓	✗	✓

Change of detail (COD) prior is utilized in [99] which can remove the weather degradation from an image by utilizing multiple scattering occurrences in the dissemination of illumination. By using this technique, a thickness of weather degradation can be evaluated to restore a weather degraded image. COD prior is stable to local areas of the degraded image that contain objects in dissimilar depths [99]. However, it cannot preserve the edges of the restored images.

A superpixel technique using Multiple scattering (MS) is designed for evaluating the transmission on the sky as well as non-sky areas, to diminish the effect of halo artefacts around edges and decreases the color distortion in the sky area. Therefore, it can overcome the halo artefacts issues associated with most of the existing visibility restoration techniques [97]. However, this technique can be improved further by efficiently estimating the atmospheric veil to restore the image in a more consistent manner [100].

2.1.3 Filtering based visibility restoration

The gamma correction and median filtering by utilizing a look-up table can determine the restored images in an efficient way. It has minimum computation time than the existing techniques without losing the brightness of restored image [95]. This technique uses median filter as it cannot preserve the edges of the restored image.

L2-norm based visibility restoration technique can evaluate the depth by calculating average vector L2-norm of the sample window. Thereafter, it filters the evaluated transmission map by utilizing a guided filter. Thus, it uses the guided filter to preserve edges of the restored image [101]. However, it still suffers from halo artefacts issue, which may introduce during the fusion process. The weighted guided image filter utilizes an edge-aware weighting to further improve the guided image filter. This technique has overcome the problem of halo artefacts. Weighted guided image filter has minimum computation time than the existing techniques without losing the brightness of restored image [102]. The bilateral filter is utilized to attain local smoothness and edge preservation of a restored image. This technique reduces the adverse effects due to the difference in evaluating the global atmospheric illumination [103]. However, the bilateral filter suffers from halo artefacts issue that may introduce during the fusion process [71]. Jiang *et al.* [104] designed a Guided image filter (GIF) with color transfer to restore night time hazy images. The weighted guided image filter and Koschmiedars law [105] are utilized to simplify the dark channel of a degraded image into a base and detail layer. The transmission map is evaluated using the base layer. It is used to recover the restored image. But, this technique has poor computation time than the majority of existing techniques.

Table 2.3: Comparative analysis of filter based restoration techniques

Ref.	Technique	Year	EP	S_P	CD	HA	LHG	GRA	BA
[106]	Optimized restoration	2013	✓	Average	✗	✗	✗	✗	✗
[45]	Joint trilateral filter	2014	✓	Good	✗	✗	✗	✗	✗
[102]	Trilateral filter	2015	✓	Good	✗	✓	✗	✗	✗
[105]	Weighted image filter	2015	✓	Average	✗	✓	✓	✗	✗
[107]	Fast Smoothing	2015	✗	Average	✗	✓	✗	✓	✓
[104]	Guided image filter	2018	✓	Average	✗	✓	✓	✓	✓

2.1.4 Fusion based visibility restoration

A Multiscale depth fusion (MDF) technique is described for removing the effect of weather degradation from single image [108]. The results of multiscale filtering are probabilistically combined into a fused depth map. The fusion is devised as an energy minimization issue that integrates spatial Markov dependence. The multiscale depth fusion technique can estimate the depth map in a more consistent way. This technique has the ability to preserve the edges of the restored image with sharp details.

An efficient technique for transmission map estimation by using the guided fusion is presented in [82]. By utilizing the reliability guided fusion of block and pixel level dark channels, an efficient transmission map is evaluated. It effectively decreases the failure possibility of DCP and restoration artefacts. DCP fail in brighter segments by decreasing the contrast of brighter segments. Therefore, it provides an even more natural restoration of the brighter segments.

Image regions that have a low light intensity and dense weather degradation still get affected adversely with lesser visibility. In [17], the techniques which deal with contrast improvement on a global level are studied. The effect of weather degradation on the image objects depends upon its varying intensity and color contrast of the pixels. Now, there is a family of contrast enhancement schemes which can be applied to the whole image. The white balance, histogram equalization, and gamma correction are the examples of popular image enhancement operators.

To fix this limitation, the fusion based restoration technique has considered three different measures. It uses the weight maps. They take pixels into consideration and define customized spatial functions for poor contrast regions.

Luminance weight map calculates pixel visibility of an image and assign values proportional to their visibility. For weather degraded images, color loss is calculated based upon RGB information as they have low saturation. Let R, G, B, and L are colors and luminance intensities for each input image with index n. The weight is calculated as follows [82]:

$$W_n^L = \frac{1}{\sqrt{3}}\sqrt{(L^n - R^n)^2 + (L^n - G^n)^2 + (L^n - B^n)^2} \tag{2.1}$$

Luminance is calculated from the average of RGB intensities. Hence, the restored regions will yield greater value of W^L. Thus, W^L is an index for degradation identification due to haze effect.

Initially, the weather degraded image (I) is white balanced to obtain I_1 [109]. Then, I_2 is obtained by taking the scaled difference of illumination value of an image (pixels) and its average luminance (I_{avg}). I_2 is mathematically computed as:

$$I_2 = \alpha(I - I_{avg}) \tag{2.2}$$

The weighted luminance helps a smooth transition among derived input images (I_1, I_2). To reduce the global color and contrast, two additional weighted maps based on chromaticity and saliency are defined as [109]:

$$W_n^C = exp\left(\frac{(S_n - S_{max})^2}{-2\sigma^2}\right) \tag{2.3}$$

W^C represents the squared difference in saturation value and its maximum value. The default value for our experiments σ and S_{max} are set to 0.3 and 1, respectively. Thus, the value is proportional to the saturation of the pixel values.

Saliency weighted map calculates the visibility degree relative to the neighborhood areas. It basically measures the relative contrast of a region or a segment in an image with respect to its surroundings. It is based upon neighboring orientation, color or intensities.

The saliency weight map is defined as follows [110]:

$$W_n^S = \|I_n^f - I_n^{avg}\| \tag{2.4}$$

Here, I_n^{avg} is the average pixel value of input I_n and I_n^{avg} is the blurred input. It is obtained by using high frequency value of cutt-off ($f = \pi/2.75$) into a separable binomial kernel. Binary kernel is efficient for small kernels if calculated in this way with 5×5 $(1/16)$ [1 4 6 4 1]. This technique yields uniform contrast regions with well-separated boundaries while preventing unnecessary artefacts in the fused image. The impact of three measures are important in different aspects but the first one which is luminance weight map has greater visibility impact. The aggregated weight map (W_n) is obtained by multiplicative expression:

$$W_n = W_n^L \times W_C^n \times W_n^S \tag{2.5}$$

The normalized form of an aggregate weight guarantees that the sum will be equal to 1 for each pixel.

$$\overline{W}_n = \frac{W_n}{\sum W_n} \tag{2.6}$$

During the image fusion, weighted inputs are computed in order to detect the features for each pixel.

$$F = \sum_n \overline{W}_n I_n \quad \text{s.t.} \ \sum_n \overline{W}_n = 1 \tag{2.7}$$

Intensity scale of the resulted image is maintained because the normalized weighted map is used. But, this may result in halo artefacts where the weighted maps have stronger transitions. Therefore, a technique [111] known as pyramidal refinement is used to get rid of this degradation.

In this technique, I_n is actually decomposed using Laplacian operator into a pyramid with different scales. On the parallel track, $\overline{W}_n$ is also derived to a Gaussian pyramid for each of its weighted normalized map. At each pyramid level i, the mixing is computed as:

$$F_i = \sum_n G_i(\overline{W_n})L_i(I_n) \tag{2.8}$$

Here, L_i depicts the Laplacian operation on I. $G_i(\overline{W_n})$ is the Gaussian operator on the weighted normalized map $\overline{W}_n$. Bottom up direction is adopted for pyramid layers and the final restored version of I is calculated after adding all the pyramid levels using upsampling operator $U(x)$ with $x = 2^{i-1}$.

$$G(x) = \sum_i F_i(x)U(x) \tag{2.9}$$

In fusion based restoration technique, all three weights have equal weighted contribution towards the results of final fusion .

A fusion strategy based visibility restoration technique is implemented in [112], which fuses the outcomes of linear transform with the guided image filtering. It improves the visibility of images at better computational speed.

Table 2.4: Comparative analysis of fusion based restoration techniques

Ref.	Technique	Year	EP	S_P	CD	HA	LHG	GRA	BA
[74]	Multi-scale fusion	2013	✗	Average	✓	✓	✗	✗	✓
[108]	Multi-scale depth fusion	2014	✓	Average	✗	✓	✓	✗	✗
[113]	Pixel level fusion	2014	✓	Average	✓	✗	✗	✓	✓
[82]	Reliability guided fusion	2016	✓	Good	✗	✓	✓	✗	✓
[78]	Multi-scale gradient	2016	✓	Average	✓	✓	✗	✗	✓
[112]	Guided image filter	2016	✗	Average	✗	✓	✗	✓	✓
[50]	Block coordinate	2016	✗	Good	✓	✓	✓	✗	✓
[48]	Similarity based fusion	2017	✓	Average	✗	✓	✓	✓	✗

2.1.5 Meta-heuristic based visibility restoration

Most of the existing visibility restoration techniques are unable to select the best parameters for better visibility restoration. Therefore, these do not provide optimal results. Genetic algorithm is widely used in visibility restoration for parameter selection. Genetic algorithm can attain the optimistic visibility restoration parameters by using contrast gain as fitness function [114]. However, a genetic algorithm does not guarantee the global optimal solution. Therefore, it should be hybrid with others.

Noise Filtering Perspective is proposed by [22] for visibility restoration. Images contaminated by weather in the form of noise possess two main characteristics such as high intensity and low saturation. Therefore, a weighted sum of input image intensity and saturation is used to describe the weather severity. Atmospheric light can be estimated by the same principle, while a small correction is needed when images contain over-bright objects. Thereafter, two weighted maps are constructed local statistics of the severity map are applied in image noise filtering. The objective function is to maximize the saturation of the output image. Furthermore, a penalty function is used to control the hue change while calculating the overall fitness.

Song *et al.* [115] used Particle swarm optimization (PSO) and Genetic algorithm (GA) with fuzzy logic to restore the visibility of degraded images. Zhang *et al.* [19] proposed a techniques to estimate the atmospheric light using Ant colony optimization (ACO).

Table 2.5: Comparative analysis of meta-heuristic based restoration techniques

Ref.	Technique	Year	EP	S_P	CD	HA	LHG	GRA	BA
[115]	Fuzzy System	2014	✗	Average	✗	✓	✓	✗	✗
[114]	Genetic Algorithm	2016	✓	Average	✗	✓	✓	✓	✗
[116]	Fuzzy system	2016	✓	Average	✗	✓	✗	✓	✗
[117]	Temporal coherence	2017	✓	Average	✗	✓	✓	✓	✗
[19]	Ant colony optimization	2017	✓	Average	✓	✗	✓	✗	✓

2.1.6 Variational image restoration

The existing restoration techniques estimate the depth map to remove the weather degradation from images. Thus, these techniques are vulnerable to failure whenever the physical assumptions are violated. Image enhancement techniques do not evaluate the depth map. Therefore, these techniques did not suffer from this issue. However, these suffer from over-enhancement issue. Fortunately, variational image restoration technique can overcome the physical failure assumptions and over-enhancement problem. The preceding subsection describes some well-known variational image restoration techniques [118].

To restore haze-degraded outdoor images, the Enhanced variational image restoration (EVID) energy minimization function has been proposed. It is computed as [119]:

$$\begin{aligned} E_{\text{EVID}}(I_s^c) = \frac{\alpha}{2}\sum_i (I^c(j)-\mu^c)^2 + \frac{\beta}{2}\sum_i (I^c(j)-I_0^c(j))^2 - \\ \frac{\gamma}{2}\sum_j \omega(j)|I^c(j)-I^c(j)| - \frac{\eta}{2}\sum_j \omega(j,j)|I^c(j)-I^{c+1}(j)| \\ -\frac{\eta}{2}\sum_j \omega(j)|I^c(j)-I^{c+2}(j)| \end{aligned} \tag{2.10}$$

Here, I_s^c represents the color channel $\in [0,1]$. I_0 represents the input image with i and j pixel coordinates. α, β, γ and η are positive constants. $\omega(j)$ is a distance parameter whose values decreases as the distance between i and j increases. μ^c represents the predicted mean of the restored image and $c \in \mathbb{Z}_3$.

Fang *et al.* [120] designed a unified variational technique to restore degraded images. Galdran *et al.* [118] utilized a perceptually inspired variational based restoration technique to develop an energy minimization model. The energy model is dependent upon a degraded image under a gray-world assumption. This technique outperforms the others in terms of visible edges. However, the dark masks are unwanted artefacts, which may be found in close-range areas.

Chen *et al.* [121] designed a restoration technique for reliable suppression of several artefacts in images. Initially, the depth-edge-aware smoothing technique is implemented to improve the initial atmosphere veil estimated using local priors. In the image restoration step, Gradient Residual Minimization is used to remove the weather degradation from an image while explicitly decreasing the various artefacts. Galdran *et al.* [122] designed fusion based variational image-restoration technique. Fusion based variation restoration does not rely on a physical model [123, 124].

Table 2.6 shows the comparative analysis between variational based visibility restoration techniques. It has been observed that these techniques provide efficient results as compared to the existing techniques. However, these techniques suffer from poor computation speed [125, 126].

Table 2.6: Comparative analysis of variational model based restoration techniques

Ref.	Technique	Year	EP	S_P	CD	HA	LHG	GRA	BA
[120]	Adaptive technique	2010	✓	Average	✗	✓	✓	✓	✗
[118]	Variational model	2015	✓	Average	✓	✓	✓	✓	✗
[127]	Fast smoothing	2015	✓	Average	✗	✓	✓	✓	✓
[128]	Variational model	2016	✓	Average	✗	✓	✓	✓	✗
[121]	Gradient minimization	2016	✓	Average	✓	✓	✓	✓	✗
[129]	Wavelet transform	2017	✓	Average	✗	✓	✓	✓	✓
[122]	Variational model	2017	✓	Average	✓	✓	✓	✓	✓

2.2 Comparative analysis

Table 2.7 shows the comparative analysis between the existing techniques based upon various factors. These factors are: Depth estimation (DE), Multi-images (MI), Polarizing filter (PF), Known depth (KD), and Single image (SI) based visibility restoration techniques by considering the attributes known in prior.

Table 2.7: Comparative analysis of existing works on vision through atmospheric scattering media.

Ref.	Type	Known in prior	Attribute(s) going to be estimated	Key principle
[130]	DE**	$I_g(j)$ & $I_r(j)$	$t(j)$ & $d_p(j)$	Direct solving
[131]	DE**	I_2^g	$t(j)$ & $d_p(j)$	Comparing different β
[81]	DE**	$I_g(j)$ & Υ	$t(j)$ & $d_p(j)$	Direct solving
[24]	DE**	$I^c(j)$	$t(j)$, $d_p(j)$ & Υ	Dichromatic model
[132]	MI*	$I_2^c(j)$	$t(j)$, $d_p(j)$	Colour decomposition
[30]	MI*	$I_2^g(j)$ & $I_2^c(j)$	$\gamma(j)$, $d_p(j)$, Υ & $I_r(j)$	Color decomposition
[133]	PF**	$I_2^g(j)$ & $I_2^c(j)$	Υ, $\gamma(j)$, $d_p(j)$ & $I_r(j)$	$d_p(j)$ has insignificant polarization
[134]	PF**	$I_2^g(j)$ & $I_2^c(j)$	Υ, $\gamma(j)$, $d_p(j)$ & $I_r(j)$	Υ & $d_p(j)$ are independent
[135]	KD*	$I_g(j)$ & $d_p(j)$	Υ, β & $I_r(j)$	Uniform color
[136]	KD*	$I^c(j)$	$I_r(j)$	Dichromatic model
[137]	KD*	$I^c(j)$ & $d_p(j)$	$I_r(j)$	Dichromatic model
[138]	KD*	$I^c(j)$	Υ, $I_r(j)$	Depth from calibrated camera
[139]	KD*	$I^c(j)$	$\gamma(j)$ & $I_r(j)$	Transmission estimation by mean texture
[31]	SI**	$I^c(j)$	Υ, $\gamma(j)$ & $I_r(j)$	Brightest value assumption
[17]	SI**	$I^c(j)$	Υ, $\gamma(j)$ & $I_r(j)$	Υ & $\gamma(j)$ are uncorrelated
[140]	SI**	$I^c(j)$	Υ, $\gamma(j)$ & $I_r(j)$	At least one color channel has low intensity
[43]	SI**	$I^c(j)$	Υ, $\gamma(j)$ & $I_r(j)$	Normalized Υ is upper-bounded
[86]	SI**	$I^c(j)$	$\gamma(j)$ & $I_r(j)$	$I_r(j)$ & Υ are independent
[74]	SI**	$I^c(j)$	Υ & $I_r(j)$	Global contrast enhancement
[88]	SI**	$I^c(j)$	Υ, $\gamma(j)$ & $I_r(j)$	Dark channel for $\gamma(j)$
[141]	SI**	$I^c(j)$	$\gamma(j)$, $I_r(j)$	Machine learning of $\gamma(j)$
[91]	SI**	$I^c(j)$	Υ, $\gamma(j)$ & $I_r(j)$	Uniform color and depth
[35]	SI**	$I^c(j)$	$\gamma(j)$ & $I_r(j)$	Learning by neural network
[142]	SI**	$I^c(j)$	$\gamma(j)$ & $I_r(j)$	Finite color approximation

Note: * states that given restoration technique does not require any kind of mathematical model.

** states that given restoration technique requires a well-designed mathematical model to restore images.

In Table 2.7, $I_g(j)$ represents single gray image. $I_r(j)$ shows actual ground truth image (*i.e.,* actual image radiance). $I_2^g(j)$ depicts two gray images with different scattering coefficients $\beta 1$ and $\beta 2$. $\gamma(j)$ represents transmission map. d_p represents depth map. Υ depicts atmospheric light. $I^c(j)$ shows single color image. $I_2^c(j)$ indicates different weather conditions $(\beta 1, \beta 2)$.

The visibility restoration techniques can be divided into two categories. These are the techniques which require a mathematical model or not require any kind mathematical model. Here, KD and MI do not need any mathematical model to compute the depth information for images. DE, PF, and SI are examples of mathematical model based restoration techniques.

From the extensive review of existing restoration techniques, it has been found that the visibility restoration of weather degraded images is still an ill-posed issue. Many techniques have been found to be effective for removing the effect of weather degradation of images [143, 144].

Li *et al.* [99] used Change of detail prior (COD) to remove the fog from an image by using multiple scattering occurrences in the dissemination of illumination. The thickness of fog is evaluated in COD to restore the foggy image. It is stable for local regions of fog image that comprise objects in different depths [99]. A restoration technique proposed by Zhao *et al.* utilized the local extrema to figure out three pyramid levels for estimating atmospheric veil and manipulating contrast of details at different scales [81]. However, quadtrees[84], COD [99], and local extrema [81] cannot preserve the edges of the restored images.

L_2 norm based fog removal method can evaluate the depth by computing the average vector L_2 norm of the sample window. It used a guided filter to preserve the edges of the restored image [101]. However, it still suffers from halo artefact issues which may introduce during the fusion process. Li *et al.* [102] used a Weighted guided image filter (WGIF) to remove halo artefacts. However, the main drawback of WGIF is poor computation time as compared to the existing restoration techniques [91], [145], and [146].

Fattal [91] proposed Color-lines (CL) to evaluate the transmission map in an efficient manner. It has better computation time. Anwar and Khosla [33] designed a hybrid restoration method namely Weighted the least square and high dynamic range (WHDR). It is based on weighted least square and high dynamic range. This technique has an ability to preserve sharp details while maintaining the color quality of restored images.

Cui *et al.* [147] proposed a weighted L_1 norm regularization based restoration technique. They utilized half-quadratic splitting minimization procedure to monitor the reliable global atmospheric light. Wang *et al.* [148] proposed a Linear transform and quadtree (LTQ) based restoration technique. An additional channel method is based upon quadtree subdivision to efficiently monitor the atmospheric light. However, these techniques CL [91], WHDR [33], L_1 [147], and LTQ [148], do not have depth knowledge of roadside images in practice.

2.3 Research gaps

After the detailed analysis of the existing visibility restoration techniques, the following research gaps are identified.

i. The majority of existing techniques may lose significant detail of restored images with large weather gradients. Thus, most of the existing visibility restoration techniques are effective for thin haze/fog only.

ii. Fail to restore image under the inhomogeneous bad weather. It may happen in many real-life inhomogeneous environmental conditions occur. But, the majority of techniques developed so far work successfully only for the homogeneous environment.

iii. The effect of edge preservation on visibility restored images has been neglected by majority of the existing researchers. Thus, the potential edges may degrade during the visibility restoration process.

iv. Limited removal of multiplicative artefacts in degraded images. The existing restoration techniques estimate patch-wise transmission. This patch-wise estimation introduces multiplicative artefacts around the edge. A transmission map refinement step is required to reduce multiplicative artefacts.

v. The existing restoration may produce poor results in the sky (bright) regions. The depth map estimation techniques are unable to evaluate the consistent depth map in the brighter regions.

2.4 Objectives

To address the aforementioned research gaps, the following objectives are formulated:

i. To study and explore the different existing techniques for visibility restoration of weather degraded images.

ii. To design and development of modified filter(s) for reducing the multiplicative artefacts.

iii. To develop adaptive restoration models, in order to handle the issues of sky (bright) regions and inhomogeneous bad weather.

iv. To compare and analyze the developed visibility restoration techniques on standard and real-life weather degraded images.

2.5 Thesis contributions

To achieve the aforementioned objectives, the following contributions are presented in this thesis.

i Initially, various filters (*i.e.,* (a) Modified gain intervention trilateral filter (GITF) and (b) Fourth-order partial differential equations based trilateral filter (FPDETF)) have been designed and implemented to restore the weather degraded images. These filters are used to refine the transmission map obtained from DCP. These filters overcome various issues of the existing techniques such as sky-region, halo artefact, inhomogeneity of weather degradation, gradient reversal artefacts, color distortion, edge degradation, and poor computational speed. The proposed techniques have been tested on the benchmark foggy and hazy images. The experimental results have proven that the proposed filters based restored images provide a lesser number of halo and gradient reversal artefacts and preserve more significant edges as compared to the existing restoration techniques. The proposed image filters are computationally faster than the existing techniques. Therefore, the proposed filters are more suitable for real-time computer vision applications. It has been found that GITF improves the contrast gain by 1.76 % as compared to the existing competitive visibility restoration techniques. Also, GITF significantly reduces the percentage of saturated pixels and execution time by 1.96 % and 3.21%, respectively. Comparative analysis has proven that FPDETF outperforms the existing techniques in terms of contrast gain, ratio of new visible edges, and ratio of the average gradient by 1.98%, 1.72% and 1.81%, respectively. Also, FPDETF reduces the percentage of saturated pixels and execution time by 2.07% and 3.41%, respectively.

ii A novel restoration technique is designed by utilizing DCP, Bright channel prior (BCP), and gain intervention filter. BCP is used to solve the sky-region problem associated with DCP based visibility restoration techniques. The gain intervention filter is used to improve computational speed and edge preservation rate of restored images. The experimental results reveal that the integrated model provides better computational time as compared to the existing restoration techniques. It also provides superior restored images over the existing restoration techniques.

IVRM outperforms the existing techniques in terms of new visible edges and average gradient by 1.84% and 1.85%, respectively. IVRM reduces the percentages of saturated pixels by 2.13% as compared to competitive visibility restoration techniques.

However, GITF, FPDETF, and IVRM suffer from the issue of noise when estimated transmission map approaches toward zero. As a consequence, the restored color could deviate from the actual object and the restored images look like the artificial image.

iii A Modified restoration model (MRM) based DCP is proposed to solve color distortion and halo artefacts issues. MRM redefines the transmission map to reduce the color distortion problem. The modified joint trilateral filter is also utilized to improve the coarse estimated atmospheric veil. The experimental results reveal that MRM provides visually significant restored images and also preserves the significant detail. The experimental results have proven that MRM outperforms other visibility restoration techniques in terms of contrast gain, a ratio of new visible edges, and ratio of the average gradient by 2.13%, 1.91% and 1.92%, respectively. Also, MRM reduces the percentage of saturated pixels by 2.34%.

iv Two gradient based profile priors such as Gradient profile prior (GPP) and Oblique gradient profile prior (OGPP)) are proposed. The modified filters are also designed to remove the halo and gradient reversal artefacts problems. The developed gradient based profile priors are able to minimize the color and texture distortion issues. Extensive experiments reveal that the proposed techniques outperform the existing visibility restoration techniques various parameter such as Contrast gain (C_g) and Percentage of saturated pixels (ρ), Visible edges ratio, and Perceptual weather degradation density (D_f), PSNR and SSIM. The proposed techniques significantly improve the spatial and radiometric information of weather degraded images. Extensive experiments have shown that GPP outperforms the existing image techniques in terms of contrast gain, the ratio of new visible edges, and ratio of the average gradient by 1.91%, 1.97% and 1.98%, respectively. GPP also reduces the percentages of saturated pixels, perceptual fog density and execution time by 2.31%, 1.47% and 2.43%, respectively as compared to the existing visibility restoration techniques. It has been found that OGPP outperforms the existing image techniques in terms of contrast gain (C_g), a ratio of new visible edges, a ratio of an average gradient, Peak signal to noise ratio (PSNR), and Structural similarity index metric (SSIM) by 1.94%, 2.01%, 2.17%, 3.72% and 1.31%, respectively. OGPP also reduces the percentages of saturated pixels, perceptual fog density, and execution time by 2.41%, 1.52% and 2.79%, respectively as compared to the competitive visibility restoration techniques.

Chapter 3

Transmission map refinement using modified filters

Outline

In this Chapter, various filters are designed and implemented to restore haze and fog from the weather degraded images. These filters are used to refine the transmission map obtained by applying the DCP to weather degraded images. The main objective of these filters is to overcome various issues associated with the existing restoration techniques. These issues are sky-region, halo artefact, inhomogeneity of weather degradation, gradient reversal artefacts, color distortion, edge degradation, and poor computational speed. The proposed filters are Modified gain intervention trilateral filter (GITF) and Fourth-order partial differential equations based trilateral filter. Initially, depth information of weather degraded image by applying DCP. Thereafter, transmission map and atmospheric veil are computed from the evaluated depth map. Then, the proposed filter is applied to evaluating the transmission map. Finally, the restored image is obtained by applying the modified restoration model. The proposed filters are tested on benchmark foggy and hazy images.

3.1 Gain intervention based trilateral filter

This section describes the motivation behind the Gain intervention based trilateral filter (GITF) followed by mathematical formulation of GITF.

3.1.1 Motivation

Filtering techniques have been extensively used to refine the transmission map. However, some of these filters fail to preserve significant edges and require guidance image. In general, source image is taken as a guided image. But, in a foggy environment, input image contains fog which means guided image also contains fog. Therefore, filter based coarse estimated atmospheric veil is not so efficient when images contain large fog density. It leads to halo and gradient reversal artefacts in the restored image. To solve these problems, the following modifications have been done in GITF. (1) The modification has been done in a trilateral filter [45] with the help of gain intervention filter to remove the sky region problem and halo artefacts in a more efficient way. (2) The images generated from the standard restoration model as used in [45] may seem to be artificial, especially in case of high-density fog. Therefore, the refinement has also been done in the restoration model of GITF.

3.1.2 Proposed trilateral filter

GITF consists of five main stages. These are DCP, atmospheric veil estimation, coarse atmospheric veil evaluation, modified gain coefficient based trilateral filter, and visibility restoration model. Figure 3.1 shows the flow-diagram of GITF. The brief description of these steps is given below.

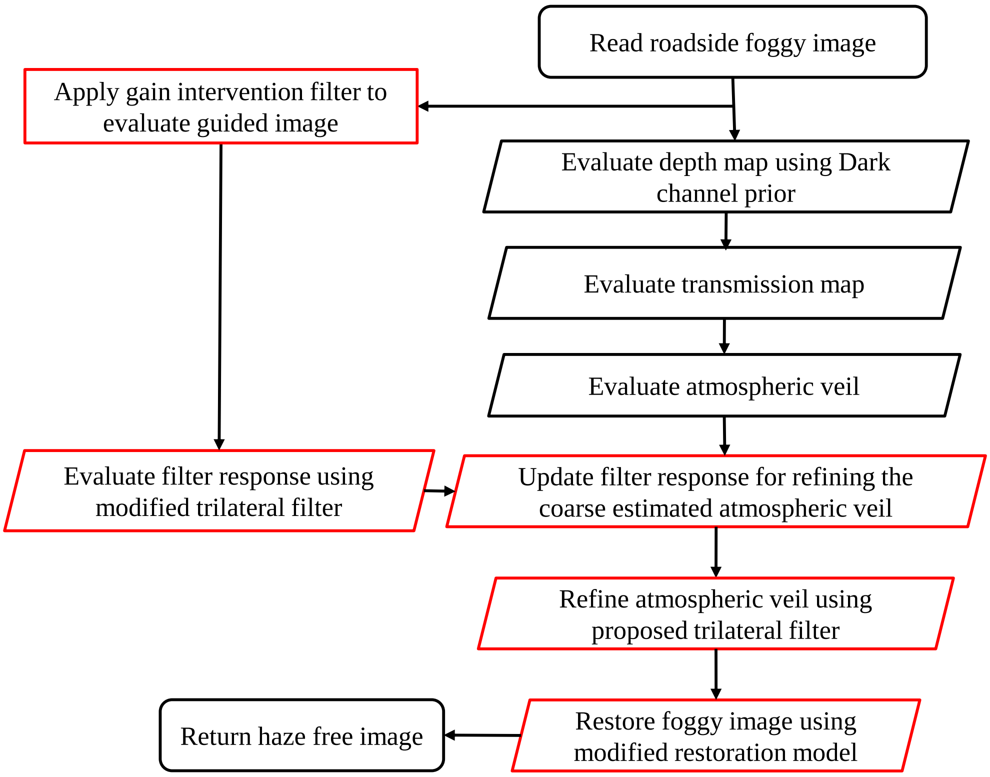

Figure 3.1: Flow-diagram of gain intervention trilateral filter

Initially, DCP is obtained using Eq. (1.3) (see Section 1.3.1). Thereafter, the global atmospheric light estimation model (Υ) is obtained using Eq. (1.8) (see Section 1.3.2). The coarse atmospheric veil is then evaluated using Eq. (1.16) (see Section 1.3.3).

The trilateral filter is used to refine the coarse estimated atmospheric veil. This filter has an ability to remove noise from images and preserve edges in a more prominent manner than bilateral [42] and guided image filter [149]. Also, it has better computational speed than the majority of existing filters. The standard trilateral filter uses the input image itself as a guided image. The guided image has been improved by applying gain coefficient based image filter. Hence, it improves the coarse estimated atmospheric veil [37].

The gain coefficient based filter is used for better guidance image creation for a trilateral filter. Most of the researchers have taken the source image as a guided image. However, if the input image includes fog, thus, guided image based trilateral filter may possibly provide poor restoration results. Therefore, gain coefficient based trilateral filter has an ability to enhance the coarse estimated $\gamma(j)$ for real-time restoration. The gain coefficient (G_{cf}) can be mathematically defined as:

$$G_{cf} = \frac{\sum_{p,q}^{|M_i|-1} d(p,q)}{|d|} \tag{3.1}$$

Here, M_i is determined using the following formula:

$$M_i(p,q) = \min_{c\in\{R,G,B\}} I(p,q) \tag{3.2}$$

where $|M_i|$ and $|d|$ represent the number of pixels in M_i and d, respectively. $d(p,q)$ represents the variance at (p,q) involving the minimal intensity. $d(p,q)$ can be determined as:

$$d(p,q) = M_i(p,q) - I_c(p,q) \tag{3.3}$$

G_{cf} is employed to produce the filtered guided image (G_d) and maintain the natural information of each and every window. Therefore, the improved G_d can be evaluated as:

$$G_d(p,q) = (1 - M_i(p,q)) + G_{cf} \times P_{cf} \tag{3.4}$$

where P_{cf} is the response factor.

A gain coefficient based trilateral filter has the capability to overcome the gradient reversal artefacts of a restored image. The filtering procedure is initially prepared under the guidance image (G_d), which is obtained by applying the gain intervention filter on the input image (I).

Let I_q and G_q be illumination values at pixel q of minimum channel object and guided image (G_d), respectively. K_r represents a kernel mask at j, which is to be dependable upon bilateral filter. Therefore, gain coefficient based trilateral filter (J_f) is devised as:

$$J_f(I) = \frac{1}{\sum\limits_{q\in K_r} M_c^{pq}(G_d)} \left(\sum_{q\in k_r} M_c^{pq}(G_d) \times I_q \times \sigma^2(I_q, G_q) \right) \tag{3.5}$$

Here, the kernel weight function ($M_c^{pq}(G_d)$) is defined as:

$$M_c^{pq}(G_d) = \frac{1}{|n|^2} \sum_{n:(p,q)\in k_r} \left(1 + \frac{\Big(G_{dp} - \mu_n)(G_{dq} - \mu_n\Big)}{\sigma_n^2 + \theta} \right) \tag{3.6}$$

where μ_n and σ_n^2 represent the mean and variance of G_d, respectively. In local mask k_r, $|n|$ is the total pixels in the mask. θ shows the regularization attribute to provide the balance between pixel similarity and filtering. Note that $\theta \neq 0$. When G_{dp} and G_{dq} are present simultaneously on the similar side of an edge, the weight allocated to pixel q is maximized. When G_{dp} and G_{dq} are on opposite sides, a minimum weight will be allocated to pixel q.

To improve the atmospheric veil, a GITF is designed. From [45], the value of of refined atmospheric veil is computed as:

$$\gamma(j) = \Upsilon_{(}1 - t(j)) \tag{3.7}$$

Long *et al.* [44] utilized well-known Gaussian filter to refine the atmospheric veil. It has been achieved by using the following mathematical formulation:

$$t(j) = \frac{1}{W_g} \sum GF(||i - j||) \tag{3.8}$$

Here, W_g represents weighted sum of local patch at j. Also, Gaussian filter (GF) is calculated as:

$$GF(j) = e^{-j^2/2\sigma^2} \tag{3.9}$$

By deriving from Eq. (3.8), GITF has been designed and implemented. The transmission refinement map is achieved by using the following mathematical formula:

$$t(j) = \sigma^2(j) - J_{\mathscr{W}}^{f}\Big(|M_c(j) - \sigma^2(j)|\Big) \tag{3.10}$$

Here, $J_{\mathscr{W}}^{f}$ shows GITF. $\sigma^2(j)$ represents the variance of pixel centred at position j, with its neighbors in local mask of 7×7. Also, minimum color channel ($M_c(j)$) of $I(j)$ is computed as:

$$M_c(j) = \min_{c\in[R,G,B]} \Big(I(j)\Big) \tag{3.11}$$

Here, c represents color channel of $I(j)$. Hence, the atmospheric veil ($\gamma(j)$) can be rewritten as:

$$\gamma(j) = \max\left(\left(\min\left(t^f(j), M_c(j)\right)\right), 0\right) \tag{3.12}$$

Here, $t^f(j)$ shows refined transmission map by using GITF. Transmission of every mask (t) can be redefined as:

$$\bar{\mathrm{t}} = 1 - \frac{\gamma}{\Upsilon} \tag{3.13}$$

Υ is typically supposed to be a pixel illumination with maximum luminosity in an object. However, in real time, this hypothesis frequently delivers invalid outcomes because of the occurrence of self luminous organisms. In the same way, the sky pixel values are also computed between all the local minimum that correspond to background illumination Υ, which is computed as:

$$\Upsilon = \max_{z \in I}\left(\min_{z \in \mathscr{W}(j)}\left(I^c(z)\right)\right) \tag{3.14}$$

Here, $I^c(z)$ represent color components of $I(j)$ in every mask.

After improving the coarse estimated atmospheric veil, there is a need to restore the foggy image by applying a fog removal restoration model. The actual scene radiance can be restored by using Eq. (1.33) (see Section 1.3.5).

3.1.3 Performance evaluation

GITF is tested on ten different roadside foggy images (*i.e.,* five standard and five real-time images) and compared with seven competitive restoration techniques. The benchmark images are taken from FRIDA [150] and FRIDA2 [150] datasets. DCP [16], WHDR [33], COD [99], WGIF [102], CL [91], LTQ [148], and L_1 [147] based restoration techniques are used for comparative analysis. To restore the foggy images, 8-bit images have been normalized within the range of $[0,1]$.

A. Visual analysis

This section contains the visual analysis of GITF on ten different roadside foggy images.

Figure 3.2 shows the depth map estimated by different image restoration techniques. Figure 3.2 (a) shows the actual depth map. From Figures 3.2 (b) - (j), it has been observed that the depth map estimated by GITF seems to be closer to the actual depth map. Therefore, GITF can efficiently estimate the depth map as compared to the other techniques.

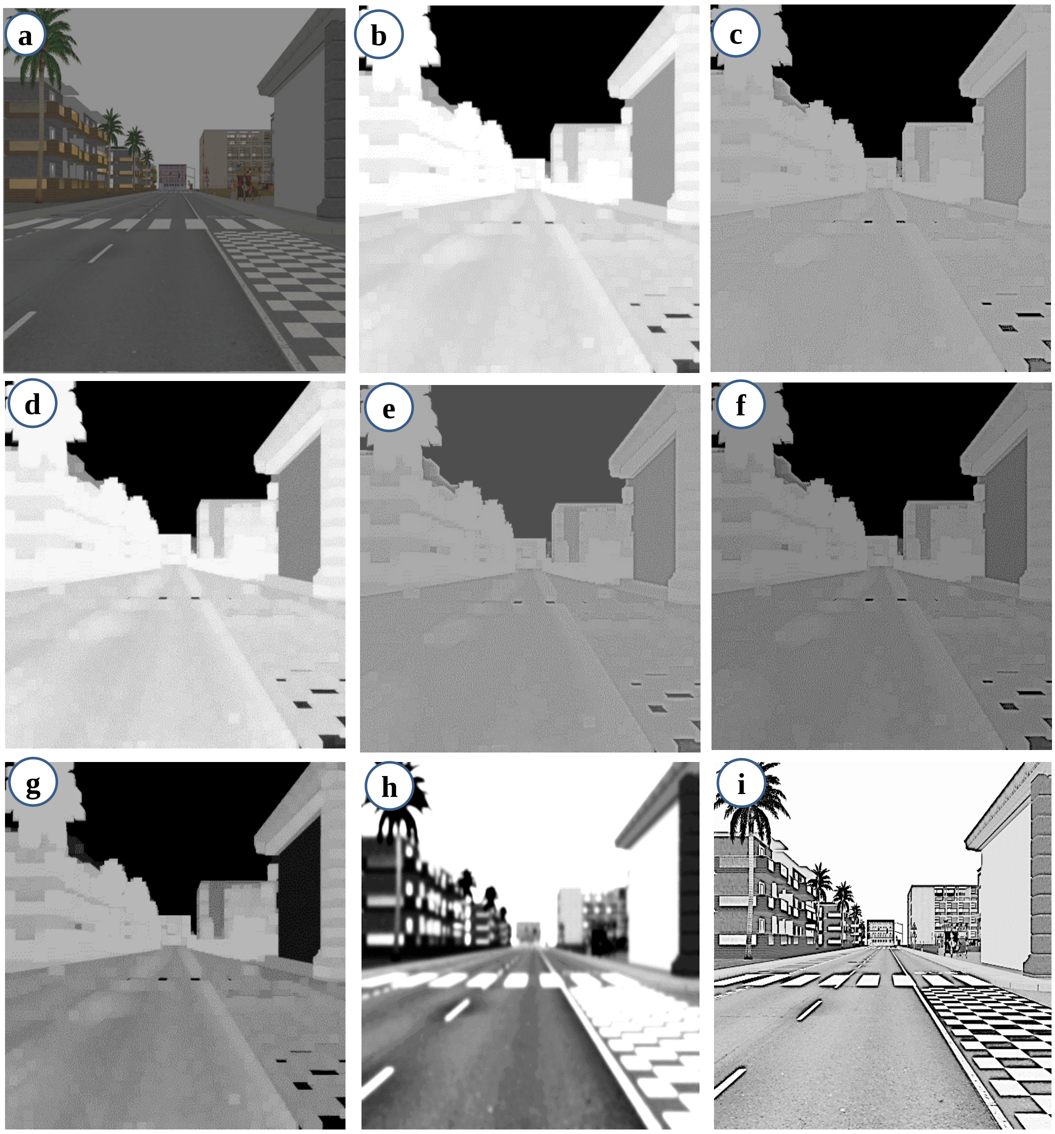

Figure 3.2: Results of estimated depth map for FRIDA foggy image (a) Input image, (b) DCP, (c) WHDR, (d) COD, (e) WGIF, (f) CL, (g) LTQ, (h) L_1, and (j) GITF.

Figure 3.3 (b) shows the result of DCP [16] based restoration technique. DCP [16] has reduced the fog from an input image in an efficient way. The output image has preserved the edges of the restored images in an efficient manner. However, halo and gradient reversal artefacts are present in the restored image. Figures 3.3 (c) and 3.3 (g) show restored images using WHDR [33] and LTQ [148] based restoration techniques, respectively. Restored images using WHDR [33] and LTQ [148] techniques have shown lesser color distortion. However, edges are not preserved. Figures 3.3 (d) and 3.3 (f) demonstrate the restored images using COD [99] and CL [91] based restoration techniques, respectively. It has been observed that these techniques contain lesser halo artefacts. But, these techniques are unable to preserve edges in an efficient manner. Figures 3.3 (e) and 3.3 (h) show the restored images using L_1 [147] and WGIF [102] based restoration techniques. From these figures, it is also observed that the minimum number of saturated pixels is present in restored images. But, the restored images obtained from these techniques contain halo and gradient reversal artefacts. Figure 3.3 (j) shows the restored image obtained by GITF. It has achieved a remarkable visual quality with a lesser number of halo and gradient reversal artefacts.

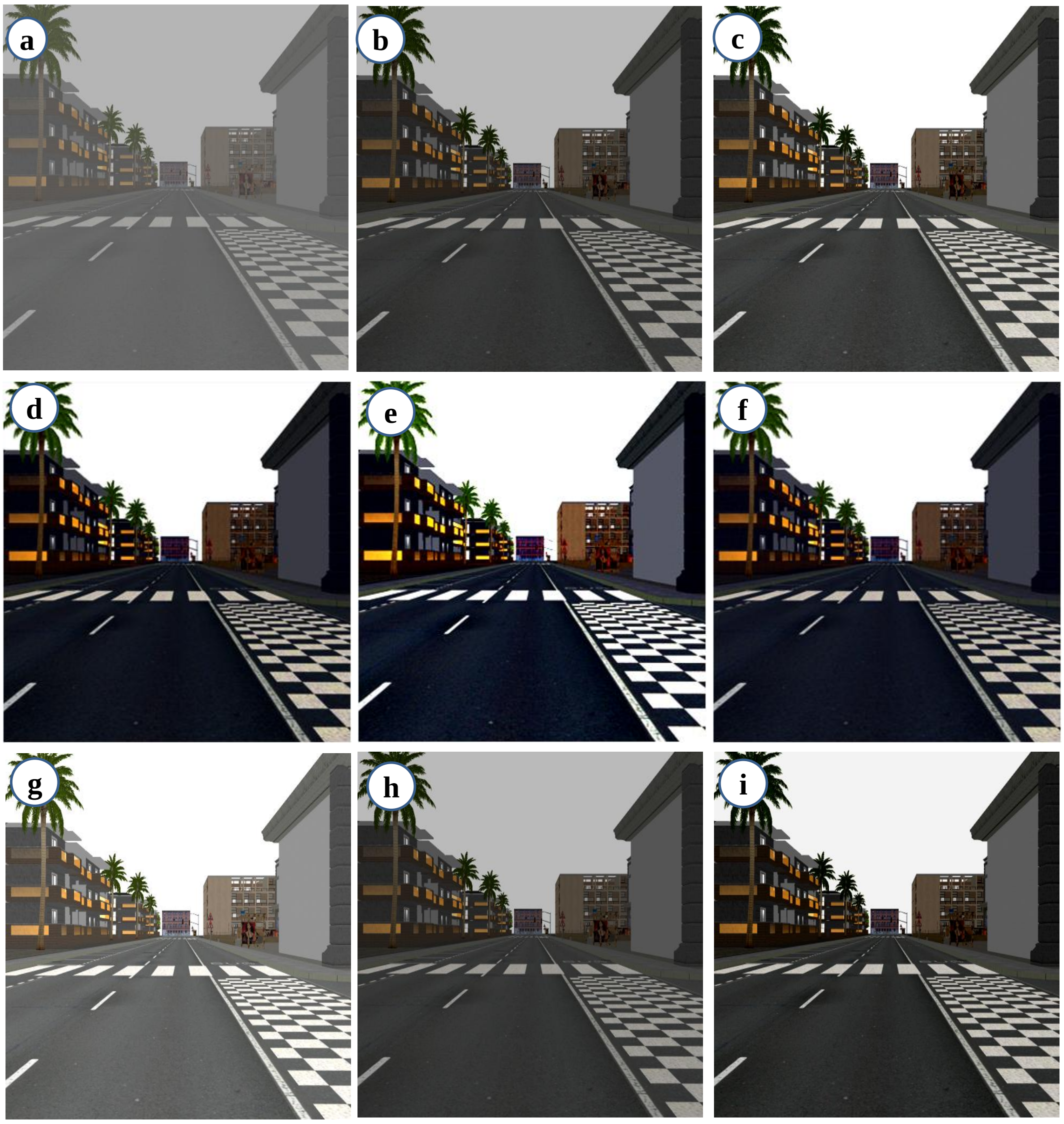

Figure 3.3: Results of restoration techniques for FRIDA foggy image (a) Input image, (b) DCP, (c) WHDR, (d) COD, (e) WGIF, (f) CL, (g) LTQ, (h) L_1, and (j) GITF.

Figure 3.4 shows the subjective analysis of bike foggy image. Figure 3.4 (b) shows the restored image by DCP [16]. Although, edges have been preserved. However, the restored images contain halo and gradient reversal artefacts. Figures 3.4 (c) and 3.4 (g) show the restored images using WHDR [33] and LTQ [148] techniques, respectively. The restored images have shown lesser color distortion in the restored images. However, the edges are not preserved. Figures 3.4 (d) and 3.4 (f) illustrate the restored images using COD [99] and CL [91] techniques, respectively. The restored images have lesser halo and gradient reversal artefacts. However, edges are not preserved. Figures 3.4 (e) and 3.4 (h) demonstrate the results obtained from L_1 [147] and WGIF [102] techniques. Restored images have lesser number of saturated pixels. However, these images suffer from halo and gradient reversal artefacts. Figure 3.5 (j) shows the restored image obtained from GITF. GITF has lesser number of gradient reversal artefacts as compared to the other existing techniques.

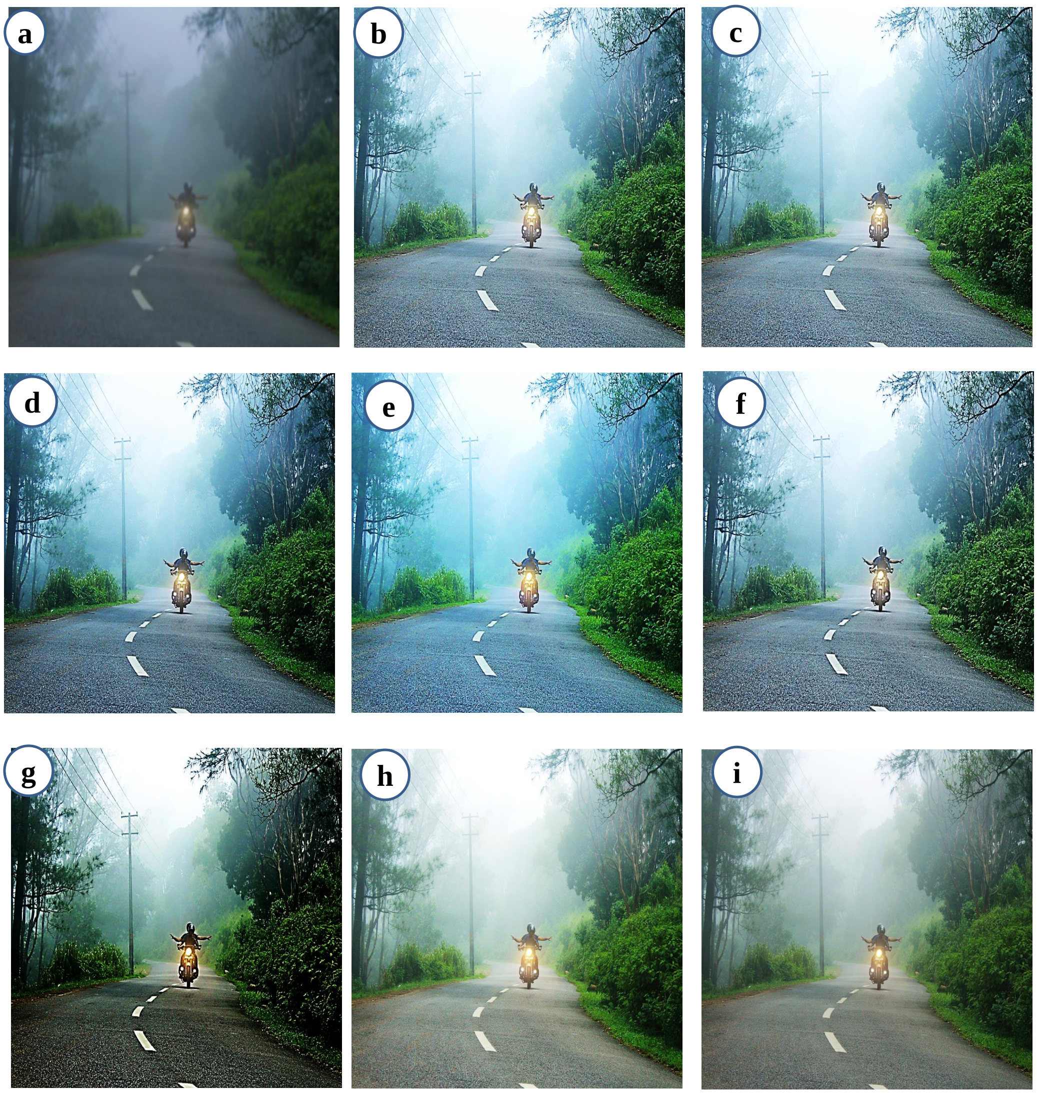

Figure 3.4: Results of restoration techniques for bike foggy image (a) Input image, (b) DCP, (c) WHDR, (d) COD, (e) WGIF, (f) CL, (g) LTQ, (h) L_1, and (j) GITF.

The restoration results for tollway foggy image are shown in Figure 3.5. The restored image obtained by DCP [16] restoration technique suffers from halo and gradient reversal artefacts. WHDR [33], LTQ [148], COD [99] and CL [91] based restoration have shown lesser number of gradient reversal artefacts. However, the edges are not preserved in restored images.

Figures 3.5 (e) and 3.5 (h) show the restored images obtained from L_1 [147] and WGIF [102] based visibility restoration techniques. These restored images have lesser number of saturated pixels. However, these figures suffer from halo and gradient reversal artefacts. The restored image obtained from GITF is demonstrated in Figure 3.5 (j). As compared to the earlier techniques, GITF is least affected by gradient reversal artefacts.

Figure 3.5: Results of restoration techniques for tollway foggy image (a) Input image, (b) DCP, (c) WHDR, (d) COD, (e) WGIF, (f) CL, (g) LTQ, (h) L_1, and (j) GITF.

Figures 3.6 shows the results of restoration techniques for highway roadside image. DCP [16] based restoration technique suffers from a saturated pixel problem. The restored images obtained by WHDR [33] and LTQ [148] have less number of gradient and halo artefacts. But, the several edges are distorted in restored images. Figures 3.6 (d) and 3.6 (f) illustrate the outcomes of COD [99] and CL [91] techniques, respectively.

These techniques have lesser halo artefacts. These are not effective for conserving the edges of the restored image. Figures 3.6 (e) and 3.6 (h) show the outcomes of L_1 [147] and WGIF [102] restoration techniques. These techniques have a minimum number of saturated pixels. However, the restored images may have halo and gradient reversal artefacts. Figure 3.6 (j) shows that GITF has an ability to remove the fog from images with good edge preservation and a lesser number of halo and gradient reversal artefacts.

Figure 3.6: Results of restoration techniques for highway foggy image (a) Input image, (b) DCP, (c) WHDR, (d) COD, (e) WGIF, (f) CL, (g) LTQ, (h) L_1, and (j) GITF.

Figure 3.7 (b) illustrates the result of DCP [16] technique for hilly roadside image. It is observed that the resorted image has conserved the edges in an efficient manner. However, the restored image suffers from halo and gradient reversal artefacts. Figures 3.7 (c) and 3.7 (g) show the restored images obtained by WHDR [33] and LTQ [148]'s techniques. The restored image have shown lesser color distortion rate. But, it is also observed that the several edges are distorted. Figures 3.7 (d) and 3.7 (f) demonstrate the restored images obtained from COD [99] and CL [91] techniques, respectively. It is observed that COD [99] and CL [91] techniques have lesser halo artefacts. However, these are not so effective to conserve edges of visibility restored image. Figures 3.7 (e) and 3.7 (h) show the restored images obtained L_1 [147] and WGIF [102] techniques. The restored images have lesser number of saturated pixels. But, these may contain several haloes and gradient reversal artefacts. Figure 3.7 (j) demonstrates the restored image obtained from GITF. It attains a remarkable visual superiority with lesser number of halo and gradient reversal artefacts.

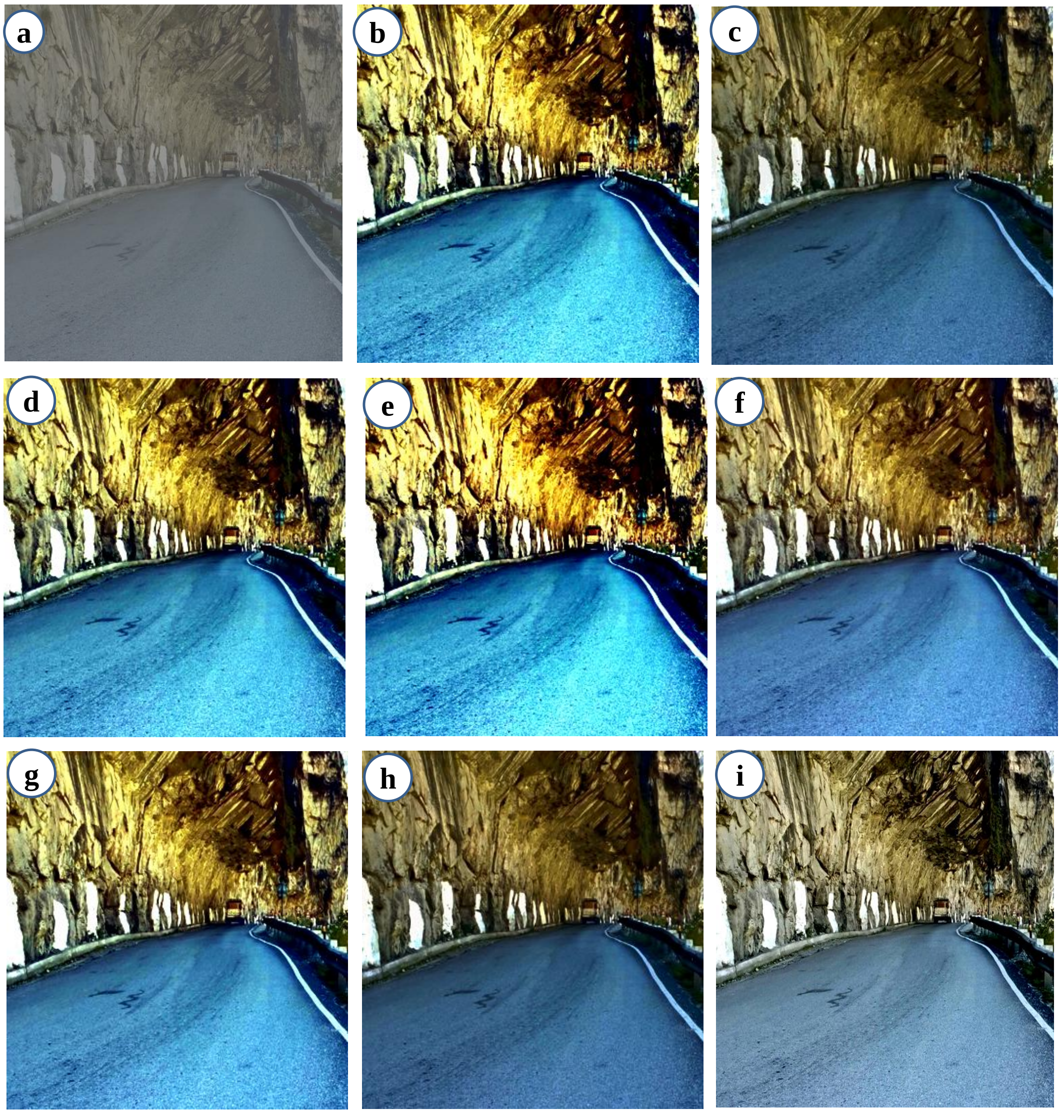

Figure 3.7: Results of restoration techniques for hill-roadside foggy image (a) Input image, (b) DCP, (c) WHDR, (d) COD, (e) WGIF, (f) CL, (g) LTQ, (h) L_1, and (j) GITF.

In summary, COD [99], WGIF [102], CL [91], LTQ [148], and L_1 [147] techniques have the ability to remove fog from roadside images with satisfactory visual results.

But, COD [99] and WGIF [102] techniques are prone to produce distorted sky color, while the color information of fog free images developed using CL [91], LTQ [148], and L_1 [147] look somewhat faint. In contrast, it is observed that GITF attains significant visual quality with lesser number of halo and gradient reversal artefacts.

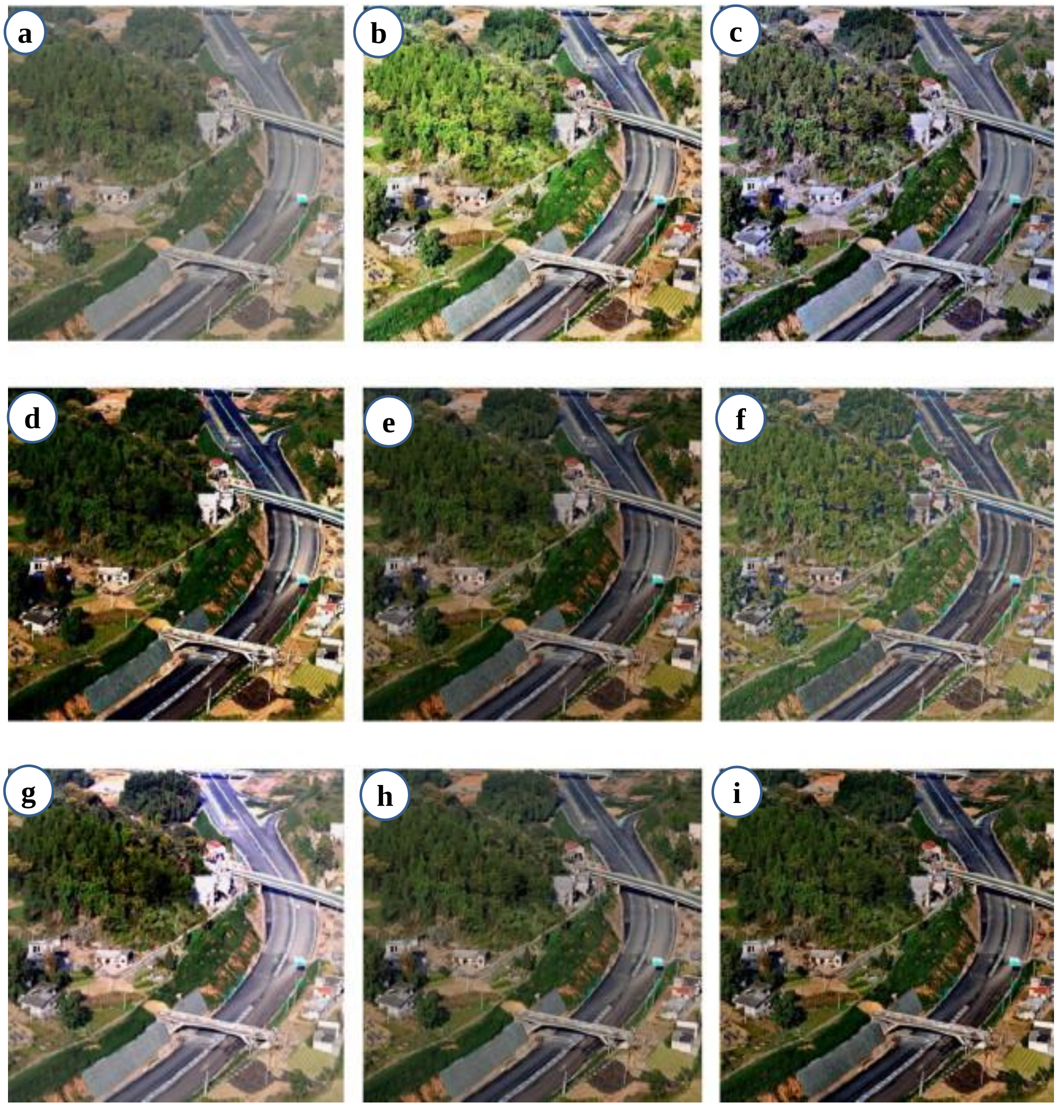

Figure 3.8: Results of restoration techniques for remote sensing foggy image (a) Input image, (b) DCP, (c) WHDR, (d) COD, (e) WGIF, (f) CL, (g) LTQ, (h) L_1, and (j) GITF.

Figure 3.8 (b) shows the restored image of a remote sensing image obtained from DCP [16] technique. The resorted image has preserved the edges. However, it has halo and gradient reversal artefacts. Figures 3.8 (c) and 3.8 (g) show the fog free images obtained from WHDR [33] and LTQ [148] techniques, respectively. The restored images have lesser color distortion than DCP [16]. However, these techniques suffer from edge distortion problem. Figures 3.8 (d) and 3.8 (f) show the fog free images obtained from COD [99] and CL [91] techniques, respectively. These techniques have lesser number of halo artefacts as compared to WHDR [33] and LTQ [148]. However, these techniques do not preserve the edges. Figures 3.8 (e) and 3.8 (h) show the restored images obtained from L_1 [147] and WGIF [102] techniques, respectively. These images show a lesser number of saturated pixels. However, these techniques suffer from halo and gradient reversal artefacts. Figure 3.8 (j) shows the restored image obtained from GITF. It achieves a remarkable visual superiority with lesser number of halo and gradient reversal artefacts.

B. Quantitative analysis

In addition to visual analysis, three performance measures such as Contrast gain (C_g), Percentage of saturated pixels (ρ), Execution time (ET) are utilized to evaluate the performance of GITF. Table 3.1 demonstrates the performance analysis of GITF with others in terms of C_g. It shows that GITF has better C_g than other restoration techniques such as DCP [16], WHDR [33], COD [99], WGIF [102], CL [91], LTQ [148], and L_1 [147]. The average improvement of C_g using GITF over other techniques is 0.0436 (Approx).

Table 3.1: Comparative analysis of GITF with respect to contrast gain (C_g)

Images	DCP	CL	COD	WGIF	LTQ	L_1	WHDR	GITF
$FRIDA1_1$	0.0105	0.0977	0.1382	0.1558	0.1425	0.1399	0.1682	0.1857
$FRIDA1_2$	0.0027	0.1287	0.1331	0.1275	0.1567	0.1484	0.1625	0.1815
$FRIDA1_3$	0.0135	0.1059	0.1998	0.1857	0.2190	0.1987	0.2389	0.2730
$FRIDA2_1$	0.0087	0.1005	0.1781	0.1952	0.1736	0.2528	0.1927	0.2191
$FRIDA2_2$	0.0157	0.0395	0.1931	0.1570	0.1596	0.1432	0.1769	0.1957
$Bike$	0.1725	0.1915	0.2171	0.1875	0.2010	0.1670	0.2202	0.2358
Tollway	0.0197	0.0291	0.1515	0.1587	0.1641	0.1399	0.1701	0.1871
$Highway$	0.0177	0.0251	0.1257	0.1297	0.1945	0.1899	0.2009	0.2137
$Hillside_1$	0.0098	0.0127	0.1559	0.1855	0.1576	0.1599	0.2100	0.2291
$Hillside_2$	0.0159	0.0285	0.1258	0.1158	0.1366	0.1602	0.1299	0.1759
$Satellite$	0.0271	0.0291	0.1346	0.1247	0.1214	0.1367	0.1387	0.1417

Table 3.2 demonstrates that GITF has lesser ρ as compared to DCP [16], WHDR [33], COD [99], WGIF [102], CL [91], and L_1 [147]. The results reveal that the average reduction in ρ using GITF over other restoration techniques is 0.0296 (Approx).

Table 3.2: Experimental analysis of GITF with respect to percentage of saturated pixels (ρ)

Images	DCP	CL	COD	WGIF	LTQ	L_1	WHDR	GITF
$FRIDA2_1$	0.1449	0.0315	0.0469	0.0961	0.0541	0.0341	0.0289	0.0159
$FRIDA2_2$	0.1170	0.0179	0.0149	0.0116	0.0157	0.0123	0.0134	0.0114
$FRIDA2_3$	0.1537	0.0715	0.1697	0.0373	0.0472	0.0231	0.0314	0.0157
$FRIDA2_1$	0.1417	0.0110	0.0415	0.0993	0.0872	0.0651	0.0276	0.0110
$FRIDA2_2$	0.1739	0.1077	0.1411	0.0717	0.0623	0.0239	0.0189	0.0137
Bike	0.1311	0.0341	0.1159	0.0754	0.0601	0.0451	0.0378	0.0317
Highway	0.1317	0.1316	0.0941	0.0739	0.0454	0.0410	0.0202	0.0117
Tollway	0.1107	0.0954	0.0995	0.0749	0.0648	0.0411	0.0599	0.0477
$Hillside_1$	0.1771	0.1667	0.1317	0.0916	0.0821	0.0561	0.0731	0.0317
$Hillside_2$	0.1791	0.1111	0.1419	0.0954	0.0421	0.0399	0.0532	0.0339
Satellite	0.1472	0.1287	0.1046	0.0846	0.0819	0.0647	0.0612	0.0587

Table 3.3 demonstrates the analysis of ET in seconds. It clearly shows that GITF takes lesser time as compared to earlier restoration techniques. The results reveal that the average reduction in ET by using GITF over the earlier techniques is approximately 0.0987 (in seconds).

Table 3.3: Experimental analysis of GITF with respect to execution time (ET) in seconds

Images	DCP	CL	COD	WGIF	LTQ	L_1	WHDR	GITF
$FRIDA1_1$	59.9±6.7	9.7±2.9	9.5±1.8	6.8±0.9	7.6±0.5	6.5±1.1	1.9±0.2	1.6±0.2
$FRIDA1_2$	57.8±5.7	8.7±1.8	9.6±2.4	6.1±0.8	6.7±0.8	7.1±1.0	1.7±0.8	1.6±0.3
$FRIDA1_3$	58.7±6.3	8.6±2.1	9.7±2.3	6.7±1.0	5.6±0.6	5.5±1.2	1.6±0.9	1.1±0.5
$FRIDA2_1$	71.8±4.8	9.6±3.7	9.6±2.1	6.4±0.7	4.8±1.3	5.2±1.4	1.7±0.8	1.4±0.4
$FRIDA2_2$	65.9±4.4	9.7±3.2	9.7±1.8	4.7±1.1	6.3±0.6	5.8±1.4	1.6±0.7	1.2±0.3
Bike	69.7±5.2	8.1±2.3	8.9±3.7	6.3±0.7	6.2±1.1	7.1±0.9	1.8±0.9	1.7±0.5
Highway	64.6±7.4	9.5±3.1	9.1±2.6	6.7±0.6	6.3±0.7	5.8±1.2	1.5±0.7	1.5±0.2
Tollway	64.6±7.1	9.5±2.3	9.5±2.0	6.0±0.5	6.3±0.4	5.9±0.8	1.6±0.8	1.3±0.4
$Hillside_1$	68.1±4.7	7.6±4.8	9.3±1.7	7.2±0.8	6.9±0.7	5.4±1.3	1.7±0.8	1.1±0.3
$Hillside_2$	61.7±6.1	9.8±3.1	9.6±2.6	6.6±0.8	7.1±0.7	5.9±0.8	1.7±0.9	1.3±0.2
Satellite	59.1±7.9	9.7±4.1	8.5±3.1	7.4±2.7	6.9±1.2	5.4±1.2	2.8±0.8	1.9±0.4

The investigations demonstrated that GITF efficiently removes the fog from roadside images, without introducing halo and gradient reversal artefacts. Also, the restored images have preserved significant edges of roadside images.

3.2 Fourth order partial differential equations based trilateral filter

Although, GITF outperforms the existing techniques in case of foggy images, but, not so effective against remote sensing hazy images. Therefore, a fourth-order partial differential equation based trilateral filter (FPDETF) based filter is proposed to restore hazy remote sensing images. This section demonstrates step by step description of FPDET.

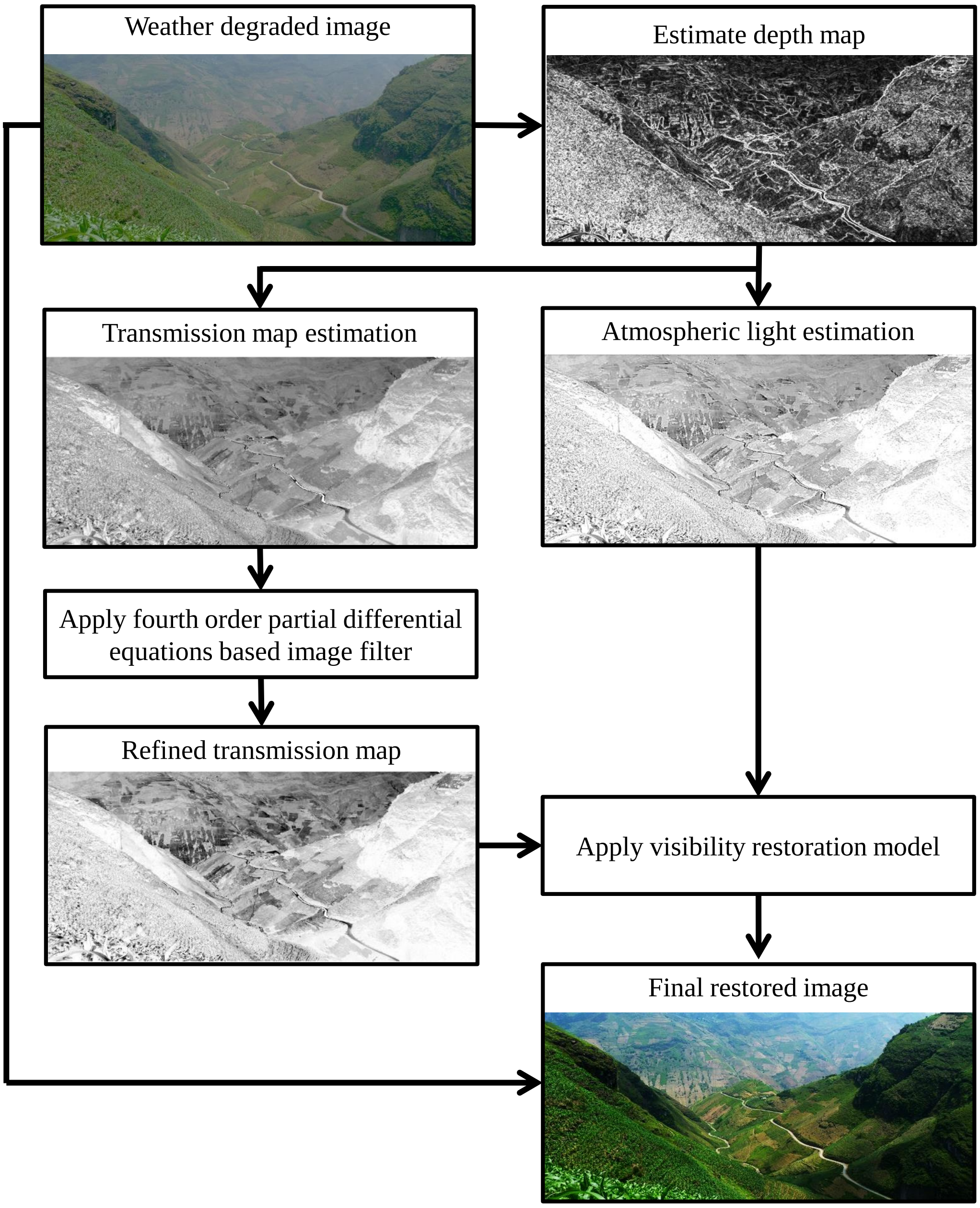

Figure 3.9: Fourth order partial differential equations based visibility restoration model

It consists of five main steps (see Figure 3.9). These steps are DCP, airlight estimation, transmission map estimation, coarse estimated atmospheric veil estimation, and modified restoration model. These steps are described in the preceding subsections.

Initially, DCP is obtained using Eq. (1.3) (see Section 1.3.1). Thereafter, the global atmospheric light estimation model (Υ) will be obtained using Eq. (1.8) (see Section 1.3.2). The coarse atmospheric veil is then evaluated using Eq. (1.16) (see Section 1.3.3).

3.2.1 Fourth order partial differential equations based filter

In this work, FPDETF is proposed to improve the coarse estimated atmospheric veil. FPDETF has an ability to overcome gradient reversal artefacts. Initially, the filtering procedure is prepared under the guidance of image (G_d) called reference image and computed using gradient preserving [151, 152] on the actual weather degraded image (I). A class of fourth-order partial differential equations is used to optimize the trade-off between restoration and edge preservation. Image gradients are used to evaluate the fourth-order partial differential equations. The image gradients are computed as follows [151, 152]:

$$[I_x, I_y] = \nabla_G(I) \tag{3.15}$$

where I_x and I_y are image gradients in x and y direction, respectively. ∇_G is the gradient magnitude of the given image.

The fourth-order partial differential equations can be defined as follows [151, 152]:

$$c = \frac{1}{\sqrt{{I_x}^2 + {I_y}^2}} + \varepsilon \tag{3.16}$$

where c is the decreasing function, which is used to evaluate fourth-order partial differential equations. The value of epsilon (ε) is the constant parameter and it is set to be 0.001.

$$[d_{iv1}, d_{iv2}] = \nabla_G(c.^* I_x) \tag{3.17}$$

$$[d_{iv3}, d_{iv4}] = \nabla_G(c.^* I_y) \tag{3.18}$$

where d_{iv1}, d_{iv2}, d_{iv3}, and d_{iv4} represents fourth-order partial differential equations obtained from input image (I). The fourth-order partial differentiate of I (d_{iv}) is given below:

$$d_{iv} = d_{iv1} + d_{iv4} \tag{3.19}$$

Here, d_{iv} represents the evaluated fourth-order partial differentiate of I.

$$G_d = I - (d_t.^* d_{iv}) \tag{3.20}$$

Here, the value of step size (d_t) is set to be 0.1.

Let I_q and G_q be illumination value at pixel q of minimum channel object and guided image, respectively. K_r is the kernel mask at (j), to be dependable upon bilateral filter. Gradient magnitude based trilateral filter (GJ_{tf}) is devised as:

$$GJ_{tf}(I) = \frac{1}{\sum_{q \in K_r} \gamma^{pq}(G_d)} \left(\sum_{q \in k_r} \gamma^{pq}(G_d) \times I_q \times var(I_q, G_q) \right) \tag{3.21}$$

Here, $\gamma^{pq}(G_d)$ is the kernel weight function and is computed as:

$$\gamma(G_d) = \frac{1}{|n|^2} \sum_{n:(p,q) \in k_r} \left(1 + \frac{\left(G_{d_p} - \mu_n\right)\left(G_{d_q} - \mu_n\right)}{\sigma_n^2 + \varepsilon} \right) \tag{3.22}$$

where μ_n and σ_n^2 represent mean and variance of G_d in local mask k_r, respectively. $|n|$ represents the total number of pixels in a mask. When G_{d_p} and G_{d_q} are on the similar side of an edge, then the weight allocated to pixel q is maximum. When G_{d_p} and G_{d_q} are on different sides, then the minimum weight will be assigned to pixel q.

Finally, the restored image can be restored by using Eq. (1.33) (see Section 1.3.5).

3.2.2 Results and discussions

In order to demonstrate the effectiveness of FPDETF, ten well-known remote sensing images have been taken from QUICKBIRD [153], IKONOS [154] and MODIS [155] sensors. The images are resized to 512 × 512 as these images take large storage space. The performance of FPDETF is compared with seven well established restoration techniques. These techniques are COD [99], WGIF [102], WHDR [33], CL [91], LTQ [148], MS [97], and L_1 [147].

A. Experimentation 1: Transmission map estimation

Figure 3.10 (a) shows the DCP of hazy image taken from QUICKBIRD [153] dataset. The filtered transmission map obtained from COD [99] is shown in Figure 3.10 (b). It shows over-smoothed transmission map. It is observed from Figures 3.10 (c) and 3.10 (g) that peak of transmission map obtained from WGIF [102] and MS [97] are not so accurate. Furthermore, the edges of the object are not accurate as expected. Figures 3.10 (d) and 3.10 (f) show the refined transmission map images produced from WHDR [33] and LTQ [148]'s restoration techniques, respectively. These techniques produce over an enhanced transmission map.

Figures 3.10 (e) and 3.10 (h) show the refined transmission map images by L_1 [147] and CL [91]'s techniques. These techniques are unable to preserve edges and attain perceptual superiority in sky regions (see 3.10 (e) and 3.10 (h)). Figure 3.10 (j) shows filtered transmission map obtain from FPDETF. From this figure, it is observed that FPDETF achieves remarkable refined transmission map as compared to the above-mentioned techniques. It also reduces halo artefacts and preserves image information.

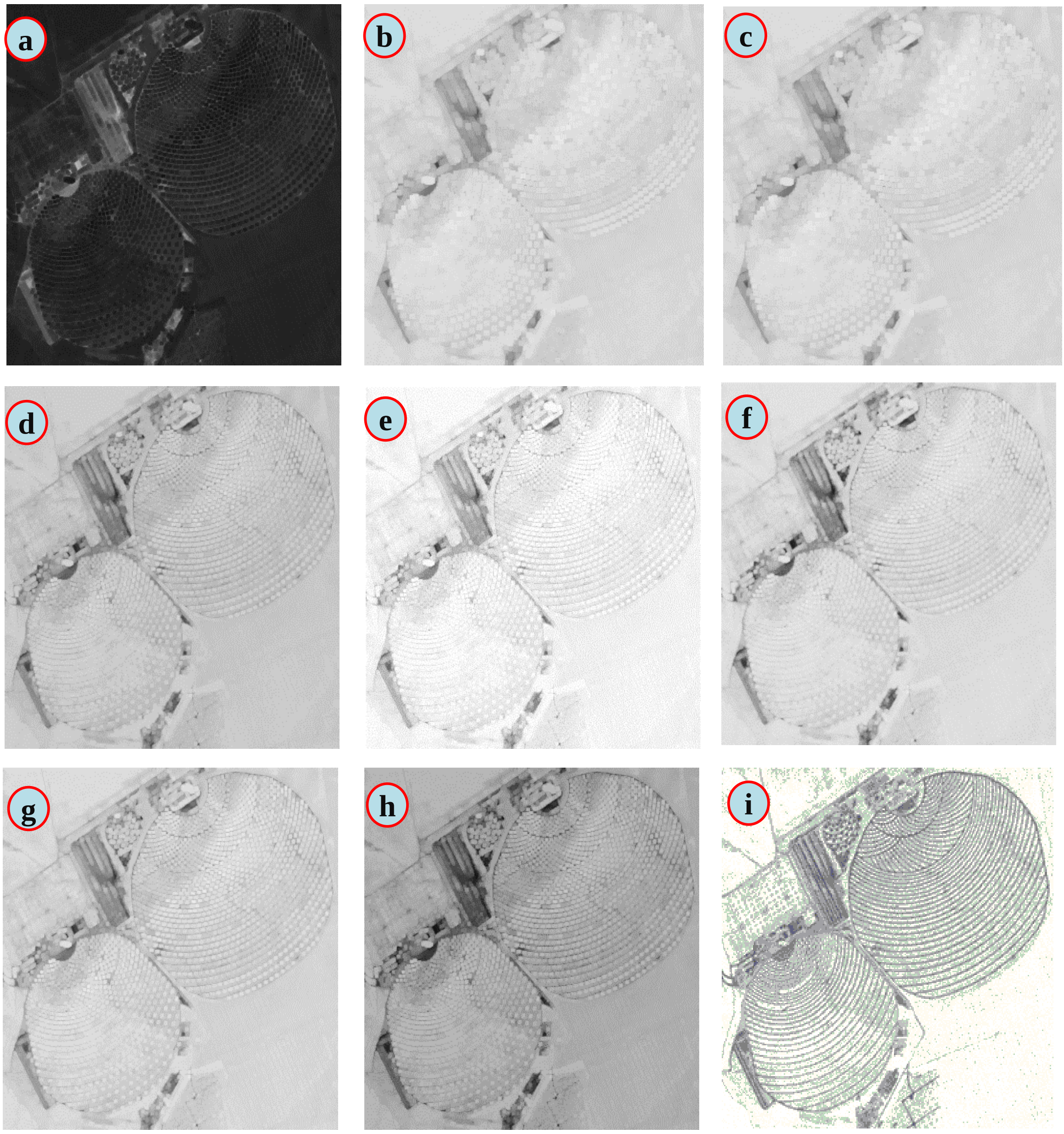

Figure 3.10: Refined transmission map of restoration techniques of QUICKBIRD dataset (a) Actual depth map, (b) COD, (c) WGIF, (d) WHDR, (e) CL, (f) LTQ, (g) MS, (h) L_1, and (j) FPDETF.

B. Experimentation 2: Analysis of patch size

The next experiment is carried out to see the effect of patch size on FPDETF. The values of patch size in experimentation are taken as 1×1, 5×5, and 11×11. Figure 3.11 shows the effect of different patch sizes on transmission maps and restored images. It can be seen from Figure 3.11 (b) that for lesser patch size, dark channel becomes less accurate, and restored image become oversaturated (see Figure 3.11 (c)). It is further observed that the transmission map is uniform in this patch size (*i.e.,* 1×1). Figure 3.11 (d) shows that dark channel becomes more efficient for moderate patch size, *i.e.,* 5×5. The restored image shows less saturated pixels and lesser number of halo and gradient reversal artefacts (see Figure 3.11 (e)). From Figures 3.11 (f) and 3.11 (g), it can be seen that halo and gradient artefacts become stronger for large patch size.

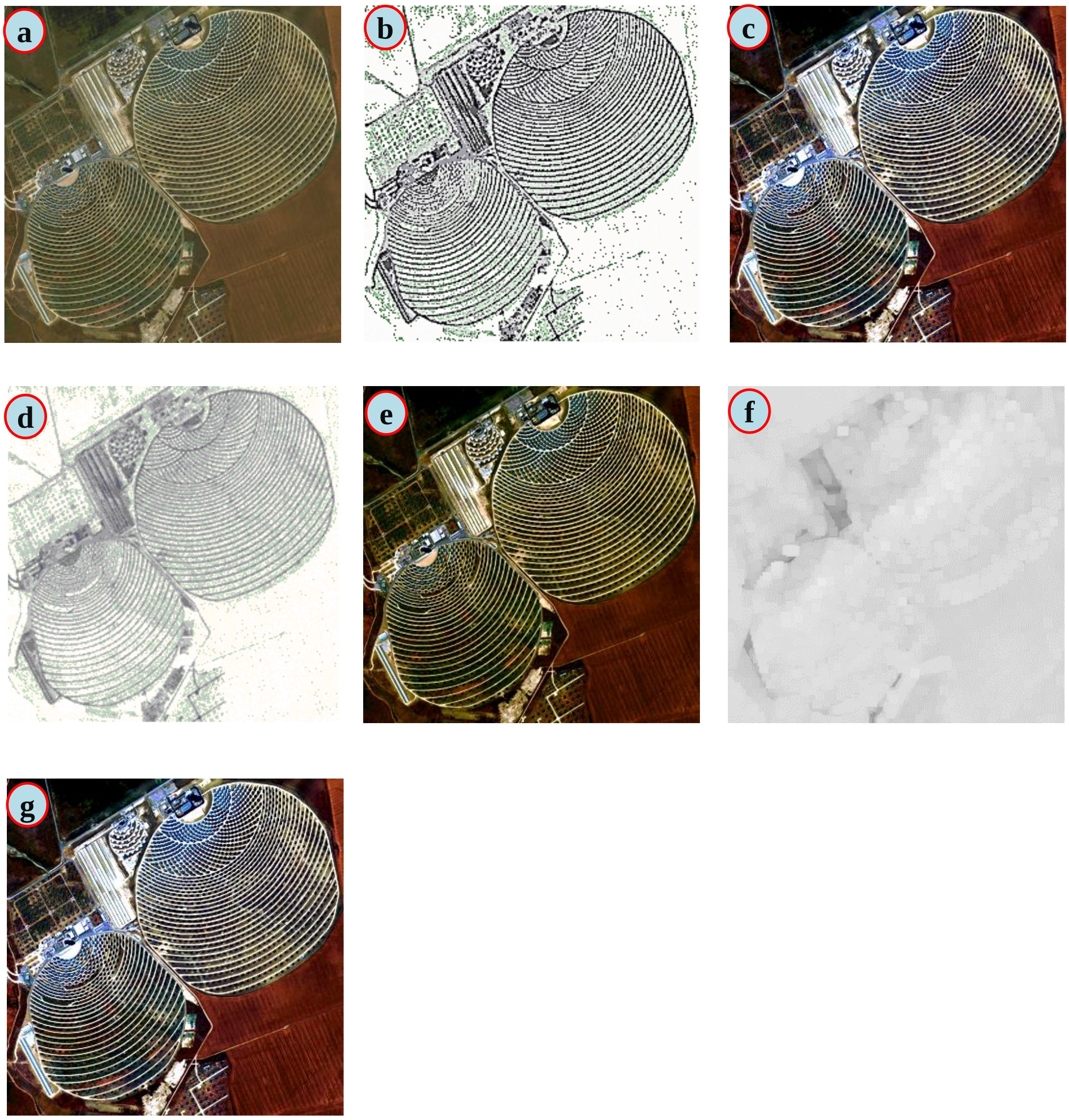

Figure 3.11: Patch size analysis of FPDETF on QUICKBIRD dataset's image (a) Actual image, (b) Transmission map with 1×1 patch size, (c) Restored image with 1×1 patch size, (d) Transmission map with 5×5 patch size, (e) Restored image with 5×5 patch size, (f) Transmission map with 11×11 patch size, and (g) Restored image with 11×11 patch size

C. Experimentation 3: Performance evaluation

The performance of FPDETF is compared with seven well-known restoration techniques on ten well-known remote sensing haze affected images are taken from QUICKBIRD [153], IKONOS [154], and MODIS [155] satellite sensors.

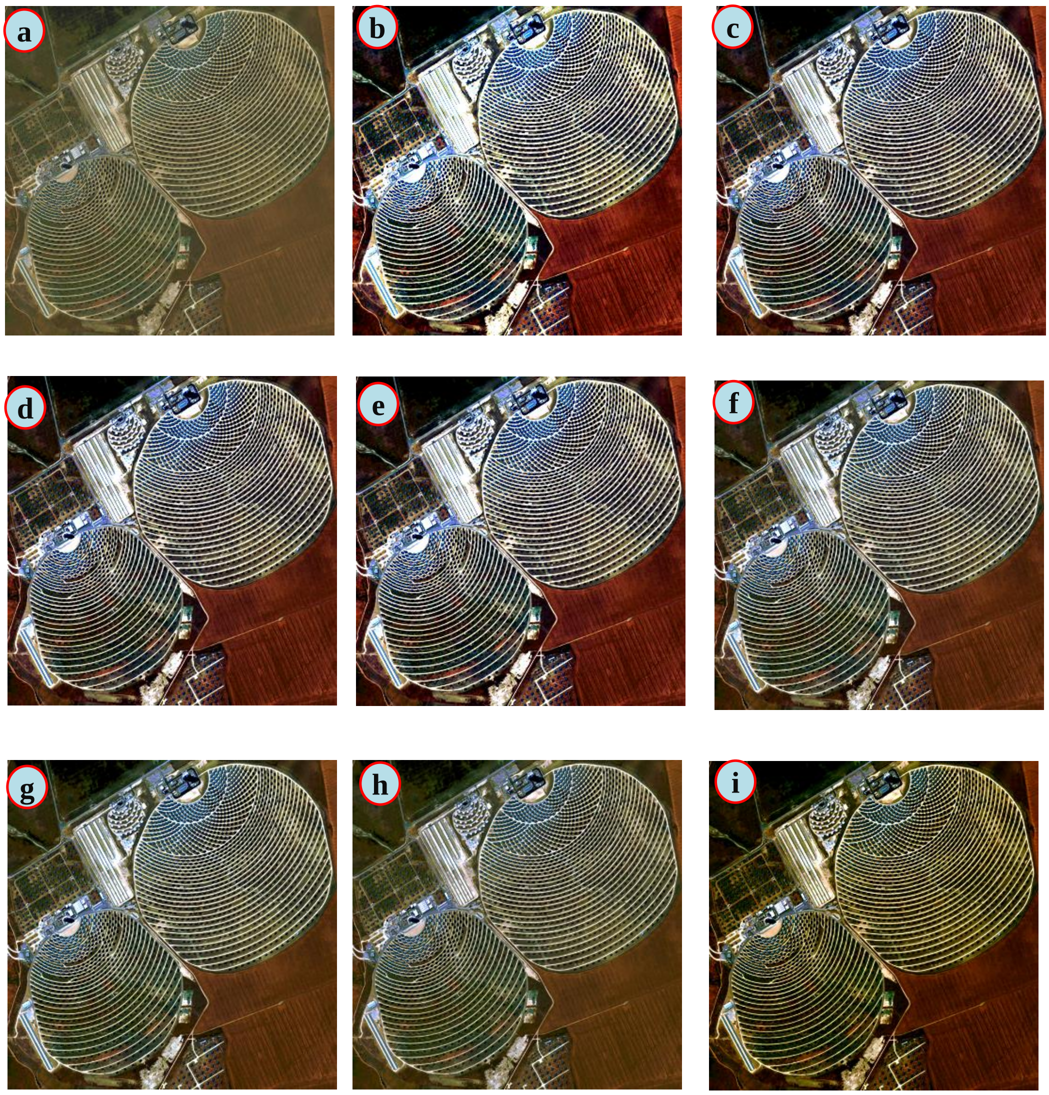

Figure 3.12: Results of restoration techniques for QUICKBIRD dataset (a) Input image, (b) COD, (c) WGIF, (d) WHDR, (e) CL, (f) LTQ, (g) MS, (h) L_1, and (j) FPDETF.

Figure 3.12 (b) shows the restored image obtained from COD [99]. However, this technique suffers from halo and gradient reversal artefacts (see Figure 3.12 (b)). Figures 3.12 (c) and 3.12 (g) show the restored images obtained from WGIF [102] and MS [97]'s techniques, respectively. Form these figures, it can be seen that the color distortion is much smaller than the previous one. Figures 3.12 (d) and 3.12 (f) show the restored images obtained from WHDR [33] and LTQ [148]'s restoration techniques, respectively. From these figures, it is observed that these techniques may have lesser number of halo artefacts as compared to WHDR [33] and MS [97]'s techniques. However, these techniques do not preserve edges in the restored image. Figures 3.12 (e) and 3.12 (h) show the restored images obtained from L_1 [147] and CL [91]'s techniques, respectively. The haze free images have lesser number of saturated pixels. However, the restored images have halo and gradient reversal artefacts. These techniques are unable to attain a suitable perceptual superiority in a case of sky regions (see Figures 3.12 (e) and 3.12 (h)). Figure 3.12 (j) shows the restored image generated from FPDETF. From this figure, it is observed that FPDETF achieves remarkable visual superiority with lesser number of halo and gradient reversal artefacts and better color appearance.

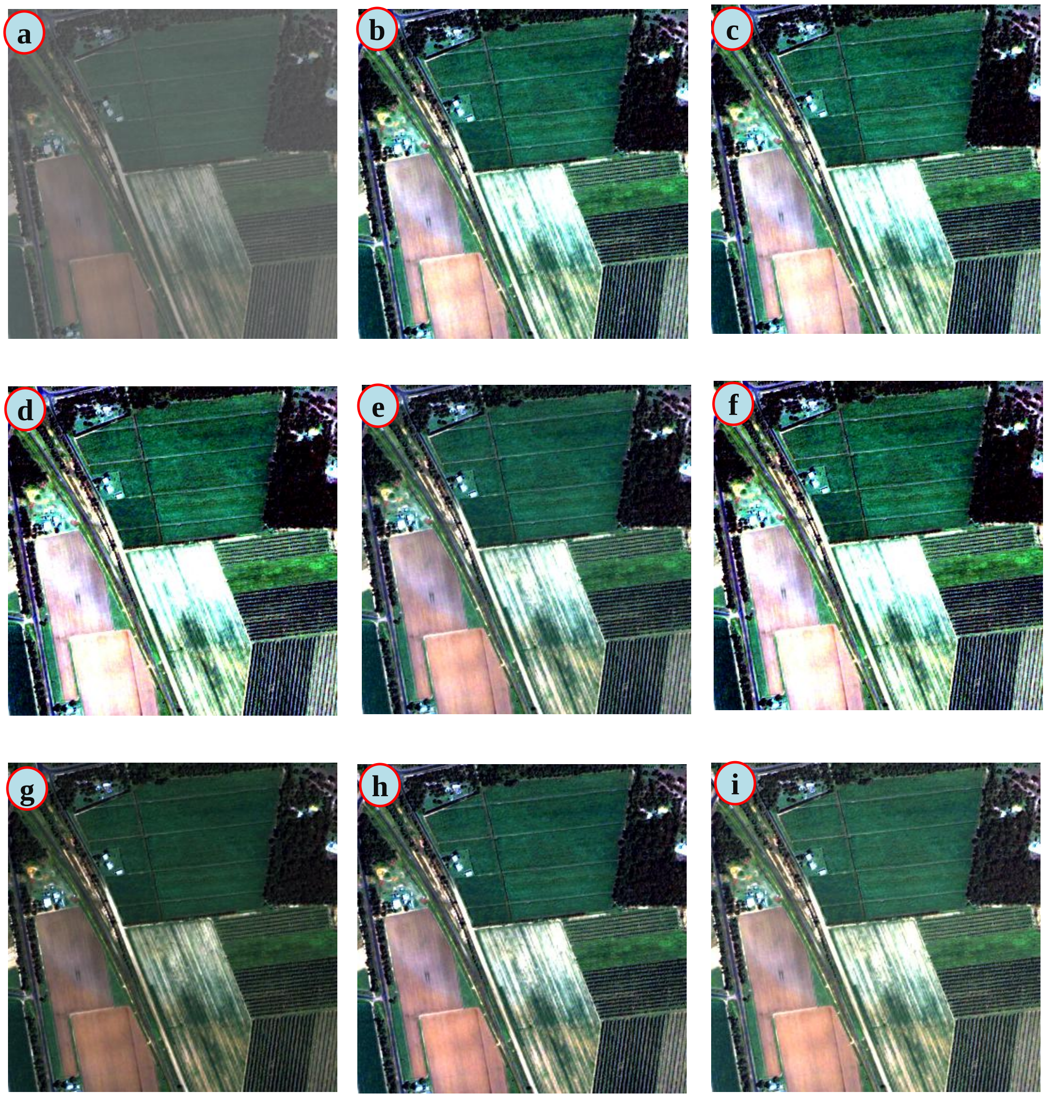

Figure 3.13: Results of restoration techniques for QUICKBIRD dataset (a) Input image, (b) COD, (c) WGIF, (d) WHDR, (e) CL, (f) LTQ, (g) MS, (h) L_1, and (j) FPDETF.

Figure 3.13 shows visual analysis of different restoration techniques on QUICKBIRD [153] dataset. Figure 3.13 (b) shows the restored image obtained from COD [99]. It is able to remove haze from the given image and preserve edges. However, it contains halo and gradient reversal artefacts (see Figure 3.13 (b)). The restored image obtained from WGIF [102] and MS [97]'s techniques are shown in Figure 3.13 (c) and 3.13 (g), respectively. These techniques provide lesser color distortion as compared to COD [99]. However, these techniques do not preserve the edges in restored images. Figures 3.13 (d) and 3.13 (f) show the haze free images obtained from WHDR [33] and LTQ [148]'s restoration techniques, respectively. These techniques provide lesser number of halo artefacts as compared to WHDR [33] and MS [97]'s techniques. The restored image obtained from L_1 [147]'s and CL [91]'s techniques are shown in Figures 3.13 (e) and 3.13 (h), respectively. These techniques suffer from halo and gradient reversal problems (see Figures 3.13 (e) and 3.13 (h)).

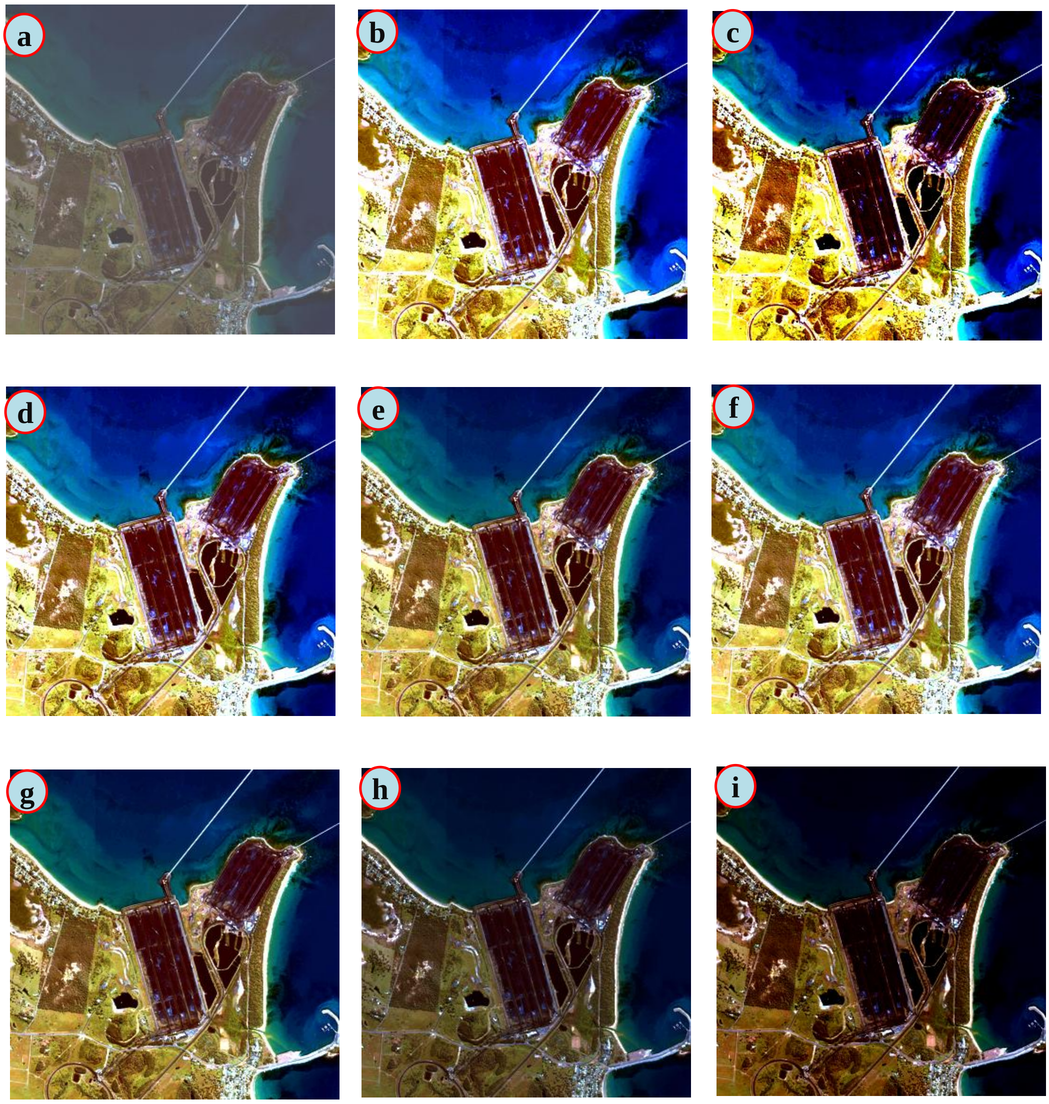

Figure 3.14: Results of restoration techniques for IKONOS dataset (a) Input image, (b) COD, (c) WGIF, (d) WHDR, (e) CL, (f) LTQ, (g) MS, (h) L_1, and (j) FPDETF.

Figure 3.14 shows the results obtained using different restoration techniques for QUICKBIRD [153] dataset. From Figure 3.14 (b), it is observed that the restored image using COD [99]. The restored image shows better edge preservation. However, restored image obtained from COD [99] shows halo and gradient reversal artefacts. Figures 3.14 (c) and 3.14 (g) show the haze free images obtained using WGIF [102] and MS [97]'s techniques, respectively. However, the restored image does not preserve the edges. Figures 3.14 (d) and 3.14 (f) show the restored images obtained from WHDR [33] and LTQ [148]'s techniques, respectively. These images show lesser number of halo artefacts as compared to WHDR [33] and MS [97]'s techniques.

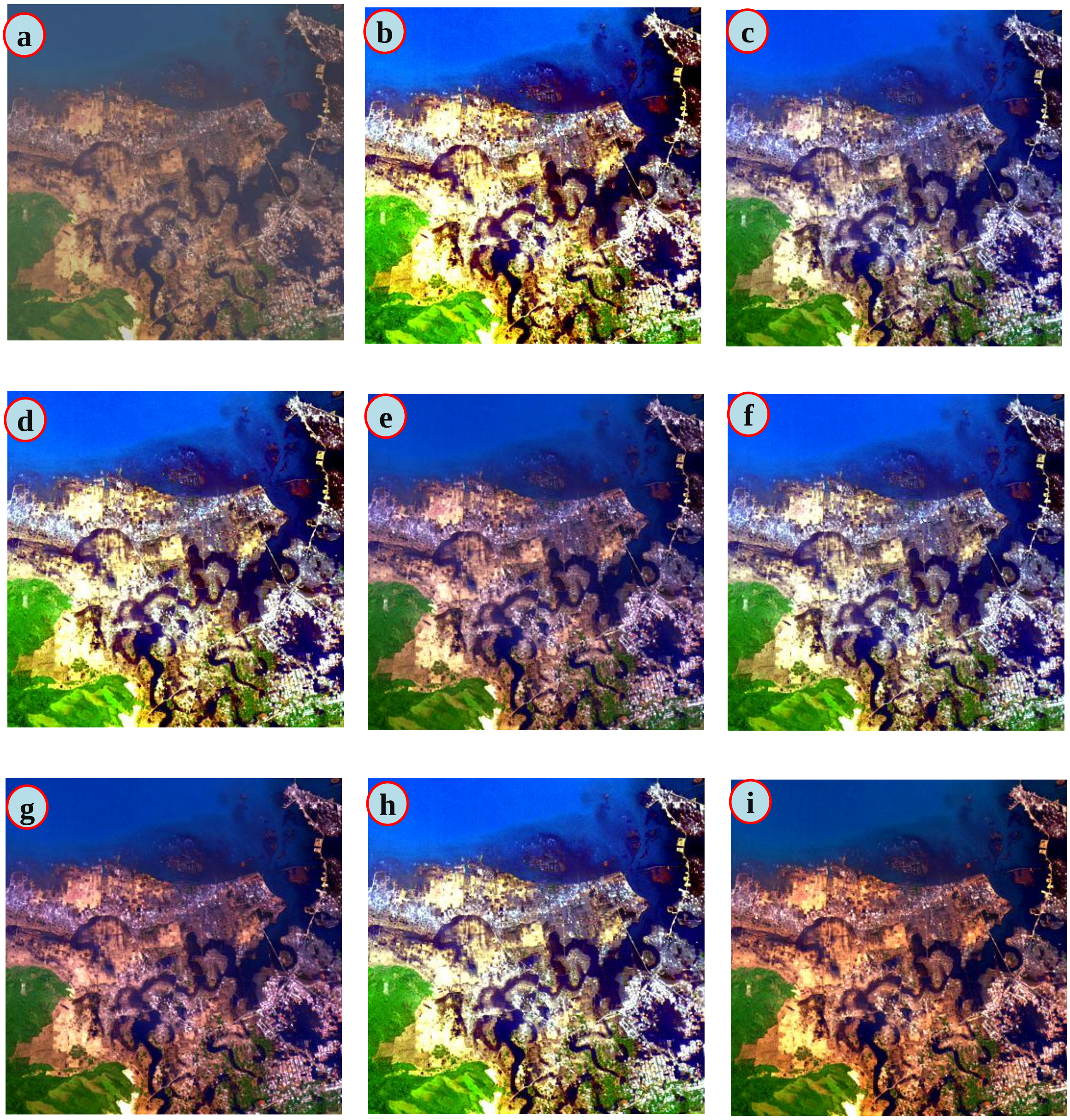

Figure 3.15: Results of restoration techniques for IKONOS dataset (a) Input image, (b) COD, (c) WGIF, (d) WHDR, (e) CL, (f) LTQ, (g) MS, (h) L_1, and (j) FPDETF.

Figures 3.14 (e) and 3.14 (h) show the restored images produced from L_1 [147] and CL [91]'s techniques, respectively. The restored images have lesser number of saturated pixels. However, these techniques suffer from halo and gradient reversal artefacts. Figure 3.14 (j) shows the restored images using FPDETF. Figure 3.15 (b) shows the restored image of IKONOS [154] obtained from COD [99]'s restoration technique. Although, it reduces the haze from a hazy image with better edge preservation. However, a restored image obtained using COD [99] has halo and gradient reversal artefacts. Figures 3.15 (c) and 3.15 (g) show the restored images obtained from WGIF [102] and MS [97]'s techniques, respectively. These images have lesser color distortion. However, these techniques suffer from edge distortion problem.

Figures 3.15 (d) and 3.15 (f) show haze free images obtained from WHDR [33] and LTQ [148]'s techniques, respectively. From these figures, it is observed that these techniques have lesser halo artefacts. However, these are unable to preserve a significant amount of edges. Figures 3.15 (e) and 3.15 (h) show the restored images obtained using L_1 [147]'s and CL [91]'s techniques, respectively. The restored images have lesser number of saturated pixels. However, these techniques suffer from halo and gradient reversal artefacts. Figure 3.15 (j) shows the restored image obtained from FPDETF. From this figure, it can be seen that FPDETF achieves remarkable visual superiority with less number of halo and gradient reversal artefacts.

Figure 3.16 (b) shows the restored image of an IKONOS [154] dataset obtained from COD [99]'s technique. The resorted image has preserved the edges. However, it has halo and gradient reversal artefacts. Figures 3.16 (c) and 3.16 (g) show the haze free images obtained from WHDR [33] and MS [97]'s techniques, respectively. The restored images have lesser color distortion than COD [99]. However, these techniques suffer from edge distortion problem. Figures 3.16 (d) and 3.16 (f) show the haze free images obtained from WHDR [33] and LTQ [148]'s techniques, respectively. These techniques have lesser number of halo artefacts as compared to WHDR [33] and MS [97]. However, they do not preserve the edges. Figures 3.16 (e) and 3.16 (h) show the restored images obtained from L_1 [147] and CL [91]'s techniques, respectively. These images show a lesser number of saturated pixels. However, these techniques suffer from halo and gradient reversal artefacts. Figure 3.16 (j) shows restored image obtained from FPDETF. It achieves remarkable visual superiority with lesser number of halo and gradient reversal artefacts.

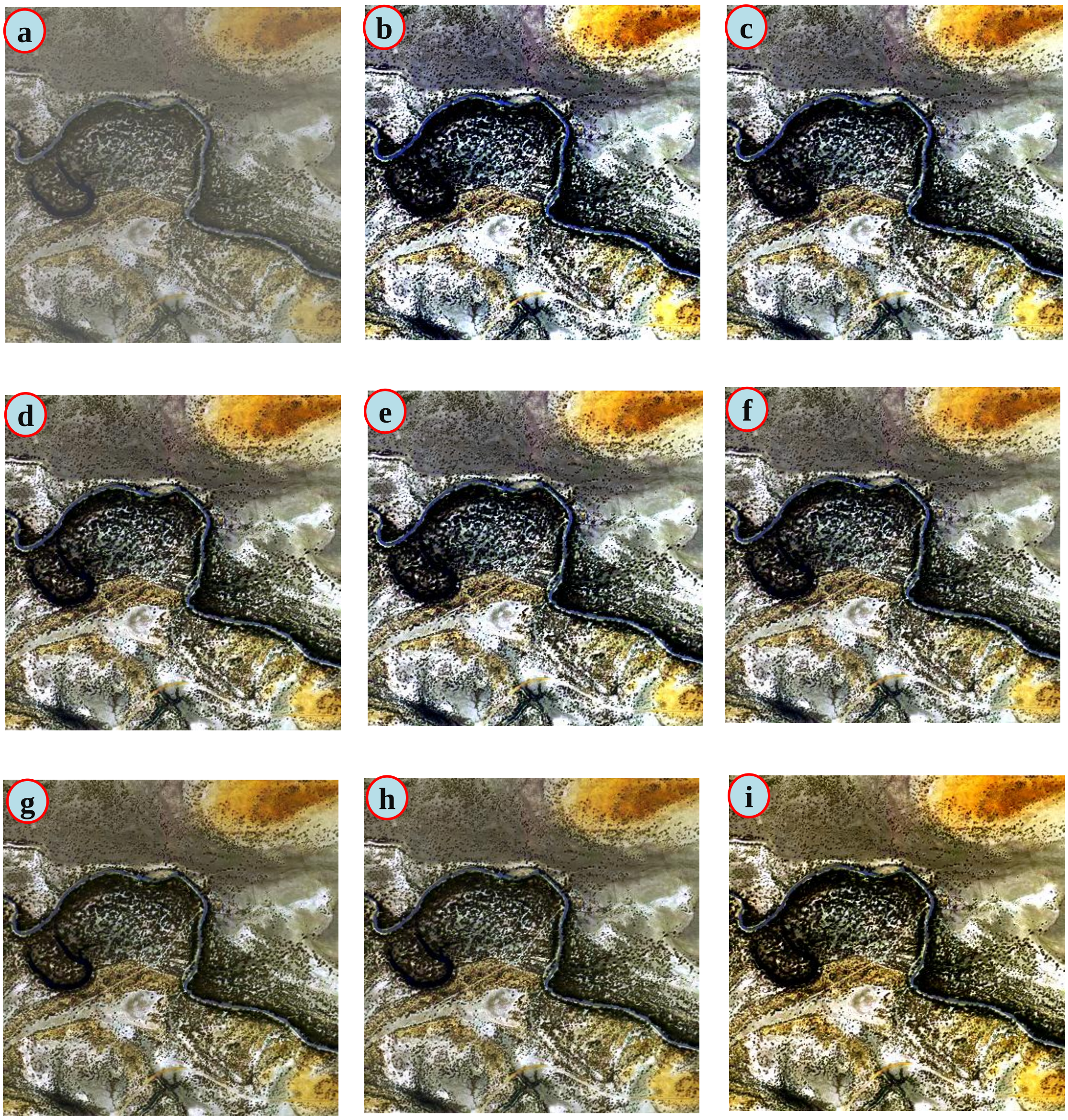

Figure 3.16: Results of restoration techniques for MODIS dataset (a) Input image, (b) COD, (c) WGIF, (d) WHDR, (e) CL, (f) LTQ, (g) MS, (h) L_1, and (j) FPDETF.

D. Experimentation 4: Quantitative analysis

In addition to visual evaluations, three well-known performance measures considered for quantitative analysis such as C_g, ρ, and E_t.

The value of C_g is evaluated for hazy images are tabulated in Table 3.4. FPDETF has significant C_g than COD [99], WGIF [102], WHDR [33], CL [91], LTQ [148], MS [97], and L_1 [147]. Table 3.4 reveals that the mean improvement in terms of C_g using FPDETF over available techniques is 0.0319 (Approx).

Table 3.4: Comparative analysis of FPDETF with respect to contrast gain (C_g) per pixel

Images	COD	WGIF	WHDR	CL	LTQ	MS	L_1	FPDETF
Hazy1	0.0498	0.0628	0.0836	0.0853	0.1282	0.1287	0.1379	0.1476
Hazy2	0.0175	0.0184	0.0328	0.0739	0.0815	0.0892	0.0939	0.0987
Hazy3	0.0739	0.0732	0.0868	0.0925	0.0971	0.1104	0.1341	0.1571
Hazy4	0.0572	0.0807	0.0930	0.0929	0.0923	0.0946	0.0987	0.1091
Hazy5	0.0528	0.0581	0.0469	0.0557	0.0725	0.0762	0.0814	0.0876
Hazy6	0.0330	0.0461	0.0381	0.0661	0.0741	0.0853	0.0822	0.0892
Hazy7	0.0728	0.0863	0.0869	0.0910	0.0926	0.1127	0.1149	0.1193
Hazy8	0.0918	0.0880	0.0894	0.0833	0.0745	0.0893	0.0912	0.1031
Hazy9	0.0907	0.0917	0.0816	0.0973	0.1095	0.1196	0.1198	0.1246
Hazy10	0.0799	0.0678	0.0754	0.0549	0.0694	0.0957	0.0909	0.0971

Table 3.5 depicts ρ values of the existing and FPDETF techniques. FPDETF provides lesser ρ as compared to COD [99], WGIF [102], WHDR [33], CL [91], LTQ [148], and L_1 [147]. The mean reduction in ρ using FPDETF over the existing techniques is 0.0137 (Approx).

Table 3.5: Comparative analysis of FPDETF with respect to percentage of saturated pixels (ρ) per pixel

Images	COD	WGIF	WHDR	CL	LTQ	MS	L_1	FPDETF
Hazy1	0.0751	0.0686	0.0582	0.0574	0.0359	0.0357	0.0311	0.0262
Hazy2	0.0912	0.0908	0.0836	0.0631	0.0593	0.0554	0.0531	0.0507
Hazy3	0.0631	0.0634	0.0566	0.0538	0.0515	0.0448	0.0330	0.0215
Hazy4	0.0714	0.0597	0.0535	0.0536	0.0539	0.0527	0.0507	0.0455
Hazy5	0.0736	0.0710	0.0766	0.0722	0.0638	0.0619	0.0593	0.0562
Hazy6	0.0835	0.0770	0.0810	0.0670	0.0630	0.0574	0.0589	0.0554
Hazy7	0.0636	0.0569	0.0566	0.0545	0.0537	0.0437	0.0426	0.0404
Hazy8	0.0541	0.0560	0.0553	0.0584	0.0628	0.0554	0.0544	0.0485
Hazy9	0.0547	0.0542	0.0592	0.0514	0.0453	0.0402	0.0401	0.0377
Hazy10	0.0601	0.0661	0.0623	0.0726	0.0653	0.0522	0.0546	0.0515

The values of E_t for different restoration techniques are tabulated in Table 3.6. From table, it is observed that FPDETF takes lesser computation time as compared to COD [99], WGIF [102], WHDR [33], CL [91], LTQ [148], and L_1 [147]. The results reveal that the average reduction in E_t for FPDETF over the existing techniques is approximately 0.0917 (in seconds).

Table 3.6: Comparative analysis of FPDETF with respect to execution time (E_t) in seconds

Images	COD	WGIF	WHDR	CL	LTQ	MS	L_1	FPDETF
Hazy1	1.9180	1.1128	0.8046	0.8039	0.7870	0.7868	0.7832	0.6794
Hazy2	1.4307	1.1303	0.8247	0.8084	0.8054	0.8024	0.8006	0.5987
Hazy3	1.5084	0.9787	0.8034	0.8011	0.7993	0.7940	0.7847	0.6756
Hazy4	17150	0.9758	0.8009	0.8010	0.8012	0.8003	0.7987	0.6946
Hazy5	1.2168	0.9147	0.8191	0.8156	0.8090	0.8075	0.8055	0.5830
Hazy6	1.9246	1.0194	0.8226	0.8115	0.8084	0.8039	0.8052	0.7124
Hazy7	1.4089	1.1036	0.8033	0.8017	0.8011	0.7931	0.7923	0.5905
Hazy 8	1.6014	1.3029	0.8023	0.8047	0.8082	0.8024	0.8016	0.6969
Hazy9	1.7018	1.4014	0.8054	0.7992	0.7944	0.7904	0.7903	0.6784
Hazy10	1.3061	1.2109	0.8079	0.8159	0.8102	0.7998	0.8017	0.5993

From Tables 3.7 and 3.8, it has been observed that FPDETF has better e and $\bar{r}$ as compared to the existing restoration techniques. Therefore, FPDETF has more visible edges and gradient as compared to the existing techniques.

Table 3.7: Comparative analysis of FPDETF with respect to new visible edges (e)

Images	COD	WGIF	WHDR	CL	LTQ	MS	L_1	FPDETF
Hazy1	1.7315	1.8326	17448	1.8518	1.8763	1.9129	1.9246	1.9678
Hazy2	2.1011	2.1612	1.9763	2.1904	2.2797	2.3742	2.4544	2.5746
Hazy3	2.2663	2.1819	2.3909	2.4171	2.4178	2.4985	2.5376	2.5746
Hazy4	2.1391	2.2692	2.2183	2.1653	2.3657	2.3819	2.4214	2.4746
Hazy5	1.8781	1.9784	2.0820	2.1244	2.1944	2.2959	2.3184	2.4891
Hazy6	2.0665	1.9689	1.9206	2.1827	2.2585	2.2999	2.4186	2.3678
Hazy7	1.7781	1.9607	2.1495	2.1902	2.2453	2.2385	2.2813	2.3487
Hazy8	1.7280	1.7816	1.8262	1.7439	1.8127	1.8336	1.9251	1.9779
Hazy9	1.6991	1.7564	1.7846	1.8741	1.8915	1.9218	1.9386	1.9678
Hazy10	1.7711	1.7978	1.7830	1.8778	1.9848	1.9796	2.1547	2.2949

Table 3.8: Comparative analysis of FPDETF with respect to ratio of average gradient ($\bar{r}$)

Images	COD	WGIF	WHDR	CL	LTQ	MS	L_1	FPDETF
Hazy1	1.5788	1.6181	1.6548	1.7160	1.8759	1.8691	1.9476	1.9876
Hazy2	1.5235	1.6436	1.7240	1.8162	1.8218	1.8655	1.8947	1.9348
Hazy3	1.4147	1.4379	1.4678	1.5624	1.5735	1.6887	1.7358	1.8947
Hazy4	1.3665	1.4579	1.6782	1.7243	1.7527	1.7875	1.8452	1.8949
Hazy5	1.2537	1.3407	1.4445	1.5609	1.5411	1.6911	1.7189	1.8349
Hazy6	1.4810	1.5761	1.6815	1.6702	1.7274	1.8562	1.8993	1.9357
Hazy7	1.5401	1.5891	1.6753	1.6915	1.7217	1.7834	1.9362	1.9681
Hazy8	1.3271	1.4718	1.4967	1.6847	1.7384	1.7891	1.8164	1.8749
Hazy9	1.4574	1.4951	1.4978	1.5714	1.7428	1.8257	1.8673	1.9147
Hazy10	1.4754	1.4680	1.4868	1.5358	1.6174	1.6874	1.7871	1.8347

E. Experimentation 5: Comparison with histogram based restoration techniques

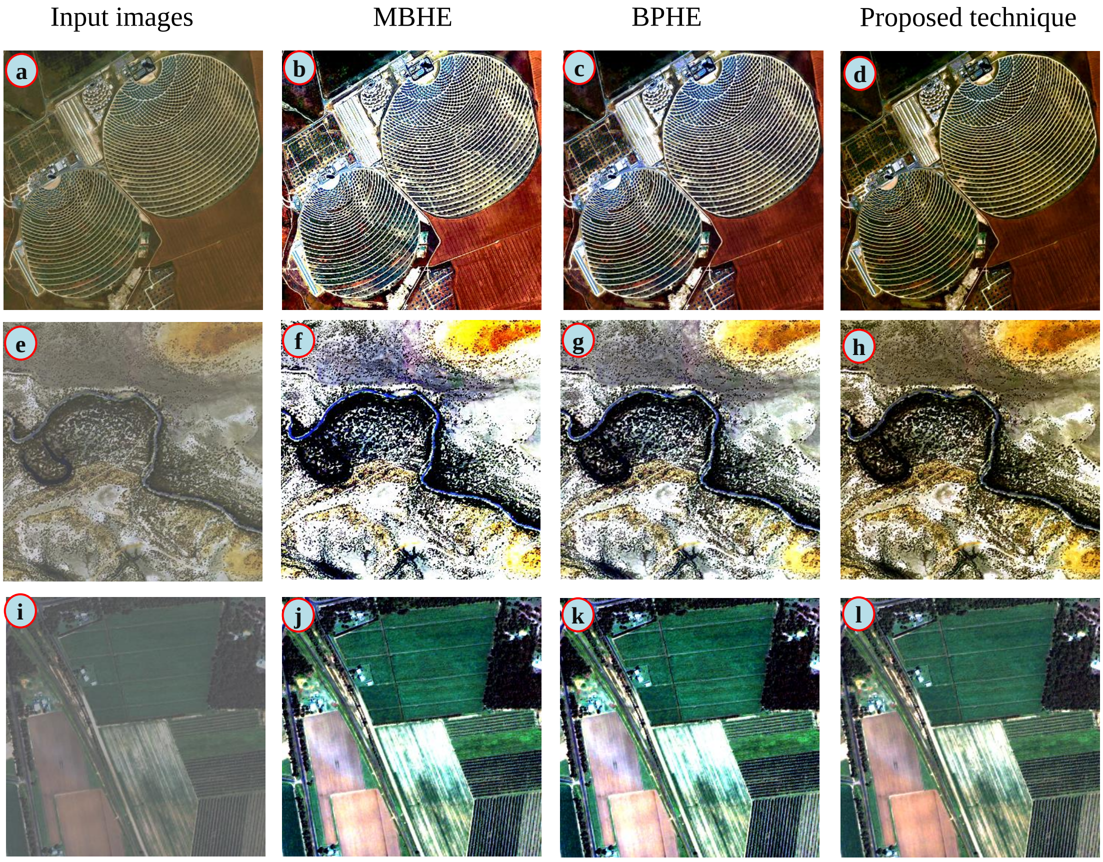

Figure 3.17: Comparison of FPDETF with BHE and RSWHE

This section describes the visual and quantitative analysis of FPDETF with histogram equalization based restoration techniques. Figure 3.17 shows the comparison between FPDETF, Bi-histogram equalization (BHE) [156], and Recursively separated weighted histogram equalization (RSWHE) [157] based restoration techniques. It is observed that FPDETF have lesser number of saturated pixels, halo, and gradient reversal artefacts as compared to BHE [156] (see Figures 3.17 (b), 3.17 (f) and 3.17 (j)) and RSWHE [157] (see Figures 3.17 (c), 3.17 (g) and 3.17 (k)).

Table 3.9: Comparative analysis of FPDETF over enhancement based restoration techniques

Images	C_g			ρ		
	BHE	RSWHE	FPDETF	BHE	RSWHE	FPDETF
Hazy1	0.0582	0.0574	0.0359	0.0357	0.0311	0.0262
Hazy2	0.0836	0.0631	0.0593	0.0554	0.0531	0.0507
Hazy3	0.0566	0.0538	0.0515	0.0448	0.0330	0.0215
Hazy4	0.0535	0.0536	0.0539	0.0527	0.0507	0.0455
Hazy5	0.0766	0.0722	0.0638	0.0619	0.0593	0.0562
Hazy6	0.0810	0.0670	0.0630	0.0574	0.0589	0.0554
Hazy7	0.0566	0.0545	0.0537	0.0437	0.0426	0.0404
Hazy8	0.0553	0.0584	0.0628	0.0554	0.0544	0.0485
Hazy9	0.0592	0.0514	0.0453	0.0402	0.0401	0.0377
Hazy10	0.0623	0.0726	0.0653	0.0522	0.0546	0.0515

Table 3.9 shows the performance of FPDETF and histogram based restoration techniques. A look at table demonstrates that FPDETF provides better C_g and minimum ρ. It outperforms over other histogram based restoration techniques.

3.3 Summary

In this chapter, two filters have been designed and implemented in order to refine the transmission map obtain from DCP. It has been found that GITF improves the contrast gain by 1.76 % as compared to the existing competitive visibility restoration techniques. Also, GITF significantly reduces the percentage of saturated pixels and execution time by 1.96 % and 3.21%, respectively. Comparative analysis has proven that FPDETF outperforms the existing techniques in terms of contrast gain, ratio of new visible edges, and ratio of the average gradient by 1.98%, 1.72% and 1.81%, respectively. Also, FPDETF reduces the percentage of saturated pixels and execution time by 2.07% and 3.41%, respectively.

Chapter 4

Integrated visibility restoration model

Outline

Although, GITF and FPDETF perform significantly better than the existing visibility restoration techniques. However, both techniques suffer from sky-regions and color distortion, especially in the case of images affected by large weather gradients (*i.e.,* density of fog or haze is significantly more as compared to normal hazy or foggy day). Therefore, in this chapter, an Integrated visibility restoration model (IVRM) is proposed to solve the above-mentioned problems. It utilizes DCP, Bright channel prior (BCP), and gain intervention filter. BCP is used to solve the sky-region problem associated with DCP based restoration. The gain intervention filter is also used to improve computational speed and edge preservation.

4.1 Integrated visibility restoration model

Physics based restoration techniques have an ability to overcome the issue of over-saturation [17, 16]. However, these techniques suffer from halo artefacts and color distortion problems. Weighted guided image filter (WGIF) based restoration technique can restore the hazy image in a more promising way [105]. It can significantly preserve the edges of a restored image. Fog aware density evaluator (FADE) based restoration technique can evaluate the visibility of an image without using the salient features of an original image. It utilized the measured deviations from statistical regularities observed in naturally hazy and restored images [67].

Effective contrast-based restoration (ECBD) technique does not require any geometrical data [158]. However, [67], [158], and [105] based restoration models may suffer from gradient reversal artefacts [159, 160]. A fusion based strategy so-called MSF is proposed which merge the features of white balanced and contrast-enhanced images. The three weight maps namely luminance, saliency, and chromaticity are used to fuse information in an efficient manner [74]. But, it suffers from poor computational speed.

In recent times, the suppositions and priors are utilized in restoration techniques for further improvement. New mask based DCP techniques (*i.e.,* Remote sensing dehazing (RSD) [44] and PBDCP [20]) are developed to solve halo artefacts problem. However, DCP is worthless whenever the objects are intrinsically similar to airlight, and no shadow is directed at them. The hybridization of DCP and scene radiance constraint are used to solve sky-regions problem [161].

A Fast haze removal technique (FHRT) is introduced that utilizes an infinite sky area and white area to evaluate atmospheric light [84]. Change of detail (COD) prior is employed in [99], which can remove the haze from an image by using multiple scattering occurrences in the dissemination of illumination. By using this technique, the thickness of fog can be evaluated successfully to restore a hazy image. However, [84] and [99] cannot preserve the edges of the restored images [161, 162].

A Guided filter (GF) is designed which calculates the filtering image by considering the content of a guidance image. It is utilized as an edge-preserving filter. It uses fast and non-approximate linear time technique regardless of kernel size and intensity range [163]. However, GF based restoration technique suffers from gradient reversal artefacts [164].

To handle the above-mentioned issues, an Integrated visibility restoration model (IVRM) is proposed for remote sensing images. It has the following features over the existing restoration models.

i Initially, the gain coefficient filter is modified by local variance. Thereafter, the modified filter is used to improve the coarse estimated atmospheric veil (γ) and transmission map (t).

ii An integrated visibility restoration model is proposed by considering the integration of DCP and BCP.

Figure 4.1 shows the diagrammatic flow of IVRM. Initially, DCP is obtained using Eq. (1.3) (see Section 1.3.1). Thereafter, the global atmospheric light estimation model (Υ) is obtained using Eq. (1.8) (see Section 1.3.2). A coarse atmospheric veil is then evaluated using Eq. (1.16) (see Section 1.3.3). The depth information obtained from DCP and BCP is then integrated with each other. Thereafter, designed gain intervention filter is used to refine the obtained integrated depth information. Finally, the restored image is obtained by using the improved visibility restoration model.

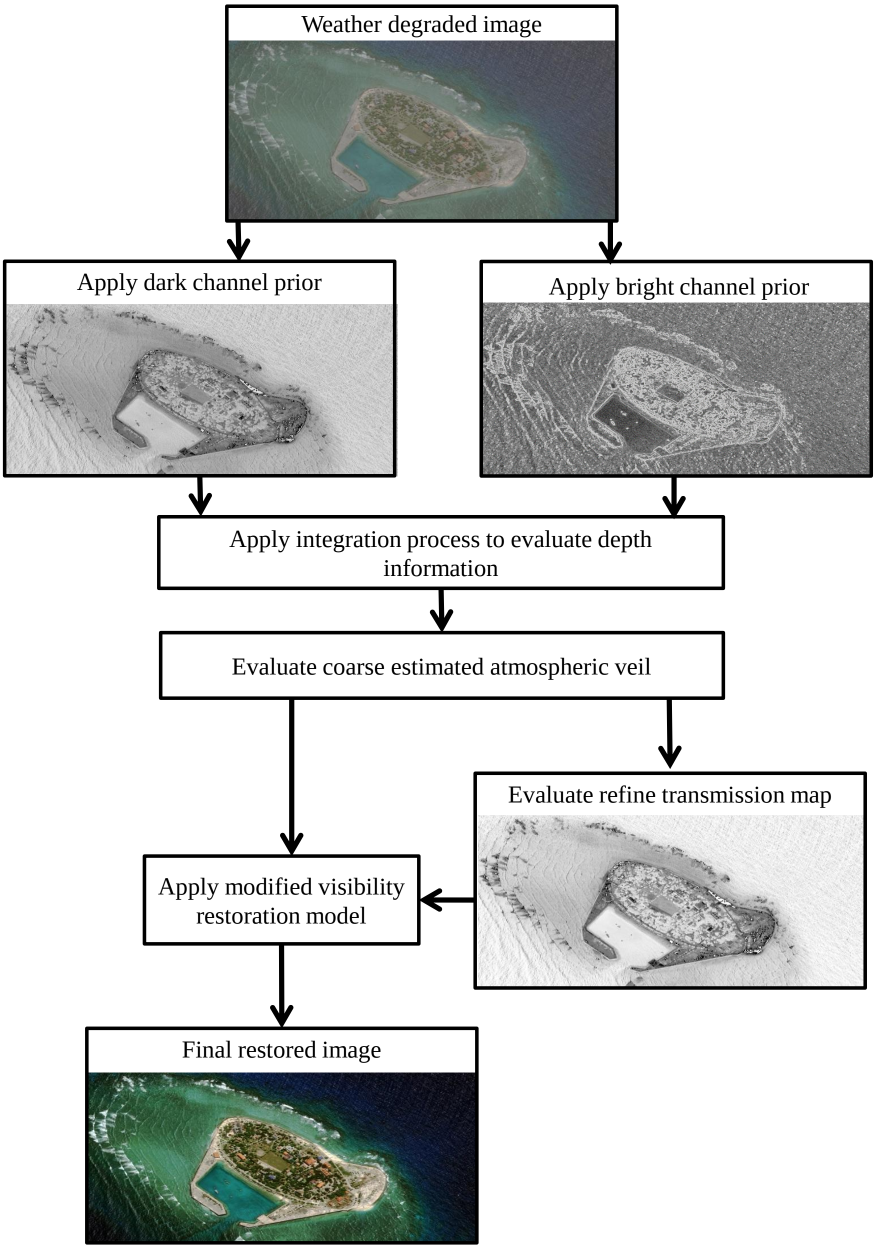

Figure 4.1: Diagrammatic flow of the integrated visibility restoration model

4.1.1 Gain intervention filter

As reported in the literature, it has been found that the evaluation of γ has been done by considering the minimum operation of object $\frac{I_m(k)}{\varphi}$. It will result in $\gamma(k)$'s discontinuity, even if no unexpected depth discontinuities occur. Therefore, gain coefficient based filter was designed to remove halo artefacts from the restored image with good computational speed [165]. However, it is not effective for the gradient reversal artefacts. Therefore, the modification in gain intervention filter is proposed by utilizing the local variance. The modified gain intervention filter (G_{cf}) can be evaluated as:

$$G_{cf} = \frac{\sum_{j}^{|M_i|-1} d(j)}{|d|} \tag{4.1}$$

Here, the minimum intensity (M_i) can be evaluated as:

$$M_i(j) = \min_{c\in\{R,G,B\}} \Big(I_m(j)\Big) \tag{4.2}$$

where $|M_i|$ and $|d|$ represents the total number of pixels in M_i and d, respectively.

$d(j)$ represents the variance at pixel coordinates (j). It is computed between $M_i(j)$ and DCP intensity ($I^d(j)$).

The mathematical representation of d is:

$$d(j) = M_i(j) - G_{cf}(j) \tag{4.3}$$

G_{cf} is used to estimate the intensity of DCP and preserve the inherent information of every mask. Therefore, the improved γ without block artefacts can be computed as:

$$\gamma(j) = \big(1 - M_i(j)\big) + G_{cf} \times P_{cf} \tag{4.4}$$

Here,the calibration factor (P_f) $\in$ [0.7, 0.95] as reported in literature [70].

4.1.2 Bright channel prior

Bright channel prior (BCP) states that the majority of hazy image patches have some pixels which contain very bright illuminations in at least one color channel [166]. In this chapter, an IVRM is proposed to solve sky-regions problem. For an arbitrary image I, its BCP ($I^b(j)$) is defined as:

$$I^b(j) = \max_{(j)\in\Theta(j)} \Big(\max_{c\in(R,G,B)} I^c(j) \Big) \tag{4.5}$$

Here, I^c represents color channels of I. $\Theta(j)$ defines the local mask centred at coordinates (j).

BCP of clear day images always have significantly higher intensity, while in the weather degraded images the bright channel intensity of the near scene is high. Otherwise, the bright channel intensity of the distant scene is low. Therefore, atmospheric light ($\tilde{\chi}(j)$) can be rewritten as:

$$\tilde{\chi}(j) = \max_{(j)\in\Theta(j)} \Big(\max_{c\in(R,G,B)} I^b(j) \Big) \tag{4.6}$$

Here, I^c represent color channels of BCP. Therefore, the atmospheric light of a hazy image can be evaluated using BCP. Because, $I_r(j) \leq \chi(j)$ in hazy image, thus it is required to improve $\tilde{\chi}(j)$ using following formula:

$$\chi(j) = \gamma\tilde{\chi}(j) + \delta\chi_0 \tag{4.7}$$

Here, χ_0 is evaluated by He *et al.* [16]. Also, Xu *et al.* [166] utilized γ and δ as adjustment coefficients:

$$\gamma + \delta < 1.0 \tag{4.8}$$

4.1.3 Improved visibility restoration model

Let us assume that $I^{gc}(j)$ represents DCP refined by using gain intervention filter and $\chi^{gc}(j)$ represents BCP refined using gain intervention filter. Then, the improved transmission map ($\tilde{\eta}^{gc}(j)$) can be evaluated as:

$$\tilde{\eta}^{gc}(j) = 1 - \varepsilon \times \frac{I^{gc}(j)}{\chi^{gc}(j)} \tag{4.9}$$

Here, ε represents the restoration level. Therefore, by using Eq. (4.9), restoration model defined in Eq. 1.33 can be rewritten as:

$$I_r(j) = c \times \tilde{\eta}^{gc}(j) + \frac{I(j) - c \times \Upsilon}{max(\tilde{\eta}^{gc}(j)(j), x_0)} \tag{4.10}$$

4.2 Experimental set-up and results

This section describes the experimental setup, visual, and quantitative analysis of IVRM. The well-known restoration techniques such as DCP ([16]), RSD [44], FHRT [84], and COD [99] are compared with IVRM on a set of well-known benchmark hazy images [167].

4.2.1 Visual analysis

Figure 4.2 (a) shows the input hazy image obtained from SPOT sensor dataset. The radiometric information has been considerably improved in restored images by using DCP [16] (see Figure 4.2 (b)). It can be seen that the colors are distorted in the global and local regions. Therefore, the spectral distortion has occurred. From Figure 4.2 (c), it has been observed that the edges have been preserved and lesser spectral distortion are there in the images obtained from RSD [44].

Figure 4.2 (d) shows the outcome of FHRT [84], which indicate that the restored image has lesser number of halo artefacts as compared to the existing techniques. However, the above-mentioned techniques fail to preserve edges as compared to COD [99] and IVRM. Figure 4.2 (e) depicts the results obtained from COD [99]. It has been observed that an image has good spectral information. However, it seems more artificial as compared to the other techniques.

Figure 4.2 (f) shows the restored image obtained from IVRM. The edges of the restored images have been preserved significantly than DCP [16]. IVRM has lesser number of halo artefacts as compared to the other techniques. IVRM achieves remarkable visual superiority with lesser number of halo and gradient reversal artefacts.

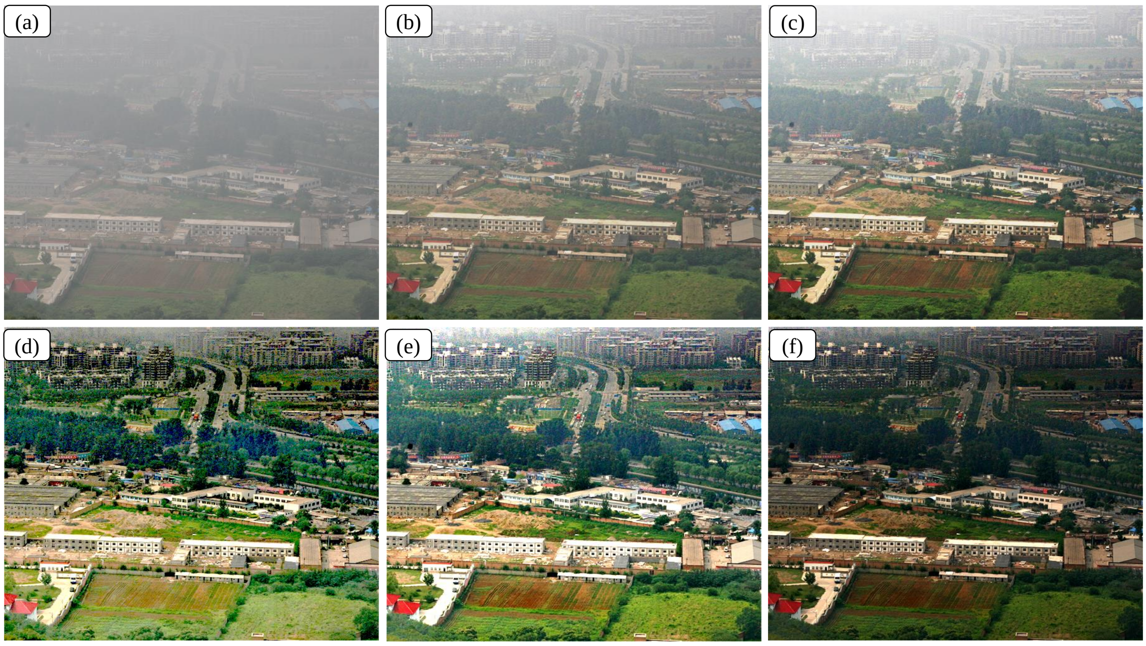

Figure 4.2: Results of restoration techniques for SPOT hazy image (a) Input image, (b) DCP, (c) RSD, (d) FHRT, (e) COD, (f) IVRM.

4.2.2 Quantitative analysis

In addition to visual analysis, the quantitative analysis has also been done to demonstrate the superiority of IVRM. The three well-known performance measures such as ratio of new visible edges (e) [66], ratio of average gradient $(\bar{r})$ [66], and percentage of saturated pixels (ρ) are used to evaluate the performance of IVRM and the existing techniques.

Figures 4.3, 4.4, and 4.5 show the performance evaluation on ten well-known satellite visual sensors images by considering e, $\bar{r}$, and ρ, respectively.

Figures 4.3 and 4.4 reveal that IVRM provides better image quality as compared to the other techniques in terms of visible edges and average gradient. Therefore, IVRM outperforms the existing restoration techniques.

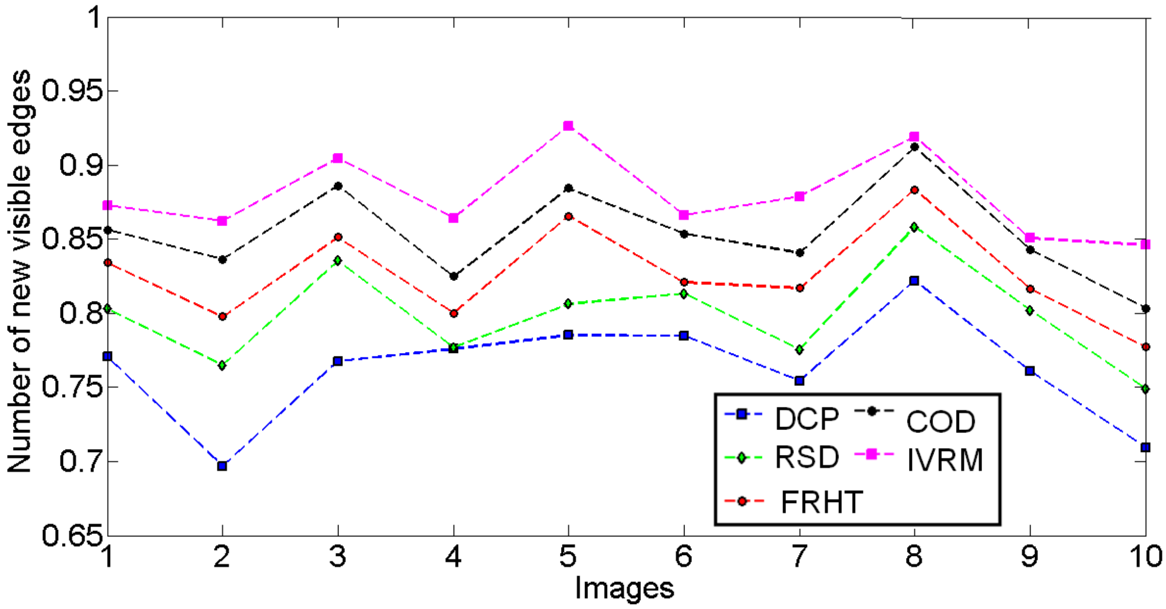

Figure 4.3: Comparative analysis in terms of new visible edges (e)

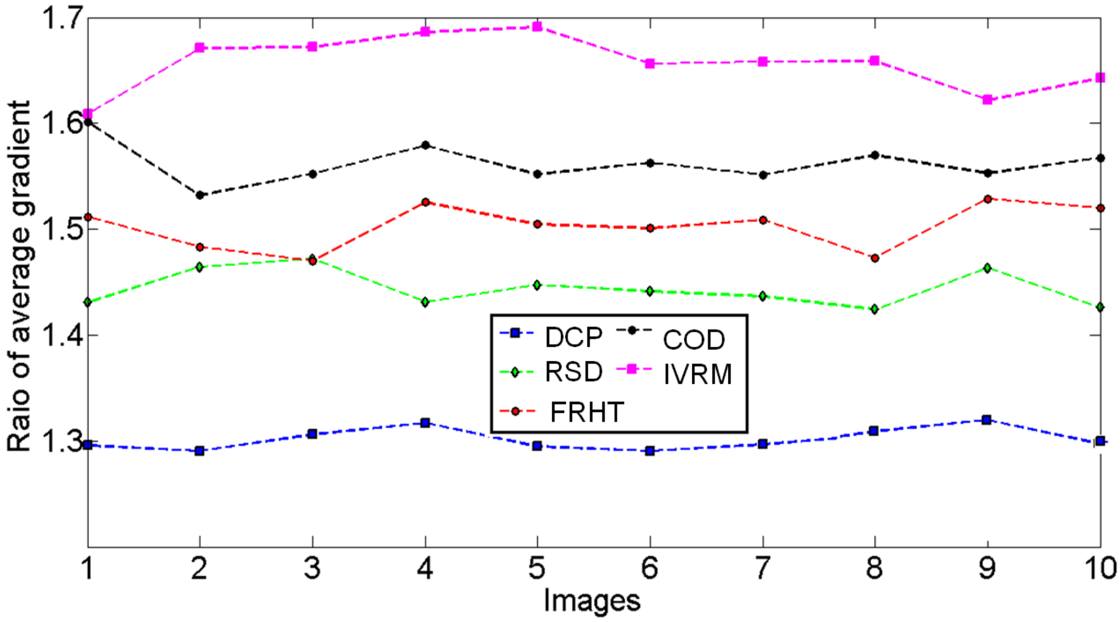

Figure 4.4: Comparative analysis in terms of average gradient $(\bar{r})$

Figure 4.5 depicts that IVRM provides a lesser number of saturated pixels as compared to the existing restoration techniques.

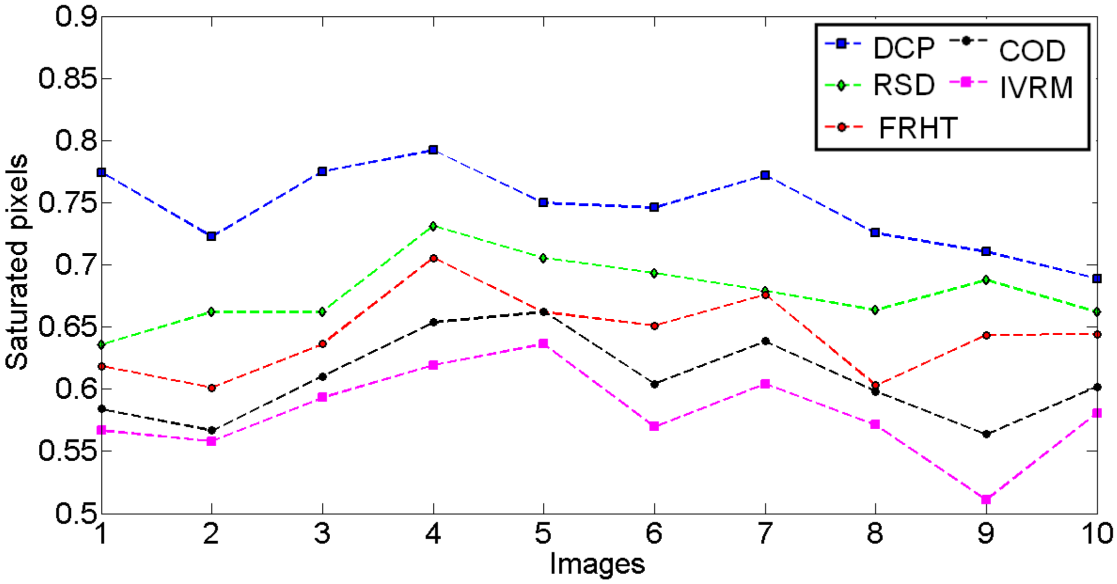

Figure 4.5: Comparative analysis in terms of percentage of saturated pixels (ρ)

4.3 Summary

In this chapter, a modification in gain intervention filter has been implemented. IVRM utilizes BCP to resolve the sky-regions issue associated with DCP. IVRM has been tested on ten well-known remote sensing images. The simulation results show that IVRM is effective to restore the haze in color images. IVRM is able to remove halo and gradient reversal artefacts. IVRM outperforms the existing techniques in terms of new visible edges, average gradient, and computational speed.

Chapter 5

Modified restoration model based visibility restoration

Outline

The existing haze removal techniques such as GITF, FPDETF, and IVRM suffer from noise when transmission map approaches toward zero. Thus, the evaluated atmospheric veil is more than the actual value, (*i.e.,* transmission evaluated by utilizing DCP) is lesser as compared to the actual one. As a consequence, the restored color could deviate from the actual object and the restored restored image looks like an artificial image. To overcome this issue, a novel Modified restoration model (MRM) is proposed in this chapter.

5.1 Proposed modification in restoration model

The detailed description of Modified restoration model (MRM) is presented in this section. Initially, DCP is obtained using Eq. (1.3) (see Section 1.3.1). Thereafter, the global atmospheric light estimation model (Υ) is obtained using Eq. (1.8) (see Section 1.3.2). The coarse atmospheric veil is then evaluated using Eq. (1.16) (see Section 1.3.3).

5.1.1 Modified joint trilateral filter based atmospheric veil refinement

To improve the atmospheric veil further, a modified joint trilateral filter is also proposed. From [43], $A_{\varepsilon}^{\theta}(k) = G_{\upsilon}(1 - M_{t_x}(k))$ is set as the transmission veil, $M_{\theta}(k) = \min_{\theta}(I_{\theta}(k))$ is the minimum color channel of $I_{\kappa}(k)$. As known in prior, $0 \leq A_{\varepsilon}(k) \leq M_{\theta}(k)$, therefore, for gray image, $M_{\theta} = I_{\kappa}$. By designing modified guided image filter, transmission refinement will be achieved by evaluating $t_x(k) = \sigma^2(k) - J_\Gamma^{tf}\left(|M_\theta - \sigma^2(k)|\right)$. $\sigma^2(k)$ represents σ^2 of pixel centered at position k with its neighbors in local mask of 7×7 . Then, atmospheric veil is rewritten as:

$$A_\varepsilon(k) = \max\left(\left(\min\left(\gamma t_{xf}(k), M_\theta(k)\right)\right), 0\right) \tag{5.1}$$

Here, $\gamma \in [0,1]$. Transmission of every mask is redefined as:

$$\overline{\mathrm{M}_{\mathrm{t_x}}} = 1 - \frac{A_\varepsilon}{G_\upsilon^\theta} \tag{5.2}$$

The environment G_υ^θ is typically supposed to be pixel illumination with maximum illumination in an object. But, in real time, this hypothesis frequently delivers invalid outcomes because of the occurrence of self luminous organisms. In the same way, the sky pixel values are also calculated between all local minimum corresponds to background illumination G_υ^θ as:

$$G_\upsilon = \max_{z\in I_\kappa}\left(\min_{z\in\Gamma(k)}\left(I_\kappa^\theta(z)\right)\right) \tag{5.3}$$

where $I_\kappa^\theta(z)$ is color components of $I_\kappa(k)$ in every mask.

MJTF has capability to overcome the gradient reversal artefacts of haze free image. The filtering procedure is initially prepared under the guidance of image G_d, called as reference image which is actual image I_κ itself. Let I_q and G_q be illumination value at pixel q of minimum channel object and guided image. W_r shows the kernel mask at k which is dependable upon bilateral filter. Modified joint trilateral filter (J_{tf}) is then devised as:

$$J_{tf}(I_\kappa) = \frac{1}{\sum\limits_{q\in K_r} M_\theta^{pq}(G_d)}\left(\sum_{q\in k_r} M_\theta^{pq}(G_d)\times I_q\times\sigma^2(I_q, G_q)\right) \tag{5.4}$$

where kernel weights function ($M_\theta^{pq}(G_d)$) is defined as:

$$M_\theta^{pq}(G_d) = \frac{1}{|n|^2}\sum_{n:(p,q)\in k_r}\left(1 + \frac{\left(G_{d_p} - \mu_n)(G_{d_q} - \mu_n\right)}{\sigma_n^2 + \varepsilon}\right) \tag{5.5}$$

where μ_n and σ_n^2 represent mean and variance of G_d in local mask k_r, respectively. $|n|$ indicates the total pixels in mask. When G_{d_p} and G_{d_q} are simultaneously located on a similar side of an edge, the weight allocated to pixel q is maximum. When G_{d_p} and G_{d_q} are on diverse sides, a minimum weight will be allocated to pixel q.

5.1.2 Visibility restoration model

After refining the depth map, it is required to restore the hazy image using haze removal restoration function. After a refinement on transmission, which is discontinuous due to discrete operations, the scene radiance can be recovered from Eq. (1.1). The coarse atmospheric veil ($A_\varepsilon(k)$) is evaluated by utilizing the minimum component of object $\frac{I_\kappa(k)}{\alpha}$, the dissimilarity among image $\frac{I_\kappa(k)}{\alpha}$ and coarse atmospheric veil $A_\varepsilon(k)$ is near to zero with huge probability. Hence, a constant parameter k is used to limit the variation. The minimum value of actual transmission is evaluated using Eq. (5.5) could be very small and even near to zero. Therefore, the recovered image may have some sort of noise [44]. Thus, it is essential to limit transmission by a lower bound γ_{x0}. In fact, γ_{x0} and k are restricted to 0.1 and 0.95, respectively. The object brightness $\beta(k)$ can be recovered as:

$$\beta(k) = \alpha \times \frac{\frac{I_\kappa(k)}{\alpha} - kA_\varepsilon(k)}{max(\gamma_x(k), \gamma_{x0})} \tag{5.6}$$

The object brightness states that the dissimilarity among the color channels will be stated numerous times after dividing the tiny transmission t even if $I_\kappa^r, I_\kappa^g, I_\kappa^b$ are very near to each other. Apart from DCP, an efficient atmospheric veil is computed as:

$$\tilde{A_\varepsilon}(k) = 1 - \frac{1 - \min\limits_{l \in \Gamma(k)} \left(\min\limits_{\theta \in (r,g,b)} \left(\frac{I_\kappa^\theta(l)}{\alpha^\theta} \right) \right)}{1 - \min\limits_{l \in \Gamma(k)} \left(\min\limits_{\theta \in (r,g,b)} \left(\frac{\beta^\theta(l)}{\alpha^\theta} \right) \right)} \tag{5.7}$$

According to Eq. (1.16), a mask with the size of 1×1 is utilized to monitor the atmospheric veil. Thus, minimum element of red, green or blue channel of the restored image cannot be zero. In other words, $\min\limits_{l \in \Gamma(k)} \left(\min\limits_{\theta \in (r,g,b)} \left(\frac{\beta^\theta(l)}{\alpha^\theta} \right) \right)$ will not be near to zero when mask size is 1×1. Hence, real atmospheric veil $A_\varepsilon(k)$ is lesser as compared to $\tilde{A_\varepsilon}(k)$, which is monitored by utilizing DCP. Moreover, in brighter segments like white objects and water surface, DCP is unacceptable since their intensities are maximum even on clear days [44].

The probability of $\min\limits_{l \in \Gamma(k)} \left(\min\limits_{\theta \in (r,g,b)} \left(\frac{\beta^\theta(l)}{\alpha^\theta} \right) \right)$ will be near to zero which is very low. Thus, the evaluated atmospheric veil is more than the actual value (*i.e.,* transmission evaluated by utilizing DCP) is lesser as compared to the actual one. As a consequence, the restored color could deviate from the actual object and the restored restored image looks like an artificial image [44].

To reduce the color distortion, transmission ($\gamma_x(k)$) is redefined. Therefore, initially the dissimilarity among the color channel of image $I_\kappa(k)$ and global atmospheric brightness (α) are constrained by utilizing a predefined value χ. If the dissimilarity is fewer than χ, re-estimation of the transmission is computed as:

$$\gamma_x(k) = min\Big(max\Big(\Big|\frac{\chi}{I_\kappa(k)} - \alpha\Big|, 1\Big).\gamma_x(k), 1\Big) \tag{5.8}$$

where $\gamma_x(k)$ is the refined transmission and threshold χ is calculated experimentally. It states that a brighter pixel will obtain maximum transmission. For remote sensing images, threshold (χ) value 120 is found to be efficient with the mask size of 5×5. Therefore, the atmospheric veil can be written as:

$$A'_\varepsilon(k) = 1 - \gamma_x(k) \tag{5.9}$$

For the brighter segment, the illumination of pixels is larger as compared to global atmospheric luminosity, and their equivalent transmission is more. In fact, this occurrence is due to rewritten transmission by Eq. (5.8). The redefined transmission states that the transmission of brighter segments whose illumination is near to global atmospheric luminosity will turn out to be the maximum value. Therefore, by putting Eq. 5.9 in Eq. (1.33), the restored image (I_r) can be easily recovered as:

$$I_r(j) = c \times A'_\varepsilon + \frac{I(j) - c \times A'_\varepsilon}{max(\gamma_x(j), x_0)} \tag{5.10}$$

5.2 Experimental set-up and results

To demonstrate the effectiveness of MRM, ten well-known remote sensing images from QUICKBIRD [153], IKONOS [154] and MODIS [155] sensors are taken. The images are resized to 256×256 because remote sensing images are huge in size. MRM and other techniques such as DCP [16], Remote sensing restoration (RSD) [44], Color attenuation prior (CAP) [96], and Fusion [112] are considered for comparative analysis.

5.2.1 Visual analysis

Figure 5.1 shows the results of hazy image taken from QUICKBIRD sensor [153]. Figure 5.1 (a) shows the hazy input image and has poor visibility. Therefore, restoration techniques are required to improve the visibility of hazy image. The radiometric information has been considerably enhanced in the restored image by using DCP [16]'s technique as shown in Figure 5.1 (b). However, colors are distorted in global and local regions. Therefore, the spectral distortion has occurred. Although, the edge sharpening is preferable, but, the conserved spectral information is more significant in Fusion [112] and CAP [96]'s techniques which are shown in Figures 5.1 (c) and (d). Figure 5.1 (e) shows the outcomes of RSD [44]'s technique, which clearly indicates that the restored image has the lowest number of halo artefacts as compared to DCP [16], Fusion [112] and CAP [96]'s techniques. However, it has a poor edge preservation than CAP [96] and Fusion [112]'s restoration algorithms.

In the case of Fusion [112] and CAP [96]'s techniques, the colors have distorted, and edges are not sharpened sufficiently. Therefore, the restored images shown in Figures 5.1 (c) and 5.1 (d) has minimum spectral information than RSD [44]'s technique. But, they have good spatial information than DCP [16]. Figure 5.1 (f) demonstrates that the colors of restored images are not distorted in the case of MRM. The edges of the restored images are preserved significantly than DCP [16] and RSD [44]. Also, the proposed technique has a lesser number of halo artefacts as compared to CAP [96] and Fusion [112].

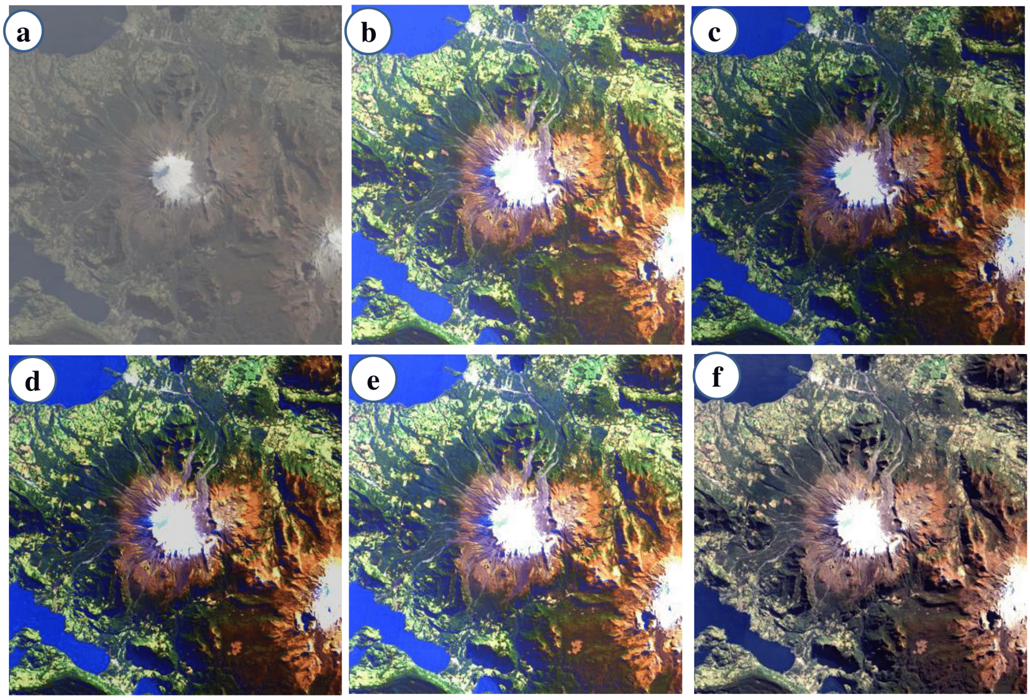

Figure 5.1: Results of restoration techniques on QUICKBIRD dataset's snow image (a) Input image, (b) DCP, (c) RSD, (d) CAP, (e) Fusion and (f) MRM

Figures 5.2 and 5.3 show the outcomes of haze affected image, which taken from IKONOS [154] and MODIS [155] sensors respectively. The input hazy images are represented in Figures 5.2 (a) and 5.3 (a). It can be clearly observed from the input images that they have lesser significant visibility. As shown in Figures 5.2 (b) and 5.3 (b), the radiometric information is improved as compared to input images by DCP [16]. However, spectral distortion is also found in global as well as in the case of local segments.

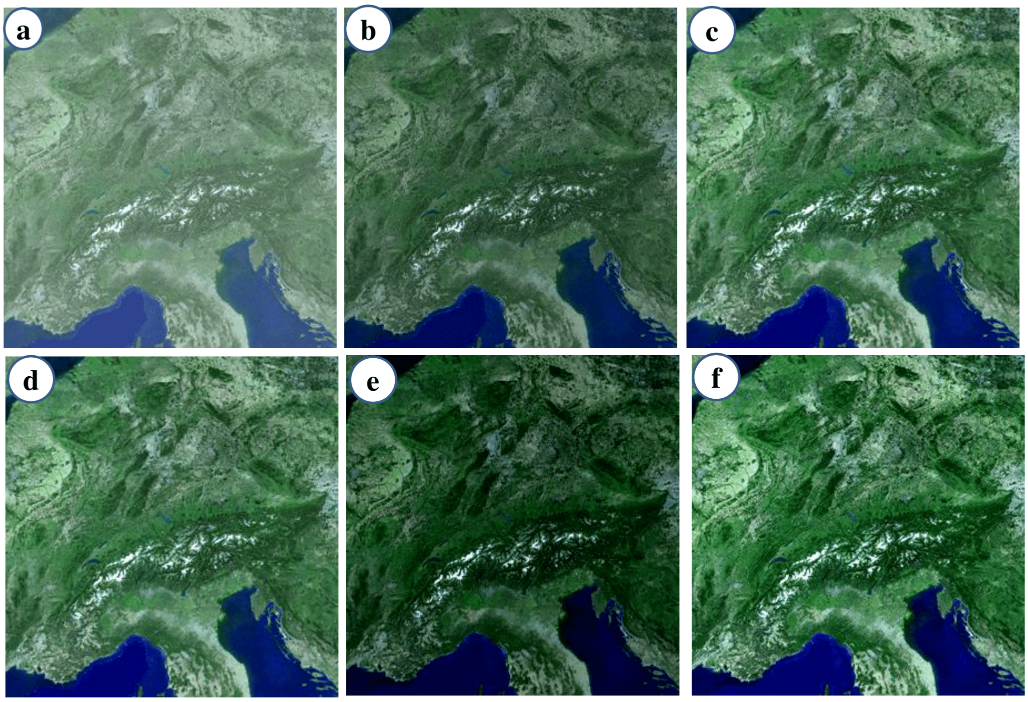

Figure 5.2: Results of restoration techniques on MODIS dataset's image (a) Input image, (b) DCP, (c) RSD, (d) CAP, (e) Fusion and (f) MRM

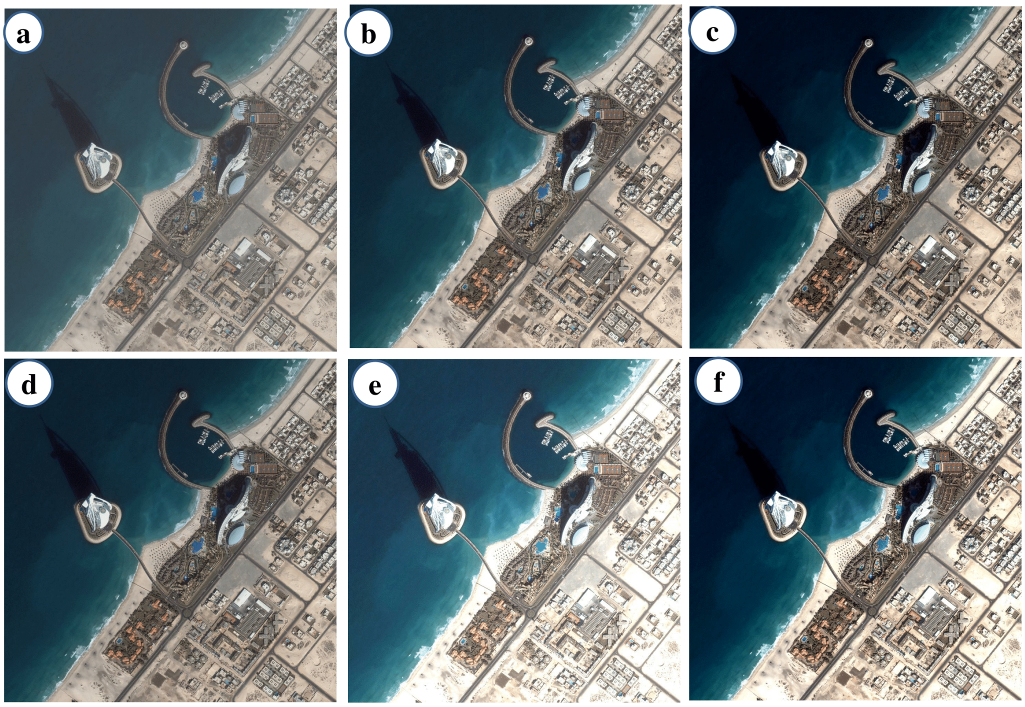

Figure 5.3: Results of restoration techniques on IKONOS dataset's image (a) Input image, (b) DCP, (c) RSD, (d) CAP, (e) Fusion and (f) MRM

Fusion [112] and CAP [96]'s techniques are shown in Figures 5.2 (c), 5.3 (c), 5.2 (d), and 5.3 (d) have overcome the issue of spectral distortion found in case of DCP

[16]'s technique. But, Fusion [112] and CAP [96]'s techniques produce halo artefacts as demonstrated in Figures 5.2 (c), 5.3 (c), 5.2 (d) and 5.3 (d).

Figures 5.2 (e) and 5.3 (e) show that the restored image produced by RSD [44]'s restoration technique has lesser number of halo artefacts. However, it has a poor edge preservation than CAP [96] and Fusion [112]'s restoration techniques. Figures 5.2 (f) and 5.3 (f) prove that the results produced by MRM do not suffer from edge distortion and a lesser number of halo artefacts as compared to CAP [96], Fusion [112], DCP [16] and RSD [44] techniques.

5.2.2 Quantitative analysis

In addition to visual observation, the four well-known quality metrics such as Contrast gain (C_g), Percentage of saturated pixels (ρ), Ratio of new visible edges (e), and Ratio of average gradient ($\bar{r}$) are used to compare the proposed technique with existing techniques. Table 5.1 shows the analysis of C_g, which needs to be maximized. It is observed from Table 5.1 that the proposed technique has a better value of C_g than DCP [16], RSD [44], CAP [96] and Fusion [112]. The mean improvement in C_g obtained from the proposed technique in comparison to the available techniques is approximately 0.0895.

Table 5.1: Comparative analysis of MRM with respect to contrast gain (C_g)

Images	DCP	RSD	CAP	Fusion	MRM
1	0.0105	0.0967	0.1382	0.1548	0.1856
2	0.0026	0.1287	0.1331	0.1274	0.1814
3	0.0134	0.1049	0.1998	0.1856	0.3730
4	0.0086	0.1004	0.1781	0.1952	0.3591
5	0.0147	0.0395	0.1931	0.1570	0.1956
6	0.1724	0.1914	0.2171	0.1874	0.2358
7	0.0197	0.0291	0.1414	0.1487	0.1871
8	0.0176	0.0241	0.1247	0.1297	0.2137
9	0.0098	0.0126	0.1459	0.1845	0.2291
10	0.0149	0.0284	0.1248	0.1158	0.1359

Table 5.2 shows the comparative analysis of ρ on restoration techniques. The proposed technique has lesser value of ρ as compared to DCP [16], RSD [44], CAP [96], and Fusion [112]. The mean reduction in ρ obtained from the proposed technique over existing techniques is approximately 0.1768.

Table 5.2: Comparative analysis of MRM with respect to percentage of saturated pixels (ρ)

Images	DCP	RSD	CAP	Fusion	MRM
1	0.1449	0.0325	0.0469	0.0962	0.0259
2	0.1180	0.0089	0.0149	0.0226	0.0214
3	0.3537	0.0715	0.2698	0.4383	0.0258
4	0.1427	0.0220	0.0415	0.0993	0.0220
5	0.1739	0.1087	0.2421	0.4778	0.0238
6	0.1311	0.0342	0.1159	0.1754	0.0317
7	0.1328	0.1326	0.0941	0.0739	0.0227
8	0.2207	0.1954	0.1995	0.1249	0.0487
9	0.1782	0.1668	0.1318	0.0916	0.0318
10	0.2891	0.1211	0.1429	0.0954	0.0739

Tables 5.3 and 5.4 demonstrate that MRM has more e and $\bar{r}$ as compared to DCP [16], RSD [44], CAP [96], and Fusion [112]. Thus, the proposed technique has more visible edges and gradient as compared to the existing techniques.

Table 5.3: Comparative analysis of MRM with respect to new visible edges (e)

Images	DCP	RSD	CAP	Fusion	MRM
1	2.0213	2.8927	3.0119	3.7643	3.4528
2	3.2271	2.196437	3.1127	2.5319	2.8172
3	3.0316	3.6150	3.5547	3.9836	3.2209
4	2.7616	2.13	2.6043	2.0957	3.0156
5	3.1243	3.2367	3.4020	3.0927	3.1718
6	2.5027	2.1379	2.9818	2.3723	2.4621
7	3.0134	3.2047	3.3152	3.4243	3.5350
8	2.1109	2.3333	2.5847	2.9046	2.9520
9	3.0517	3.0916	3.0729	3.0428	3.2234
10	3.1537	3.5936	3.5731	3.6143	3.7849

Table 5.4: Comparative analysis of MRM with respect to ratio of average gradient ($\bar{r}$)

Images	DCP	RSD	CAP	Fusion	MRM
1	0.9646	1.1143	1.1441	1.6163	1.8480
2	1.3791	1.7925	1.9736	2.1648	2.5738
3	1.8734	1.7929	2.1602	2.3716	2.4746
4	1.1764	1.3860	1.4567	1.9360	2.0863
5	1.1768	1.0749	1.3401	1.7138	1.6276
6	0.8327	0.9419	0.9528	1.0424	1.6137
7	2.1346	2.1627	2.4104	2.7350	2.9451
8	1.2569	1.5462	1.9531	2.0932	2.0694
9	0.9106	0.8719	1.0715	1.0964	1.2283
10	1.1080	1.2141	1.8949	1.9562	2.0484

5.3 Summary

In this chapter, a MRM is designed and implemented. To analyze the performance of MRM, benchmark remote sensing hazy images are taken from various satellite sensors. The experimental results reveal that MRM has significantly removed the haze from remote sensing hazy images when it has been compared to the existing techniques. Also, MRM has a lesser number of artefacts and color distortion as compared to the existing techniques.

Chapter 6

Gradient based channel priors

Outline

In this chapter, two novel channel priors are proposed to evaluate the depth map from weather degraded images. The main advantages of these channel priors over the existing priors are (a) do not suffer from sky region problem and (b) preserve better texture information of a restored image. These channels are (a) Gradient profile prior (GPP) and (b) Oblique gradient profile prior (OGPP).

6.1 Gradient profile prior

Three novel concepts, *i.e.,* gradient profile prior, guided L_0 gradient minimization filter, and modified restoration model have been used in the proposed fog removal technique. The gradient profile prior is designed to estimate the transmission map and atmospheric veil in an efficient manner. The main advantages of gradient profile prior over existing techniques are (a) does not suffer from sky region problem (b) preserves better texture information of the restored image. The main advantages of guided L_0 minimization based filter over trilateral filter are (a) provides better computational time (b) reduces halo and gradient reversal artefacts. The guided L_0 gradient minimization filter has also improved the coarse estimated atmospheric veil. The standard restoration model fails for sky regions. To resolve this, the modification in the restoration process has also been done. The dynamic threshold (lower bound) has been used to minimize the color distortion rate.

A novel Gradient profile prior (GPP) is designed. GPP is decomposed into five main steps. The mathematical formulation of each step is discussed in succeeding sections.

6.1.1 Gradient profile prior

Initially, the gradient profile prior of a foggy image will be evaluated. It is used to estimate the airlight (Υ) and transmission map (t) from foggy image (I). To evaluate the depth information of foggy image (I), the image gradients are utilized. The gradient of I represented by Δ_I provides magnitude and direction information of I. Since, Δ_I has both direction and magnitude information. Thus, it can be easily decomposed into a vector (v_r) [168]. The size of v_r contains the magnitude information of I, while its direction depicts Δ_I direction. As Δ_I may be different at each location, therefore it has been represented with a different v_r at every location of I [169].

Δ_I is evaluated as [170]:

$$\Delta_I = \left(\frac{\partial I}{\partial m}, \frac{\partial I}{\partial n}\right) \tag{6.1}$$

Here, $\frac{\partial I}{\partial m}$ represents the partial derivative of an image in m direction. $\frac{\partial I}{\partial n}$ shows the partial derivative of n direction.

The partial derivative of I with respect to m represents how quickly the illumination of I changes with respect to m [171]. For a continuous function, partial derivatives of I in m direction are computed as [172]:

$$\frac{\partial I(j)}{\partial m} = \lim_{\partial m \to 0} \frac{I(m+\Delta_j) - I(j)}{\Delta_m} \tag{6.2}$$

In case of discrete function, only differences at one pixel intervals will be considered [173]. Therefore, the difference between $I(j)$ and the pixel before it or the pixel after it will be considered. Therefore, $\frac{\partial I(j)}{\partial m}$ in case of discrete function is evaluated as:

$$\frac{\partial I(j)}{\partial m} \approx \frac{I(m+1,\, n) - I(m-1,\, n)}{2} \tag{6.3}$$

In similar fashion, $\frac{\partial I(j)}{\partial n}$ is computed as:

$$\frac{\partial I(j)}{\partial n} \approx \frac{I(m,\, n+1) - I(m\, n-1)}{2} \tag{6.4}$$

By using Eqs. (6.3) and (6.4), Δ_I is computed as:

$$\Delta_I = \left(\frac{I(m+1, n) - I(m-1,\, n)}{2}, \frac{I(m,\, n+1) - I(m,\, n-1)}{2}\right) \tag{6.5}$$

A. Properties of Gradient profile prior

As mentioned earlier, Δ_I indicates how quickly I changes when we move in either m or n direction. However, what will happen if we move in other directions. It means that how

I changes with a very small movement in position. To handle this issue, consider how I changes as we move from position (j) by a small amount Δ in an arbitrary direction such as θ, it will take us to the position $(m+\Delta_{cos\,\theta}, n+\Delta_{sin\ \theta})$.

From calculus, it has been observed that if Δ is small then:

$$I(m+\Delta_{cos\,\theta}, n) \approx I(j) + \Delta_{cos\,\theta} \frac{\partial I(j)}{\partial m} \tag{6.6}$$

Therefore, it determines how illumination changes with a little movement in m direction.

By using the same concept, $I(m+\Delta_{cos\,\theta}, n+\Delta_{sin\,\theta})$ is computed as:

$$\begin{aligned} I(m+\Delta_{cos\,\theta}, n+\Delta_{sin\,\theta)} &\approx I(m+\Delta_{cos\,\theta}, n) + \Delta_{sin\,\theta} \frac{\partial I(j)}{\partial m} \\ &\approx I(j) + \Delta_{cos\,\theta} \frac{\partial I(j)}{\partial m} + \Delta_{sin}\,\theta \frac{\partial I(j)}{\partial m} \end{aligned} \tag{6.7}$$

It assumes that the derivative of I does not change much if we move a small amount in I.

Assume that v_r encodes how we have moved in I. The v_r is computed as:

$$v_r \equiv (\Delta_{cos\,\theta}, \Delta_{sin\,\theta}) \tag{6.8}$$

Therefore, Eq. (6.7) is redefined as:

$$I(m+\Delta_{cos\,\theta}, n+\Delta_{sin\,\theta)} - I(j) \approx \langle v_r, \Delta_I \rangle \tag{6.9}$$

It states that any change in illumination as we move by a small amount in I is found by taking the inner product between Δ_I and v_r that describes the movement.

The inner product ($\langle v_r, \Delta_I \rangle$) is defined as :

$$\langle v_r, \Delta_I \rangle = \|v_r\|\|\,\Delta_I\|cos\,\alpha \tag{6.10}$$

Here, α indicates the angle between v_r, v, and Δ_I.

B. Key points of the gradient profile prior

For different options of $v_r, < v_r, \Delta_I >$ is proportional to cosine of the angle between v_r and Δ_I. It also have peak value whenever the angle is 0 (*i.e.,* when v_r points in the direction of Δ_I). Therefore, direction of Δ_I represents the direction in which I changes maximum number of times. Also, if v_r is a unit vector in the direction of Δ_I, then the amount I illumination change will be $\parallel \Delta_I \parallel$, $\parallel V \parallel = 1$, and $cos\,\alpha = 1$. Thus, the magnitude of Δ_I indicates I illumination is changing when we move in the direction of peak change.

In case, if v_r is perpendicular to Δ_I, then the inner product between vectors is 0 *i.e.*, I illumination does not change at all whenever we move in that direction.

C. Analysis of gradient profile prior

In this section, a detailed analysis of the gradient profile prior of the restored outdoor images has been discussed.

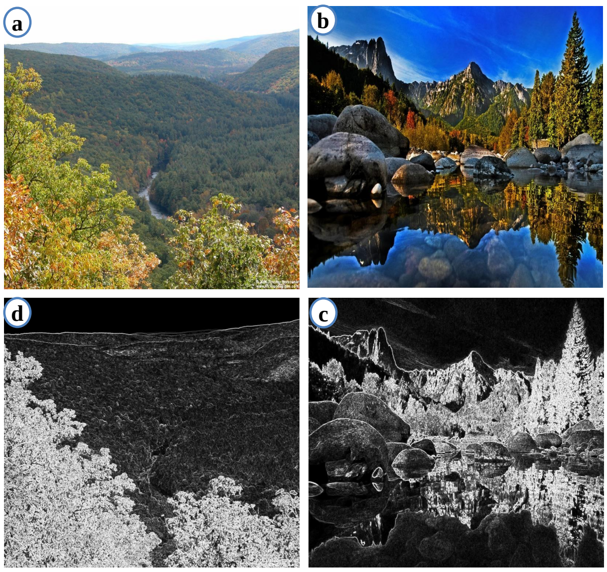

Figure 6.1: Analysis of gradient profile prior (a) Outdoor images. (b) Equivalent gradient channels.

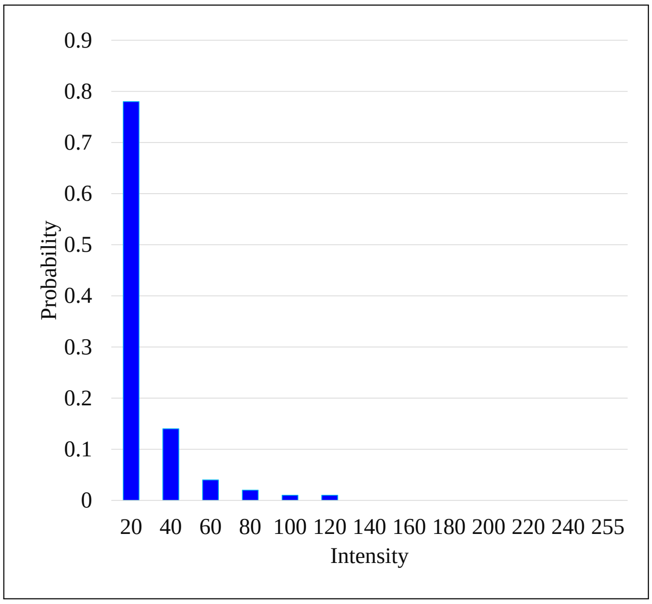

Figure 6.2: Histogram of the intensity of pixels in all 500 gradient channels (each bin has 20 intensity levels).

To evaluate the effectiveness of gradient profile prior on outdoor images, 500 restored images are taken. These images are resized to 512×512 pixels. The patch size gradient channel images is set to 7×7 pixels.

Figure 6.1 shows fog free images along with their respective gradient profile prior. Figure 6.2 shows the intensity histogram over all 500 gradient channels.

It has been observed that the intensity of approximately 78 % of the pixels in the gradient channels is under 20 and the intensity greater than 92 % of the pixels is under 40. These experimental analysis show that the gradient profile prior is applicable for outdoor images. However, for images captured in a foggy environment, the gradient channel turns out to be invalid. Affected from the additive airlight, pixels in fog affected segments have maximum intensity values in all color channels and the minimal intensity of local masks is maximum. Thus, the gradient channel of a foggy image will have maximum intensity in regions having higher fog. Therefore, it proves that the intensity of the gradient channel is a rough approximation of the thickness of fog.

D. Airlight estimation

The estimation of airlight (Υ) is the second step of the fog removal technique. Eq. (1.1) indicates that Υ is an extra dominant factor as the distance from object to camera increases [16]. Υ is measured from I using similar regions as its gradient channel image. The pixel with maximum gradient in I_r is called global atmospheric light. The highest gradient values are utilized to estimate global atmospheric light(Υ) as:

$$\Upsilon(j) = I\left(\max_{c}\left(I_m^c\right)\right). \tag{6.11}$$

E. Transmission map estimation

This subsection describes the estimation of transmission map (t). To evaluate t, I is normalized by Υ. Assume that Υ is known. Therefore, Eq. (1.1) is redefined as:

$$\frac{I(j)}{\Upsilon} = \frac{t(j){I_r}^c(j)}{\Upsilon} + 1 - t(j) \tag{6.12}$$

Assume t in local path ($\Psi(j)$) be constant. The mathematical computation of t is defined as $\tilde{t}(j)$. Apply gradient profile prior on both sides of Eq. (6.12). Similarly, apply gradient operators on both sides as:

$$\Delta_{y\in\Psi(j)}\left(\Delta_c \frac{I^c(y)}{\Upsilon_l^c}\right) = \tilde{t}(j)\Delta_{y\in\Psi(j)}\left(\Delta_c \frac{{I_r}^c(y)}{\Upsilon_l^c}\right) + 1 - \tilde{t}(j) \tag{6.13}$$

where $\tilde{t}(j)$ is a constant value. Thus, $\tilde{t}(j)$ can be placed outside of Δ. c shows color channel of I. The gradient profile prior of I_r approaches toward zero, it is represented as $\Delta(O)(j)$. It is defined as:

$$\Delta(O)(j) = \Delta_{n\in\Psi(j)}\big(\Delta_c {I_r}^c(n)\big) = 0 \tag{6.14}$$

As $\Upsilon_l^c \in \mathbb{R}$, it results in:

$$\Delta_{n\in\Psi(j)}\left(\Delta_c \frac{{I_r}^c(n)}{\Upsilon_l^c}\right) = 0 \tag{6.15}$$

where $\Delta_{n\in\Psi(j)}\left(\Delta_c \frac{{I_r}^c(n)}{\Upsilon_l^c}\right)$ is the gradient channel of normalized fog free image $\frac{{I_r}^c(n)}{\Upsilon_l^c}$.

Putting Eq. (6.15) into Eq. (6.13), the multiplicative term can be discard and $\tilde{t}$ is evaluated as:

$$\tilde{t}(j) = 1 - \Delta_{n\in\Psi(j)}\left(\Delta_c \frac{I_m^c(n)}{\Upsilon_l^c}\right) \tag{6.16}$$

It has been observed that the main issue with DCP is the color of sky in I is identical to Υ. In sky region, $\Delta_{n\in\Psi(j)}\left(\Delta_c \frac{I^c(n)}{\Upsilon_l^c}\right)$ approaches toward one. Thus, $\tilde{t}$ approaches toward zero. Thus, the estimated t by utilizing gradient profile prior, *i.e.,* Eq. (6.16) is able to handle sky and non-sky regions. Therefore, there is no requirement to handle the brighter segments. If we restore fog free image in an efficient manner, then the fog free image may appear artificial. Thus, some amount of fog is allowed using a lower bound ($\beta \in [0,1]$). Eq. (6.16) is redefined as:

$$\tilde{t}(j) = 1 - \beta\Delta_{n\in\Psi(j)}\left(\Delta_c \frac{I_m^c(n)}{\Upsilon_l^c}\right) \tag{6.17}$$

F. Transmission map refinement using Guided L_0 filter

This subsection describes the coarse atmospheric light estimation ($\gamma(j)$). Initially, $\gamma(j)$ is computed as follows [105]:

$$\gamma(j) = 1 - \tilde{t}(j) \tag{6.18}$$

From Eqs. (6.17) and (6.18), the normalized value of $\gamma(j)$ is rewritten as:

$$\gamma(j) = \beta\Delta_{n\in\Psi(j)}\left(\Delta_c \frac{I_m^c(n)}{\Upsilon_l^c}\right) \tag{6.19}$$

The estimation of $\gamma(j)$ is achieved by considering Δ on object $\frac{I_m^c(n)}{\Upsilon_l^c}$, it results in $\gamma(j)$'s discontinuity even if no unexpected depth discontinuities occur. To remove the issue of halo artefacts with restored images, an efficient filter is required to estimate $\gamma(j)$.

In this research work, guided L_0 minimization based image filter is implemented to refine $\gamma(j)$. From [174] and [105], $\gamma^c(j)$ is estimated as:

$$\gamma^c(j) = \Upsilon(1 - t(j)) \tag{6.20}$$

Also, $t(j)$ can be estimated as:

$$t(j) = \Delta_c(I_m^c(j)) \tag{6.21}$$

where the value of $\gamma \in [0, t]$. Hence, it does not affect the grayscale image. Therefore, guided L_0 image filter has been used in this research work to refine the transmission map (t).

Firstly, L_0 gradient minimization is described. Afterward, based on L_0 minimization, the guided L_0 filter is implemented. In the end, an effect of guided L_0 filter is discussed for refining the transmission map.

L_0 minimization plays a significant role to minimize gradient distortion rate by minimizing the sharpness of transition while removing the low-amplitude structures [175]. L_0 minimization is evaluated as [176]:

$$\min_{t} \ ||t - t^*||_2^2 + \lambda||\nabla t||_0, \tag{6.22}$$

Here, ∇t represents the gradients of transmission map (t). t^* shows evaluated gradient image. λ shows the weight to estimate the intensity level. Auxiliary variable (δ) is utilized to derive the objective function for ∇t. Therefore, minimization problem is defined as [177]:

$$\min_{t,\,\delta} \ ||t - t^*||_2^2 + \beta||\delta - \nabla f||_2^2 + \lambda||\delta||_0, \tag{6.23}$$

Here, λ must be minimum to keep all gradients information. β monitors the similarity between δ and ∇t. The filtering level is regularized by λ [178]. The δ is a vector with two components (*i.e.,* δ_m and δ_n). Thereafter, Eq. (6.23) is normalized through alternatively minimizing λ and δ.

L_0 gradient minimization has an ability to reduce the gradient distortion rate of filtered image (s^*). However, in the case of foggy images, we do not intend to preserve all gradients except ones with minimum gradient information. Therefore, L_0 minimization is unable to provide efficient results in case of fog removal techniques.

Thus, a guided L_0 filter is designed and implemented in this research work. It utilizes the benefits of a well-known guided filter and L_0 minimization. It preserves the gradient of transmission map $(\tilde{t}^*)$ according to foggy guidance image (t^*). Specifically, $\tilde{t}^*$'s gradients will be preserved if the corresponding locations of t^* have large gradient information. Also, these will be filtered if the corresponding locations have low gradient information.

Additionally, the level of t^*'s gradient can be perceived in the filtered image $(\tilde{t})$ by optimizing the following criteria. It preserves the significant gradient information of $\tilde{t}^*$.

Initially, when t^k is known in prior, we tune δ^k by:

$$\min_{\delta^k} \ \beta^k ||\nabla t^k - \delta^k||_2^2 + \lambda ||\delta^k||_0 \ (k = 1,\ 2,\ 3\ldots). \tag{6.24}$$

Here, λ must be minimum to preserve the information of gradients.

Eq. (6.24) can be rewritten as:

$$\delta^k = \begin{cases} 0 & \nabla t^k \leq \frac{\lambda}{\beta} \\ \nabla t^k & otherwise \end{cases} \tag{6.25}$$

Secondly, when t^k and δ^k are known, tuning of t^{k+1} is achieved by:

$$\min_{t^{k+1}} \ ||t^{k+1} - t^*||_2^2 + \beta^k ||\delta^k - \nabla t^{k+1}||_2^2. \tag{6.26}$$

After that Eq. (6.26) is rewritten as:

$$\begin{cases} \min\limits_{t^{k+1}} ||t^{k+1} - t^*||_2^2 \beta^k ||\nabla t^{k+1} - H.*\nabla t^k||_2^2 \\ H = \begin{cases} 0 \delta^k = 0 \\ 1 \delta^k \neq 0 \end{cases} (k = 1,2,3\ldots) \end{cases} \tag{6.27}$$

The objective function is quadratic. Therefore, it is a convex optimization problem. The least square technique and Fast Fourier transformation (f_{ft}) have been used to tune it. Afterwards, the outcomes of Eqs. (6.26) or (6.27) are defined as:

$$t^{k+1} = i_{fft}\left(\frac{f_{ft}(f^*) + \beta(f_{ft}(\partial_m^T) f_{ft}(\delta_m^k) + f_{ft}(\partial_m^T) f_{ft}(\delta_n^k))}{f_{ft}(1) + \beta(f_{ft}(\partial_m^T) f_{ft}(\partial_m) + f_{ft}(\partial_n^T) f_{ft}(\partial_n))}\right), \tag{6.28}$$

where i_{fft} represents the inverse of f_{ft}. ∂_m and ∂_n symbolize difference functions in horizontal and vertical directions, respectively.

Finally, based on the values of $\tilde{t}^k$ and δ^k, $\tilde{t}^{k+1}$ is obtained by:

$$\begin{cases} \min\limits_{\tilde{t}^{k+1}} ||\tilde{t}^{k+1} - \tilde{t}^*||_2^2 \beta^k ||\nabla \tilde{t}^{k+1} - H.*\nabla \tilde{t}^k||_2^2 \\ H = \begin{cases} 0 \delta^k = 0 \\ 1 \delta^k \neq 0 \end{cases} (k = 1,2,3\ldots) \end{cases} . \tag{6.29}$$

Eq. (6.29) can be rewritten as:

$$\tilde{t}^{k+1} = iff\left(\frac{f_{ft}(\tilde{t}^*) + \beta(f_{ft}(\partial_x^T) f_{ft}(H.*\nabla \tilde{t}_m^k) + f_{ft}(\partial_m^T) f_{ft}(H.*\nabla \tilde{t}_n^k))}{f_{ft}(1) + \beta(f_{ft}(\partial_m^T) f_{ft}(\partial_m) + f_{ft}(\partial_n^T) f_{ft}(\partial_n))}\right). \tag{6.30}$$

In the proposed filter, most of the attributes assignments are identical to L_0 minimization's, *i.e.,* β_0, β_{max}, and k are set to 2λ, 105, and 2, respectively. λ is set to be 0.0002. The step by step description of Guided L_0 filter is mentioned in Algorithm 1.

Algorithm 1: Guided L_0 filter

```
Input: $\tilde{t}^*$, $t^*$, $\lambda$, $\beta_0$, $\beta_{max}$, $k$
Output: $\tilde{t}$
Initialization: $t^1 \leftarrow t^*$, $\tilde{t}^1 \leftarrow \tilde{t}^*$, $\beta^1 \leftarrow \beta_0$ , $k \leftarrow 1$
while $\beta > \beta_{max}$ do
    with $t^k$, solve for $\delta^k$ using (6.25);
    with $t^k$ and $\delta^k$ , solve for $t^{k+1}$ using Eq. (6.28);
    with $\tilde{t}^k$ and $\delta^k$ , solve for $t^{k+1}$ using (6.30);
    $\beta \leftarrow k\beta$
    $k++$;
end
```

G. Restoration model

The last step of fog removal technique is restoration model. It restores I_r from I. It is an ill-posed problem because only I is available in prior [179]. Therefore, it requires an efficient estimation of γ and t [104]. The estimation of γ and t will be done with the help of the proposed gradient profile prior. Therefore, I_r can be computed by [16]:

$$I_r(j) = \frac{I(j) - \gamma}{t(j)} + \gamma \tag{6.31}$$

However, the restored image (I_r) suffers from noise when t approaches toward zero. Also, if the fog is restored completely, then I_r may seem as an artificial image. Thus, lower bound (x_0) has been introduced to allow some fog in γ and I_r. Therefore, t has been constrained with the help of x_0. According to related work, x_0 is experimentally set to 0.1 [16]. Therefore, I_r is rewritten as:

$$I_r(j) = \frac{I(j) - \gamma}{\max(\tilde{t}(j), x_0)} + \gamma \tag{6.32}$$

6.1.2 Experimental set-up and results

The performance of the existing competitive fog removal techniques and GPP have been tested on ten foggy images obtained from [153]. Both subjective and quantitative evaluation has been done to evaluate the effectiveness of GPP over the existing fog removal techniques. GPP is compared with seven well-known fog removal techniques such as DCP [16], COD [99], WHDR [33], GITF, FPDETF, IVRM and MRM. The mask size of the gradient profile prior has been set to be 5×5 pixels. The parameters setting of the above-mentioned techniques are set as they are recommended in their original work.

A. Experimentation 1: Transmission map estimation

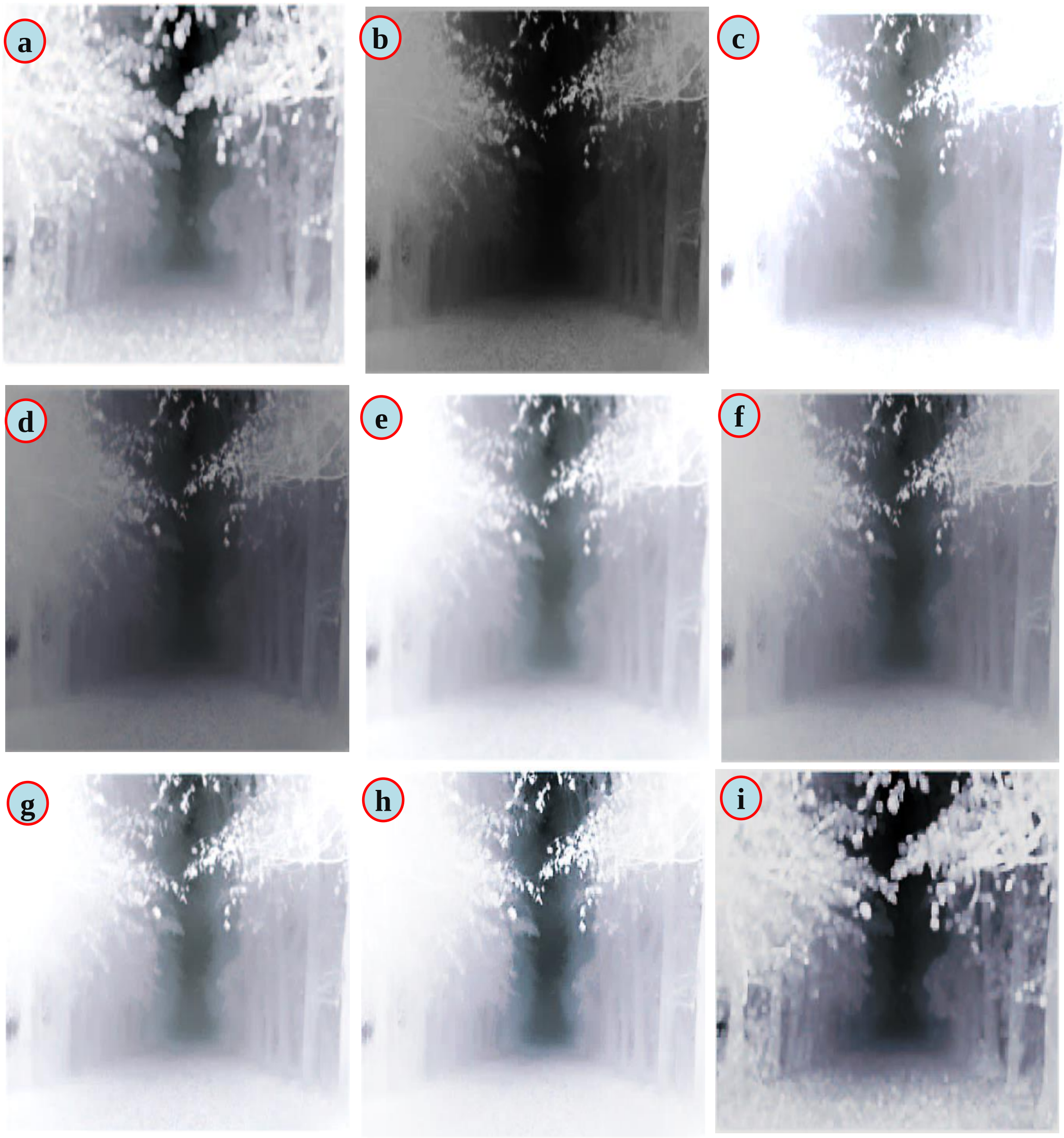

Figure 6.3: Refined transmission map of fog removal techniques for tree foggy image (a) Actual depth information, (b) DCP, (c) COD, (d) WHDR, (e) GITF, (f) FPDETF, (g) IVRM, (h) MRM, and (j) GPP.

Figure 6.3 (a) shows the input foggy image, *i.e.,* Tree foggy image. Figure 6.3 (b) shows the refined transmission map obtained from DCP [16]. It has been observed that DCP [16] has over-smoothed transmission map. Therefore, the restored image obtained from this transmission map may have halo artefacts, color, and edge distortion problems. Figures 6.3 (c) and 6.3 (g) demonstrate the transmission map evaluated using COD [99] and IVRM based restoration techniques. These maps have shown significant detail, therefore, the restored image obtained using these maps will not suffer from halo artefacts, color, and edge distortion problems. However, these maps are not showing enough texture detail.

From Figures 6.3 (d) and 6.3 (f), it has been observed that the refined transmission map images obtained using WHDR [33] and FPDETF. It has significant information to restore restored images in an efficient manner. However, these techniques will produce saturated restored images. Therefore, unable to preserve the significant colors of an image.

Figures 6.3 (e) and 6.3 (h) show the refined transmission map obtained from GITF and MRM, respectively. It has been observed that restored images using these transmission maps will suffer from sky regions and texture preservation problems. Figure 6.3 (j) shows refined transmission map obtained using GPP. GPP achieves remarkably refined transmission map than the above-mentioned techniques. It has significant edge and texture information of objects. Therefore, the restored image using this map will have a lesser number of halo artefacts, edge degradation, and color distortion rate. Also, the restored image will have significant texture information.

B. Experimentation 2: Analysis of patch size

The main objective of this experiment is to evaluate the effect of patch size on the evaluated gradient map. The value of patch size is 1×1, 7×7, and 11×11, respectively.

Figure 6.4 demonstrates the effect of different patch sizes on transmission maps and restored foggy images. Figure 6.4 (b) shows that for a patch size of 1×1, gradient channel becomes less effective and restored image becomes saturated (see Figure 6.4 (c)). For the patch size of 1×1, the gradient profile prior takes more execution time to evaluate the transmission map. Figure 6.4 (d) shows the gradient channel turns out to be more efficient for 5×5 patch size. The restored image has less number of saturated pixels, halo and gradient reversal artefacts and edge distortion rate (see Figure 6.4 (e)).

From Figures 6.4 (f) and 6.4 (g), it has been observed that the restored image has more halo and gradient artefacts for a patch size of 11×11.

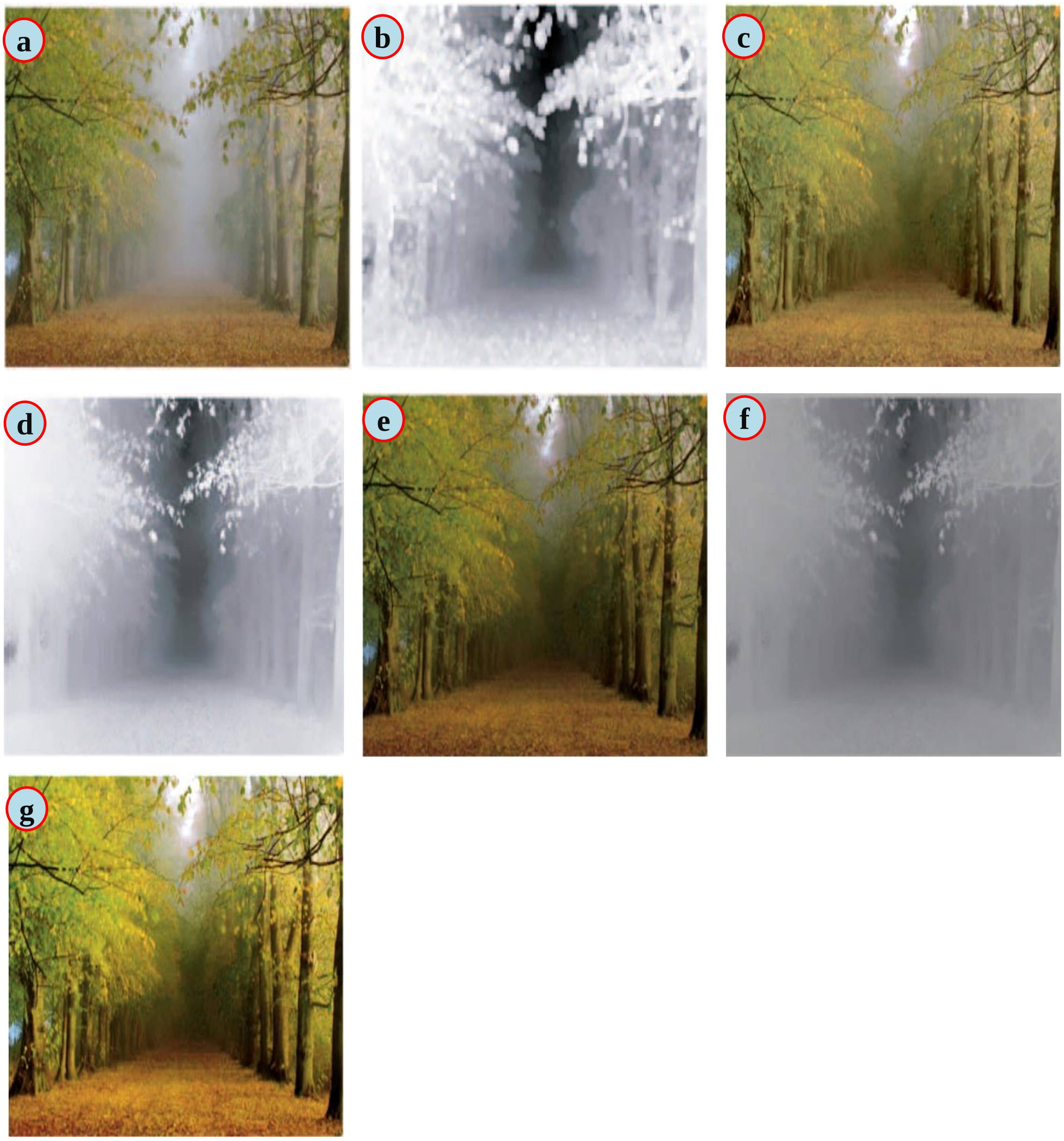

Figure 6.4: Effect of patch size on tree foggy image (a) Foggy image, (b) Transmission map with 1 × 1 patch size, (c) Restored image with 1 × 1 patch size, (d) Transmission map with 7 × 7 patch size, (e) Restored image with 7 × 7 patch size, (f) Transmission map with 11 × 11 patch size, and (g) Restored image with 11 × 11 patch size

C. Experimentation 3: Performance evaluation

To evaluate the effectiveness of the gradient profile prior based fog removal techniques, ten well-known foggy images are taken from [153]. The comparison of GPP is drawn and compared with seven competitive fog removal techniques.

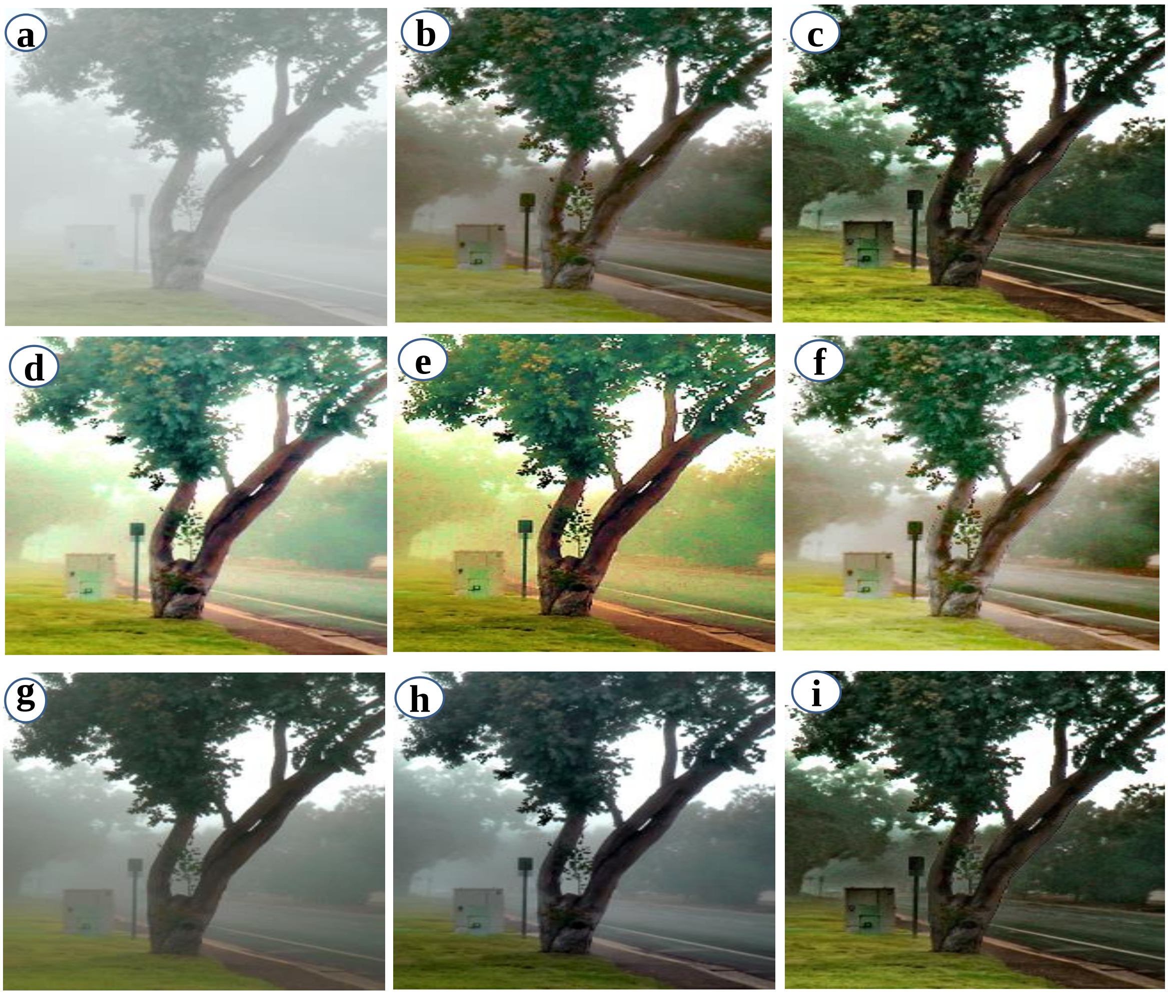

Figure 6.5: Outcomes of fog removal techniques for single tree foggy image (a) Input image, (b) DCP, (c) COD, (d) WHDR, (e) GITF, (f) FPDETF, (g) IVRM, (h) MRM, and (j) GPP.

Figure 6.5 (b) shows the restored results of single tree foggy image evaluated using DCP [16]. It suffers from colors and edge distortion issues. Also, the obtained images have halo and gradient reversal artefacts. Figures 6.5 (c) and 6.5 (g) show the restored images evaluated using COD [99] and IVRM based fog removal techniques, respectively. These images have shown minimum colors and texture distortion as compared to DCP [16]. But, these images have shown an edge degradation issue. Figures 6.5 (d) and 6.5 (f) show the restored images evaluated using WHDR [33] and FPDETF based fog removal techniques, respectively. These images have shown a minimum number of halo and gradient reversal artefacts as compared to COD [99]. But, these techniques unable to preserve the significant edges. Figures 6.5 (e) and 6.5 (h) show the restored images obtained from GITF and MRM, respectively. These images suffer from the saturated problem. But, these techniques suffer from color and edge distortion issues. Figure 6.5 (j) shows restored image obtained using the gradient profile prior. It achieves significant visual superiority with a minimum number of halo and gradient reversal artefacts.

Figure 6.6 shows restored cropped images obtained using different fog removal techniques. It has been observed that GPP achieves remarkable texture information with minimum color and edge distortion issues.

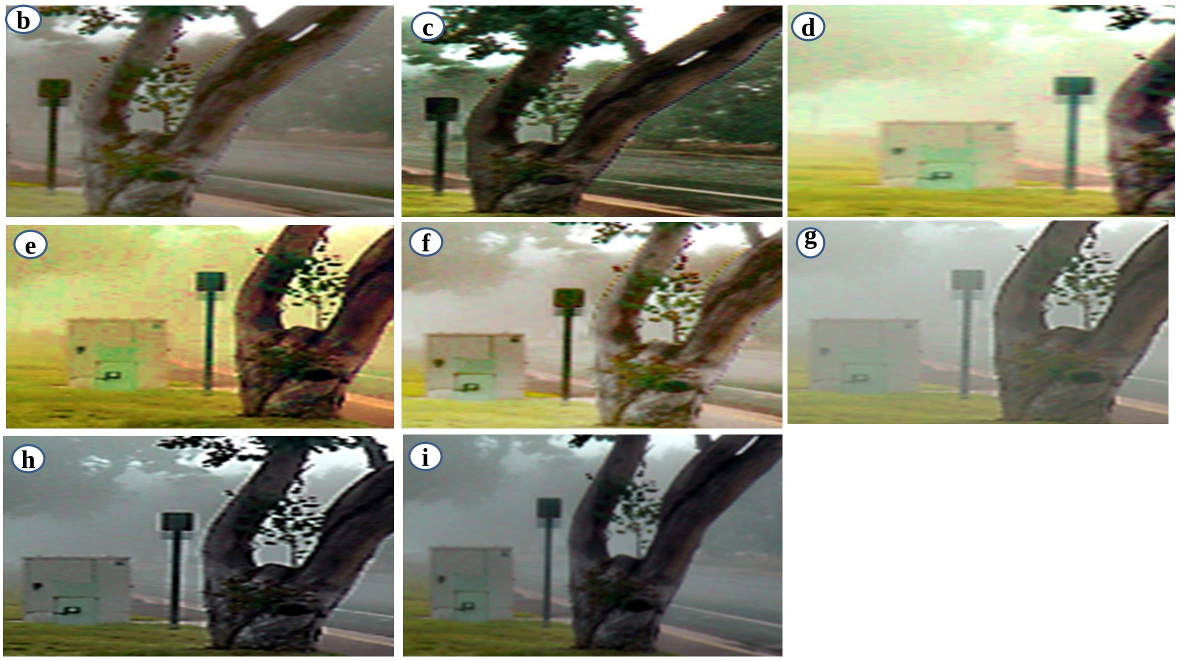

Figure 6.6: Fog removal techniques for tree image (a) DCP, (b) COD, (c) WHDR, (d) GITF, (e) FPDETF, (f) IVRM, (g) MRM, and (h) GPP.

D. Experimentation 4: Quantitative analysis

In addition to visual observation, the quantitative analysis has also been done. The comparison of GPP is made with the existing fog removal techniques using acceptable quality metrics such as Contrast gain (C_g), Percentage of saturated pixels (ρ), Visible edges ratio, Perceptual fog density (D_h), and Execution time (ET).

Figure 6.7 demonstrates the performance analysis of GPP with others in terms of C_g. It has been observed that GPP has better C_g than the other restoration techniques such as DCP [16], COD [99], WHDR [33], GITF, FPDETF, IVRM, and MRM. The average improvement of C_g using the GPP over available techniques is 0.0436 (Approx).

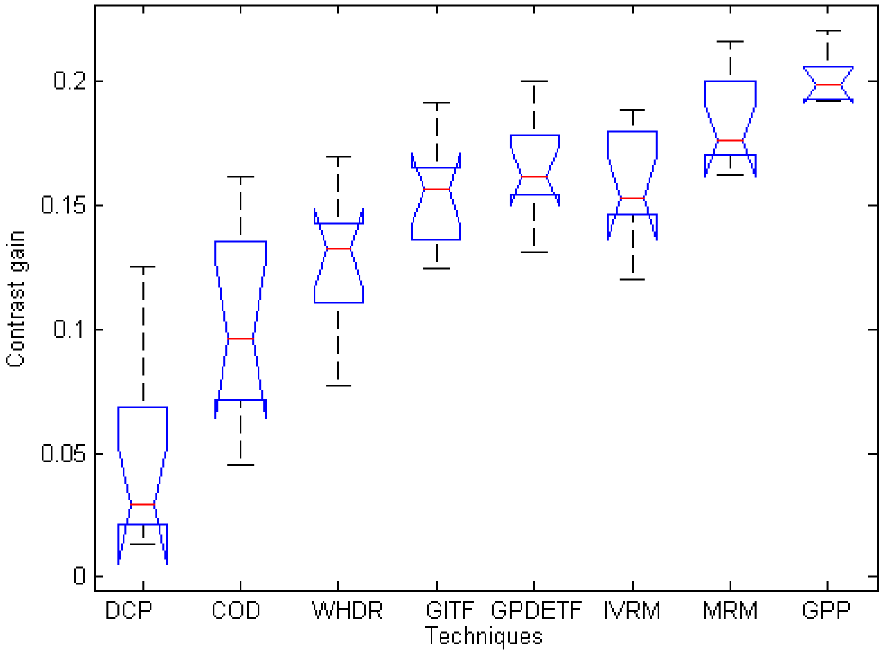

Figure 6.7: Comparative analysis of contrast gain (C_g)

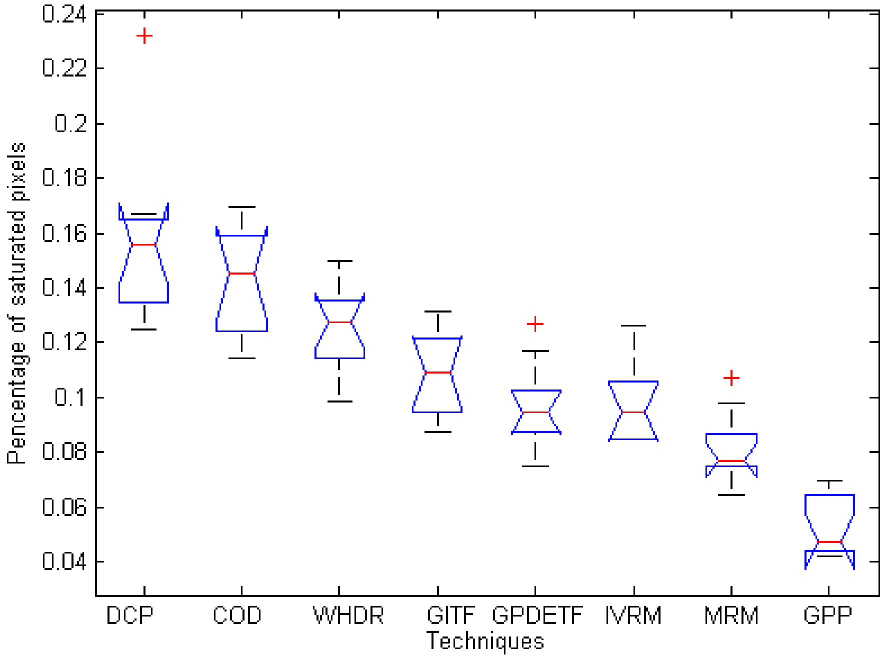

Figure 6.8: Comparative analysis of percentage of saturated pixels (ρ)

Figure 6.8 shows the analysis of ρ which needs to be minimized. Figure 6.8 depicts that guided L_0 gradient minimization filter based fog removal technique has minimum ρ as compared to DCP [16], COD [99], WHDR [33], GITF, FPDETF, IVRM, and MRM. The average reduction in ρ by using the GPP than the existing techniques is approximately 0.0876.

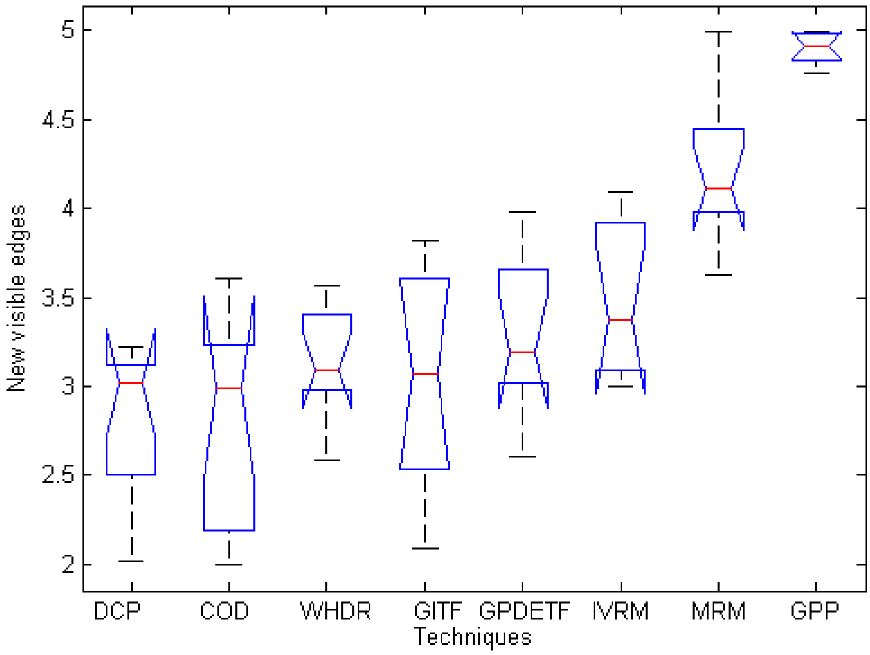

Figure 6.9: Comparative analysis of new visible edges (e)

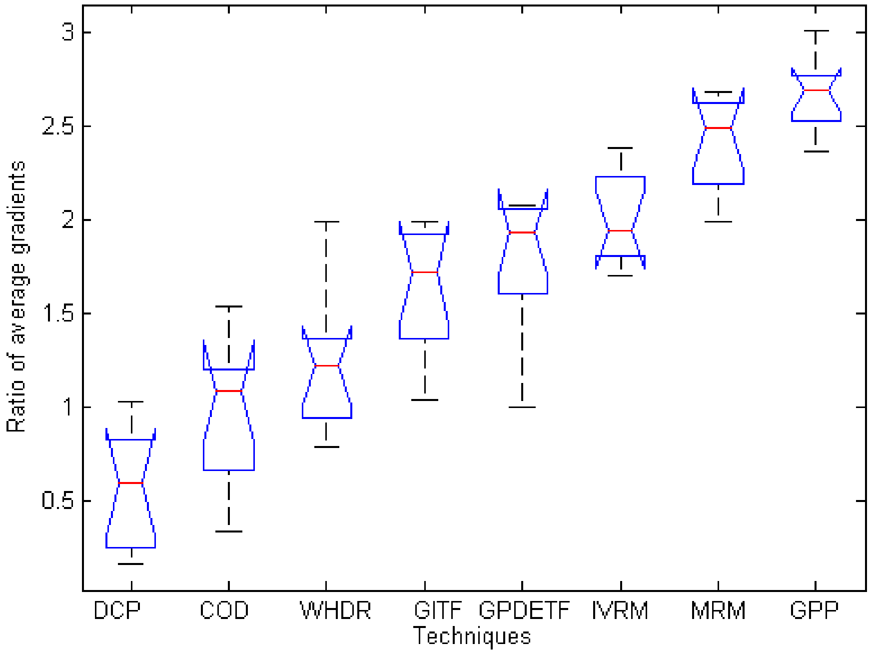

Figure 6.10: Comparative analysis of ratio of average gradients ($\bar{r}$)

Figures 6.9 and 6.10 show the guided L_0 gradient minimization filter based fog removal technique has more e and $\bar{r}$ as compared to DCP [16], COD [99], WHDR [33], GITF, FPDETF, IVRM, and MRM. Therefore, GPP has more significant edges and texture information than the existing fog removal techniques.

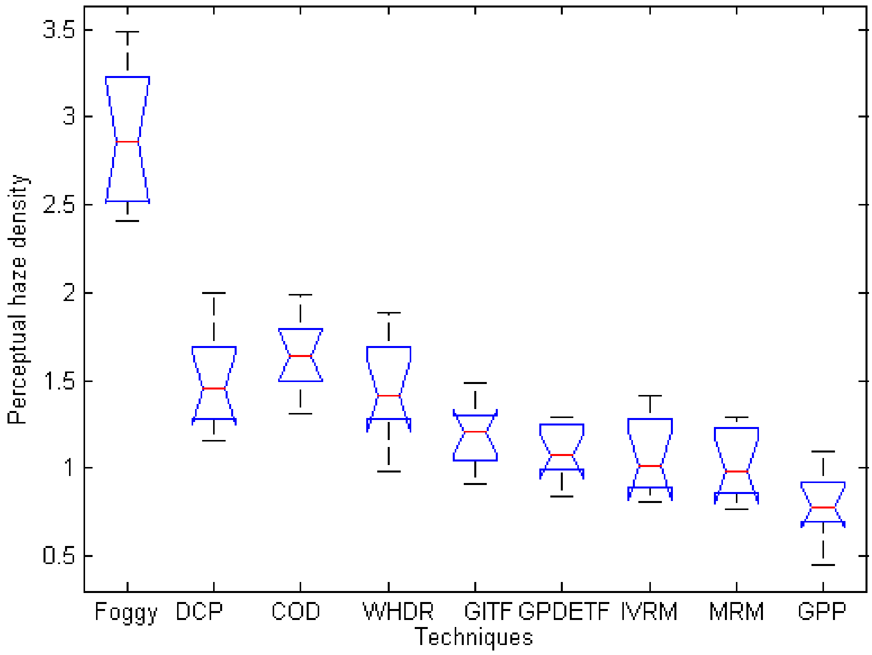

Figure 6.11: Comparative analysis of perceptual haze density (D_h)

Figure 6.11 shows the images obtained from GPP have a lesser effect of fog as compared to the existing techniques. Also, GPP provides more promising results as compared to the existing restoration techniques.

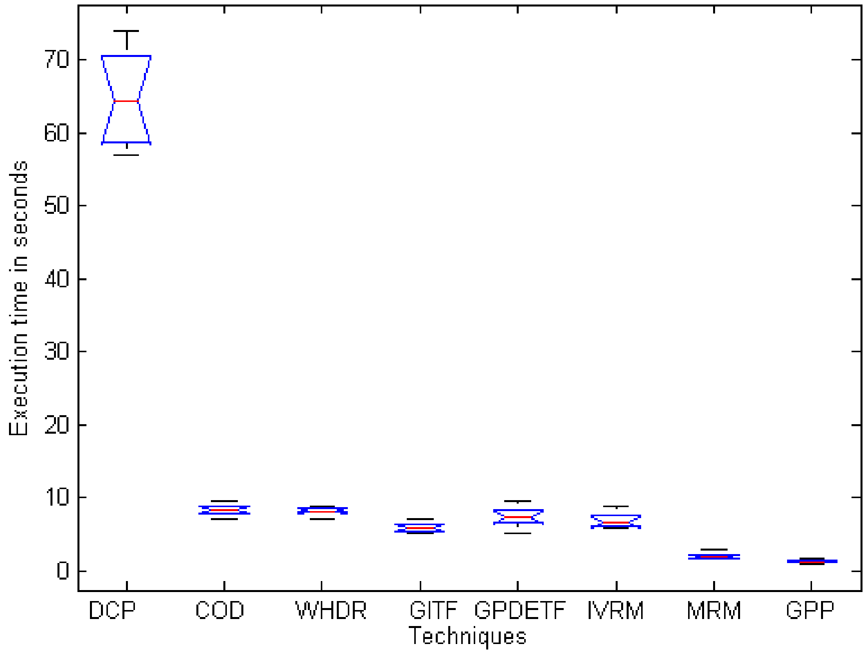

Figure 6.12: Comparative analysis of execution time in seconds (ET)

Figure 6.12 shows the GPP restores images at good computational speed. Therefore, GPP is more efficient for real-time restoration systems.

6.2 Oblique gradient profile prior

In this section, an oblique gradient profile prior is designed. It is able to accurately estimate the transmission map and atmospheric veil. Additionally, the transmission map is also refined by designing a local activity-tuned anisotropic diffusion based image filter. Thereafter, the image restoration process is implemented to restore the hazy images.

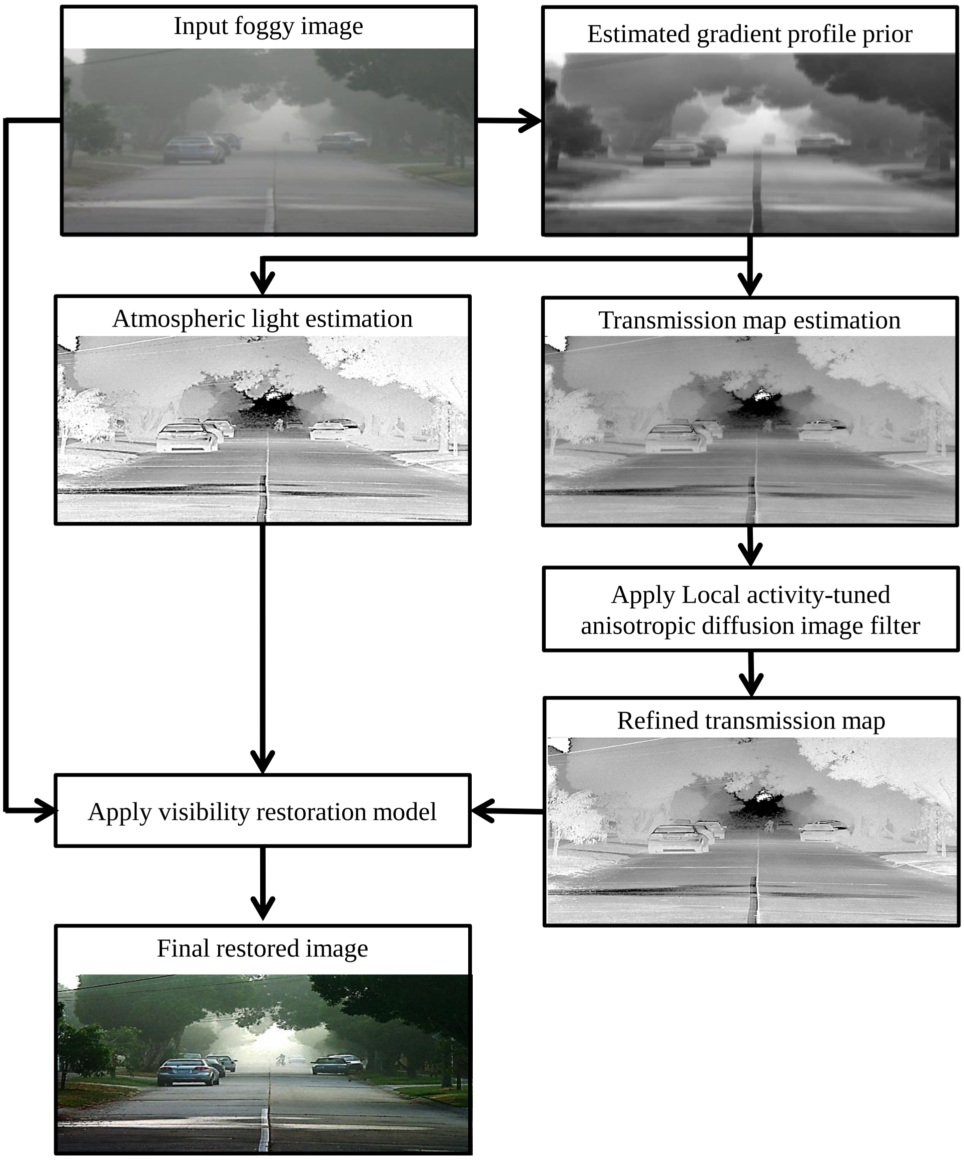

Figure 6.13: Diagrammatic flow of the oblique gradient profile prior based restoration technique

6.2.1 Proposed oblique gradient based visibility restoration

This section describes a novel Oblique gradient profile prior (OGPP) based restoration technique. Fig. 6.13 shows the five main steps of OGPP. The mathematical formulation of each step is described in the preceding sections.

Initially, an oblique gradient profile prior of a hazy image (I) is evaluated. It is used to estimate the atmospheric light (Υ) and transmission map (t) from (I). The oblique gradients are utilized to evaluate the depth information of I. The oblique gradient of I is represented by β. It provides magnitude and direction information of I.

A. Oblique gradient filter

The gradient of a hazy image(I) is calculated as:

$$\nabla I(j) = \begin{pmatrix} \psi_m \\ \psi_n \end{pmatrix} = \begin{pmatrix} \partial I / \partial m \\ \partial I / \partial n \end{pmatrix} \tag{6.33}$$

The amplitude of I is defined as:

$$mag(I) = \sqrt{(\psi_m^2 + \psi_n^2)} \tag{6.34}$$

The orientation angle of ∇I is evaluated by:

$$\nabla_O(j) = \arctan\left(\frac{\psi_n}{\psi_m}\right) \tag{6.35}$$

For $I(m,n)$, ψ_m and ψ_n are evaluated by different patches. The nine different oblique gradients according to different patches. A patch (W) with 3×3 size is represented in Fig. 6.14. The intensity value of central pixel is denoted by I_c. $I_k (k = 1, 2, \ldots, 8)$ represents k^{th} neighbor of I_c.

I_1	I_2	I_3
I_4	I_c	I_5
I_6	I_7	I_8

Figure 6.14: Oblique gradients based patch (W)

The standard gradient is evaluated with n and m axes. Therefore, it is able to evaluate horizontal and vertical edges in local patch. It is found that many oblique edges are present in I. Thus, the standard gradient filter is unable to evaluate the oblique edges [180].

Li *et al.* [177] designed a multiple oblique gradient filter to evaluate oblique edges. Fig. 6.15 shows the various oblique gradient filter with different patch sizes. In Figs. 6.15 (a) and (b)show the oblique gradient filters having patch size of 2×2.

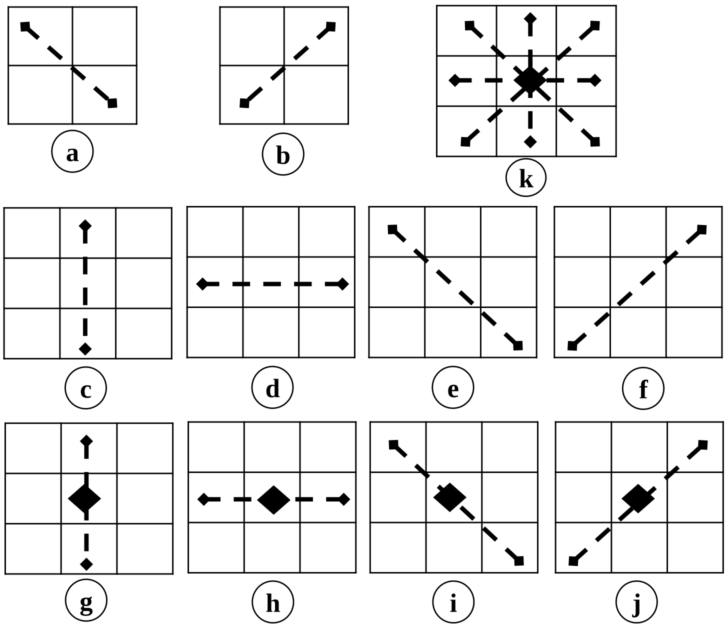

Figure 6.15: Oblique gradients with different patch sizes

From these figures, it can evaluate two oblique edges, i.e, $\frac{\pi}{4} \leftrightarrow \frac{5\pi}{4}$ and $\frac{3\pi}{4} \leftrightarrow \frac{7\pi}{4}$. By considering $W \in \mathbb{R}^{3\times3}$ (see Fig. 6.14), four 2×2 patches can be evaluated as: $\begin{bmatrix} I_1 & I_2 \\ I_4 & I_c \end{bmatrix}$, $\begin{bmatrix} I_2 & I_3 \\ I_c & I_5 \end{bmatrix}$, $\begin{bmatrix} I_4 & I_c \\ I_6 & I_7 \end{bmatrix}$, and $\begin{bmatrix} I_c & I_5 \\ I_7 & I_8 \end{bmatrix}$ with respect to I_c. The corresponding oblique gradient angles are evaluated using Eqs.(6.36)-(6.39). If $\beta^1(m,n)$ =0, then an oblique edge (i.e, $\frac{\pi}{4} \leftrightarrow \frac{5\pi}{4}$) exists in patch $\begin{bmatrix} I_1 & I_2 \\ I_4 & I_c \end{bmatrix}$. If $\beta^1(m,n)$ is trend to $\pi/2(or-\pi/2)$, then oblique edge can be evaluated (along $3\pi/4 \leftrightarrow 7\pi/4$) in the patch $\begin{bmatrix} I_1 & I_2 \\ I_4 & I_c \end{bmatrix}$. Similarly, the different oblique edges can be found in other patches. Figs. 6.15 (b)-(j) show 8 different oblique gradient filters with patch size of 3×3. Fig. 6.15 (k) represents a combined oblique gradient filter. In Fig. 6.15 (c)-(j), additional oblique edges (i.e, $\frac{\pi}{4} \leftrightarrow \frac{5\pi}{4}$, $\frac{3\pi}{4} \leftrightarrow \frac{7\pi}{4}$, $0 \leftrightarrow \pi$ and $\frac{\pi}{2} \leftrightarrow \frac{3\pi}{2}$) can be evaluated. The corresponding oblique gradients can be computed using Eqs. (6.40)-(6.43). I_c is utilized in Eqs. (6.40) and Eqs. (6.41). But, I_c is not considered in Eqs. (6.42) and (6.43).

$$\beta^1(j) = \arctan\left(\frac{\psi_n^1}{\psi_m^1}\right) = \arctan\left(\frac{I_1 - I_c}{I_2 - I_4}\right) \tag{6.36}$$

$$\beta^2(j) = \arctan\left(\frac{\psi_n^2}{\psi_m^2}\right) = \arctan\left(\frac{I_3 - I_c}{I_2 - I_5}\right) \tag{6.37}$$

$$\beta^{3}(j)=\arctan\left(\frac{\psi_{n}^{3}}{\psi_{m}^{3}}\right)=\arctan\left(\frac{I_{6}-I_{c}}{I_{7}-I_{4}}\right) \tag{6.38}$$

$$\beta^{4}(j)=\arctan\left(\frac{\psi_{n}^{4}}{\psi_{m}^{4}}\right)=\arctan\left(\frac{I_{8}-I_{c}}{I_{7}-I_{5}}\right) \tag{6.39}$$

$$\beta^{5}(j)=\arctan\left(\frac{\psi_{n}^{5}}{\psi_{m}^{5}}\right)=\arctan\left(\frac{I_{2}+I_{7}-2\times I_{c}}{I_{4}+I_{5}-2\times I_{c}}\right) \tag{6.40}$$

$$\beta^{6}(j)=\arctan\left(\frac{\psi_{n}^{6}}{\psi_{m}^{6}}\right)=\arctan\left(\frac{I_{1}+I_{8}-2\times I_{c}}{I_{3}+I_{6}-2\times I_{c}}\right) \tag{6.41}$$

$$\beta^{7}(j)=\arctan\left(\frac{\psi_{n}^{7}}{\psi_{m}^{7}}\right)=\arctan\left(\frac{I_{2}-I_{7}}{I_{4}-I_{5}}\right) \tag{6.42}$$

$$\beta^{8}(j)=\arctan\left(\frac{\psi_{n}^{8}}{\psi_{m}^{8}}\right)=\arctan\left(\frac{I_{1}-I_{8}}{I_{3}-I_{6}}\right) \tag{6.43}$$

Fig. 6.15 (k) considers all the neighbors of I_c and evaluate a combined gradient filter. It evaluates radial oblique edges. The corresponding oblique gradient filter is defined as:

$$\beta^{9}(j)=\arctan\left(\frac{\psi_{n}^{9}}{\psi_{m}^{9}}\right)=\arctan\left(\frac{\sum_{k=1}^{8}(I_{c}-I_{k})}{8}\right) \tag{6.44}$$

The oblique gradients (β) of an image are evaluated using Eqs. (6.36)-(6.44). The arctangent function ($\arctan(.)$) is used to evaluate $\beta^{s}(m,n)$. $\arctan(.)$ can prevent $\beta(m,n)$ from increasing or decreasing too quickly when I becomes larger or smaller. Therefore, the pixel values of I are normalized to $[0,255]$. The range of pixel angle in orientation image ($\theta(m,n)$) is limited to $(\frac{-\pi}{2},\frac{\pi}{2})$.

Eq. (6.43) is used to evaluate the oblique gradient channel prior from an input image. As, Eq. (6.43) compose all possible oblique edges in an input image (see Figure 3fig:2 (k)). To evidently proof it, we have considered the depth map analysis of a tree hazy image. Fig. 6.16 shows the effect of various oblique gradient based depth maps computed using Eqs. (6.36)-(6.44). Fig. 6.16 (a) shows the input hazy image. Figs. 6.16 (b)-(j) represent the effect of various depth maps. The depth map shown in Figs. 6.16 (b)-(j) are not so effective for evaluating the transmission map and atmospheric light. It is found that the combined oblique gradient filter has an ability to evaluate depth map in a more efficient way (see Fig. 6.16 (j)).

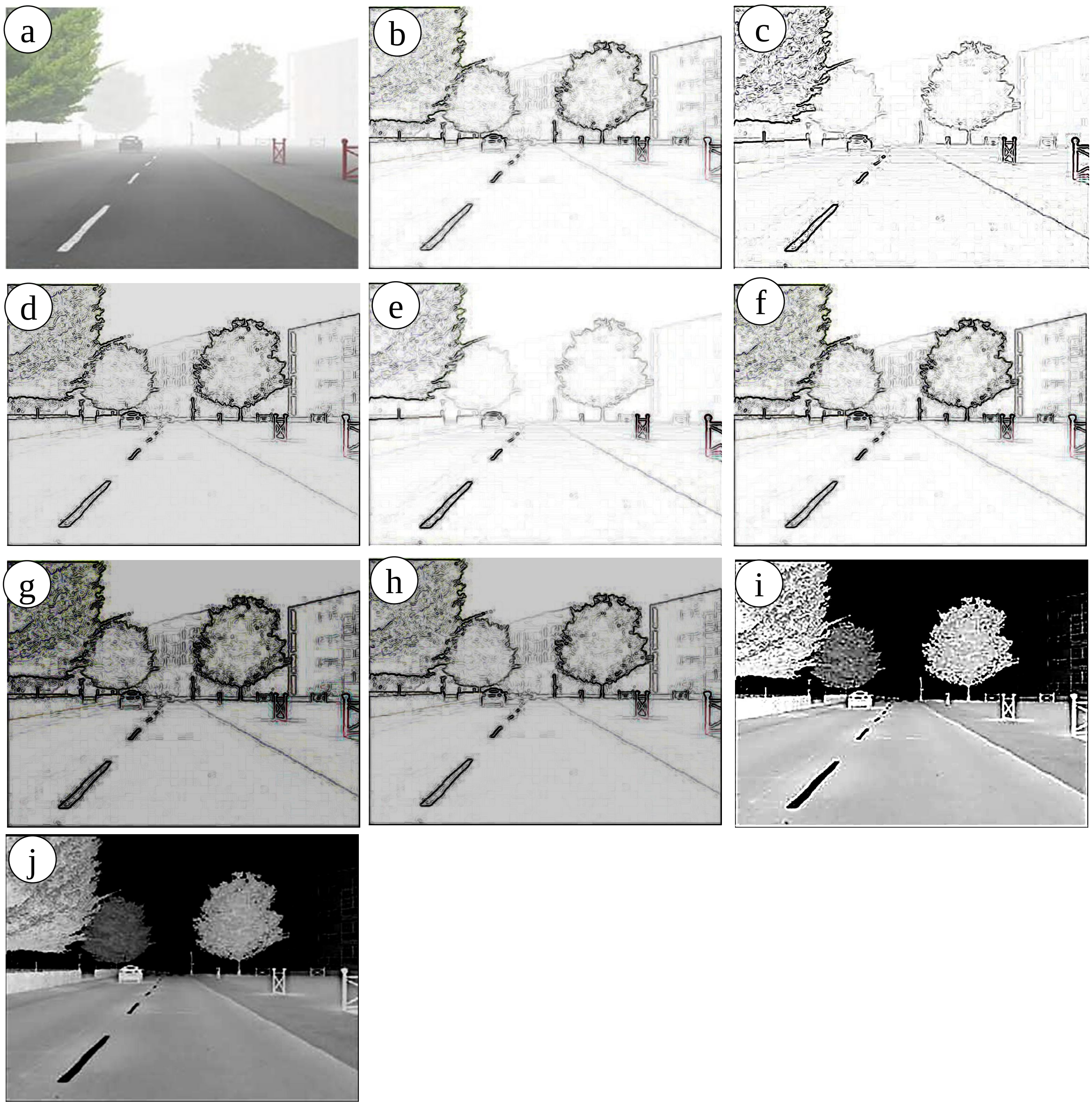

Figure 6.16: Oblique gradients based depth map (a) Input hazy image, (c) - (j) Depth map evaluated from Eqs. (6.36)-(6.44)

To evaluate the effectiveness of the oblique gradient profile prior on outdoor images, 500 haze free images are selected for experimentation. These images are resized to 512×512 pixels. Afterward, their oblique gradient profile channel images with a patch size of 7×7 pixels have been evaluated.

Figure 6.17 shows haze free images along with their respective oblique gradient profile prior. Figure 6.17 (c) shows the intensity histogram over all 500 oblique gradient profile channels.

It has been observed that the intensity of approximately 78 % of the pixels in the oblique gradient profile channels is under 20 and the intensity greater than 92 % of the pixels is under 40. These experimental analyses show that the oblique gradient profile prior is applicable for outdoor images. However, for images captured in the hazy environment, the oblique gradient profile channel turns out to be invalid. Affected from the additive airlight, pixels in haze affected segments have maximum intensity values in all color channels and the minimal intensity of local masks is maximum. Thus, the oblique gradient profile channel of a hazy image will have maximum intensity in regions with higher haze. Visually, the intensity of oblique gradient profile channel is a rough approximation of thickness of haze.

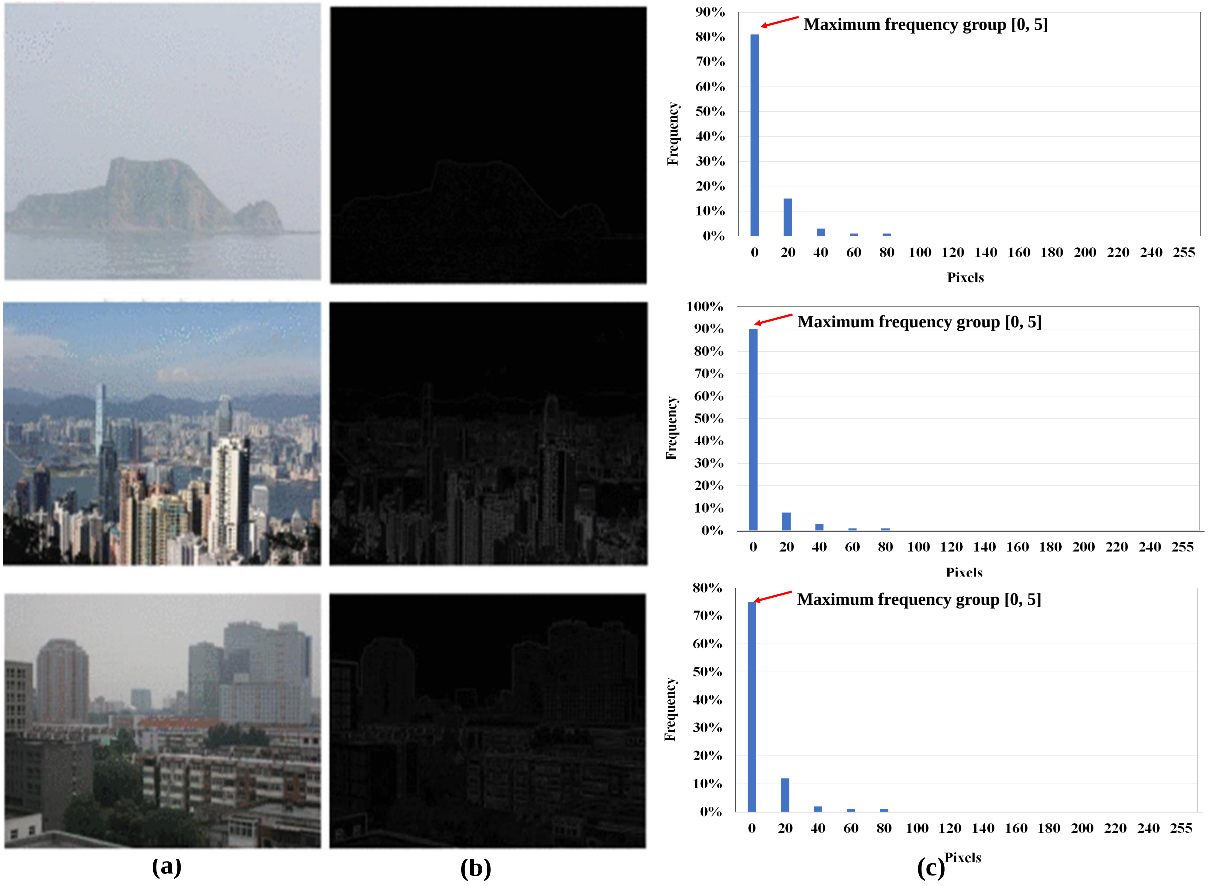

Figure 6.17: (a) Outdoor images and (b) Equivalent oblique gradient profile prior channels and (c) Histogram of the intensity of pixels in all 500 oblique gradient profile channels (each bin has 20 intensity levels).

Figure 6.18 demonstrates the halo artefacts analysis of the existing and OGPP. Figure 6.18 (b) and (c) show the results (*i.e.,* transmission map and restored images, respectively) obtained using DCP. It clearly shows that the restored image obtained using DCP has certain artefacts. Figure 6.18 (d) and (e) show the outcomes of OGPP (*i.e.,* transmission map and restored images, respectively). It is observed that OGPP provides a significantly better-restored image with a lesser number of halo artefacts.

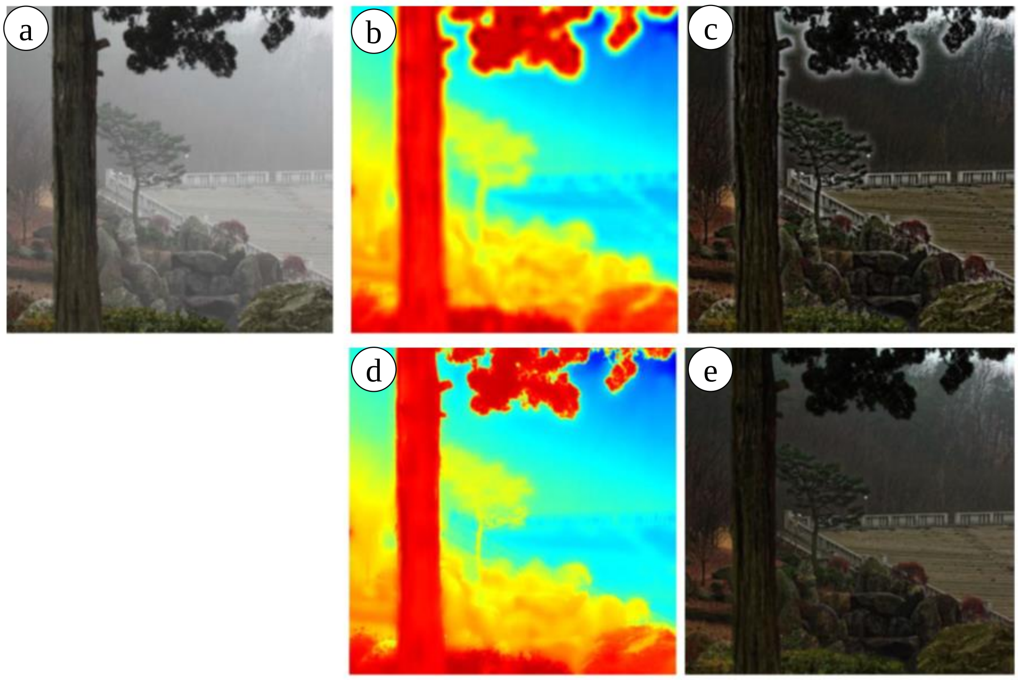

Figure 6.18: Halo artefacts in the restored images (a) Hazy image, (b) Transmission map, and (c) Restored images obtained using DCP, (d) Transmission map obtained, and (e) Restored images using OGPP

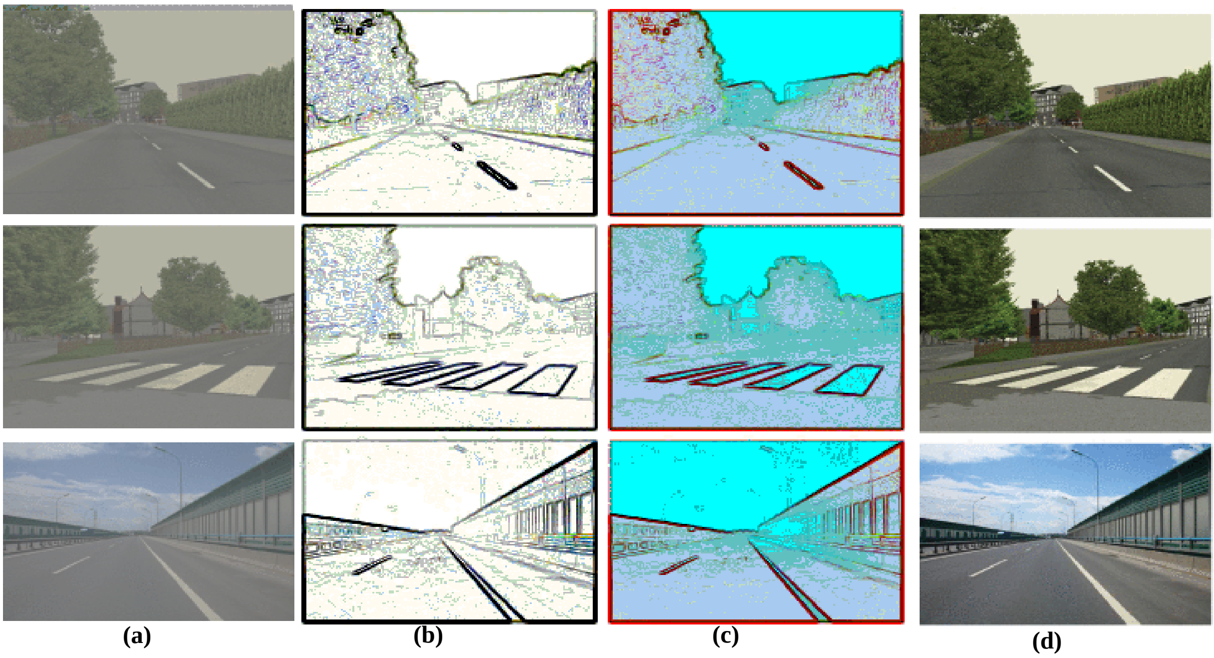

Figure 6.19: Analysis of oblique gradient profile prior (a) Input images, (b) Evaluated oblique gradient profile map, (c) Transmission map analysis and (d) Restored images obtained from oblique gradient profile prior

Figure 6.19 shows the analysis of the oblique gradient profile prior. Figure 6.19 (a) shows input hazy images. The evaluated oblique gradient profile prior and transmission map obtained using OGPP are shown in Figures (b) and (c), respectively. The restored images obtained using OGPP are shown in Figure (d). It is observed that OGPP provides efficiently restored images with significant preservation of colors and edges.

B. Atmospheric light estimation

The estimation of atmospheric light (Υ) is the second step of haze removal technique (For more detail please see Section 1.3.2). From Eq. (1.1), the airlight (Υ) becomes more dominant as the distance between object and camera increases. The haze formation model demonstrates that two objects with different radiant energy, placed at the similar distance from the camera, have same value of Υ [44]. As observed by Narasimhan and Nayar [24], Υ is best evaluated in the most haze-opaque segments. The pixel with maximum oblique gradient in I_r is called global atmospheric light. The highest gradient values are used to estimate Υ.

$$\Upsilon(j) = I\left(\max_c\left(\beta_j^c\right)\right) \tag{6.45}$$

C. Transmission map estimation

This sub-section describes the estimation of transmission map (t). To evaluate t, I is normalized by Υ. Assume that Υ is known. Therefore, Eq. (1.1) can be redefined as:

$$\frac{I^c(j)}{\Upsilon^c} = \frac{t(j){I_r}^c(j)}{\Upsilon^c} + 1 - t(j) \tag{6.46}$$

Assume t in local path ($\Psi(j)$) be constant. The mathematical computation of t is defined as $\tilde{t}(j)$. Apply oblique gradient profile prior on both sides of Eq. (6.46). Similarly, apply gradient operators on both sides.

$$\beta_y\left(\beta_c\frac{I^c(y)}{\Upsilon^c}\right) = \tilde{t}(j)\beta_y\left(\beta_c\frac{{I_r}^c(y)}{\Upsilon^c}\right) + 1 - \tilde{t}(j) \tag{6.47}$$

Here, $y \in \Psi(j)$. $\tilde{t}(j)$ is a constant value. Thus, $\tilde{t}(j)$ can be placed outside of β. c shows color channel of I. The oblique gradient profile prior of I_r approaches toward zero. It is represented as $\beta(O)(j)$. It is defined as:

$$\beta(O)(j) = \beta_y\left(\beta_c{I_r}^c(y)\right) = 0 \tag{6.48}$$

As $\Upsilon^c \in \mathbb{R}$, it results in:

$$\beta_y\left(\beta_c\frac{{I_r}^c(y)}{\Upsilon^c}\right) = 0 \tag{6.49}$$

where $\beta_y\left(\beta_c\frac{I_r{}^c(y)}{\Upsilon^c}\right)$ is the oblique gradient of normalized haze free image $\frac{I_r{}^c(y)}{\Upsilon^c}$.

Putting Eq. (6.49) into Eq. (6.47), the multiplicative term can be discard and $\tilde{t}$ is evaluated as:

$$\tilde{t}(j) = 1 - \beta_y\left(\beta_c\frac{I^c(y)}{\Upsilon^c}\right) \tag{6.50}$$

It has been observed that the main issue with DCP is that the color of sky in I is identical to Υ. In sky region, $\beta_y\left(\beta_c\frac{I^c(y)}{\Upsilon^c}\right)$ approaches toward one. Thus, $\tilde{t}$ approaches toward zero. Thus, the estimated t by utilizing oblique gradient profile prior, *i.e.,* Eq. (6.50) is able to handle sky and non-sky regions. Therefore, there is no requirement to handle the brighter segments. If we restore hazy image completely, then the restored image may appear artificial. Thus, some amount of haze is allowed using a lower bound ($\rho \in [0,1]$). Eq. (6.50) can be redefined as:

$$\tilde{t}(j) = 1 - \rho \times \beta_y\left(\beta_c\frac{I^c(y)}{\Upsilon^c}\right) \tag{6.51}$$

D. Coarse atmospheric light estimation

This sub-section describes the coarse atmospheric light estimation ($\Upsilon(j)$). Initially, $\Upsilon(j)$ is computed as follows [181]:

$$\Upsilon(j) = 1 - \tilde{t}(j) \tag{6.52}$$

From Eqs. (6.51) and (6.52), the normalized value of $\Upsilon(j)$ can be rewritten as:

$$\Upsilon(j) = \beta_y\left(\beta_c\frac{I^c(y)}{\Upsilon^c}\right) \tag{6.53}$$

The estimation of $\Upsilon(j)$ is achieved by considering β on object $\frac{I^c(y)}{\Upsilon^c}$, it results in $\Upsilon(j)$'s discontinuity even if no unexpected depth discontinuities occur. To remove the issue of halo artefacts with restored images, an efficient filter is required to estimate $\Upsilon(j)$.

$$\Upsilon^c(j) = \Upsilon(1 - t(j)) \tag{6.54}$$

Also, $t(j)$ is estimated as:

$$t(j) = \beta_c(I^c(j)) \tag{6.55}$$

Here, the value of $\Upsilon \in [0,\ t]$. Hence, it does not affect the grayscale image. Therefore, a local activity-tuned filter is used in this research work to refine a transmission map ($\tilde{t}$).

In this section, we will discuss variants of diffusion filter which can be used to refine transmission map (t). Zhao *et al.* [182] designed Local activity-tuned filter to refine t.

E. Modified anisotropic diffusion

Anisotropic diffusion is a well-known image filter. It utilizes the concept of heat equation with respect to iterations (i) as [183]:

$$\frac{\partial t}{\partial i} = \nabla \cdot (\nabla t) \tag{6.56}$$

Here, ∇t represents the gradient of transmission map (t). $\nabla \cdot (\nabla t)$ represents the divergence of ∇t. Thus, diffusion will come in action whenever the divergence is nonzero. Eq. (6.56) has the same diffusion strength in every direction. However, anisotropic diffusion based image filter suffers from edge degradation issue. To overcome this issue, Perona-Malik designed a anisotropic diffusion filter [184]:

$$\frac{\partial t}{\partial i} = \nabla \cdot (d(||\nabla t||)\nabla t), \tag{6.57}$$

Here, $d(||\nabla t||)$ represents an edge-stop function such that no diffusion happens across the edges.

In [184], two gradient based edge-stop functions are defined as:

$$d(||\nabla t||) = e^{-(\frac{||\nabla t||}{\rho})^2} \tag{6.58}$$

$$d(||\nabla t||) = \frac{1}{1+(\frac{||\nabla t||}{\rho})^2} \tag{6.59}$$

Here, ρ controls the strength of $d(||\nabla t||)$.

The discrete form of Eq. (6.57) can be rewritten as:

$$t_m^{i+1} = t_m^i + \delta \sum_{n \in \mathbb{N}_{b_m}} d(||\nabla t_{mn}^i||)\nabla t_{mn}^i, \tag{6.60}$$

Here, δ adjusts the convergence speed. i represents iteration number. ∇t_{mn}^i shows the gradient between t_m and t_n pixels in the neighboring $\mathbb{N}_{b_m}$ around pixel t_m.

In [185], the local intensity variance is utilized to adapt the diffusion process as:

$$t_m^{i+1} = t_m^i + \delta \sum_{n \in \mathbb{N}_{b_m}} e^{-\left(\frac{||\nabla t_{mn}^i||}{d_{f_{mn}}}\right)^2} \nabla t_{mn}^i \tag{6.61}$$

$$d_{f_{mn}} = d_{f_{max}} - \sigma_{mn}^2 \frac{d_{f_{max}} - d_{f_{min}}}{max(\sigma^2)}, \tag{6.62}$$

Here, $d_{f_{mn}}$ represents the diffusion parameter. σ_{mn}^2 shows the local variance around pixel t_m^0 in the initial t. $max(\sigma^2)$ represents the maximal value of the variance. $d_{f_{max}}$ and $d_{f_{min}}$ represent maximal and minimal of $d_{f_{mn}}$, respectively. This filter has an ability to refine

t in an efficient manner without degrading the edges. However, it utilizes the variance of t. It is not effective because the initial images variance cannot catch up with the updated diffused t's information. An anisotropic diffusion filter is designed by Chao *et al.* [186].

$$t_m^{i+1} = t_m^i + \delta \sum_{n \in \mathbb{N}_{b_m}} e^{-\left(\frac{||\nabla t_{mn}^i|| d_{f_{m,i}}^2}{\rho}\right)^2} \nabla t_{mn}^i \tag{6.63}$$

$$d_{f_{m,i}}^2 = 1 + \frac{\vartheta_{m,i} - min(\vartheta_i)}{max(\vartheta_i) - min(\vartheta_i)} \cdot 254, \tag{6.64}$$

Here, $max(\vartheta_i)$ and $min(\vartheta_i)$ are the maximal and minimal variance of the diffused t at i^{th} iteration. $\vartheta_{m,i}$ is the variance of m^{th} pixel. It incorporates both local gradient and variance to preserve edges and significant information while effectively refining t. Note that Eqs. (6.61) and (6.62) utilize the ratio of gradient and variance, whereas Eqs. (6.63) and (6.64) utilize their product.

Zhao *et al.* [182] proved that the depth images are characterized by smooth regions with sharp edges. However, anisotropic diffusion based refinement of t suffers from halo and gradient reversal artefacts [182]. Therefore, a local activity-tuned anisotropic diffusion based filter is used in this thesis. It is defined as [182]:

$$\frac{\partial t}{\partial i} = \nabla \cdot (d(||\nabla t||, t_k) \nabla t) \tag{6.65}$$

Here, t_k is evaluated using the local activity of t. The discrete version of Eq. (6.61) can be rewritten as:

$$t_m^{i+1} = t_m^i + \delta \sum_{n \in \mathbb{N}_{b_m}} d(||\nabla t_{mn}^i||, t_{k_m}^i) \nabla t_{mn}^i \tag{6.66}$$

Here, $t_m^0 = t_m$ in the first iteration, $t_{k_m}^i$ is a clipped and normalized local activity. Motivated from Zaz *et al.* [185], two new edge-stop functions are defined as:

$$d(||\nabla t_{mn}^i||, t_{k_n}^i) = e^{-\left(\frac{||\nabla t_{mn}^i||}{\rho_1 t_{k_m}^i}\right)^2} \tag{6.67}$$

$$d(||\nabla t_{mn}^i||, t_{k_n}^i) = e^{-\left(\frac{(||\nabla t_{mn}^i||)^2}{(\rho_2)^2 t_{k_m}^i}\right)} \tag{6.68}$$

Here, ρ_1 and ρ_2 are diffusion parameters. Note that $t_{k_m}^i$ squared in Eq. (6.67), but not in Eq. (6.68).

Similar to Eq. (6.57), the ratio of the gradient and local activity are utilized. It can capture the filtering artefacts exist in t. Moreover, the diffusion parameter is adaptively tuned according to the ratio such that larger diffusion parameters are assigned to more severely distorted pixels. Therefore, the pixels with larger local activity would receive

more diffusion from neighboring pixels than the pixels with smaller activity under the control of gradient. It will overcome halo and gradient reversal artefacts.
The local mean ($\bar{t}^i_m$) and standard variation (v^i_m) of 8-connected neighborhood around each pixel are computed as:

$$\bar{t}^i_m = \frac{1}{9}(t^i_m + \sum_{n \in \mathbb{N}_{b_m}} t^i_n) \tag{6.69}$$

$$v^i_m = \left[\frac{1}{9}((t^i_m - \bar{t}^i_m)^2 + \sum_{n \in \mathbb{N}_{b_m}} (t^i_n - \bar{t}^i_m)^2) \right]^{0.5} \tag{6.70}$$

Next, a clipped version of v^i_m (i.e, $t^i_{v_m}$) is obtained as:

$$t^i_{v_m} = \begin{cases} 0.5, & \text{if } 0 \leq v^i_m < 0.5 \\ v^i_m, & \text{if } 0.5 \leq v^i_m < g \\ g, & \text{if } g \leq nu^i_m, \end{cases} \tag{6.71}$$

Here, g is a predefined parameter.
Thereafter, $t^i_{v_m}$ is normalized by $max(t^i_v)$ in Eq. (6.72), which is the maximal value across t.

$$\bar{t}^i_{v_m} = \frac{t^i_{v_m}}{max(t^i_v)} \tag{6.72}$$

To make the iteration more stable, $t^i_{k_m}$ is updated from $\bar{t}^i_{v_m}$ for every p iterations.

$$t^i_{k_m} = \begin{cases} \bar{t}^i_{v_m}, & \text{if } (i\%p) = 0 \\ \bar{t}^{i-(i\%p)}_{v_m}, & \text{if } (i\%p) \neq 0 \end{cases} \tag{6.73}$$

Let q be the maximum number of iterations. The updating interval (p) is chosen as $p \in [1, q]$.

The fixed local activity-tuned anisotropic diffusion using Eq. (6.67) as edge-stop function is denoted as FLAT-AD. The time-updated local activity-tuned anisotropic diffusion Eq. (6.67) is denoted as TLAT-AD. Periodically local activity-tuned anisotropic diffusion based on edge-stop function of Eq. (6.67) is denoted as PLAT-AD. Moreover, Eq. (6.68) is utilized, the three other techniques are denoted as $FLAT-AD(t)$, $TLAT-AD(t)$, and $PLAT-AD(t)$, respectively.
When p is set to be 1, it becomes TLAT-AD. If $1 \leq p \leq q$, then it reduces to PLAT-AD. If p is set to be q, then it becomes FLAT-AD.

Since the difference between neighboring pixel's variance is relatively greater than the difference of the corresponding standard deviation. If 8-connected activity is larger than 0.5, then standard variation is considered instead of variance. Let v_a and v_b represent two standard deviations. We assume that $v_a \geq 0.5$, $v_b \geq 0.5$, and $v_a > v_b$. We look at the difference $(v_a - v_b) - (v_a^2 - v_b^2) = (v_a - v_b)[1 - (v_a + v_b)]$. Based on the above assumptions, $1 - (v_a + v_b) \leq 0$ and $v_a - v_b > 0$. Therefore, $(v_a - v_b) - (v_a^2 - v_b^2) \leq 0$, *i.e.*, $(v_a - v_b) \leq (v_a^2 - v_b^2)$.

In this filter, the local activity is leveraged which makes the relative impacts more efficient. To achieve fast refinement of t, only 3×3 patch centered at pixel D_m is used to obtain 8-connected standard deviation v_m instead of the variance. Because, if the variance is used, then the small variance can be easily dominated by large variance and will have a little contribution towards diffusion. A clipped function is also used for local action to make diffusion stable during anisotropic diffusion because of the pixels with very large local activity render local activity-tuned anisotropic diffusion useless for pixels with smaller local activity measurement. During the iterative diffusion, the updated activity is used to control the degree of diffusion.

F. Restoration model

The last step of haze removal technique is restoration model. It restores I_r from I. It is an ill-posed problem because only I is available in prior [179]. Therefore, it requires an efficient estimation of Υ and t [104]. The estimation of Υ and t will be done with the help of OGPP. Therefore, I_r can be computed as [16]:

$$I_r(j) = \frac{I(j) - \Upsilon}{t(j)} + \Upsilon \tag{6.74}$$

However, the restored image (I_r) suffers from noise when t approaches toward zero. Also, if the haze is restored completely, then I_r may be seen as an artificial image. The lower bound (x_0) is introduced to allow some haze in Υ and I_r. Therefore, t has been constrained with the help of x_0. According to related work, x_0 is experimentally set to 0.1 [16]. Therefore, I_r can be rewritten as:

$$I_r(j) = \frac{I(j) - \Upsilon}{\max(\tilde{t}(j), x_0)} + \Upsilon \tag{6.75}$$

6.2.2 Performance analysis

In order to demonstrate the effectiveness of OGPP, it is tested on 9 hazy dataset of synthetic images and 200 real-life images. Table 6.1 provides detail of various standard hazy image datasets and real-life images used for experimental purpose. Majority of datasets contain synthetic hazy images. These datasets are Realistic single image restoration (RESIDE) [187], Foggy road image database (FRIDA) [188], Foggy road image database 2(FRIDA2) [189], Waterloo IVC restored image database [190], and D-HAZY [191]. Additionally, some real-life hazy images are also used for experimental purpose.

Table 6.1: Hazy images used

Dataset	Description	Number of images
RESIDE (ITS)	ITS (Indoor Training Set)	50
RESIDE (OTS)	OTS (Outdoor Training Set)	50
RESIDE (SOTS)	SOTS (Synthetic Objective Testing Set)	50
RESIDE (RTTS)	RTTS (Real-world Task-Driven Testing Set)	50
RESIDE (HSTS)	HSTS (Hybrid Subjective Testing Set)	20
FRIDA	Foggy Road Image Database	90
FRIDA2	Foggy Road Image Database 2	120
IVC	Waterloo IVC restored image database	25
D-HAZY	Dataset to evaluate restoration algorithms	100
Real-life	Real-life images	200

OGPP is compared with seven competitive restoration techniques such as DCP [16], LTQ [148], MDF [108], GITF, IVRM, FPDETF, and WHDR [33]. The quantitative evaluations are assessed by using the different metrics such as Contrast gain (C_g), Percentage of saturated pixels (ρ), visible edges ratio [66], Perceptual haze density (D_h) [67], Peak signal to noise ratio ($PSNR$), Structural similarity index metric ($SSIM$) and Execution time (ET). The mask size of oblique gradient profile prior is set to be 3×3 pixels as discussed in Section 3. The parameters setting of the existing restoration techniques are set as they are recommended by their respective researchers.

A. Experimentation 1: Transmission map estimation

Fig. 6.20 (a) shows the input hazy image, *i.e.,* Tree hazy image. Fig. 6.20 (b) shows the refined transmission map obtained from DCP [16]. It is observed that DCP [16] has over-smoothed transmission map. Therefore, the restored image of this transmission map may have halo artefacts, color, and edge distortion problems. Figs. 6.20 (c) and 6.20 (g) depict the transmission map evaluated from LTQ [148] and FPDETF based restoration techniques. These maps have significant details. Therefore, the restored image obtained using these maps will not suffer from halo artefacts, color, and edge distortion problems. However, these maps do not have enough texture detail.

From Figs. 6.20 (d) and 6.20 (f), it can be seen that the refined transmission map images obtained from MDF [108] and IVRM have significant information to restore hazy images in an efficient manner. These techniques produce saturated restored images. Therefore, these techniques are unable to preserve the colors of an image.

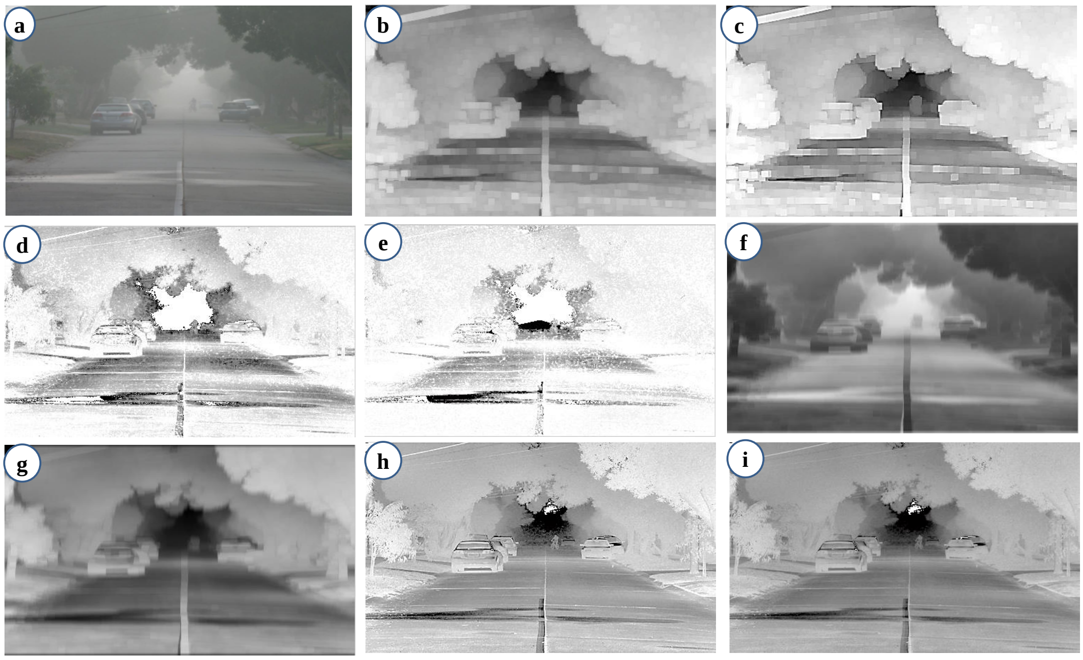

Figure 6.20: Refined transmission map of haze removal techniques for road hazy image (a) Input hazy image, (b) DCP, (c) LTQ, (d) MDF, (e) GITF, (f) IVRM, (g) FPDETF, (h) WHDR, and (j) OGPP.

The refined transmission map obtained from GITF and WHDR [33] are shown in Figs. 6.20 (e) and 6.20 (h), respectively. It is observed that the restored images using these transmission maps may suffer from sky regions and texture preservation problems. Fig. 6.20 (j) shows refined transmission map obtained from OGPP. It is observed from this figure that the oblique gradient profile prior achieves a remarkably refined transmission map than the above-mentioned techniques. It has a significant edge and texture information of objects. Therefore, the restored image using this map has a lesser number of halo artefacts, edge degradation, and color distortion rate. Also, the restored image has significant texture information.

Fig. 6.21 shows the results obtained from a OGPP. Figs. 6.21 (a), (b), and (c) show input hazy images, *i.e.,* Hill-hazy image, Road-hazy image, and Persons-hazy image, respectively. From Figs. 6.21 (d), (e), and (f), it is observed that the transmission maps are efficiently obtained by using OGPP. These transmission maps are efficiently refined using local activity-tuned anisotropic diffusion based image filter (see Figs. 6.21 (g), (h) and (j)). It can be seen from these figures that the edge and gradient information is significantly preserved. The restored images are shown in Figs. 6.21 (j)-(l).

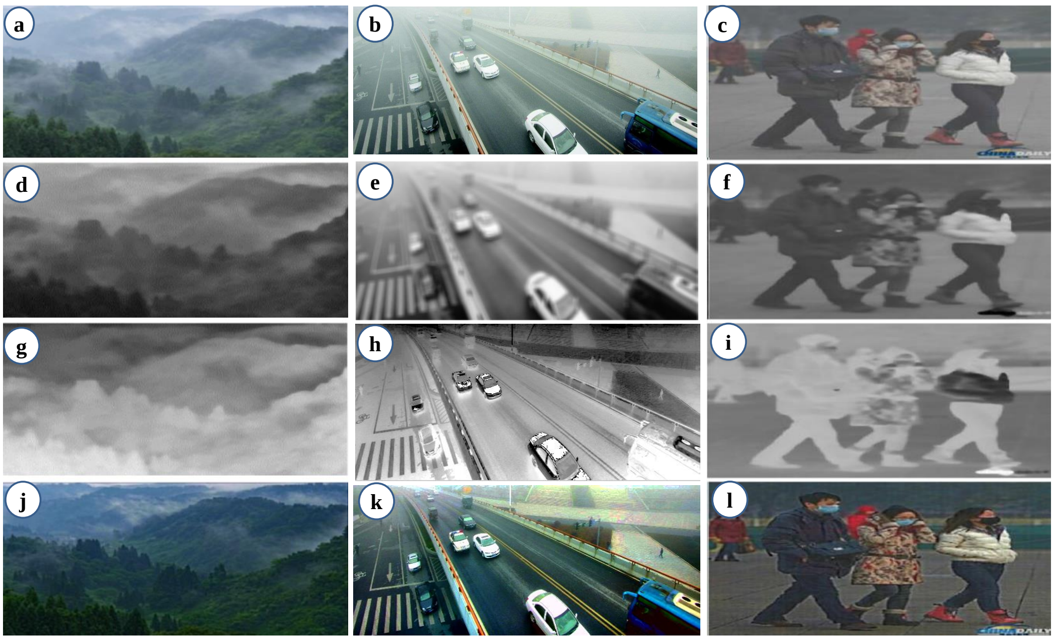

Figure 6.21: Results obtained from OGPP (a)-(c) Input hazy images, (d)-(f) Depth maps obtained using oblique gradient profile prior, (g)-(j) Refined transmission map obtained from local activity-tuned anisotropic diffusion, and (j)-(l) Restored images.

B. Visual analysis of synthetic images

Figure 6.22 shows the visual results of REalistic Single Image Restoration (RESIDE) [187] dataset's image of Hybrid subjective testing set (HSTS) image. From Figures 6.22 (b)-(g), it is observed that the restored images suffer from sky-region and pixel saturation problems. Also, Figures 6.22 (b)-(h) suffer from halo and gradient artefacts problems.

Figures 6.22 (b)-(h) shows that the images obtained from the existing restoration techniques. It is seen that these techniques restore the dense haze in the region of distant objects. However, fewer haze remains in the restored images obtained form DCP [16], LTQ [148], MDF [108], GITF, IVRM, FPDETF, (see Figure 6.22 (b) - (e)).

Figures 6.22 (g) and (h) shows significant results as compared to Figures 6.22 (b) and (g), but, they suffer from the over-enhancement in the sky region where noise is significantly amplified.

Figure 6.22 (j), it is observed that OGPP provides significantly better restore results with the lesser number of artefacts as the sky in the image is more clear and details of the distant objects are enhanced moderately. Also, the restored image obtained from OGPP does not suffer from sky-region and saturation problems. In Figure 6.22 (j), it is found that the ringing and color aliasing artefacts around the depth edges are removed while the fine structure is well-restored as compared to the results obtained from the existing techniques.

Figure 6.22: Haze removal techniques for tree image (a) Input image (b) DCP, (c) LTQ, (d) MDF, (e) GITF, (f) IVRM, (g) FPDETF, (h) WHDR, and (j) OGPP.

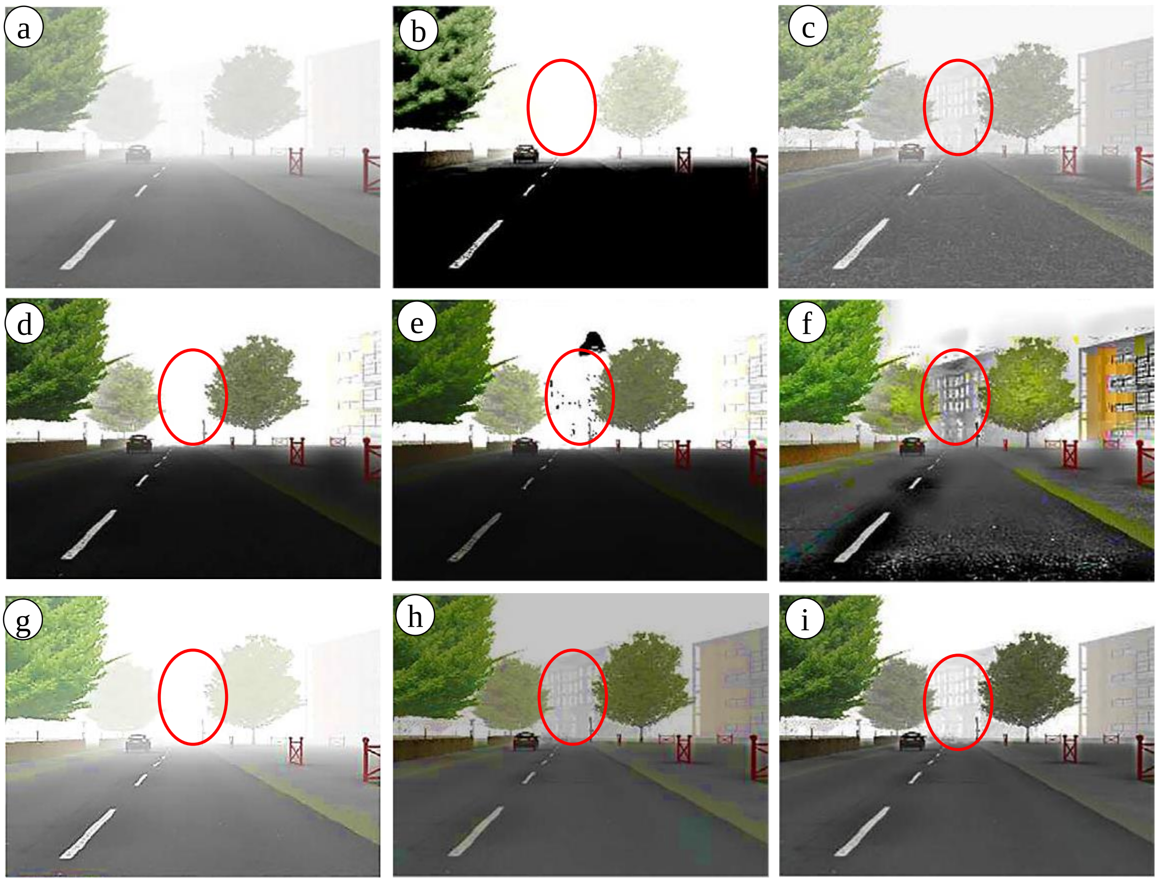

Figure 6.23: Haze removal techniques for synthetic image (a) Input image (b) DCP, (c) LTQ, (d) MDF, (e) GITF, (f) IVRM, (g) FPDETF, (h) WHDR, and (j) OGPP.

Figure 6.23 demonstrates the visual analysis of OGPP and the existing restoration techniques on FRIDA dataset's synthetic image. Although, these results contain a lesser number of artefacts, the image details have become blurred. The sky region and distant objects are over-saturated and become less visible as shown in Figure 6.23 (b), (d), (e), (g) and (h). It is observed from Figure 6.23 (j) that OGPP provides quite significant spatial and spectral information as compared to the existing techniques. From Figure 6.23 (j), it can be seen that OGPP provides a lesser number of halo and gradient reversal artefacts. Additionally, OGPP shows a lesser number of saturated pixels. Marked areas with red circles show the building in the restored image. Among these images, OGPP provides significantly better texture information.

Figure 6.24: Haze removal techniques for tree image (a) Input image (b) DCP, (c) LTQ, (d) MDF, (e) GITF, (f) IVRM, (g) FPDETF, (h) WHDR, and (j) OGPP.

Figure 6.24 shows the visual analysis of OGPP and the existing restoration techniques on FRIDA 2 dataset's synthetic image. It is found that OGPP provides a lesser number of halo and gradient reversal artefacts. Also, OGPP shows the lesser number of saturated pixels. Marked areas with red ovals demonstrate buildings in the restored images. In the case of Figure 6.24 (g) and (h) far away buildings are visible but surrounded by severe ringing artefacts. However, these results are suppressed effectively in the restored image obtained from OGPP (Figure 6.24 (j)). OGPP provides significantly good texture information and a lesser number of ringing artefacts.

C. Visual analysis of real-world hazy image

Figure 6.25 shows the visual analysis of OGPP and the existing image restoration techniques on a real-life hazy image. It is observed that the existing techniques suffer from color distortion and pixel saturation issues. Figure 6.25 (h) shows more natural restored images. But, it suffers from the bluish artefact issue. The restored image obtained from OGPP provides significantly better results as compared to the existing techniques. It shows good spatial and spectral information.

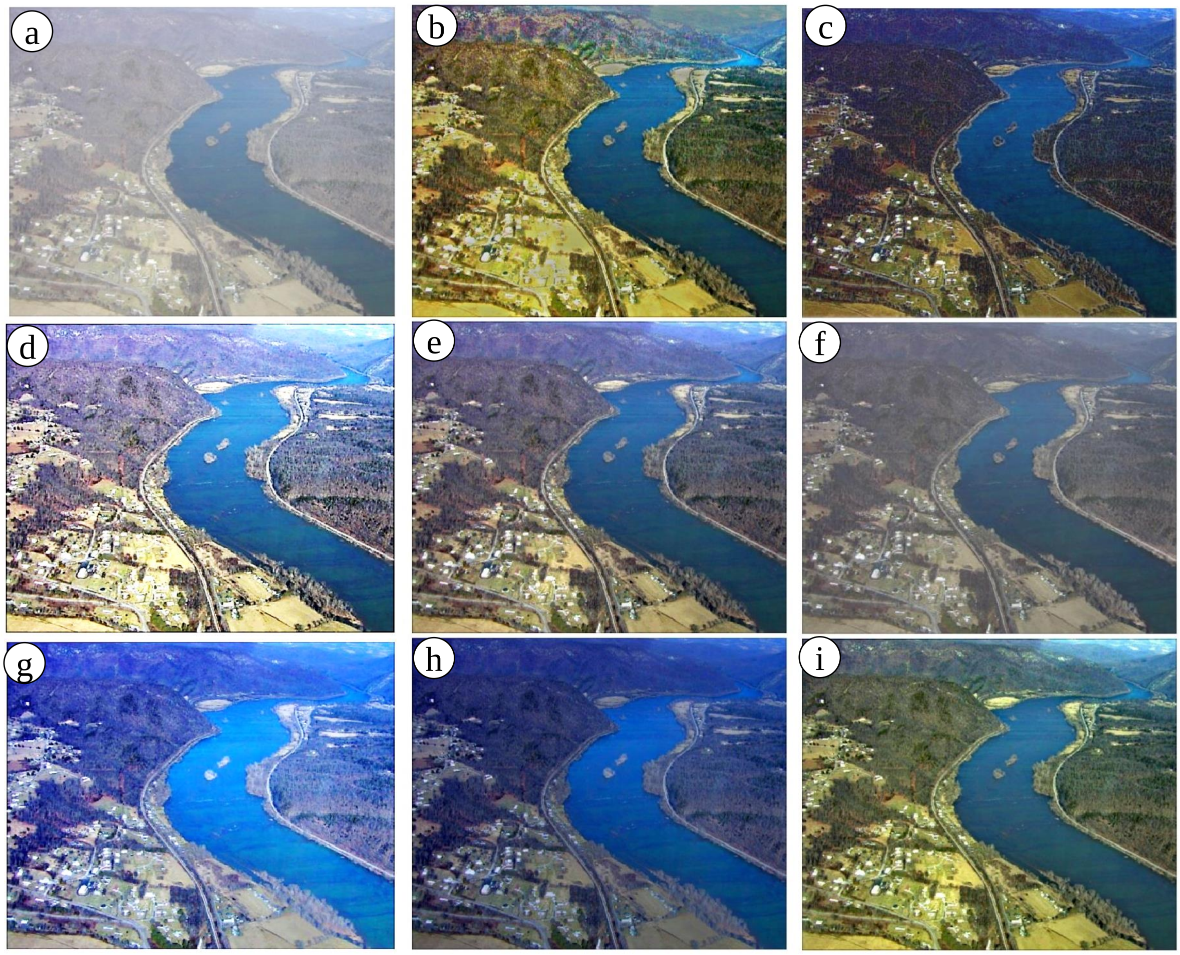

Figure 6.25: Haze removal techniques for real-life lake image (a) Input image (b) DCP, (c) LTQ, (d) MDF, (e) GITF, (f) IVRM, (g) FPDETF, (h) WHDR, and (j) OGPP.

D. Experimentation 3: Quantitative analysis

In addition to visual observation, the quantitative analysis has also been done. The performance comparison of OGPP has been done with the existing haze removal techniques using acceptable quality metrics such as Percentage of saturated pixels (ρ), Visible edges ratio [66], Perceptual haze density (D_h) [67], Peak signal to noise ratio ($PSNR$) and Structural similarity index metric ($SSIM$), and Execution time (ET).

Percentage of saturated pixels (ρ) is a well-known measure to estimate the saturated pixels in the restored image.

Table 6.2: Experimental analysis of percentage of saturated pixels (ρ)

Dataset	DCP	LTQ	MDF	NIF	LTQ	GITF	WHDR	OGPP
ITS	0.1563	0.0433	0.0543	0.0872	0.0633	0.0522	0.0391	0.0181
OTS	0.1334	0.0624	0.0553	0.0493	0.0584	0.0463	0.0292	0.0131
SOTS	0.1614	0.1504	0.1725	0.0934	0.0843	0.0573	0.0353	0.0272
RITS	0.1505	0.1445	0.1614	0.0984	0.0803	0.0714	0.0513	0.0292
HSTS	0.1796	0.1375	0.1224	0.0814	0.0704	0.0422	0.0291	0.0111
FRIDA	0.1454	0.1344	0.1044	0.0573	0.0642	0.0492	0.0352	0.0131
FRIDA2	0.1594	0.1664	0.1044	0.0833	0.0783	0.0592	0.0362	0.0211
IVC	0.1133	0.0984	0.1023	0.0773	0.0672	0.0442	0.0622	0.0502
D-Hazy	0.1743	0.1633	0.1293	0.0882	0.0793	0.0532	0.0702	0.0291
Real-world	0.1815	0.1145	0.1445	0.0984	0.0454	0.0423	0.0532	0.0362

Table 6.2 shows the analysis of ρ which needs to be minimized. It can be seen from this table that the guided L_0 gradient minimization filter based haze removal technique has minimum ρ as compared to DCP [16], LTQ [148], MDF [108], GITF, IVRM, IVRM, and WHDR [33]. The average reduction in ρ by using OGPP than the existing techniques is approximately 0.0876.

The visible edges ratio image assessment technique [66] *i.e.,* ratio of new visible edges (e) and ratio of average gradient ($\bar{r}$) have been implemented to validate the effectiveness of OGPP.

Higher the values of e indicate that the edges of the restored images are more powerful. The maximum value of $\bar{r}$ shows the degree of edge and texture information of the restored image. Tables 6.3 and 6.4 show the guided L_0 gradient minimization filter based haze removal technique has more e and $\bar{r}$ as compared to DCP [16], LTQ [148], MDF [108], GITF, IVRM, IVRM, and WHDR [33]. Therefore, OGPP has more significant edges and texture information than the existing haze removal techniques.

Table 6.3: Comparative analysis of ratio of new visible edges (e)

Img	DCP	LTQ	MDF	NIF	GITF	GIF	WHDR	OGPP
ITS	1.1221	1.9247	2.1258	2.8527	2.5214	3.4627	3.5497	3.9378
OTS	1.2238	1.3941	2.3203	1.4572	1.7048	2.6098	3.1297	3.8868
SOTS	2.1441	2.5313	2.4694	3.2791	3.2596	3.4538	3.5218	4.0596
RITS	1.5419	1.6807	1.5928	1.4896	2.1676	2.2049	2.9538	3.2606
HSTS	2.3308	2.4994	2.3897	3.2282	3.1973	3.7241	4.1921	4.6704
FRIDA	1.1973	1.2751	1.6747	1.5931	2.9926	3.4721	3.9889	4.2771
FRIDA2	2.0974	2.1993	2.4179	2.6043	3.1129	3.6476	3.9381	4.3667
IVC	2.3662	2.5153	2.2843	3.0816	3.4502	3.3693	3.5291	4.5861
D-Hazy	1.7343	1.9929	2.1036	2.5918	2.9402	3.2981	3.8676	4.4948
Real-world	1.6846	1.9231	2.6817	2.9394	3.6782	3.7967	4.2145	4.7322

Table 6.4: Comparative analysis of ratio of average gradient $(\bar{r})$

Img	DCP	LTQ	MDF	NIF	GITF	GIF	WHDR	OGPP
ITS	0.9621	1.3032	1.2044	1.5343	1.7924	2.0815	2.7737	2.9326
OTS	1.3067	1.7089	1.9060	2.1627	2.3432	2.1053	2.4825	2.8067
SOTS	1.8645	1.7832	2.2157	2.3318	2.4028	2.6984	2.8821	2.9243
RITS	1.1097	1.3142	1.4215	1.9528	2.1440	2.6627	2.7184	2.8921
HSTS	1.1259	1.1864	1.3893	1.5668	1.8224	1.7235	1.9454	2.2856
FRIDA	0.9447	1.2040	1.2838	1.4516	1.6811	1.9285	2.3946	2.4812
FRIDA2	2.0841	2.1517	2.4838	2.6823	2.7882	3.0489	3.1454	3.8026
IVC	1.2334	1.6166	1.9041	2.1112	2.1888	2.4667	2.6232	2.8118
D-Hazy	1.5447	1.7623	1.9079	2.1034	2.2040	2.3969	2.5023	2.7427
Real-world	1.1524	1.2046	1.6990	1.9987	2.3034	2.4156	2.5950	2.7681

The no-reference perceptual haze density assessment metric (D_f) proposed by Choi *et al.* [67] is used to compare the proposed and the existing restoration technique. A lower value of D_h indicates significant restoration performance. It is observed from Table 6.5 that OGPP outperforms the existing restoration techniques for the majority of hazy images. The mean reduction in D_h by using OGPP over available techniques is approximately 0.0329.

Table 6.5: Analysis of perceptual haze density (D_h)

Img	Hazy	DCP	LTQ	MDF	NIF	LTQ	GITF	WHDR	OGPP
ITS	2.521	1.084	0.993	0.988	0.912	0.842	0.981	0.847	0.454
OTS	3.854	1.255	1.192	1.124	0.991	0.893	0.812	0.986	0.682
SOTS	2.408	1.194	1.125	1.293	1.042	0.991	0.892	0.858	0.795
RITS	2.824	1.485	1.297	1.492	1.423	1.294	1.285	1.225	1.024
HSTS	2.919	1.256	1.495	1.452	1.484	1.247	1.413	1.287	1.096
FRIDA	4.982	1.424	1.512	1.414	1.297	1.282	1.296	1.295	0.923
FRIDA2	2.523	1.244	1.482	1.523	1.222	1.197	1.282	1.189	0.863
IVC	3.229	1.225	1.494	1.282	1.286	1.127	1.045	0.981	0.764
D-Hazy	2.894	1.256	1.285	1.298	1.192	1.023	0.984	0.929	0.742
Real-world	2.813	1.295	1.214	1.282	1.128	1.017	0.893	0.768	0.693

Table 6.6 shows the Peak signal to noise ratio (*PSNR*) in decibels (dB) analysis of the existing techniques and OGPP by considering the five synthetic hazy images taken from RESIDE [187]. It can be seen from this table that the mean improvement in *PSNR* by using the OGPP over available techniques is approximately 1.1736.

Table 6.6: Analysis of peak signal to noise ratio in dB

Dataset	DCP	LTQ	MDF	NIF	LTQ	GITF	WHDR	OGPP
ITS	16.500	17.422	18.225	19.527	19.280	20.638	20.901	23.118
OTS	17.168	18.269	19.332	19.662	20.111	20.232	21.141	22.083
SOTS	16.262	17.327	17.162	18.407	19.586	19.988	21.215	22.566
RITS	18.337	18.111	19.429	17.163	19.217	20.268	20.683	21.439
HSTS	16.209	16.607	17.091	17.539	19.344	18.896	19.561	21.068
FRIDA	17.403	16.902	17.606	17.901	18.090	20.093	21.101	22.409
FRIDA2	18.201	18.403	17.969	19.110	18.495	20.729	20.992	22.120
IVC	18.083	18.345	18.899	19.405	19.860	20.089	20.398	21.481
D-Hazy	17.308	17.724	18.267	18.779	19.090	19.558	20.401	21.503
Real-world	16.316	16.684	17.529	18.020	18.495	18.849	19.245	20.400

Table 6.7 shows Structural similarity index (*SSIM*) analysis of the existing techniques and OGPP by considering five synthetic hazy images taken from RESIDE [187]. It is observed that the mean improvement in *SSIM* by using OGPP over available techniques is approximately 0.0179.

Table 6.7: Analysis of structural similarity index metric

Img	DCP	LTQ	MDF	NIF	LTQ	GITF	WHDR	OGPP
ITS	0.7830	0.8018	0.8166	0.8335	0.8293	0.8444	0.8643	0.8831
OTS	0.7956	0.8152	0.8376	0.8478	0.8624	0.8734	0.8341	0.8728
SOTS	0.7687	0.7891	0.7992	0.8159	0.8371	0.8671	0.8830	0.9114
RITS	0.7328	0.7944	0.7621	0.7852	0.8253	0.8314	0.8539	0.8815
HSTS	0.7528	0.7765	0.7449	0.7956	0.8039	0.8249	0.8422	0.8637
FRIDA	0.7638	0.7952	0.7549	0.7966	0.8009	0.8260	0.8441	0.8520
FRIDA2	0.8052	0.8243	0.8439	0.8285	0.8349	0.8644	0.8690	0.8883
IVC	0.7712	0.7750	0.7921	0.8041	0.8258	0.8469	0.8670	0.8933
D-Hazy	0.7819	0.8120	0.8235	0.8366	0.8514	0.8578	0.8676	0.8843
Real-world	0.7653	0.7824	0.7936	0.8020	0.8152	0.8364	0.8771	0.8889

Execution time (ET) is measured as the time (in seconds) taken to execute a given haze removal technique. All the images are resized to 1024×1024 pixels. The 'tic' and 'toc' operators in MATLAB script are used to compute ET.

Table 6.8: Experimental analysis of execution time (ET) in seconds

Img	DCP	LTQ	MDF	NIF	LTQ	GITF	WHDR	OGPP
ITS	98.8±7	8.6±2.8	8.5±1.9	7.9±0.8	6.7±0.5	7.5±1.1	1.8±0.2	1.7±0.2
OTS	86.9±5	9.6±1.9	8.7±2.4	7.1±0.9	7.6±0.9	6.1±1.0	1.6±0.9	1.7±0.3
SOTS	99.6±7	9.7±2.1	8.6±2.3	7.6±1.0	5.7±0.7	5.5±1.2	1.7±0.8	1.1±0.5
RITS	81.9±9	8.7±3.6	8.7±2.1	7.4±0.6	4.9±1.3	5.2±1.4	1.6±0.9	1.4±0.4
HSTS	85.8±4	8.6±3.2	8.6±1.9	4.6±1.1	7.3±0.7	5.9±1.4	1.7±0.6	1.2±0.3
FRIDA	98.6±5	9.1±2.3	9.8±3.6	7.3±0.6	7.2±1.1	6.1±0.8	1.9±0.8	1.6±0.5
FRIDA2	84.7±6	8.5±3.1	8.1±2.7	7.6±0.7	7.3±0.6	5.9±1.2	1.5±0.6	1.5±0.2
IVC	86.7±6	8.5±2.3	8.5±2.0	7.0±0.5	7.3±0.4	5.8±0.9	1.7±0.9	1.3±0.4
D-Hazy	89.1±4	6.7±4.9	8.3±1.6	6.2±0.9	7.8±0.6	5.4±1.3	1.6±0.9	1.1±0.3
Real-world	87.6±7	8.9±3.1	8.7±2.7	7.7±0.9	6.1±0.6	5.8±0.9	1.6±0.8	1.3±0.2

Table 6.8 depicts the analysis of ET in seconds. It can be seen from this table that OGPP take less execution time as compared to DCP [16], CAP [96], MDF [108] and GITF. The mean reduction in ET by using OGPP over available techniques is approximately 0.1279.

6.3 Summary

In this chapter, various gradient based profile priors have been designed. The modified filters have been implemented to remove the halo and gradient reversal artefact problems. Designed gradient based profile priors have an ability to minimize the color distortion rate and it also preserves the texture information of weather degraded images in an efficient manner. From the visual analysis, it has been observed that the proposed techniques restore the weather degraded images in more efficient manner compared to the existing techniques. The proposed techniques have shown more naturally restored images with vivid color, enhanced visibility, rich spatial, spectral, and texture information. The proposed techniques also provide more real sky color without introducing halo and gradient reversal artefacts around edges. Therefore, if the restored image has good quantitative analysis that means it has lesser number of artefacts, colors and edge distortion values. Moreover, the proposed techniques are computational faster than the existing visibility restoration techniques. Therefore, the proposed channel priors are more suitable for real-time imaging systems.

Chapter 7

Conclusions and future work

Outline

This chapter gives the concluding remarks on the research by highlighting the significant contributions of the work done. This chapter concludes the thesis by explaining the outcome of each chapter. Future directions of the research work have also been presented towards the end of this chapter.

7.1 Conclusions

Images captured in poor weather conditions such as fog, haze, and smog are degraded by the scattering of atmospheric particles. Therefore, the captured images have poor visibility and low contrast. It directly affects the performance of various computer vision applications. The degradation in obtained images is represented by the transmission map, which is one of the most significant step in the visibility restoration model. However, the estimation of transmission map is an under-constraint issue. Dark channel prior (DCP) is one of the commonly used technique to estimate the transmission map. DCP stated that most of the non-sky regions have at least one color channel (*i.e.,* red, green, or blue) containing low-intensity pixels. Extensive analyses demonstrated that most of the images satisfy same observation of DCP. It has achieved remarkable results when combined with the soft matting. But, soft matting greatly affects the computational speed. With this, DCP may become invalid when the objects in an image are inherently similar to the airlight. It is also not capable to restore the gray regions of weather degraded images.

From the existing literature, it has been found that the visibility restoration techniques are still a challenging research area due to different types of image scenes, climate, and illumination circumstances. Weather degradation is produced by the suspension of moisture droplets in the air. When light hits these droplets then it scatters and results in loss of contrast. Most of the techniques used for removing the effect of the weather degradation from outdoor images are based on the concept of Dark channel prior (DCP). DCP mainly depends upon the geometric examination of an image that identifies several regions in a foggy image having pixels with dark intensity. However, the transmission estimated by DCP introduces halo and gradient reversal artefacts. It also suffers from poor computational speed. Also, the major drawbacks of existing visibility restoration techniques are distortion in edges, texture, and color. These techniques also produce halo and gradient reversal artefacts.

To overcome these issues, in this research work, initially, efficient visibility restoration techniques have been designed and implemented by designing suitable filters such as Gain intervention trilateral filter (GITF) and Fourth-order partial differential equations based trilateral filter (FPDETF) to refine the transmission map obtained from DCP. Thereafter, modified restoration models have been developed by designing an Integrated visibility restoration model (IVRM) and Modified restoration model (MRM). In the end, novel channel priors have been proposed to overcome the shortcomings of DCP.

GITF has been tested on ten (five benchmarks and five real times) roadside foggy images. The experimental results reveal that the images obtained from GITF contains a lesser number of artefacts and also preserves more significant edges as compared to the competitive restoration techniques. It has been found that GITF improves the contrast gain by 1.76 % as compared to the existing competitive visibility restoration techniques. Also, GITF significantly reduces the percentage of saturated pixels and execution time by 1.96 % and 3.21%, respectively.

FPDETF has been tested on ten well-known remote sensing images and compared with seven competitive techniques. Comparative analysis has proven that FPDETF outperforms the existing techniques in terms of contrast gain, ratio of new visible edges, and ratio of the average gradient by 1.98%, 1.72% and 1.81%, respectively. Also, FPDETF reduces the percentage of saturated pixels and execution time by 2.07% and 3.41%, respectively. But, FPDETF suffers from sky-regions and color distortion problems especially in case of images affected by large weather gradients.

To overcome this issue, an Integrated visibility restoration model (IVRM) has been proposed. IVRM has integrated DCP, Bright channel prior (BCP), and gain intervention filter. Extensive experiments have been done to evaluate the effectiveness of IVRM. It has been found that IVRM has an ability to remove halo and gradient reversal artefacts. IVRM outperforms the existing techniques in terms of new visible edges and average gradient by 1.84% and 1.85%, respectively. IVRM reduces the percentage of saturated pixels by 2.13% as compared to competitive visibility restoration techniques. However, GITF, FPDETF, and IVRM suffer from the issue of noise when estimated transmission map approaches toward zero. As a consequence, the restored color could deviate from the actual object and the restored images look like the artificial images.

To overcome this issue, a Modified restoration model (MRM) based DCP has been proposed. To improve the atmospheric veil further, a modified joint trilateral filter has also been implemented to refine the transmission map. The experimental results have proven that MRM outperforms other visibility restoration techniques in terms of contrast gain, a ratio of new visible edges, and ratio of the average gradient by 2.13%, 1.91% and 1.92%, respectively. Also, MRM reduces the percentage of saturated pixels by 2.34%.

However, the techniques designed so far such as GITF, FPDETF, IVRM, and MRM are not so-effective to preserve the texture details of weather degraded images with a complex background and large weather gradient. Therefore, in this research work, two novel channel priors namely Gradient profile prior (GPP) and Oblique gradient profile prior (OGPP) have been designed and implemented to estimate depth map in a more efficient manner. Extensive experiments have shown that GPP outperforms the existing image techniques in terms of contrast gain, the ratio of new visible edges, and ratio of the average gradient by 1.91%, 1.97% and 1.98%, respectively. GPP also reduces the percentages of saturated pixels, perceptual fog density and execution time by 2.31%, 1.47% and 2.43%, respectively as compared to the existing visibility restoration techniques. Thus, GPP significantly improves the spatial and radiometric information of remote sensing images.

However, GPP is not capable to evaluate oblique edges. Therefore, an Oblique gradient profile prior (OGPP) has been proposed to efficiently evaluate the transmission map and atmospheric veil. The transmission map has also been refined by developing a local activity-tuned anisotropic diffusion based filter. Thereafter, image restoration is performed using estimated transmission function. The performance of OGPP has been compared with seven recently developed visibility restoration techniques over synthetic and real-life foggy images. Extensive analysis has shown the supremacy of OGPP in removing the fog from still images as compared to the existing techniques. It has been found that OGPP outperforms the existing image techniques in terms of Contrast gain (C_g), a ratio of new visible edges, a ratio of an average gradient, Peak signal to noise ratio (PSNR), and Structural similarity index metric (SSIM) by 1.94%, 2.01%, 2.17%, 3.72% and 1.31%, respectively. OGPP also reduces the percentages of saturated pixels, perceptual fog density, and execution time by 2.41%, 1.52% and 2.79%, respectively as compared to the competitive visibility restoration techniques.

Therefore, GPP and OGPP have an ability to minimize the color distortion rate and also preserve the texture information of weather degraded images. From the visual analysis, it has been found that GPP and OGPP restore the weather degraded images with vivid color, enhanced visibility, rich spatial, spectral and texture information, and real color sky, without the halo and gradient reversal artefacts around edges. Therefore, if the restored image has the good quantitative analysis that means it has lesser number of artefacts and colors and edge distortion values. Moreover, the proposed techniques are faster than the existing visibility restoration techniques. Therefore, the proposed techniques are more suitable for real-time imaging systems.

7.2 Future work

The work presented in this thesis can be extended in the following future directions.

i It would be exciting to examine the possible fusion of the proposed visibility restoration techniques to improve the spatial resolution and spectral information of restored images.

ii Multi-objective meta-heuristic techniques can be used to tune the parameters of the proposed techniques.

iii All the proposed techniques can be enhanced to remove the effect of smog from the weather degraded images.

iv The proposed techniques can be applied to other types of images such as underwater images, indoor images, *etc.*

v The transform domain based visibility restoration techniques can be considered to restore the weather degraded images in a more efficient manner.

List of publications

1. Dilbag Singh and Vijay Kumar. "A comprehensive review of computational dehazing techniques", **Accepted** in Archives of Computational Methods in Engineering, Springer. **[SCI Indexed, Impact Factor 6.6]**
2. Dilbag Singh and Vijay Kumar. "Image Dehazing using Moore neighborhood based Gradient Profile Prior", **Accepted** in Signal Processing: Image Communication, Elsevier. **[SCI Indexed, Impact Factor 2.073]**
3. Dilbag Singh and Vijay Kumar. "Modified gain intervention filter based dehazing technique." Journal of Modern Optics, vol. 64, issue. 20, pp. 2165-2178, 2017. **[SCI Indexed, Impact Factor 1.328]**
4. Dilbag Singh and Vijay Kumar. "Dehazing of remote sensing images using improved restoration model based dark channel prior." Imaging Science Journal vol. 65, issue. 5, pp. 282-292, 2017. **[SCI Indexed, Impact Factor 0.451]**
5. Dilbag Singh and Vijay Kumar. "Dehazing of remote sensing images using fourth-order partial differential equations based trilateral filter." IET Computer Vision, vol. 12, issue. 2, pp. 208 - 219, 2017. **[SCI Indexed, Impact Factor 0.878]**
6. Dilbag Singh and Vijay Kumar. "Comprehensive survey on haze removal techniques." Multimedia Tools and Applications, vol. 77, issue. 8, pp. 9595-9620, 2018. **[SCI Indexed, Impact Factor 1.530]**
7. Dilbag Singh and Vijay Kumar. "Defogging of road images using the gain coefficient based trilateral filter." Journal of Electronic Imaging, vol 27, issue. 1 pp. 013004, 2018. **[SCI Indexed, Impact Factor 0.754]**
8. Dilbag Singh and Vijay Kumar. "Single image haze removal using integrated dark and bright channel prior." Modern Physics Letters, vol. 32, issue 04, 2018. **[SCI Indexed, Impact Factor 0.617]**

9. Dilbag Singh and Vijay Kumar. "Single image defogging by gain gradient image filter." Science China Information Sciences, 2018. **[SCI Indexed, Impact Factor 1.628]**

10. Dilbag Singh and Vijay Kumar. "Dehazing of outdoor images using notch based integral guided filter." Multimedia Tools and Applications, pp. 1-24, 2018. **[SCI Indexed, Impact Factor 1.530]**

11. Dilbag Singh and Vijay Kumar. "A novel dehazing model for remote sensing images." Computers & Electrical Engineering, vol. 69, pp. 14-27, 2018. **[SCI Indexed, Impact Factor 1.570]**

12. Dilbag Singh and Vijay Kumar. "A novel fog removal technique for still images using oblique gradient prior", **Accepted with major revision** in IEEE transactions on multimedia. **[SCI Indexed, Impact Factor 3.509]**

13. Dilbag Singh and Vijay Kumar. " Image dehazing using gradient profile prior and guided L_0 filter", **Minor Revision** in Information science, Elsevier **[SCI Indexed, Impact Factor 4.305]**

Bibliography

[1] Y. Xu, J. Wen, L. Fei, and Z. Zhang, “Review of video and image defogging algorithms and related studies on image restoration and enhancement,” *IEEE Access*, vol. 4, pp. 165–188, 2016.

[2] J. M. Crebolder and R. B. Sloan, “Determining the effects of eyewear fogging on visual task performance,” *Applied ergonomics*, vol. 35, no. 4, pp. 371–381, 2004.

[3] M. Singh, M. C. Govil, and E. S. Pilli, “Chact: Convex hull enabled active contour technique for salient object detection,” *IEEE Access*, vol. 6, pp. 22441–22451, 2018.

[4] N.-E. Rikli and M. Alabdulkarim, “Cross-layer-based adaptive video transport over low bit-rate multihop wsns,” *Canadian Journal of Electrical and Computer Engineering*, vol. 37, no. 4, pp. 182–191, 2014.

[5] B. H. Chen, S. C. Huang, and F. C. Cheng, “A high-efficiency and high-speed gain intervention refinement filter for haze removal,” *Journal of Display Technology*, vol. 12, no. 7, pp. 753–759, 2016.

[6] H.-Y. Yang, P.-Y. Chen, C.-C. Huang, Y.-Z. Zhuang, and Y.-H. Shiau, “Low complexity underwater image enhancement based on dark channel prior,” in *Innovations in Bio-inspired Computing and Applications (IBICA), 2011 Second International Conference on*, pp. 17–20, IEEE, 2011.

[7] L. Guan, “Model-based neural evaluation and iterative gradient optimization in image restoration and statistical filtering,” *Journal of Electronic Imaging*, vol. 4, no. 4, pp. 407–413, 1995.

[8] X. Lian, Y. Pang, and A. Yang, “Learning intensity and detail mapping parameters for dehazing,” *Multimedia Tools and Applications*, pp. 1–26, 2017.

[9] Y. Yang, X. Sun, H. Yang, and C.-T. Li, “Removable visible image watermarking algorithm in the discrete cosine transform domain,” *Journal of Electronic Imaging*, vol. 17, no. 3, pp. 033008–033008, 2008.

[10] H. Tan, X. He, Z. Wang, and G. Liu, “Parallel implementation and optimization of high definition video real-time dehazing,” *Multimedia Tools and Applications*, pp. 1–22, 2016.

[11] K. B. Gibson and T. Q. Nguyen, “An analysis of single image defogging methods using a color ellipsoid framework,” *EURASIP Journal on Image and Video Processing*, vol. 2013, no. 1, p. 37, 2013.

[12] V. Paidi, H. Fleyeh, J. Hakansson, and R. G. Nyberg, “Smart parking sensors, technologies and applications for open parking lots: a review,” *IET Intelligent Transport Systems*, vol. 12, no. 8, pp. 735–741, 2018.

[13] R. T. Tan, “Visibility in bad weather from a single image,” in *2008 IEEE Conference on Computer Vision and Pattern Recognition*, pp. 1–8, June 2008.

[14] R. Srivastava and S. Srivastava, “Restoration of poisson noise corrupted digital images with nonlinear pde based filters along with the choice of regularization parameter estimation,” *Pattern Recognition Letters*, vol. 34, no. 10, pp. 1175–1185, 2013.

[15] R. Kawakami, H. Zhao, R. T. Tan, and K. Ikeuchi, “Camera spectral sensitivity and white balance estimation from sky images,” *International Journal of Computer Vision*, vol. 105, no. 3, pp. 187–204, 2013.

[16] K. He, J. Sun, and X. Tang, “Single image haze removal using dark channel prior,” *IEEE Transactions on Pattern Analysis and Machine Intelligence*, vol. 33, no. 12, pp. 2341–2353, 2011.

[17] R. Fattal, “Single image dehazing,” *ACM transactions on graphics (TOG)*, vol. 27, no. 3, p. 72, 2008.

[18] X. Fu, J. Wang, D. Zeng, Y. Huang, and X. Ding, “Remote sensing image enhancement using regularized-histogram equalization and dct,” *IEEE Geoscience and Remote Sensing Letters*, vol. 12, no. 11, pp. 2301–2305, 2015.

[19] W. Zhang and X. Hou, “Estimation algorithm of atmospheric light based on ant colony optimization,” in *Proceedings of the 2017 International Conference on Intelligent Systems, Metaheuristics & Swarm Intelligence*, pp. 20–25, ACM, 2017.

[20] L. Wang, W. Xie, and J. Pei, “Patch-based dark channel prior dehazing for rs multi-spectral image,” *Chinese Journal of Electronics*, vol. 24, no. 3, pp. 573–578, 2015.

[21] W. Zhang, J. Liang, H. Ju, L. Ren, E. Qu, and Z. Wu, “Study of visibility enhancement of hazy images based on dark channel prior in polarimetric imaging,” *Optik International Journal for Light and Electron Optics*, vol. 130, pp. 123 – 130, 2017.

[22] S. Liu, M. A. Rahman, S. C. Liu, C. Y. Wong, C.-F. Lin, H. Wu, and N. Kwok, “Image de-hazing from the perspective of noise filtering,” *Computers and Electrical Engineering*, 2016.

[23] Y. Kaufman, D. Tanré, H. Gordon, T. Nakajima, J. Lenoble, R. Frouin, H. Grassl, B. Herman, M. King, and P. Teillet, “Passive remote sensing of tropospheric aerosol and atmospheric correction for the aerosol effect,” *Journal of Geophysical Research: Atmospheres*, vol. 102, no. D14, pp. 16815–16830, 1997.

[24] S. G. Narasimhan and S. K. Nayar, “Vision and the atmosphere,” *International Journal of Computer Vision*, vol. 48, no. 3, pp. 233–254, 2002.

[25] H. Koschmieder, “Luftlicht und sichtweite,” *Naturwissenschaften*, vol. 26, no. 32, pp. 521–528, 1938.

[26] E. J. McCartney, “Optics of the atmosphere: scattering by molecules and particles,” *New York, John Wiley and Sons, Inc., 1976. 421 p.*, 1976.

[27] A. K. S. Kushwaha and R. Srivastava, “Framework for dynamic background modeling and shadow suppression for moving object segmentation in complex wavelet domain,” *Journal of Electronic Imaging*, vol. 24, no. 5, p. 051005, 2015.

[28] Y. Song, J. Li, X. Wang, and X. Chen, “Single image dehazing using ranking convolutional neural network,” *IEEE Transactions on Multimedia*, 2017.

[29] L.-F. Shi, B.-H. Chen, S.-C. Huang, A. Larin, O. Seredin, A. Kopylov, and S.-Y. Kuo, “Removing haze particles from single image via exponential inference with support vector data description,” *IEEE Transactions on Multimedia*, vol. 20, no. 9, pp. 2503–2512, 2018.

[30] S. G. Narasimhan and S. K. Nayar, “Contrast restoration of weather degraded images,” *IEEE transactions on pattern analysis and machine intelligence*, vol. 25, no. 6, pp. 713–724, 2003.

[31] R. T. Tan, “Visibility in bad weather from a single image,” in *Computer Vision and Pattern Recognition, 2008. CVPR 2008. IEEE Conference on*, pp. 1–8, IEEE, 2008.

[32] P. Purkait and B. Chanda, “Morphologic gain-controlled regularization for edge-preserving super-resolution image reconstruction,” *Signal, image and video processing*, vol. 7, no. 5, pp. 925–938, 2013.

[33] M. I. Anwar and A. Khosla, "Vision enhancement through single image fog removal," *Engineering Science and Technology, an International Journal*, vol. 20, no. 3, pp. 1075 – 1083, 2017.

[34] K. Pal, M. C. Govil, and M. Ahmed, "Slack time–based scheduling scheme for live video streaming in p2p network," *International Journal of Communication Systems*, vol. 31, no. 2, p. e3440, 2018.

[35] B. Cai, X. Xu, K. Jia, C. Qing, and D. Tao, "Dehazenet: An end-to-end system for single image haze removal," *IEEE Transactions on Image Processing*, vol. 25, no. 11, pp. 5187–5198, 2016.

[36] F. Serdio, E. Lughofer, A.-C. Zavoianu, K. Pichler, M. Pichler, T. Buchegger, and H. Efendic, "Improved fault detection employing hybrid memetic fuzzy modeling and adaptive filters," *Applied Soft Computing*, vol. 51, pp. 60–82, 2017.

[37] J. Park, J.-H. Han, and B.-U. Lee, "Performance of bilateral filtering on gaussian noise," *Journal of Electronic Imaging*, vol. 23, no. 4, pp. 043024–043024, 2014.

[38] D. Hao, Q. Li, and C. Li, "Single-image-based rain streak removal using multidimensional variational mode decomposition and bilateral filter," *Journal of Electronic Imaging*, vol. 26, no. 1, pp. 013020–013020, 2017.

[39] S. Fang, Q. Shi, and Y. Cao, "Adaptive removal of real noise from a single image," *Journal of Electronic Imaging*, vol. 22, no. 3, pp. 033014–033014, 2013.

[40] H. Kishan and C. S. Seelamantula, "Patch-based and multiresolution optimum bilateral filters for denoising images corrupted by gaussian noise," *Journal of Electronic Imaging*, vol. 24, no. 5, pp. 053021–053021, 2015.

[41] Z. Wang and J. Y. Hardeberg, "Development of an adaptive bilateral filter for evaluating color image difference," *Journal of Electronic Imaging*, vol. 21, no. 2, pp. 023021–1, 2012.

[42] H.-H. Chang and W.-C. Chu, "Restoration algorithm for image noise removal using double bilateral filtering," *Journal of Electronic Imaging*, vol. 21, no. 2, pp. 023028–1, 2012.

[43] J.-P. Tarel and N. Hautiere, "Fast visibility restoration from a single color or gray level image," in *2009 IEEE 12th International Conference on Computer Vision*, pp. 2201–2208, IEEE, 2009.

[44] J. Long, Z. Shi, W. Tang, and C. Zhang, "Single remote sensing image dehazing," *IEEE Geoscience and Remote Sensing Letters*, vol. 11, no. 1, pp. 59–63, 2014.

[45] S. Serikawa and H. Lu, “Underwater image dehazing using joint trilateral filter,” *Computers & Electrical Engineering*, vol. 40, no. 1, pp. 41–50, 2014.

[46] Z. Wang and Y. Feng, “Fast single haze image enhancement,” *Computers & Electrical Engineering*, vol. 40, no. 3, pp. 785–795, 2014.

[47] L. Xiong, H. Li, and L. Xu, “An enhancement method for color retinal images based on image formation model,” *Computer Methods and Programs in Biomedicine*, vol. 143, pp. 137 – 150, 2017.

[48] X. Tang and L. Jiao, “Fusion similarity-based reranking for sar image retrieval,” *IEEE Geoscience and Remote Sensing Letters*, vol. 14, no. 2, pp. 242–246, 2017.

[49] A. Ansari, H. Danyali, and M. S. Helfroush, “Hs remote sensing image restoration using fusion with ms images by em algorithm,” *IET Signal Processing*, vol. 11, no. 1, pp. 95–103, 2017.

[50] Q. Wei, J. Bioucas-Dias, N. Dobigeon, J. Y. Tourneret, M. Chen, and S. Godsill, “Multiband image fusion based on spectral unmixing,” *IEEE Transactions on Geoscience and Remote Sensing*, vol. 54, no. 12, pp. 7236–7249, 2016.

[51] M. A. Qureshi, A. Beghdadi, and M. Deriche, “Towards the design of a consistent image contrast enhancement evaluation measure,” *Signal Processing: Image Communication*, vol. 58, pp. 212 – 227, 2017.

[52] M. Ju, Z. Gu, and D. Zhang, “Single image haze removal based on the improved atmospheric scattering model,” *Neurocomputing*, vol. 260, pp. 180 – 191, 2017.

[53] C. Qing, F. Yu, X. Xu, W. Huang, and J. Jin, “Underwater video dehazing based on spatial–temporal information fusion,” *Multidimensional Systems and Signal Processing*, vol. 27, no. 4, pp. 909–924, 2016.

[54] R. Kumar, B. K. Kaushik, and R. Balasubramanian, “Fpga implementation of image dehazing algorithm for real time applications,” in *Applications of Digital Image Processing XL*, vol. 10396, p. 1039633, International Society for Optics and Photonics, 2017.

[55] L. Zheng, H. Shi, and M. Gu, “Infrared traffic image enhancement algorithm based on dark channel prior and gamma correction,” *Modern Physics Letters B*, vol. 31, no. 19-21, p. 1740044, 2017.

[56] S.-C. Huang, B.-H. Chen, and Y.-J. Cheng, “An efficient visibility enhancement algorithm for road scenes captured by intelligent transportation systems,” *IEEE Transactions on Intelligent Transportation Systems*, vol. 15, no. 5, pp. 2321–2332, 2014.

[57] A. Conca, C. Ridella, and E. Sapori, “A risk assessment for road transportation of dangerous goods: a routing solution,” *Transportation Research Procedia*, vol. 14, pp. 2890–2899, 2016.

[58] K. Fang, G. Y. Ke, and M. Verma, “A routing and scheduling approach to rail transportation of hazardous materials with demand due dates,” *European Journal of Operational Research*, vol. 261, no. 1, pp. 154–168, 2017.

[59] J. P. Kennedy and J. M. Wilson, “Liabilities and responsibilities: ocean transportation intermediaries (otis) and the distribution of counterfeit goods,” *Maritime Economics & Logistics*, vol. 19, no. 1, pp. 182–187, 2017.

[60] A. Beck, J. Henneberger, S. Schöpfer, J. Fugal, and U. Lohmann, “Hologondel: in situ cloud observations on a cable car in the swiss alps using a holographic imager,” *Atmospheric Measurement Techniques*, vol. 10, no. 2, pp. 459–476, 2017.

[61] A. S. A. Ghani and N. A. M. Isa, “Automatic system for improving underwater image contrast and color through recursive adaptive histogram modification,” *Computers and Electronics in Agriculture*, vol. 141, pp. 181 – 195, 2017.

[62] U. A. Nnolim, “Improved partial differential equation-based enhancement for underwater images using local–global contrast operators and fuzzy homomorphic processes,” *IET Image Processing*, vol. 11, no. 11, pp. 1059–1067, 2017.

[63] M. Amintoosi, M. Fathy, and N. Mozayani, “Video enhancement through image registration based on structural similarity,” *The Imaging Science Journal*, vol. 59, no. 4, pp. 238–250, 2011.

[64] A. K. Tripathi and S. Mukhopadhyay, “Removal of fog from images: A review,” *IETE Technical Review*, vol. 29, no. 2, pp. 148–156, 2012.

[65] A. Tripathi and S. Mukhopadhyay, “Single image fog removal using anisotropic diffusion,” *IET Image processing*, vol. 6, no. 7, pp. 966–975, 2012.

[66] N. Hautiere, J.-P. Tarel, D. Aubert, and E. Dumont, “Blind contrast enhancement assessment by gradient ratioing at visible edges,” *Image Analysis & Stereology*, vol. 27, no. 2, pp. 87–95, 2011.

[67] L. K. Choi, J. You, and A. C. Bovik, “Referenceless prediction of perceptual fog density and perceptual image defogging,” *IEEE Transactions on Image Processing*, vol. 24, no. 11, pp. 3888–3901, 2015.

[68] N. Vuković and Z. Miljković, “A growing and pruning sequential learning algorithm of hyper basis function neural network for function approximation,” *Neural Networks*, vol. 46, pp. 210–226, 2013.

[69] R. O. Duda, P. E. Hart, and D. G. Stork, *Pattern classification*. John Wiley & Sons, 2012.

[70] S. He, Q. Yang, R. W. Lau, and M.-H. Yang, "Fast weighted histograms for bilateral filtering and nearest neighbor searching," *IEEE Transactions on Circuits and Systems for Video Technology*, vol. 26, no. 5, pp. 891–902, 2016.

[71] B.-H. Chen, S.-C. Huang, and J. H. Ye, "Hazy image restoration by bi-histogram modification," *ACM Transactions on Intelligent Systems and Technology (TIST)*, vol. 6, no. 4, p. 50, 2015.

[72] S. Emberton, L. Chittka, and A. Cavallaro, "Underwater image and video dehazing with pure haze region segmentation," *Computer Vision and Image Understanding*, pp. –, 2017.

[73] W. Wang, X. Yuan, X. Wu, and Y. Liu, "Fast image dehazing method based on linear transformation," *IEEE Transactions on Multimedia*, vol. 19, no. 6, pp. 1142–1155, 2017.

[74] C. O. Ancuti and C. Ancuti, "Single image dehazing by multi-scale fusion," *IEEE Transactions on Image Processing*, vol. 22, no. 8, pp. 3271–3282, 2013.

[75] H. Wen, Y. Tian, T. Huang, and W. Gao, "Single underwater image enhancement with a new optical model," in *Circuits and Systems (ISCAS), 2013 IEEE International Symposium on*, pp. 753–756, IEEE, 2013.

[76] X. Zhao, T. Jin, and S. Qu, "Deriving inherent optical properties from background color and underwater image enhancement," *Ocean Engineering*, vol. 94, pp. 163–172, 2015.

[77] Y.-T. Peng, X. Zhao, and P. C. Cosman, "Single underwater image enhancement using depth estimation based on blurriness," in *Image Processing (ICIP), 2015 IEEE International Conference on*, pp. 4952–4956, IEEE, 2015.

[78] Z. Mi, H. Zhou, Y. Zheng, and M. Wang, "Single image dehazing via multi-scale gradient domain contrast enhancement," *IET Image Processing*, vol. 10, no. 3, pp. 206–214, 2016.

[79] Z. Bashir, G. Raja, and M. O. Ullah, "A video enhancement algorithm for low-lighting environment using field programmable gate array (fpga) architecture," *NED University Journal of Research*, vol. 13, no. 4, p. 81, 2016.

[80] Y. Li, H. Lu, J. Li, X. Li, Y. Li, and S. Serikawa, "Underwater image de-scattering and classification by deep neural network," *Computers & Electrical Engineering*, vol. 54, pp. 68–77, 2016.

[81] H. Zhao, C. Xiao, J. Yu, and X. Xu, "Single image fog removal based on local extrema," *IEEE/CAA Journal of Automatica Sinica*, vol. 2, no. 2, pp. 158–165, 2015.

[82] I. Riaz, T. Yu, Y. Rehman, and H. Shin, "Single image dehazing via reliability guided fusion," *Journal of Visual Communication and Image Representation*, vol. 40, pp. 85 – 97, 2016.

[83] F.-C. Cheng, C.-C. Cheng, P.-H. Lin, and S.-C. Huang, "A hierarchical airlight estimation method for image fog removal," *Engineering Applications of Artificial Intelligence*, vol. 43, pp. 27–34, 2015.

[84] G. Ge, Z. Wei, and J. Zhao, "Fast single-image dehazing using linear transformation," *Optik-International Journal for Light and Electron Optics*, vol. 126, no. 21, pp. 3245–3252, 2015.

[85] B. Xie, F. Guo, and Z. Cai, "Improved single image dehazing using dark channel prior and multi-scale retinex," in *Intelligent System Design and Engineering Application (ISDEA), 2010 International Conference on*, vol. 1, pp. 848–851, IEEE, 2010.

[86] K. Nishino, L. Kratz, and S. Lombardi, "Bayesian defogging," *International journal of computer vision*, vol. 98, no. 3, pp. 263–278, 2012.

[87] L. Caraffa and J.-P. Tarel, "Stereo reconstruction and contrast restoration in daytime fog," in *Asian Conference on Computer Vision*, pp. 13–25, Springer, 2012.

[88] Y. Meng, Gaofeng an d Wang, J. Duan, S. Xiang, and C. Pan, "Efficient image dehazing with boundary constraint and contextual regularization," in *Proceedings of the IEEE international conference on computer vision*, pp. 617–624, 2013.

[89] W. Sun, "A new single-image fog removal algorithm based on physical model," *Optik - International Journal for Light and Electron Optics*, vol. 124, no. 21, pp. 4770 – 4775, 2013.

[90] Y. Xue, J. Ren, H. Su, M. Wen, and C. Zhang, "Parallel implementation and optimization of haze removal using dark channel prior based on cuda," in *High Performance Computing*, pp. 99–109, Springer, 2013.

[91] R. Fattal, "Dehazing using color-lines," *ACM Transactions on Graphics (TOG)*, vol. 34, no. 1, p. 13, 2014.

[92] Z. Fu, Y. Yang, C. Shu, Y. Li, H. Wu, and J. Xu, "Improved single image dehazing using dark channel prior," *Journal of Systems Engineering and Electronics*, vol. 26, pp. 1070–1079, Oct 2015.

[93] J. Wang, N. He, and K. Lu, "A new single image dehazing method with msrcr algorithm," in *Proceedings of the 7th International Conference on Internet Multimedia Computing and Service*, p. 19, ACM, 2015.

[94] T. Yu, I. Riaz, J. Piao, and H. Shin, "Real-time single image dehazing using block-to-pixel interpolation and adaptive dark channel prior," *IET Image Processing*, vol. 9, no. 9, pp. 725–734, 2015.

[95] A. Kumari and S. K. Sahoo, "Fast single image and video deweathering using look-up-table approach," *AEU-International Journal of Electronics and Communications*, vol. 69, no. 12, pp. 1773–1782, 2015.

[96] Q. Zhu, J. Mai, and L. Shao, "A fast single image haze removal algorithm using color attenuation prior," *IEEE Transactions on Image Processing*, vol. 24, no. 11, pp. 3522–3533, 2015.

[97] R. Wang, R. Li, and H. Sun, "Haze removal based on multiple scattering model with superpixel algorithm," *Signal Processing*, vol. 127, pp. 24–36, 2016.

[98] H. Yuan, C. Liu, Z. Guo, and Z. Sun, "A region-wised medium transmission based image dehazing method," *IEEE Access*, vol. 5, pp. 1735–1742, 2017.

[99] J. Li, H. Zhang, D. Yuan, and M. Sun, "Single image dehazing using the change of detail prior," *Neurocomputing*, vol. 156, pp. 1–11, 2015.

[100] Y.-T. Peng and P. C. Cosman, "Underwater image restoration based on image blurriness and light absorption," *IEEE Transactions on Image Processing*, vol. 26, no. 4, pp. 1579–1594, 2017.

[101] M. Ding and L. Wei, "Single-image haze removal using the mean vector l2-norm of rgb image sample window," *Optik-International Journal for Light and Electron Optics*, vol. 126, no. 23, pp. 3522–3528, 2015.

[102] Z. Li, J. Zheng, Z. Zhu, W. Yao, and S. Wu, "Weighted guided image filtering.," *IEEE Transactions on Image processing*, vol. 24, no. 1, pp. 120–129, 2015.

[103] W. Sun, H. Wang, C. Sun, B. Guo, W. Jia, and M. Sun, "Fast single image haze removal via local atmospheric light veil estimation," *Computers & Electrical Engineering*, vol. 46, pp. 371–383, 2015.

[104] B. Jiang, H. Meng, X. Ma, L. Wang, Y. Zhou, P. Xu, S. Jiang, and X. Meng, "Night-time image dehazing with modified models of color transfer and guided image filter," *Multimedia Tools and Applications*, vol. 77, no. 3, pp. 3125–3141, 2018.

[105] Z. Li and J. Zheng, "Edge-preserving decomposition-based single image haze removal," *IEEE Transactions on Image Processing*, vol. 24, no. 12, pp. 5432–5441, 2015.

[106] J.-H. Kim, W.-D. Jang, J.-Y. Sim, and C.-S. Kim, "Optimized contrast enhancement for real-time image and video dehazing," *Journal of Visual Communication and Image Representation*, vol. 24, no. 3, pp. 410 – 425, 2013.

[107] D. Wang and J. Zhu, "Fast smoothing technique with edge preservation for single image dehazing," *IET Computer Vision*, vol. 9, no. 6, pp. 950–959, 2015.

[108] Y. K. Wang and C. T. Fan, "Single image defogging by multiscale depth fusion," *IEEE Transactions on Image Processing*, vol. 23, pp. 4826–4837, Nov 2014.

[109] G. Buchsbaum, "A spatial processor model for object colour perception," *Journal of the Franklin institute*, vol. 310, no. 1, pp. 1–26, 1980.

[110] R. Achanta, S. Hemami, F. Estrada, and S. Susstrunk, "Frequency-tuned salient region detection," in *Computer vision and pattern recognition, 2009. cvpr 2009. ieee conference on*, pp. 1597–1604, IEEE, 2009.

[111] P. Burt and E. Adelson, "The laplacian pyramid as a compact image code," *IEEE Transactions on communications*, vol. 31, no. 4, pp. 532–540, 1983.

[112] Z. Ma, J. Wen, C. Zhang, Q. Liu, and D. Yan, "An effective fusion defogging approach for single sea fog image," *Neurocomputing*, vol. 173, pp. 1257 – 1267, 2016.

[113] J. Zhang and S. Hu, "A gpu-accelerated real-time single image de-hazing method using pixel-level optimal de-hazing criterion," *Journal of real-time image processing*, vol. 9, no. 4, pp. 661–672, 2014.

[114] F. Guo, H. Peng, and J. Tang, "Genetic algorithm-based parameter selection approach to single image defogging," *Information Processing Letters*, 2016.

[115] H. Song, Y. Gao, and Y. Chen, "Fast image dehazing using fuzzy system and hybrid evolutionary algorithm," in *Foundations and Practical Applications of Cognitive Systems and Information Processing*, pp. 275–283, Springer, 2014.

[116] C.-L. Hung, R.-Y. Yan, and H.-H. Wang, "Parallel image dehazing algorithm based on gpu using fuzzy system and hybird evolution algorithm," in *Software Engineering, Artificial Intelligence, Networking and Parallel/Distributed Computing (SNPD), 2016 17th IEEE/ACIS International Conference on*, pp. 581–583, IEEE, 2016.

[117] X. Zhao, W. Ding, C. Liu, and H. Li, “Haze removal for uav aerial video based on optimization of spatial-temporal coherence,” *IET Image Processing*, vol. 12, pp. 88–97, 2017.

[118] A. Galdran, J. Vazquez-Corral, D. Pardo, and M. Bertalmío, “Enhanced variational image dehazing,” *SIAM Journal on Imaging Sciences*, vol. 8, no. 3, pp. 1519–1546, 2015.

[119] S. M. Yoon, “Visibility enhancement of fog-degraded image using adaptive total variation minimisation,” *The Imaging Science Journal*, vol. 64, no. 2, pp. 82–86, 2016.

[120] F. Fang, F. Li, X. Yang, C. Shen, and G. Zhang, “Single image dehazing and denoising with variational method,” in *Image Analysis and Signal Processing (IASP), 2010 International Conference on*, pp. 219–222, IEEE, 2010.

[121] C. Chen, M. N. Do, and J. Wang, “Robust image and video dehazing with visual artifact suppression via gradient residual minimization,” in *European Conference on Computer Vision*, pp. 576–591, Springer, 2016.

[122] A. Galdran, J. Vazquez-Corral, D. Pardo, and M. Bertalmío, “Fusion-based variational image dehazing,” *IEEE Signal Processing Letters*, vol. 24, no. 2, pp. 151–155, 2017.

[123] M. Zhu, B. He, and Q. Wu, “Single image dehazing based on dark channel prior and energy minimization,” *IEEE Signal Processing Letters*, vol. 25, pp. 174–178, Feb 2018.

[124] B. Li, W. Ren, D. Fu, D. Tao, D. Feng, W. Zeng, and Z. Wang, “Benchmarking single-image dehazing and beyond,” *IEEE Transactions on Image Processing*, vol. 28, pp. 492–505, Jan 2019.

[125] T. M. Bui and W. Kim, “Single image dehazing using color ellipsoid prior,” *IEEE Transactions on Image Processing*, vol. 27, pp. 999–1009, Feb 2018.

[126] Y. Song, J. Li, X. Wang, and X. Chen, “Single image dehazing using ranking convolutional neural network,” *IEEE Transactions on Multimedia*, vol. 20, pp. 1548–1560, June 2018.

[127] D. Wang and J. Zhu, “Fast smoothing technique with edge preservation for single image dehazing,” *IET Computer Vision*, vol. 9, no. 6, pp. 950–959, 2015.

[128] S. M. Yoon, “Visibility enhancement of fog-degraded image using adaptive total variation minimisation,” *The Imaging Science Journal*, vol. 64, no. 2, pp. 82–86, 2016.

[129] S. Vasamsetti, N. Mittal, B. C. Neelapu, and H. K. Sardana, “Wavelet based perspective on variational enhancement technique for underwater imagery,” *Ocean Engineering*, vol. 141, pp. 88 – 100, 2017.

[130] N. Zheng, G. Loizou, X. Jiang, X. Lan, and X. Li, “Computer vision and pattern recognition,” 2007.

[131] S. K. Nayar and S. G. Narasimhan, “Vision in bad weather,” in *Computer Vision, 1999. The Proceedings of the Seventh IEEE International Conference on*, vol. 2, pp. 820–827, IEEE, 1999.

[132] S. G. Narasimhan and S. K. Nayar, “Chromatic framework for vision in bad weather,” in *Computer Vision and Pattern Recognition, 2000. Proceedings. IEEE Conference on*, vol. 1, pp. 598–605, IEEE, 2000.

[133] Y. Y. Schechner, S. G. Narasimhan, and S. K. Nayar, “Instant dehazing of images using polarization,” in *Computer Vision and Pattern Recognition, 2001. CVPR 2001. Proceedings of the 2001 IEEE Computer Society Conference on*, vol. 1, pp. I–I, IEEE, 2001.

[134] S. Shwartz, E. Namer, and Y. Y. Schechner, “Blind haze separation,” in *Computer Vision and Pattern Recognition, 2006 IEEE Computer Society Conference on*, vol. 2, pp. 1984–1991, IEEE, 2006.

[135] J. P. Oakley and B. L. Satherley, “Improving image quality in poor visibility conditions using a physical model for contrast degradation,” *IEEE transactions on image processing*, vol. 7, no. 2, pp. 167–179, 1998.

[136] S. G. Narasimhan and S. K. Nayar, “Interactive (de) weathering of an image using physical models,” in *IEEE Workshop on color and photometric Methods in computer Vision*, vol. 6, p. 1, France, 2003.

[137] H. Xu, J. Guo, Q. Liu, and L. Ye, “Fast image dehazing using improved dark channel prior,” in *2012 IEEE International Conference on Information Science and Technology*, pp. 663–667, IEEE, 2012.

[138] N. Hautière, J.-P. Tarel, and D. Aubert, “Towards fog-free in-vehicle vision systems through contrast restoration,” in *Computer Vision and Pattern Recognition, 2007. CVPR’07. IEEE Conference on*, pp. 1–8, IEEE, 2007.

[139] J. Kopf, B. Neubert, B. Chen, M. Cohen, D. Cohen-Or, O. Deussen, M. Uyttendaele, and D. Lischinski, “Deep photo: Model-based photograph enhancement and viewing,” in *ACM transactions on graphics (TOG)*, vol. 27, p. 116, ACM, 2008.

[140] K. He, J. Sun, and X. Tang, "X.: Single image haze removal using dark channel prior," 2009.

[141] K. Tang, J. Yang, and J. Wang, "Investigating haze-relevant features in a learning framework for image dehazing," in *Proceedings of the IEEE Conference on Computer Vision and Pattern Recognition*, pp. 2995–3000, 2014.

[142] S. A. Dana Berman, Tali treibitz, "Non-local image dehazing," in *Proceedings of the IEEE conference on computer vision and pattern recognition*, pp. 1674–1682, 2016.

[143] S. Santra, R. Mondal, and B. Chanda, "Learning a patch quality comparator for single image dehazing," *IEEE Transactions on Image Processing*, vol. 27, pp. 4598–4607, Sept 2018.

[144] Q. Liu, X. Gao, L. He, and W. Lu, "Single image dehazing with depth-aware non-local total variation regularization," *IEEE Transactions on Image Processing*, vol. 27, pp. 5178–5191, Oct 2018.

[145] G. Papari, N. Idowu, and T. Varslot, "Fast bilateral filtering for denoising large 3d images," *IEEE Transactions on Image Processing*, vol. 26, no. 1, pp. 251–261, 2016.

[146] K. N. Chaudhury, D. Sage, and M. Unser, "Fast bilateral filtering using trigonometric range kernels," *IEEE Transactions on Image Processing*, vol. 20, no. 12, pp. 3376–3382, 2011.

[147] T. Cui, J. Tian, E. Wang, and Y. Tang, "Single image dehazing by latent region-segmentation based transmission estimation and weighted l1-norm regularisation," *IET Image Processing*, vol. 11, no. 2, pp. 145–154, 2017.

[148] W. Wang, X. Yuan, X. Wu, and Y. Liu, "Fast image dehazing method based on linear transformation," *IEEE Transactions on Multimedia*, vol. PP, no. 99, pp. 1–1, 2017.

[149] R. Xiang, X. Zhu, F. Wu, X. Jiang, and Q. Xu, "Guided filter based on multikernel fusion," *Journal of Electronic Imaging*, vol. 26, no. 1, pp. 26 – 26 – 8, 2017.

[150] J.-P. Tarel, N. Hautière, L. Caraffa, A. Cord, H. Halmaoui, and D. Gruyer, "Foggy road image database (frida)," *Online*, Summer 2012. http://www.lcpc.fr/english/products/image-databases/article/frida-foggy-road-image-database.

[151] Y.-L. You and M. Kaveh, “Fourth-order partial differential equations for noise removal,” *IEEE Transactions on Image Processing*, vol. 9, no. 10, pp. 1723–1730, 2000.

[152] G. Gilboa, N. Sochen, and Y. Y. Zeevi, “Image enhancement and denoising by complex diffusion processes,” *IEEE transactions on pattern analysis and machine intelligence*, vol. 26, no. 8, pp. 1020–1036, 2004.

[153] QUICKBIRD, “Global land cover facility,” *http://glcf.umd.edu/*, Dec 2016.

[154] IKONOS, “Ikonos satellites,” *http://www.geoimage.com.au/satellite/ikonos*, Dec 2016.

[155] MODIS, “Global land cover facility,” *http://glcf.umd.edu/*, Dec 2016.

[156] N. Sengee, A. Sengee, and H.-K. Choi, “Image contrast enhancement using bi-histogram equalization with neighborhood metrics,” *IEEE Transactions on Consumer Electronics*, vol. 56, no. 4, pp. 2727–2734, 2010.

[157] M. Kim and M. G. Chung, “Recursively separated and weighted histogram equalization for brightness preservation and contrast enhancement,” *IEEE Transactions on Consumer Electronics*, vol. 54, no. 3, pp. 1389–1397, 2008.

[158] C. Ancuti and C. O. Ancuti, “Effective contrast-based dehazing for robust image matching,” *IEEE Geoscience and Remote sensing letters*, vol. 11, no. 11, pp. 1871–1875, 2014.

[159] L. Wang, L. Xiao, H. Liu, and Z. Wei, “Local brightness adaptive image colour enhancement with wasserstein distance,” *IET Image Processing*, vol. 9, no. 1, pp. 43–53, 2015.

[160] L. Zheng, H. Shi, and M. Gu, “Infrared traffic image enhancement algorithm based on dark channel prior and gamma correction,” *Modern Physics Letters B*, vol. 31, no. 19-21, p. 1740044, 2017.

[161] L. Zeng and Y. Dai, “Single image dehazing based on combining dark channel prior and scene radiance constraint,” *Chinese Journal of Electronics*, vol. 25, no. 6, pp. 1114–1120, 2016.

[162] X. Zhu, R. Xiang, F. Wu, and X. Jiang, “Single image haze removal based on fusion darkness channel prior,” *Modern Physics Letters B*, vol. 31, no. 19-21, p. 1740037, 2017.

[163] K. He, J. Sun, and X. Tang, “Guided image filtering,” *IEEE transactions on pattern analysis and machine intelligence*, vol. 35, no. 6, pp. 1397–1409, 2013.

[164] X. Zhu, R. Xiang, F. Wu, and X. Jiang, “Single image haze removal based on fusion darkness channel prior,” *Modern Physics Letters B*, vol. 31, no. 19-21, p. 1740037, 2017.

[165] B. H. Chen, S. C. Huang, and F. C. Cheng, “A high efficiency and high-speed gain intervention refinement filter for haze removal,” *Journal of Display Technology*, vol. 12, no. 7, pp. 753–759, 2016.

[166] Y. Xu, X. Guo, H. Wang, F. Zhao, and L. Peng, “Single image haze removal using light and dark channel prior,” in *Communications in China (ICCC), 2016 IEEE/CIC International Conference on*, pp. 1–6, IEEE, 2016.

[167] S. Sensors, “Satellite imaging corporation,” *http://www.satimagingcorp.com/satellite-sensors/*, 2017.

[168] A. Su, X. Sun, Y. Zhang, and Q. Yu, “Efficient rotation-invariant histogram of oriented gradient descriptors for car detection in satellite images,” *IET Computer Vision*, vol. 10, no. 7, pp. 634–640, 2016.

[169] G. Liu, Z. Zhou, H. Zhong, and S. Xie, “Gradient descent with adaptive momentum for active contour models,” *IET Computer Vision*, vol. 8, pp. 287–298, August 2014.

[170] A. Kiani and M. R. Sahebi, “Edge detection based on the shannon entropy by piecewise thresholding on remote sensing images,” *IET Computer Vision*, vol. 9, no. 5, pp. 758–768, 2015.

[171] H. Dong and S. Dong, “Image-based surface deformation for multi-view three-dimensional facial reconstruction,” *IET Computer Vision*, vol. 8, no. 6, pp. 498–509, 2014.

[172] W. Y. Lee, C. Y. Li, and J. Y. Yen, “Integrating wavelet transformation with markov random field analysis for the depth estimation of light-field images,” *IET Computer Vision*, vol. 11, no. 5, pp. 358–367, 2017.

[173] R. Srivastava, O. Prakash, and A. Khare, “Local energy-based multimodal medical image fusion in curvelet domain,” *IET Computer Vision*, vol. 10, no. 6, pp. 513–527, 2016.

[174] W. Zuo, L. Zhang, C. Song, D. Zhang, and H. Gao, “Gradient histogram estimation and preservation for texture enhanced image denoising,” *IEEE transactions on image processing*, vol. 23, no. 6, pp. 2459–2472, 2014.

[175] X. Zhang and X. Feng, "Image denoising using local adaptive layered wiener filter in the gradient domain," *Multimedia Tools and Applications*, vol. 74, no. 23, pp. 10495–10514, 2015.

[176] X. Ding, L. Chen, X. Zheng, Y. Huang, and D. Zeng, "Single image rain and snow removal via guided l0 smoothing filter," *Multimedia Tools and Applications*, vol. 75, no. 5, pp. 2697–2712, 2016.

[177] Z. Li, L. Ding, and Y. Wang, "Score level fusion method based on multiple oblique gradient operators for face recognition," *Multimedia Tools and Applications*, vol. 75, no. 2, pp. 819–837, 2016.

[178] H. Ren, X. Yan, Y. Zhou, R. Cui, J. Sun, and Y. Liu, "Relative gradient local binary patterns method for face recognition under varying illuminations," *Journal of Electronic Imaging*, vol. 22, no. 4, p. 043013, 2013.

[179] H. Tan, X. He, Z. Wang, and G. Liu, "Parallel implementation and optimization of high definition video real-time dehazing," *Multimedia Tools and Applications*, vol. 76, no. 22, pp. 23413–23434, 2017.

[180] H. Lu, Q. Liu, M. Zhang, Y. Wang, and X. Deng, "Gradient-based low rank method and its application in image inpainting," *Multimedia Tools and Applications*, vol. 77, no. 5, pp. 5969–5993, 2018.

[181] Z. Ling, J. Gong, G. Fan, and X. Lu, "Optimal transmission estimation via fog density perception for efficient single image defogging," *IEEE Transactions on Multimedia*, vol. 20, no. 1, pp. 1699–1711, 2017.

[182] L. Zhao, J. Liang, H. Bai, L. Meng, A. Wang, and Y. Zhao, "Local activity-tuned image filtering for noise removal and image smoothing," *arXiv preprint arXiv:1707.02637*, 2017.

[183] L. Gun, L. Cuihua, Z. Yingpan, and H. Feijiang, "An improved speckle-reduction algorithm for sar images based on anisotropic diffusion," *Multimedia Tools and Applications*, vol. 76, no. 17, pp. 17615–17632, 2017.

[184] P. Perona and J. Malik, "Scale-space and edge detection using anisotropic diffusion," *IEEE Transactions on pattern analysis and machine intelligence*, vol. 12, no. 7, pp. 629–639, 1990.

[185] Y. Zaz, L. Masmoudi, K. Bouzouba, and L. Radouane, "A new adaptive anisotropic diffusion using the local intensity variance," in *International Conference: Sciences of Electronic, Technologies of Information and Telecommunications, Susa, Tunisia*, 2005.

[186] S.-M. Chao and D.-M. Tsai, “An improved anisotropic diffusion model for detail- and edge-preserving smoothing,” *Pattern Recognition Letters*, vol. 31, no. 13, pp. 2012–2023, 2010.

[187] B. Li, W. Ren, D. Fu, D. Tao, D. Feng, W. Zeng, and Z. Wang, “Reside: A benchmark for single image dehazing,” *arXiv preprint arXiv:1712.04143*, 2017.

[188] J.-P. Tarel, N. Hautiere, A. Cord, D. Gruyer, and H. Halmaoui, “Improved visibility of road scene images under heterogeneous fog,” in *Intelligent Vehicles Symposium (IV), 2010 IEEE*, pp. 478–485, Citeseer, 2010.

[189] J.-P. Tarel, N. Hautiere, L. Caraffa, A. Cord, H. Halmaoui, and D. Gruyer, “Vision enhancement in homogeneous and heterogeneous fog,” *IEEE Intelligent Transportation Systems Magazine*, vol. 4, no. 2, pp. 6–20, 2012.

[190] W. L. Kede Ma and Z. Wang, “Perceptual evaluation of single image dehazing algorithms,” in *in: Image Processing, Proc. IEEE*, pp. 3600–3604, Citeseer, 2015.

[191] C. D. V. Cosmin Ancuti, Codruta O. Ancuti, “D-hazy: A dataset to evaluate quantitatively dehazing algorithms,” in *IEEE International Conference on Image Processing (ICIP)*, ICIP’16, pp. 2226–2230, 2016.